

**CHARGE TRANSPORT STUDIES IN ORGANIC  
SEMICONDUCTOR FILMS**

*By*

**Soumen Samanta**

**Bhabha Atomic Research Center, Mumbai**

*Under the guidance of*

**Prof. D. K. Aswal**

*A thesis submitted to the*

*Board of Studies in Physical Sciences*

*In partial fulfillment of requirements*

*For the Degree of*

**DOCTOR OF PHILOSOPHY**

*of*

**HOMI BHABHA NATIONAL INSTITUTE**



**January, 2012**

## **STATEMENT BY AUTHOR**

This dissertation has been submitted in partial fulfillment of requirements for an advanced degree at Homi Bhabha National Institute (HBNI) and is deposited in the Library to be made available to borrowers under rules of the HBNI.

Brief quotations from this dissertation are allowable without special permission, provided that accurate acknowledgement of source is made. Requests for permission for extended quotation from or reproduction of this manuscript in whole or in part may be granted by the Competent Authority of HBNI when in his or her judgment the proposed use of the material is in the interests of scholarship. In all other instances, however, permission must be obtained from the author.

**Soumen Samanta**

## **DECLARATION**

I, hereby declare that the investigation presented in the thesis has been carried out by me. The work is original and has not been submitted earlier as a whole or in part for a degree / diploma at this or any other Institution / University.

**Soumen Samanta**

## **CERTIFICATE**

I hereby certify that I have read this dissertation prepared under my direction and recommend that this dissertation may be accepted as fulfilling the requirement for the degree of Doctor of Philosophy.

Date: January 27, 2012

**(Prof. D.K. Aswal)**

Place: Trombay

***Dedicated to my parents***

## List of Publications

### BOOK CHAPTER

- [1] Organic semiconductor films for chemiresistor gas sensor;  
A. Singh, A. K. Debnath, D. K. Aswal, A. Joshi, **S. Samanta**, V. Saxena, S. K. Gupta, J. V. Yakhmi, in *Molecular and Organic Electronics*, D.K. Aswal and J.V. Yakhmi (eds), Nova Science Publisher, New York, 2010. ISBN: 978-1-66-594-2.

### REFEREED JOURNAL

- [1] Influence of adsorbed oxygen on charge transport and chlorine gas sensing characteristics of cobalt phthalocyanine thin films;  
**S. Samanta**, A. Kumar, A. Singh, A. K. Debnath, D. K. Aswal, S. K. Gupta, *Chem. Papers* (2012, at press).
- [2] Improved charge conduction in cobalt-phthalocyanine thin films grown along  $36.8^\circ$  boundary of SrTiO<sub>3</sub> bicrystals;  
**S. Samanta**, A. Singh, A. Kumar, A. K. Debnath, D. K. Aswal, S. K. Gupta, J. V. Yakhmi, *Appl. Phys. Lett.* **98** 143301 (2011).
- [3] Bias and temperature dependent charge transport in high mobility cobalt-phthalocyanine thin films;  
**S. Samanta**, D. K. Aswal, A. Singh, A.K. Debnath, M. S. Kumar, Y. Hayakawa, S. K. Gupta, J.V. Yakhmi, *Appl. Phys. Lett.* **96** 013305 (2010).
- [4] Role of structural disorder in charge transport properties of cobalt-phthalocyanine thin films grown by molecular beam epitaxy;

- A. Singh, **S. Samanta**, A. Kumar, A. K. Debnath, D. K. Aswal, S. K. Gupta, J. V. Yakhmi, Y. Hayakawa S. K. Deshpande, *Org Electron.* **11** 1835 (2010).
- [5] Temperature dependent current-voltage characteristics of iron-phthalocyanine films;  
**S. Samanta**, A. K. Debnath, A. Singh, D. K. Aswal, S. K. Gupta J. V. Yakhmi, *J. Nanosci. Nanotechnol.* **9** 5262 (2009).
- [6] Parts-per-billion level chlorine sensors with fast kinetics using ultrathin cobalt phthalocyanine films;  
A. K. Debnath, **S. Samanta**, A. Singh, D. K. Aswal, S. K. Gupta, J. V. Yakhmi, *Chem. Phys. Lett.* **480** 185 (2009).
- [7] Oxygen induced hysteretic current-voltage characteristics of iron-phthalocyanine thin films;  
**S. Samanta**, A. Singh, A. K. Debnath, D. K. Aswal, S. K. Gupta, J. V. Yakhmi, S. Singh, S. Basu, S. K. Deshpande, *J Appl. Phys* **104** 073717 (2008).
- [8] Growth of iron phthalocyanine nanoweb and nanobrush using molecular beam epitaxy;  
A. K. Debnath **S. Samanta**, A. Singh, D. K. Aswal, S. K. Gupta, J. V. Yakhmi, S. K. Deshpande, A. K. Poswal C. Sürgers, *Physica E* **41** 154 (2008).

## CONFERENCE PROCEEDINGS

- [1] Charge transport of ultrathin CoPc films on (001) LaAlO<sub>3</sub> substrate;  
**S. Samanta**, A. Kumar, A. Singh, A. K. Debnath, D. K. Aswal, S. K. Gupta, *AIP Conference Proceedings of TFST, 2011. (to be published)*

- [2] Ordering induced enhancement of charge carrier mobility in CoPc thin films;  
**S. Samanta**, A. Singh, A. Kumar, A. K. Debnath, D. K. Aswal, S. K. Gupta, J. V. Yakhmi, *AIP Conference Proceedings 55<sup>th</sup> DAE solid state physics symposium* **1349** 1043 (2010).
- [3] Implication of structural disorder in the charge transport properties of cobalt-phthalocyanine thin films;  
A. K. Debnath, A. Kumar, **S. Samanta**, A. Singh, D. K. Aswal, S. K. Gupta, J. V. Yakhmi, *AIP Conference Proceedings of 55<sup>th</sup> DAE solid state physics symposium* **1349** 1047-1048 (2010).
- [4] Charge transport characteristics of Cobalt phthalocyanine thin films grown by molecular beam epitaxy;  
S. K. Gupta, A. Singh, **S. Samanta**, A. Kumar, A. K. Debnath, D. K. Aswal, *AIP Conference Proceedings of Physics of emerging functional materials* **1313** 60 (2010).
- [5] Estimation of ppb level chlorine concentration using Elovich equation;  
A. K. Debnath, A. Singh, **S. Samanta**, D. K. Aswal, S. K. Gupta, J. V. Yakhmi, *Proc. 54th DAE Solid State Physics Symposium*, M. S. University, Vadodara, (2009).
- [6] Substrate dependent growth and electrical charge transport property of cobalt phthalocyanine thin films;  
**S. Samanta**, A. Singh, A. K. Debnath, D. K. Aswal, S. K. Gupta, J.V.Yakhmi, *Proc. International Symposium on Nanostructured Materials: Structure, properties and applications*, Jalandhar, (2009).

- [7] Molecular Beam Epitaxy Growth of Iron Phthalocyanine Nanostructures;  
A.K. Debnath, **S. Samanta**, A. Singh, D. K. Aswal, S. K. Gupta, J. V. Yakhmi, *AIP conference proceedings of ICTOPON 1147* 347 (2009).
- [8] Selective chlorine gas sensors using cobalt phthalocyanine thin films;  
A. K. Debnath, A. Singh, **S. Samanta**, D. K. Aswal, S. K. Gupta, J. V. Yakhmi, *Proc. 53rd DAE Solid State Physics Symposium, Mumbai*, (2008).
- [9] Temperature dependent current-voltage characteristics of iron-phthalocyanine films;  
**S. Samanta**, A. K. Debnath, A. Singh, D. K. Aswal, S. K. Gupta, J. V. Yakhmi, *Proc. of ICONSAT-08, Chennai*, (2008).
- [10] Hysteretic current-voltage characteristics of iron-phthalocyanine films;  
**S. Samanta**, A. K. Debnath, A. Singh, D. K. Aswal, S. K. Gupta, J. V. Yakhmi, *Proc. 52nd DAE Solid State Physics Symposium, Mysore*, (2007).
- [11] Surface morphology and gas sensing characteristics of the iron-phthalocyanine thin films;  
A. K. Debnath, **S. Samanta**, A. Joshi, A. Singh, D. K. Aswal, S. K. Gupta, J. V. Yakhmi, *Proc. 52nd DAE Solid State Physics Symposium, Mysore*, (2007).

## ACKNOWLEDGEMENTS

Firstly, I take an extremely honored privilege to express my heartiest gratitude to my research guide **Prof. D.K. Aswal**, for his continuous guidance during the thesis work. His support and enthusiasm encouraged me to work in the field of organic semiconductors. I owe completely to him for his enormous effort for timely submission of this dissertation. It is my pleasure to express my grateful thanks to **Prof. J.V. Yakhmi** for his encouragement and support. I express my deep gratitude to **Prof. S.K. Gupta**, Head, Technical Physics division, for his supports and guidance during the course of thesis work.

I sincerely thank **Dr. A. K. Debnath** for helping me in the thin film depositions by molecular beam epitaxy and **Dr. Ajay Singh** for the analyses of the charge transport characteristics. I am thankful to **Dr. S. Basu (SSPD)** and **Dr. S. K. Deshpande (UGC-DAE)** for their help in GIXRR and GIXRD measurements. I am also thankful to **Dr. M. Senthil Kumar (IIT Bombay)** for his support in X-ray rocking measurements.

I am extremely grateful to **Ms. N. Padma, Dr. A.K. Chauhan, Dr. Vibha Saxena, Dr. S Bhattacharya, Dr. S.P. Koiry, Shri P. Jha,** and **Shri Arvind Kumar** for their continuous support during the course of the work. I am also greatly indebted to **Shri K.P. Muthe, Dr. Manmeet Kaur, Shri R. Prasad, Dr. Niranjana Ramgir, Dr. Ranu Bhatt, Mrs. Ranita Basu, Ms. Niyanta Dutta, Mrs K Ganapati, Shri K.N. Meshram, Shri P. Vereender** and **Shri Vishal Balouria** for extending support and help at various stages of the thesis work. Last but not least, I would like to offer my whole-hearted indebtedness to my **family and friends**, who have always motivated and supported me.

# CONTENTS

|  | <b>Page<br/>No.</b> |
|--|---------------------|
| SYNOPSIS   | 1                   |
| LIST OF FIGURES  | 9                   |
| LIST OF TABLES   | 19                  |
| CHAPTER  |                     |
| <b>1 INTRODUCTION</b>  | <b>20</b>           |
| <b>1.1 Current interests in organic semiconductors</b>                               | <b>21</b>           |
| <b>1.2 Origin of energy gap in organic semiconductors</b>                            | <b>23</b>           |
| <b>1.3 Phthalocyanines: A model molecular semiconductor</b>                          | <b>27</b>           |
| <b>1.4 Charge transport mechanisms: An overview</b>                                  | <b>31</b>           |
| <i>1.4.1 Charge injection mechanisms</i>   | <b>35</b>           |
| <i>1.4.1.1 Tunneling Mechanism</i>   | <b>35</b>           |
| <i>1.4.1.2 Multistep tunneling (MUST)</i>  | <b>37</b>           |
| <i>1.4.1.3 Schottky Mechanism</i>  | <b>38</b>           |
| <i>1.4.2 Bulk limited charge transport</i>   | <b>39</b>           |
| <i>1.4.2.1 Ohmic Conduction</i>  | <b>39</b>           |
| <i>1.4.2.2 Space charge limited conduction (SCLC)</i>                                | <b>40</b>           |
| <i>1.4.2.3 Poole-Frankel mechanism</i>   | <b>47</b>           |
| <b>1.5 Models for temperature dependent resistivity</b>                              | <b>48</b>           |
| <b>1.6 Literature review on charge transport of<br/>        phthalocyanine films</b> | <b>49</b>           |
| <b>1.7 Scope of the thesis</b>   | <b>52</b>           |
| <b>2 EXPERIMENTAL TECHNIQUES</b>   | <b>56</b>           |
| <b>2.1 Introduction</b>  | <b>57</b>           |

|  |           |
|--|-----------|
| <b>2.2 Phthalocyanine thin films deposition by MBE</b>                                 | <b>57</b> |
| <i>2.2.1 Configuration details of RIBER-32 EVA MBE system</i>                          | <b>58</b> |
| <i>2.2.2 Experimental procedure for phthalocyanine film deposition</i>                 | <b>64</b> |
| <i>2.2.2.1 Substrates and their preparation</i>  | <b>64</b> |
| <i>2.2.2.2 Deposition protocol</i>   | <b>67</b> |
| <b>2.3 Characterization techniques</b>   | <b>69</b> |
| <i>2.3.1 X-ray diffraction</i>   | <b>69</b> |
| <i>2.3.1.1 Powder X-ray diffraction</i>  | <b>69</b> |
| <i>2.3.1.2 Grazing angle X-ray diffraction</i>   | <b>70</b> |
| <i>2.3.1.3 X-ray rocking measurement</i>   | <b>71</b> |
| <i>2.3.2 X-ray reflectivity measurement</i>  | <b>72</b> |
| <i>2.3.3 Atomic force microscopy</i>   | <b>73</b> |
| <i>2.3.4 Scanning electron microscopy</i>  | <b>75</b> |
| <i>2.3.5 X-ray photo-electron spectroscopy</i>   | <b>76</b> |
| <i>2.3.6 Fourier transform spectroscopy</i>  | <b>77</b> |
| <i>2.3.7 UV-Visible spectroscopy</i>   | <b>79</b> |
| <b>2.4 Charge transport measurement</b>  | <b>80</b> |
| <i>2.4.1 Electrode deposition by thermal evaporator</i>                                | <b>81</b> |
| <i>2.4.2 Low temperature charge transport</i>  | <b>82</b> |
| <i>2.4.3 Transient voltage pulse method for mobility measurement</i>                   | <b>84</b> |
| <b>2.5 Gas sensing setup</b>   | <b>85</b> |
| <br>   |           |
| <b>3 GROWTH OF AMORPHOUS, POLY-CRYSTALLINE AND HIGHLY ORDERED PHTHALOCYANINE FILMS</b> | <b>86</b> |
| <br>   |           |
| <b>3.1 Introduction</b>  | <b>87</b> |
| <b>3.2 Growth of phthalocyanine films on glass</b>                                     | <b>89</b> |
| <i>3.2.1 Structure &amp; morphology as a function of growth</i>                        |           |

|  |            |
|--|------------|
| <i>parameter</i>   | <b>90</b>  |
| 3.2.1.1 <i>Effect of growth temperature</i>  | <b>91</b>  |
| 3.2.1.2 <i>Effect of film thickness</i>  | <b>94</b>  |
| 3.2.1.3 <i>Effect of deposition rate</i>   | <b>97</b>  |
| 3.2.1.4 <i>Optical absorption study</i>  | <b>98</b>  |
| 3.2.2 <i>Understanding of the morphology evolution</i>   | <b>100</b> |
| 3.2.2.1 <i>Growth mechanism of nano-web and nano-<br/>brush</i>                                | <b>101</b> |
| 3.2.2.2 <i>Growth mechanism of granular and densely<br/>packed morphology</i>                  | <b>102</b> |
| <b>3.3 Growth of phthalocyanine films on (0001) sapphire</b>                                   | <b>103</b> |
| <b>3.4 Growth of phthalocyanine films on twined (001)<br/>LaAlO<sub>3</sub></b>                | <b>106</b> |
| <b>3.5 Growth of phthalocyanine films on 36.8° cut bicrystal<br/>(001) SrTiO<sub>3</sub></b>   | <b>109</b> |
| <b>3.6 Conclusions</b>   | <b>110</b> |
| <br>   |            |
| <b>4 CHARGE TRANSPORT IN<br/>AMORPHOUS AND<br/>POLYCRYSTALLINE FILMS</b>                       | <b>112</b> |
| <br>   |            |
| <b>4.1 Introduction</b>  | <b>113</b> |
| <b>4.2 Interaction of oxygen with MPc films</b>  | <b>113</b> |
| 4.2.1 <i>XPS measurements</i>  | <b>114</b> |
| 4.2.2 <i>Conductivity measurements</i>   | <b>116</b> |
| <b>4.3 Charge transport in amorphous and polycrystalline<br/>FePc films deposited on glass</b> | <b>119</b> |
| 4.3.1 <i>Charge transport at 300K</i>  | <b>119</b> |
| 4.3.2 <i>Temperature dependent conductivity</i>  | <b>124</b> |
| <b>4.4 Charge transport in polycrystalline CoPc films on<br/>glass</b>                         | <b>125</b> |

|   |            |
|---|------------|
| <b>4.5 Charge transport in polycrystalline CoPc films on sapphire</b>                               | <b>127</b> |
| 4.5.1 <i>Temperature dependent J-V characteristics</i>  | <b>127</b> |
| 4.5.2 <i>Electric field &amp; carrier distribution</i>  | <b>129</b> |
| 4.5.3 <i>Mobility measurement by transient voltage pulse method</i>                                 | <b>131</b> |
| <b>4.6 Trap distribution in polycrystalline CoPc films grown on glass and sapphire</b>              | <b>133</b> |
| <b>4.7 Conclusions</b>  | <b>134</b> |
| <br>  |            |
| <b>5 CHARGE TRANSPORT IN HIGHLY ORDERED FILMS</b>   | <b>136</b> |
| <br>  |            |
| <b>5.1 Introduction</b>   | <b>137</b> |
| <b>5.2 Charge transport in CoPc films grown on twined (001) LaAlO<sub>3</sub></b>                   | <b>137</b> |
| 5.2.1 <i>Charge transport in CoPc films grown along twin boundaries of (001) LaAlO<sub>3</sub></i>  | <b>138</b> |
| 5.2.1.1 <i>Charge transport in the high temperature range, 300 -100K (Region I &amp; II)</i>        | <b>139</b> |
| 5.2.1.2 <i>Charge transport below 100K (Region III &amp; IV)</i>                                    | <b>142</b> |
| 5.2.2 <i>Charge transport in CoPc films grown across twin boundaries of (001) LaAlO<sub>3</sub></i> | <b>145</b> |
| <b>5.3 Charge transport in CoPc films grown on bi-crystal (001) SrTiO<sub>3</sub></b>               | <b>147</b> |
| 5.3.1 <i>Charge transport in CoPc films grown along the bi-crystal boundary</i>                     | <b>149</b> |
| 5.3.2 <i>Charge transport in CoPc films grown on single crystalline region</i>                      | <b>152</b> |
| <b>5.4 Conclusions</b>  | <b>153</b> |

|          |   |            |
|----------|---|------------|
| <b>6</b> | <b>CoPc FILMS AS ppb LEVEL Cl<sub>2</sub> SENSOR</b>                    | <b>155</b> |
| 6.1      | Introduction  | 156        |
| 6.2      | Configuration of chemiresistor sensors using MPc films                  | 158        |
| 6.3      | Gas sensing characteristics of CoPc films grown on different substrates | 159        |
| 6.4      | Optimization of gas sensing parameters of CoPc films on sapphire        | 162        |
|          | 6.4.1 <i>Operating temperature</i>                                      | 162        |
|          | 6.4.2 <i>Film thickness</i>   | 165        |
| 6.5      | Gas sensing characteristics of 20 nm CoPc films deposited on sapphire   | 166        |
|          | 6.5.1 <i>Linearity</i>  | 167        |
|          | 6.5.2 <i>Selectivity</i>  | 167        |
|          | 6.5.3 <i>Stability &amp; Repeatability</i>                              | 168        |
| 6.6      | Degradation of the sensor films   | 169        |
| 6.7      | Mechanism of gas sensing by CoPc films                                  | 170        |
| 6.8      | Impedance spectroscopy study  | 175        |
| 6.9      | Kinetics of CoPc sensor   | 176        |
| 6.10     | Elovich isotherm  | 178        |
| 6.11     | Conclusions   | 180        |
| <b>7</b> | <b>SUMMARY AND CONCLUSIONS</b>  | <b>182</b> |
|          | <b>BIBLIOGRAPHY</b>   | <b>188</b> |

# SYNOPSIS

Semiconducting organic materials, both polymeric and small molecule based, have gained worldwide attention during last two decades owing to their several interesting electrical and optical properties, and therefore, are being used in various devices, such as, organic field effect transistor (OFET), organic photovoltaics, organic light emitting diodes (OLED) and bio- and gas sensors etc. Presently some of these organic devices are available in the market. Although these devices are having low charge carrier mobility but still these can be used in some special cases like in low cost flexible electronics, large area devices application etc. For better performance of the organic semiconductor devices, it is very important to understand the charge transport mechanism in these organic semiconductors. A considerable amount of efforts have been devoted to study the charge transport mechanism(s) in organic semiconductor thin films, particularly at low temperatures (300-4 K). A literature survey however shows that it is very difficult to measure electrical conductivity at temperatures below 120 K. This is because no measurable electrical current is obtained at low temperatures due to the very low mobility ( $\mu$ ), which are usually in the range of 0.01-0.1  $\text{cm}^2\text{V}^{-1}\text{s}^{-1}$ . The low value of  $\mu$  in organic semiconductor thin films mainly arises due to the weak van der Waals forces between adjacent molecules. In addition, the  $\mu$  is also affected by energetic disorders (diagonal and non-diagonal), nature of molecular stacking (face-on or edge-on), adsorbed oxygen species and impurities. Clearly, in order to investigate the low temperature charge-transport properties of organic semiconductor films, the major issue is how to improve the mobility of films. Similar to the conventional inorganic semiconductor

films, the  $\mu$  can be enhanced by improving the crystalline structure of the films and reducing the impurities.

In this thesis, we deposit metal-phthalocyanine (Pc) films using organic molecular beam epitaxy (OMBE) system on a variety of substrates viz. glass, (100) SrTiO<sub>3</sub>, (100) LaAlO<sub>3</sub>, (0001) Al<sub>2</sub>O<sub>3</sub> and along the 38.6° grain boundary of bicrystal SrTiO<sub>3</sub>. Generally, growth of Pc epitaxial films on inorganic substrates is difficult due to (i) large lattice mismatch between film and substrate, and (ii) extended (planar) nature of the Pc molecules. Nevertheless, it has been found that the chemical nature of substrate as well as its surface roughness strongly influences the growth of the Pc films. The growth mode of large planar molecules is governed by a competition between “molecule-molecule” and “molecule-substrate” interactions. If the molecule-substrate interaction is dominant then molecules arrange in the *face-on* stacking mode, otherwise the stacking mode will be *edge-on*. *This thesis deals with growth and characterization of FePc and CoPc thin films with a motivation of improving the charge carrier mobility. We have demonstrated that by choosing appropriate substrate, the mobility can be enhanced from  $<0.5 \text{ cm}^2\text{V}^{-1}\text{s}^{-1}$  (obtain for amorphous CoPc films on glass) to  $\sim 150 \text{ cm}^2\text{V}^{-1}\text{s}^{-1}$  (for highly ordered CoPc films grown along the 38.6° grain boundary of bicrystal SrTiO<sub>3</sub>). The electronic charge transports in disordered and highly ordered Pc films have been investigated as a function of bias and temperature (down to 25K). We have generated a new bias-temperature phase-diagram for ordered Pc films on LaAlO<sub>3</sub> substrates. The Pc films have also been used for ppb level Cl<sub>2</sub> gas sensing.*

The thesis is organized into following seven chapters.

## **Chapter 1: Introduction**

In this chapter, we begin with introducing organic semiconductors and compare their electronic structure and properties with inorganic semiconductor. Theoretical electronic charge transport models are reviewed. A review on experimental study of charge transport in organic semiconductor is summarized. The electronic structure of phthalocyanine and its advantages over other organic semiconductor are discussed. Finally the scope of present thesis, that is, growth of highly ordered phthalocyanine films, charge transport in disordered, ordered and highly ordered films are presented. In addition, the application of Pc films in ppb level Cl<sub>2</sub> gas sensing is discussed.

## **Chapter 2: Experimental techniques**

This chapter describes the experimental techniques used during the present work. The details of the Molecular Beam Epitaxy (RIBER system, model no EVA 32) used for depositing CoPc and FePc films are presented. An overview of various characterization techniques, such as scanning electron microscopy (SEM), atomic force microscopy (AFM), X-ray photoelectron spectroscopy (XPS), Fourier transform infra-red spectroscopy (FTIR), UV-visible spectroscopy (UV-Vis), grazing angle X-ray diffraction (GIXRD) etc are discussed. The details of low temperature charge transport measurement system and gas sensing measurement setup are presented.

### **Chapter 3: Growth of amorphous, poly-crystalline and highly ordered phthalocyanine films**

This chapter deals with a detailed study on growth of FePc and CoPc films on different substrates *viz.* glass, (0001) sapphire, naturally twined (001) LaAlO<sub>3</sub> and SrTiO<sub>3</sub> bi-crystal. The growth morphology has been investigated as function of (i) substrate temperature (30°C to 300°C) (ii) film thickness (20 nm to 500 nm) and (iii) deposition rate (0.02 nm/s to 0.5 nm/s). The FePc films deposited on glass at room temperature are disordered and amorphous in nature where as high temperature deposited films are partially ordered and polycrystalline. The  $\alpha$ -phase to  $\beta$ -phase transition at 200°C for FePc films deposited on glass is also studied by FTIR and GIXRD. We have also established that changing growth rate from 0.02 to 0.07 nm/s the morphology of  $\alpha$ -phase FePc can be tuned from nanobrush (nearly parallel nanorods aligned normal to the substrate plane) to nanoweb (nanowires forming a web-like structure in the plane of the substrate). We propose growth mechanisms of nanoweb and nanobrush morphology based on the van-der-Waals (vdW) epitaxy. It has been also demonstrated that changing thickness from low to high, the film morphology changes from nano-wire to granular morphology, which is associated with change of molecular staking from face-on to edge-on. In the next section we have describe about the growth of CoPc films on sapphire substrate. It is found that due to substrate molecule interaction lower thickness films are face-on stacked and as thickness increases due to weakening of molecule substrate interaction molecule stack edge-on. It has been shown that at an optimum substrate temperature and film thickness partially ordered films of CoPc can be grown. In third section we have describe the growth of ordered CoPc films along

LaAlO<sub>3</sub> twin boundary. In the last section we will describe about the growth of highly ordered CoPc films along the bi-crystal boundary of on SrTiO<sub>3</sub>.

#### **Chapter 4: Charge transport in amorphous and polycrystalline films**

In this chapter we discuss the electronic charge transport of disordered and partially ordered FePc thin films on glass. In addition the charge transport of partially ordered CoPc thin films on sapphire has also been presented. Firstly we have analyzed the affect of ambient oxygen on the conductivity of Pc thin films. It is seen that amorphous films of FePc has higher hysteresis in current density-voltage (*J-V*) characteristics than the polycrystalline films on glass due to higher number of deep traps created by chemisorbed oxygen. This hysteresis is attributed to filling and emptying of these traps by injected charge carrier. The role of disorder is further investigated by studying charge transport properties of CoPc films on glass and sapphire. The films deposited on sapphire are partially ordered and exhibit non-hysteretic *J-V* characteristics which can be well described by space charge limited conduction (SCLC) up to temperature of 75K. On the other hand the films deposited on glass are highly disordered and shows hysteresis in *J-V* characteristics up to temperature 220°K due to higher number of deep traps. The low temperature charge transport is described by Poole-Frankel mechanism.

#### **Chapter 5: Charge transport in highly ordered films**

This chapter deals with charge transport measurement on high mobility CoPc thin films deposited on lanthanum aluminate (LaAlO<sub>3</sub>) and strontium titanate (SrTiO<sub>3</sub>) substrate. First, we present the result of charge transport measurement on ordered CoPc thin films

deposited on LaAlO<sub>3</sub> substrate, which has a charge mobility of  $\sim 7 \text{ cm}^2\text{V}^{-1}\text{s}^{-1}$ . It is found that above 100K the charge transport is dominated by bulk limited processes which includes a bias dependent crossover from Ohmic ( $J \sim V$ ) to trap free space charge limited conduction ( $J \sim V^2$ ). On the other hand, low temperature charge transport is governed by contact limited process where we see a bias dependent transition from Schottky ( $\ln J \sim V^{1/2}$ ) to multistep tunneling (conductivity varying exponentially on the inverse of the square-root of electric field). The high mobility is due to the ordering of CoPc molecule on LaAlO<sub>3</sub>, which has twin boundaries. In the next section we will describe the charge transport mechanism on highly ordered CoPc films deposited on SrTiO<sub>3</sub> bi-crystal. In these films we have reported record mobility of  $\sim 148 \text{ cm}^2\text{V}^{-1}\text{s}^{-1}$ . The analysis of charge transport data on the thin films deposited on single crystalline SrTiO<sub>3</sub> substrate and along bi-crystal boundary of SrTiO<sub>3</sub> shows that the conductivity of the film deposited on bi-crystal boundary are in critical region where as the conductivity of the films deposited on single crystalline region is in insulating region. Further the power law behavior of resistivity is in supportive with the fact that the conductivity of the films, deposited along the bi-crystal boundary, is in critical region.

## **Chapter 6: CoPc films as ppb level Cl<sub>2</sub> sensor**

In this chapter we present gas sensing behavior of CoPc thin films. We present the comparison of the gas sensing characteristics of the CoPc thin films on glass sapphire and other substrates. We show CoPc films on sapphire are better for gas sensing due to their high mobility, low base line resistance drift ( $< 5\%$ ). The mechanisms of gas sensing have been discussed. The effect of film thickness, operating temperature on gas sensing characteristics of the films deposited on sapphire has is presented. The linearity in the range of 5 to 2000

ppb, stability, selectivity and repeatability of these sensors has also been studied. It is usually seen that the chemical reaction of  $\text{Cl}_2$  gas with CoPc molecule is first order with activation energy of  $84.8 \text{ kJ mol}^{-1}$ . We have also analyzed the chemical adsorption of  $\text{Cl}_2$  on CoPc films using Elovich isotherm, which provides an alternative way of quantifying  $\text{Cl}_2$  concentration from response rate of the sensor.

## Chapter 7: Summary & conclusions

The summary of the thesis work and main conclusions have been presented in this chapter. The main results obtain in the course of this thesis work are as follows

- The morphology of FePc and CoPc thin films can be tuned by controlling different growth parameters, such as deposition temperature, deposition rate, substrate and thickness. The films on glass substrates are amorphous in nature where as the films on sapphire substrates are polycrystalline. The highly ordered films can be grown using twined (001)  $\text{LaAlO}_3$  and bi-crystal  $\text{SrTiO}_3$  substrates.
- The chemisorptions of ambient oxygen by CoPc films on glass lead to deep-traps, which results in hysteretic  $J$ - $V$  characteristics described by deep trap limited SCLC. The low temperature transport properties in this case are dominated by Poole Frankel mechanism. On the other hand shallow traps in CoPc films, deposited on single crystalline sapphire, results in non-hysteretic  $J$ - $V$  characteristics that can be described by trap-free SCLC in the entire investigated temperature range (300-25 K).
- A huge enhancement of  $\mu$  in the CoPc films, deposited along twin-boundaries of  $\text{LaAlO}_3$  single crystal ( $\sim 7 \text{ cm}^2\text{V}^{-1}\text{s}^{-1}$ ) and the bi-crystal boundary of  $\text{SrTiO}_3$  ( $\sim 150 \text{ cm}^2\text{V}^{-1}\text{s}^{-1}$ ), has been demonstrated. The enhancement of  $\mu$  is attributed to the ordering

of CoPc molecule along the twin or bi-crystal boundaries, which facilitates edge-on stacking of the molecules.

- The charge transport of high mobility CoPc thin films deposited on LaAlO<sub>3</sub> single crystal is governed by bulk transport in high temperature region (>100K) where as the low temperature (<100K) transport is dominated by contact limited processes. A new bias- temperature phase diagram has been proposed based on the charge transport data.
- The conductivity of the films deposited along the boundary of SrTiO<sub>3</sub> bi-crystal is in critical region where as the conductivity of the films deposited on single crystalline region is in insulating region.
- Ppb level of Cl<sub>2</sub> gas sensing by ultra thin CoPc films on sapphire has been demonstrated. It has been shown that the sensor is linear in the range 5 to 2000 ppb with low base resistance drift (< 5 %) and high selectivity.

This chapter concludes with the future scope in this field related to the thesis work.

## LIST OF FIGURES

**Figure 1.1** The specific example of organic molecules, showing different dimensionalities. (a) 12 carbon alkene thiol [1D], (b) phthalocyanine [2D], (c) DNA molecule [3D] and (d) polyphenylene vinylene (PPV) polymer [1D long chain coiled into 3D structure].

**Figure 1.2** Schematic depicting the formation of  $\sigma$ -bonds using  $s$  and  $p$  orbitals, and  $\pi$ -bonds using  $p$  orbitals.

**Figure 1.3** Schematic of chemical bonding (left) and corresponding electronic structure (right) of ethene (a), benzene (b) and conducting polymer (c).

**Figure 1.4** Molecular structure of metal phthalocyanines (MPc) (a), and schematics of  $\alpha$ -FePc (b) and  $\beta$ -FePc (c) phases projected on (100) planes.

**Figure 1.5** Packing of the phthalocyanine molecule in its  $\beta$ -form. (a) Projection on the  $ac$ -plane and (b) projection on the  $ab$ -plane where the monoclinic  $b$ -axis points in the viewing direction in (a) and is aligned vertically in (b).

**Figure 1.6** The schematic of charge transport measurement showing an active organic semiconducting layer sandwich between charge injecting and collecting electrodes.

**Figure 1.7** (a) Electronic structure of a typical metal and organic semiconductor showing relevant energy levels when they are separated, (b) electronic structure of a metal organic semiconductor interface with interface dipole, (c) electronic structure of a metal organic semiconductor interface without interface dipole ( $\Delta = 0$ ) and therefore vacuum level aligns.

**Figure 1.8** The electronic structure of the interface between MPc and Au electrode. The exponential distribution of traps is schematically shown in MPc films with shallow and deep states.

**Figure 1.9** (a) Schematic of carrier tunneling a trapezoidal potential barrier at lower voltage, (b) triangular shape of the potential barrier at higher voltage.

**Figure 1.10** Schematic of sequential tunneling of electron from metal electrode to the conduction band of insulator/semiconductor via localized states.

**Figure 1.11** Schematic of metal (electrode) organic (semiconductor) Schottky interface. In the figure 'AB', 'CD' represents potential variation due to image charge at electrode, and applied electric field, respectively. 'AD' represents the actual potential barrier at the interface.

**Figure 1.12** (a) Schematic of shallow ( $E_{tn1}$ ) and deep ( $E_{tn2}$ ) traps for electrons. (Solid circle indicates traps occupied by an electron) (b) Schematic of shallow ( $E_{tp1}$ ) and deep ( $E_{tp1}$ ) traps for holes. (An electron-occupied trap is equivalent to a hole-unoccupied trap and conversely)

**Figure 1.13** Schematic current-voltage ( $J$ - $V$ ) characteristics for one-carrier space-charge-limited current controlled by a single set of traps in log-log plot. I corresponds to  $E_{F0}$  lying above trap level ( $E_t$ ) and II corresponds to  $E_{F0}$  lying below traps level ( $E_t$ ). All the  $J$ - $V$  characteristics will be contain inside the triangle (red color) depending on the relative position of Fermi level and trap level.

**Figure 1.14** Poole-Frankel effect at a trap in the bulk of the semiconductor.

**Figure 2.1** A photograph of MBE deposition system (RIBER EVA 32 E) used for the deposition of MPc films.

**Figure 2.2** A close-up photograph of the Introduction Chamber.

**Figure 2.3** A close-up photograph of the Analysis Chamber.

**Figure 2.4** A close-up photograph of Growth chamber.

**Figure 2.5** The unit cell structure of sapphire showing top (Left) and side (Right) views.

**Figure 2.6** Schematic diagram of  $\text{LaAlO}_3$  (100) twin.

**Figure 2.7** (a)  $\text{SrTiO}_3$  unit cell at room temperature which shows a cubic structure. (b) Schematic of  $36.8^\circ$  cut (001)  $\text{SrTiO}_3$  bicrystal. Expanded view shows the schematic of the interface structure.

**Figure 2.8** Protocol for the phthalocyanine film deposition.

**Figure 2.9** Schematic diagram of powder X-Ray diffractometer.

**Figure 2.10** The schematic of the grazing angle X-ray diffraction.

**Figure 2.11** Schematic of X-ray rocking measurements

**Figure 2.12** (a) a real snap of AFM tip and sample stage. (b) Block diagram of AFM.

**Figure 2.13** Block diagram of a typical SEM setup

**Figure 2.14** Ray diagram of recording FTIR spectra along with electronic circuit of system vertex 80 V.

**Figure 2.15** The ray diagram of recording FTIR spectra in ATR mode. The accessory used for ATR spectra is also shown in the inset of the diagram.

**Figure 2.16** Block diagram of a typical double beam single monochromator UV-spectrometer.

**Figure 2.17** Schematic of thermal evaporation system for the gold electrode deposition.

**Figure 2.18** A schematic of in plane charge transport measurement geometry.

**Figure 2.19** Schematic of mobility measurement set up using transient voltage pulse method.

**Figure 2.20** Schematic of gas sensing measurement setup.

**Figure 3.1** Schematic of three different growth modes of inorganic thin films on inorganic substrate, namely Frank-van der Merwe mode (a), Volmer–Weber mode (b), Stranski–Krastanov mode (c).

**Figure 3.2** AFM image of the glass substrate.

**Figure 3.3** SEM photographs of FePc thin films (nominal thickness 60 nm, deposition rate 0.07 nm/s) grown on glass substrate at (a) 25°C, (b) 50°C, (c) 100°C, (d) 200°C, (e) 300°C.

**Figure 3.4** GIXRR spectrum (open circles) for a FePc film grown at 25°C with best-fit theoretical curve (full curve). The inset shows variation of actual thickness as a function of growth temperature.

**Figure 3.5** (a) GIXRD patterns and (b) FTIR spectra recorded for 60nm (nominal thickness) FePc films deposited at different substrate temperatures.

**Figure 3.6** SEM photographs of FePc thin films, grown at a substrate temperature of 200°C using a deposition rate of 0.07 nm/s having different nominal thickness (a) 30 nm, (b) 50 nm, (c) 100 nm, (d) 200 nm and (e) 500 nm.

**Figure 3.7** SEM photographs of 60 nm FePc thin films grown at the rate of 0.02 nm/s at different substrate temperatures (a) 50°C, (b) 100°C, (c) 200°C and (d) 300°C.

**Figure 3.8** GIXRD pattern (a) and FTIR spectrum recorded for FePc nanobrush sample.

**Figure 3.9** SEM photographs of 100 nm FePc thin films grown at substrate temperatures 200°C with different deposition rate (a) 0.02 nm/s, (b) 0.07 nm/s, (c) 0.5 nm/s.

**Figure 3.10** Optical absorption spectra recorded for (a) amorphous (b) nanoweb and (c) nanobrush  $\alpha$ -phase FePc films.

**Figure 3.11** Schematic representation depicting the growth mechanism of FePc nanoweb and nanobrush. Left: The molecular beam: (1) consisting of planar molecules impinges the substrate; molecules may undergo various processes at the surface of the substrate, such as, adsorption in 'lying-down' or 'standing-up' configurations (2), desorption (3), diffusion (4), and formation of nucleus (5). The growth of nucleus may proceed in two different ways

depending upon the deposition rate: (I) at a deposition rate of 0.07nm/s, the growth direction is along b-axis, which is due to face-on (p-stacking) of the molecules, leading to the formation of nanowires lying in the plane of the substrates, (II) at a deposition rate of 0.02nm/s, the growth direction is along a-axis due to the vdW epitaxy, resulting in the formation of the nanorod aligned vertical to the substrate plane. Right: 3-D schematic representation of growth processes I and II, eventually leading to the formation of nanoweb and nanobrush morphology as shown in SEM images.

**Figure 3.12** AFM image of (0001) sapphire substrate.

**Figure 3.13** (a,b) GIXRD pattern and  $5\mu\text{m} \times 5\mu\text{m}$  AFM image for 20 nm CoPc films on sapphire substrate. (c, d) GIXRD pattern and  $5\mu\text{m} \times 5\mu\text{m}$  AFM image for 100 nm CoPc films on sapphire substrate.

**Figure 3.14** Polarized light microscopy image (a) and (b) AFM image of twined (001)  $\text{LaAlO}_3$ .

**Figure 3.15** X-ray diffraction pattern reordered for (a) 20nm and (c) 100 nm thick CoPc film. The upper inset shows the rocking curve of (200) Bragg peak with a peak position at  $3.35^\circ$ . AFM image of 20nm (c) and 100 nm (d) thick CoPc film on twined (001)  $\text{LaAlO}_3$ .

**Figure 3.16** X-ray diffraction pattern reordered for 100 nm thick CoPc film grown on glass substrate. The upper inset shows the rocking curve of (200) Bragg peak indicating absence of ordering.

**Figure 3.17** Schematic depiction of CoPc molecules stacking along bi-crystal boundary of  $\text{SrTiO}_3$  in edge-on configuration.

**Figure 4.1** (a), (b) Core level O-1s and Co-2p<sub>3/2</sub> XPS spectra of fresh CoPc films on glass (blue data points) and sapphire (red data points) substrate. (c), (d) Core level O-1s and Co-

$2p_{3/2}$  XPS spectra of air exposed CoPc films on glass (blue data points) and sapphire (red data points) substrate.

**Figure 4.2** Core level Fe- $2p_{3/2}$  and O-1s XPS spectra of (a) air exposed FePc films in polycrystalline form. (b) Air exposed FePc amorphous films.

**Figure 4.3** (a) Conductance change of the CoPc films on glass upon exposure of air. (b) Conductance change of the CoPc films on sapphire upon exposure of air.

**Figure 4.4** (a)  $I$ - $V$  characteristics in ambient and in vacuum of CoPc films grown on glass. (b)  $I$ - $V$  characteristics in ambient and in vacuum of CoPc films grown on sapphire.

**Figure 4.5**  $J$ - $V$  characteristics for (a) amorphous and (b) polycrystalline films recorded at 300 K in log-log scale.

**Figure 4.6** (a)  $J$ - $V$  characteristics recorded at 300 K with different values of maximum voltage bias. (b) Time dependence of the current recorded for high and low conducting states measured at a voltage of 30 V. Inset shows the time dependence of current starting from high conducting state at different temperature.

**Figure 4.7** Temperature dependence of the conductance recorded for amorphous (black data points) and crystalline (red data points) FePc films. Inset shows  $J$ - $V$  characteristics of amorphous films at 300K and 180K.

**Figure 4.8** (a) Temperature dependence of  $J$ - $V$  characteristics for the films grown on glass substrate. Inset shows the temperature dependence of voltage exponent  $\alpha$ . (b) Room temperature  $J$ - $V$  characteristics of polycrystalline CoPc films grown on glass.

**Figure 4.9** (a)  $\ln J$  vs  $V^{1/2}$  plots at different temperatures showing Poole Frankel behavior. (b)  $\ln J$  versus  $1/T$  plot obtained at bias of 50 V.

**Figure 4.10** (a) Room temperature  $J$ - $V$  characteristics recorded on CoPc films grown on sapphire substrate. The inset shows same data in log-log scale. (b) Linear variation of current density with  $d^{-3}$  confirming the SCLC.

**Figure 4.11** (a) Temperature dependence of  $J$ - $V$  characteristics for films on sapphire substrate. Inset shows the temperature dependence of exponent ( $\alpha$ ,  $J \sim V^\alpha$ ) (b) Power law fit of data of Fig. 4.11 (a). The fits meet at cross overvoltage  $V_c = 460$  V.

**Figure 4.12** (a) Spatial distribution of the electric field  $E$  at bias voltage of 50 V, inset shows the injected hole concentration  $n_{inj}$  (at bias of 50 V) as a function of field and distance. (b) Field dependence of mobility for the CoPc films on (0001) sapphire substrates.

**Figure 4.13** The input and output signal transient voltage pulse data recorded for CoPc film on sapphire.

**Figure 4.14** Fermi level positions with respect to the valence band and trap distributions are shown for the CoPc films grown in glass and sapphire.

**Figure 5.1** (a) Schematic of two charge transport measurement geometry (i.e. along and across the twin boundary) on 20 nm CoPc thin film grown on twined (001)  $\text{LaAlO}_3$ . (b) Room temperature  $J$ - $V$  characteristics measured on CoPc film along (black data) and across (red data) the twin boundaries.

**Figure 5.2** Log-log plots showing current-voltage characteristics of 20 nm CoPc films at different temperatures. Due to different dependence of the current on applied bias or temperature, four regions (I, II, III, IV) have been identified.

**Figure 5.3** Log-log plots of current-voltage characteristics in the temperature range 160-100K. A transition of slopes of the linear fit to data from 1 to 2 is clearly observed.  $V_x$  is the crossover bias.

**Figure 5.4** (a) Arrhenius plot of mobility determined from the SCLC data in region II. (b) Mobility ( $\mu$ ) vs  $1/T^2$  plot showing inapplicability of disorder model.

**Figure 5.5** (a) For temperature in the 80-24 K range and at low bias,  $\ln J$  varies as  $V^{1/2}$ , indicating a Schottky barrier limited conduction. (b) For temperature in the 80-24 K range and at higher bias, conductivity varying exponentially on the inverse of the square-root of electric field, indicating the transport is governed by multistep tunneling.

**Figure 5.6** A temperature-bias plane summarizing the various conduction mechanisms in high mobility CoPc films.

**Figure 5.7** A typical temperature dependent current density Vs bias of 20 nm CoPc films measured across the ordered direction. Inset shows inverse proportionality of slope of  $J$ - $V$  characteristics with temperature.

**Figure 5.8** A schematic of two charge transport measurement configuration. (i) Along the boundary (ATB) of the bi-crystal SrTiO<sub>3</sub>, (ii) Single crystalline region (SCR) of SrTiO<sub>3</sub>.

**Figure 5.9** (a) Temperature dependence of resistivity (plotted in log-log scale) of film deposited at bicrystal boundary (ATB) and single crystalline regions (SCR) (b) Plots of reduced activation energy  $W$  ( $= -\ln[\rho(T)]/\ln T$ ) for ATB and SCR films.

**Figure 5.10** Power law behavior of resistivity of the films deposited along bi-crystal boundary (ATB) indicating critical behavior.

**Figure 5.11** (a) Log-log plots of  $J$ - $V$  characteristics in the temperature range 300-30K for ATB films. (b) Arrhenius plot of mobility determined from the slope of  $J$ - $V^2$  data in the temperature range of 170 K- 30K. Grey color filled circle shows the room temperature mobility value.

**Figure 5.12** (a) A linear fit of  $\ln \rho$  vs  $T^{-1/4}$  for SCR films indicating Mott 3D-VRH. (b) Log-log plots showing room temperature current-voltage ( $J$ - $V$ ) characteristics of ATB and SCR films.

**Figure 5.13** Log-log plots showing current-voltage ( $J$ - $V$ ) characteristics of 20 nm CoPc films grown on single crystalline region in the temperature range 300 K - 200 K.

**Figure 6.1** (a) Schematic showing the configuration of a chemiresistive sensor and (b) its equivalent circuit.

**Figure 6.2** Typical response of 20 nm CoPc films grown on glass, sapphire, twined (001) LaAlO<sub>3</sub> and 36.8° cut bicrystal (001) SrTiO<sub>3</sub> for 2 ppm Cl<sub>2</sub> gas.

**Figure 6.3** A typical temperature variation sensitivity of 20 nm CoPc films deposited on sapphire substrate for 2 ppm Cl<sub>2</sub> gas in the temperature range of 145°C to 220°C.

**Figure 6.4** Variation of sensitivity of CoPc sensor for 10 ppb (blue data) and 1000 ppb (red data) Cl<sub>2</sub> gas. The solid lines are for eye guidance.

**Figure 6.5** (a) Response curve of 20 nm CoPc films for different Cl<sub>2</sub> dose (5–2000 ppb). Inset shows magnified response curve in 5–100 ppb range. (b) Response curves of 20 nm CoPc films for 5 ppb Cl<sub>2</sub>.

**Figure 6.6** Sensitivity of 20 nm CoPc films as a function of Cl<sub>2</sub> dose.

**Figure 6.7** Bar chart showing sensitivity for different gases, which reveals high selectivity for Cl<sub>2</sub>.

**Figure 6.8** Response of 20 nm CoPc films on repetitive exposure of 500 ppb Cl<sub>2</sub> gas.

**Figure 6.9** The response of CoPc films showing a degradation of its performance due to application of higher dose of 3 ppm Cl<sub>2</sub> gas.

**Figure 6.10** XPS spectra of fresh (blue) and a high dose Cl<sub>2</sub> exposed (red) CoPc films. (a), (b), (c), (d) corresponds to Co-2p, Cl-2p, N-1s, C-1s peaks respectively.

**Figure 6.11** Model of chemisorptions of Cl<sub>2</sub> on to MPc surface. It may bind at free metal sites or replace oxygen to bind at metal sites.

**Figure 6.12** A typical response curve of CoPc sensor showing faster (a,c) and slower (b, d) response and recovery due to two different processes of chemisorptions of Cl<sub>2</sub> on to the CoPc surface.

**Figure 6.13** Impedance spectra of CoPc film in cole-cole plot (a) fresh film, inset shows the expanded view of high frequency region (b) after 2 ppm Cl<sub>2</sub> gas exposure (c) the equivalent circuit model used to analyses the data.

**Figure 6.14** (a) Variation in conductance with time on 1000 ppb Cl<sub>2</sub> exposures at temperatures 145°C (1), 155°C (2), 180°C (3), 205°C (4), 220°C (5). (b) Plots of  $\ln(G_e - G_t)$  vs  $t$  at different temperature. The slopes of linear fits correspond to  $k$  values. Inset shows Arrhenius plot of  $k$ .

**Figure 6.15** (a) Change in conductance ( $\Delta G$ ) as a function of  $\ln(t)$  for different dose of Cl<sub>2</sub>, which is derived from Fig. 6.5 (a). Straight-line fit of data is in accordance with Elovich equation and the slope of linear fits yields parameter  $b'$ . (b) A linear correlation between  $\ln b'$  and  $\ln [\text{Cl}_2]$ .

**Figure 7.1** Schematic depicting the physisorption and chemisorption of ambient oxygen on FePc/ CoPc films with different types of molecular stacking. The arrows show the direction of  $\pi$ -electron overlapping, and hence preferable direction of easy charge transport.

## LIST OF TABLES

**Table 1.1** Unit cell parameters for various phthalocyanines.

**Table 1.2** Partial literature review of mobility values for phthalocyanine thin films.

**Table 4.1** Parameters of FePc films determined from *J-V* characteristics.

**Table 4.2** Different parameters calculated from temperature dependent *J-V* characteristics of CoPc films grown on glass and (0001) sapphire substrate.

**Table 6.1** A partial review of gas sensing characteristics of various MPc films.

**Table 6.2** Comparison of sensitivity of CoPc films (20 nm) grown on different substrate for 2 ppm Cl<sub>2</sub> gas.

**Table 6.3** Resistance and capacitance value obtain from the fitting of Figure 6.13 for exposed and unexposed CoPc films to 2 ppm chlorine gas.

---

# Introduction

---

- 1.1 Current interests in organic semiconductors
- 1.2 Origin of energy gap in organic semiconductors
- 1.3 Phthalocyanines: A model molecular semiconductor
- 1.4 Charge transport in organic semiconductors: An overview
  - 1.4.1 Charge injection mechanisms*
    - 1.4.1.1 Tunneling mechanism*
    - 1.4.1.2 Multistep tunneling (MUST)*
    - 1.4.1.3 Schottky mechanism*
  - 1.4.2 Bulk limited charge transport*
    - 1.4.2.1 Ohmic conduction*
    - 1.4.2.2 Space charge limited conduction (SCLC)*
    - 1.4.2.3 Poole-Frankel mechanism*
- 1.5 Models for temperature dependent resistivity
- 1.6 Literature review on charge transport of phthalocyanine films
- 1.7 Scope of the thesis

## 1.1 Current interests in organic semiconductors

In recent years, organic semiconductors have attracted increasing interest from academia and industry for their application in ‘nano-electronics, as well as ‘macro-electronics’. Organic molecules are potential candidate for pushing the existing scaling limits of the existing silicon based microelectronics to nanoscale [1, 2]. The advantages offered by the organic molecules to be used in the nanoscale devices are (i) small size (typically 0.5 to 2.5 nm), (ii) easy tuning of electronic properties by changing chemical structure of the molecule, and (iii) possibility of forming self-assembled monolayer on various substrates (e. g. thiols on Au, silanes on oxidized and bare Si) . In recent years, various nanoelectronics molecular devices, such as, rectifiers, memory, resonant tunnel diodes and transistors have been demonstrated using two-dimensional ordered molecular monolayers and multilayers [3-6].

On the other hand, alongside the drive to miniaturization, momentum has gathered in the opposite direction, that is, fabrication of large-area electronics, or ‘macro-electronics’. In this case, the size of a transistor is less important than the ease with which it can be distributed over large areas, for example in flat-screen displays where billions of transistors must be distributed over square meters, or radio frequency identification (RFID) tags where circuitry must be cheap enough to be disposable [7, 9]. Beyond the transistor, macro-electronics applications include light-emitting diodes (LEDs) and solar cells which, if made on sufficiently large scales at low enough costs, could transform lighting and power generation respectively [8, 9]. Moreover, entirely new applications such as sensory skins and flexible displays have been inspired by the progress of macro-electronic technologies [10]. In this case also organic molecules solve the purpose due to their low and easy processing,

biocompatibility and of course aptness of depositing on flexible substrates. The flexibility in organic semiconductors comes from van der Waals interactions (typical interaction energy 1-10 meV) among molecules. Recently, several organic based devices, as required for the 'macro-electronics', such as, organic light emitting diodes (OLEDs), organic field effect transistor (OFET), organic solar cells and gas- and bio-sensors etc, have been demonstrated by many groups around the world [11 - 14]. It is not only prototype but several organic based devices has already been marketed by many major electronics firms including Sony, Philips, Kodak, IBM, Hewlett-Packard, Siemens, Pioneer. Among the marketed organic devices the automobile stereo display from Pioneer, OLEDs from Philips and full color displays Kodak digital cameras and mobile phones are well known.

The organic molecules exist in various dimensionalities ranging from 1D to 3D or even in some complex 3D structures and typical examples of various organic molecules are shown in Fig. 1.1. Depending on the dimensionality of the molecules, the interactions among the atoms in a molecule differ, and thereby, affect its electronic properties. This immensely broad spectrum of organic molecules can be broadly classified into two major groups: polymers, and small weight molecules or oligomers. Polymers are long-chain molecules formed by the repetition of molecular units. The number of repetition units is indeterminate, thus leading to a variable molecular mass. On the contrary, small weight molecules have a well defined molecular weight. From the point of view of their electronic and optic properties both groups can be considered rather similar. However, their processing in the film forms greatly differs. Polymers show an advantage of being processable from solutions e.g. by spin-coating, leading to lower production costs. Oligomers, in most of the cases, are insoluble and usually deposited by technically more demanding methods, such as, thermal evaporation

methods. However, the major advantage of molecular films with respect to the polymer films is that they can be grown with very high purity and crystalline order, which are the two major requirements for obtaining high charge carrier mobility. The semiconducting behaviour of the organic molecules depends on its electronic structure, which is described in the following section.

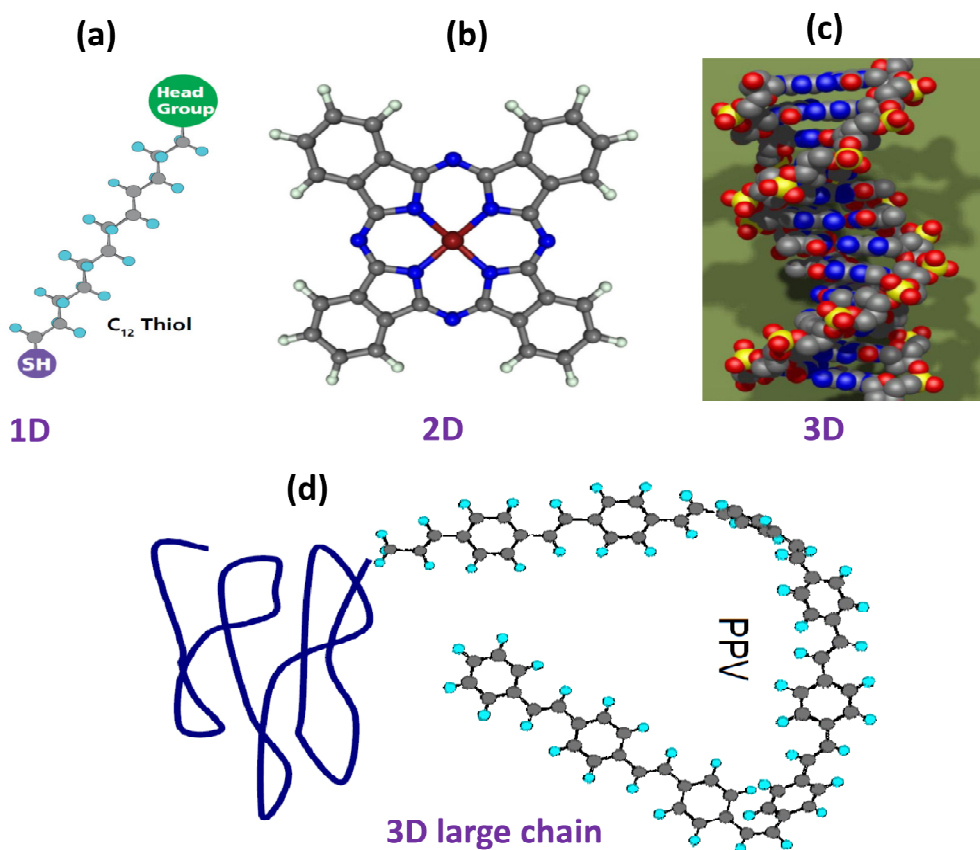


**Figure 1.1** The specific example of organic molecules, showing different dimensionalities. (a) 12 carbon functionalized alkene thiol [1D], (b) phthalocyanine [2D], (c) DNA molecule [3D] and (d) polyphenylene vinylene (PPV) polymer [1D long chain coiled into 3D structure].

## 1.2 Origin of energy gap in organic semiconductors

The semiconducting properties of the organic molecular materials can be explained by the covalent bonding between adjacent carbon atoms. In organic molecules, two different

chemical bonds, namely,  $\sigma$ - and  $\pi$ -bonds can form, as shown schematically in Fig. 1.2. A molecular orbital that is symmetric along the axis connecting two atomic nuclei is called  $\sigma$ -bond, which is formed from head-on overlapping of  $s$  or  $p$  atomic orbital. On the other hand the  $\pi$ -bonds are formed when atomic  $p$  orbitals overlap side-by-side. During bond formation the interaction between two atomic orbitals results a splitting of a molecular orbitals in energy space into two, namely, Highest Occupied Molecular Orbital (HOMO) and Lowest Un-occupied Molecular Orbital (LUMO). The splitting of molecular orbitals and the origin of HOMO and LUMO are schematically shown in Fig. 1.3 by citing the examples of ethene, benzene and a long chain of conducting polymer.

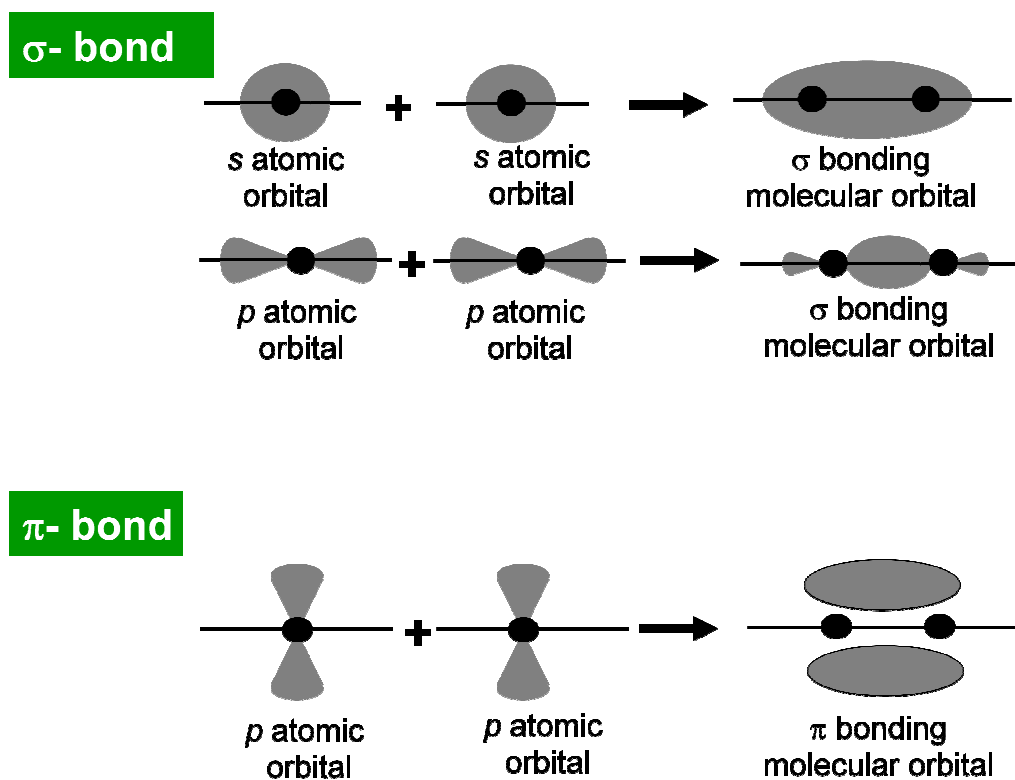


**Figure 1.2** Schematic depicting the formation of  $\sigma$ -bonds using  $s$  and  $p$  orbitals, and  $\pi$ -bonds using  $p$  orbitals.

The origin of HOMO and LUMO are first illustrated (see Fig. 1.3(a)) by considering a simple molecule i.e. ethene. In ethene molecule two carbon atoms are bonded by a  $\sigma$  and a  $\pi$  bond. Due to the interaction of  $\pi$  electrons, the  $\pi$  molecular orbital splits in to two, namely  $\pi$  and  $\pi^*$  and similarly  $\sigma$  orbital. The localized nature of  $\sigma$  electrons results a higher energy gap between  $\sigma$  and  $\sigma^*$  state as compare to the energy gap between  $\pi$  and  $\pi^*$  state. In ethene molecule  $\pi$  and  $\pi^*$  state correspond to the HOMO and LUMO, respectively. In the case of molecules having only  $\sigma$  bonds e.g. alkyl-chains, the HOMO and LUMO correspond  $\sigma$  and  $\sigma^*$  and the HOMO-LUMO gap is very large ( $\sim 8$  eV) [15]. Such molecules find applications as dielectric in molecular or organic devices. On the other hand, conjugated molecule e.g. benzene, consists of alternating single and double bonds that link the subsequent atoms. The extended series of overlapping of  $p$  orbitals and the delocalization of electrons over the entire molecule leads to the further splitting of HOMO and LUMO resulting formation of band which shown in Fig. 1.3 (b). The density of states in HOMO and LUMO bands further increases for conducting polymers where the electrons are delocalized over a large length scale due to higher conjugation. Typical example is shown in the Fig. 1.3 (c). The HOMO and LUMO for organic semiconductors are analogous to the valence and conduction bands of the conventional inorganic semiconductor. Thus the energy band gap for organic semiconductor corresponds to the gap between HOMO and LUMO of the molecule. The HOMO-LUMO separation in these conjugated molecules depends strongly on the overlapping of neighbouring  $p$  orbitals, which is in turn related to the planarity of the molecule and to side groups. In many cases, the HOMO-LUMO energy gap is relatively small ( $\sim 1$  to  $3$  eV) and the molecules can be doped to assume  $n$ - or  $p$ -type character. Thus, the  $\pi$ -conjugated molecules can act as semiconducting channels in organic devices.

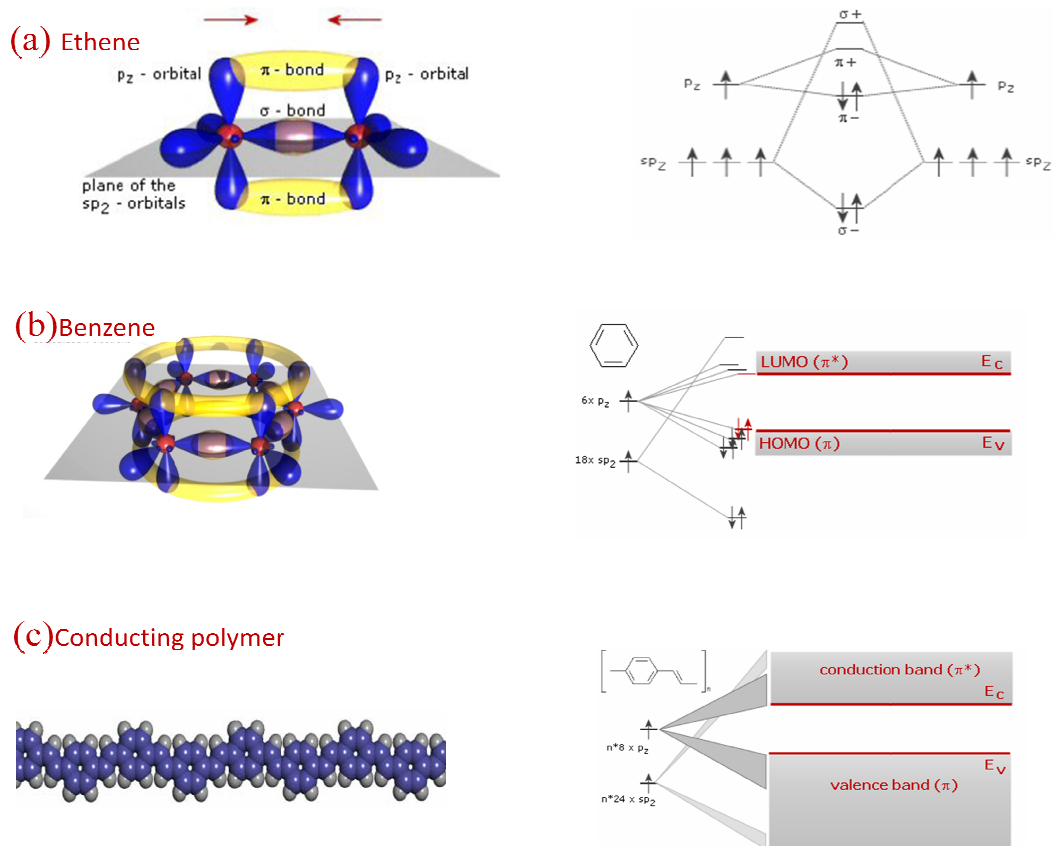


**Figure 1.3** Schematic of chemical bonding (left) and corresponding electronic structure (right) of ethene (a), benzene (b) and conducting polymer (c).

As discussed earlier organic semiconductor films can be obtained using a molecule of different dimensionality i.e. 1D to 3D molecules. Among these 2D planar molecules, porphyrins and phthalocyanines are very interesting for the following reasons:

- (i) They are easily commercially available and extensively used as dyes and pigments in industries.
- (ii) They are biocompatible as nature also uses them in various processes e.g. phthalocyanines are present in tree leaves to facilitate photosynthesis.

- (iii) The delocalization of electrons over planar molecule leads to the highest overlapping between the electron densities of adjacent molecules. This results an easy transport of charge carriers.

Therefore in thesis work we have chosen phthalocyanine as a model 2D molecule for charge transport studies.

### **1.3 Phthalocyanines: A model molecular semiconductor**

The phthalocyanines (Pc) are well known from many years due to their colorant property in fact the name ‘phthalocynine’ [combination of two Greek word naphtha (rockoli) and cyanide (dark blue)] itself suggest the same. Braun and Tcherniac accidentally produced the phthalocyanine in 1907 while they were heating the alcoholic solution of benzamide [16]. Later in 1930 Linstead and coworkers determined the molecular structure of Pc’s and showed that different metallo-phthalocyanies (MPc’s) have the same planar (within 0.3 Å) molecular structure, as schematically shown in Fig. 1.4(a) [17]. Although out-of-plane metal complexes may be formed by introducing a bigger size metal ion in Pc cavity for e.g.  $Pb^{+2}$ , which has an ionic radii of 1.20 Å [18]. MPc’s are produced in tons every year and are used as pigments in industrial paints (like car paintings or ink for color laser printers etc). After the discovery of semiconducting properties of Pc’s by Eley and Vartanyan, they are being used as data storage layer of many compact discs (CD’s) we used everyday [19, 20]. The parent molecule, hydrogenated Pc, with chemical formula  $C_{32}H_{18}N_8$ , has 2 hydrogen atoms in the center of the ring, and 16 surrounding the molecule.

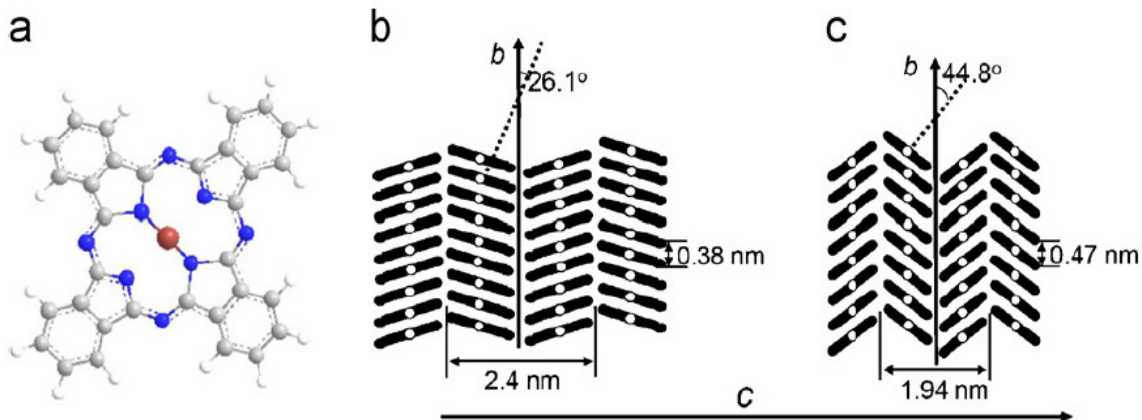


**Figure 1.4** Molecular structure of metal phthalocyanines (MPC) (a), and schematics of  $\alpha$ -FePc (b) and  $\beta$ -FePc (c) phases projected on (100) planes.

Pc's and particularly MPC's (where the two central hydrogen atoms have been replaced by a metallic atom) have many interesting properties, which make them advantageous for the application as organic semiconducting material. Some of them are discussed below:

- (i) Pc's are easily sublimed and can be crystallized with very high purity ( $10^{14}$  -  $10^{15}$  traps  $\text{cm}^{-3}$ ) exceptional in organic chemistry.
- (ii) Pc's show an exceptional thermal and chemical stability. In air MPC's undergo no noticeable degradation up to temperature 400 - 500°C and in vacuum most of them do not decompose below 900°C. They are not also affected by strong acids or bases [21].
- (iii) Pc's is highly conjugated molecule and contains 18  $\pi$  electrons in the macrocyclic ring which leads to very intense absorption bands at around 400 nm and 700 nm.

(iv) Pc's are a very versatile system as there are possibilities of tuning its electronic properties by playing with different side group and central metal atoms. There are more than thousand different Pc's have been synthesized by changing either central metal atom or side groups. The replacement of central metal atom and side group modifies its electronic properties, while its molecular structure, in most of the cases, remains unchanged [21, 22]. For example CuPc is a p-type organic semiconductor but the replacement of 16 hydrogen by fluorine makes the molecule ( $F_{16}CuPc$ ) n-type. In fact,  $F_{16}CuPc$  is one of the most stable n-type organic semiconductor known at present, and it has been used to fabricate the first n-channel organic transistor [23], in complementary logic circuits [24-26], and also in paper-like electronic displays [27].

The MPc's are known to exist in two main polymorphs, namely a metastable  $\alpha$  and stable  $\beta$  form [28]. The growth of  $\alpha$ -form is obtained in thin films when the substrate temperature is maintained below a phase transition temperature during growth [29]. The structural difference between  $\alpha$  and  $\beta$  polymorphs, as shown in Fig.1.4 (b) and (c), is in the tilt angle of the molecular stack from the b-axis, which is  $26.11^\circ$  for  $\alpha$ -phase and  $44.81^\circ$  for  $\beta$ -phase. Other less common polymorphic structures of MPc, such as,  $\gamma$ -,  $\delta$ -,  $\chi$ -forms have also been reported [28].

Pc's have monoclinic crystal structure in both  $\alpha$  and  $\beta$  phase. The stacking of Pc molecules in monoclinic structure is shown in the Fig. 1.5. The unit cell parameters for different phthalocyanine are listed in the Table-1.1. In this research work we have chosen CoPc and FePc molecules.

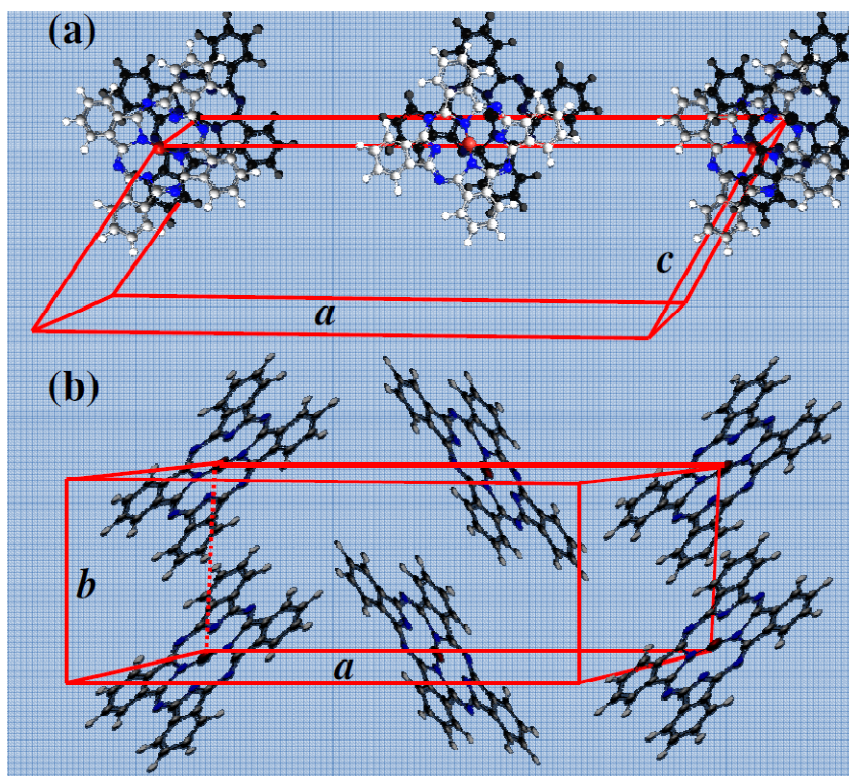


**Figure 1.5** Packing of the phthalocyanine molecule in its  $\beta$ -form. (a) Projection on the  $ac$ -plane and (b) projection on the  $ab$ - plane where the monoclinic  $b$ -axis points in the viewing direction in (a) and is aligned vertically in (b).

**Table 1.1** Unit cell parameters for various phthalocyanines.

|                 | H <sub>2</sub> Pc<br>[30] | $\beta$ -CuPc<br>[31] | F <sub>16</sub> CuPc<br>[32] | $\alpha$ -FePc<br>[33] | $\beta$ -FePc<br>[34] | $\alpha$ -CoPc<br>[33] | $\beta$ -CoPc<br>[35] |
|-----------------|---------------------------|-----------------------|------------------------------|------------------------|-----------------------|------------------------|-----------------------|
| M               | 514.55                    | 575.67                | 863.9                        | 568.38                 | 568.38                | 571.47                 | 571.47                |
| $a(\text{\AA})$ | 19.85                     | 19.407                | 20.018                       | 25.5                   | 19.39                 | 25.88                  | 19.35                 |
| $b(\text{\AA})$ | 4.72                      | 4.79                  | 5.106                        | 3.79                   | 4.79                  | 3.75                   | 4.77                  |
| $c(\text{\AA})$ | 14.8                      | 14.628                | 15.326                       | 25.2                   | 14.6                  | 24.08                  | 14.54                 |
| $\beta$         | 120.25°                   | 120.56°               | 111.83°                      | 90.4°                  | 120.85°               | 90.2°                  | 120.82°               |
| Z               | 2                         | 2                     | 2                            | 2                      | 2                     | 2                      | 2                     |

## 1.4 Charge transport in organic semiconductors: An overview

The charge transport mechanisms of insulators are usually applicable for the organic semiconductor as they have similar electronic structure. In any charge transport study there will always be a charge injecting electrode and a collecting electrode and the active layer between them as shown in Fig. 1.6. Therefore the charge conduction will depend on two processes: (i) injection of charge carrier from electrode to organic semiconductor and (ii) charge transport in the bulk. The dominant process between these two will be decided by the relative position of Fermi level of metal and semiconductor and the potential barrier existing between metal electrode and semiconductor. The nature of the interface between metal and organic semiconductor plays an important role in deciding the potential barrier. Therefore before presenting the charge transport mechanisms we discuss the electronic structure of the interface.

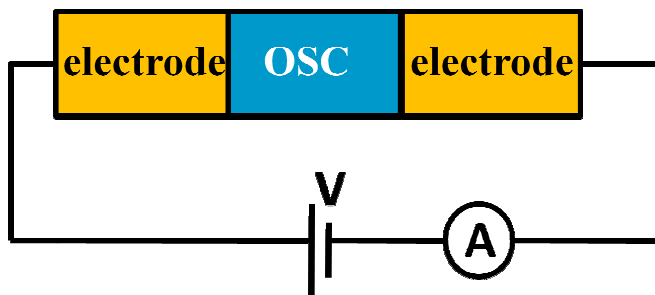


**Figure 1.6** The schematic of charge transport measurement showing an active organic semiconducting layer sandwich between charge injecting and collecting electrodes.

The typical electronic structure of metal and organic semiconductor, when they are separated, is shown in Fig 1.7 (a). The important electronic levels are the electrode Fermi level ( $E_F$ ); the semiconductor HOMO and LUMO i.e. the hole and electron transport levels;

and the vacuum level ( $E_{vac}$ ) of each material. The work function of the electrode ( $\Phi_M$ ), and the ionization energy (IE) and electron affinity (EA) of the semiconductor are defined as the energy difference between vacuum level and Fermi level for the metal, and between vacuum level and HOMO or LUMO, respectively, for semiconductor.

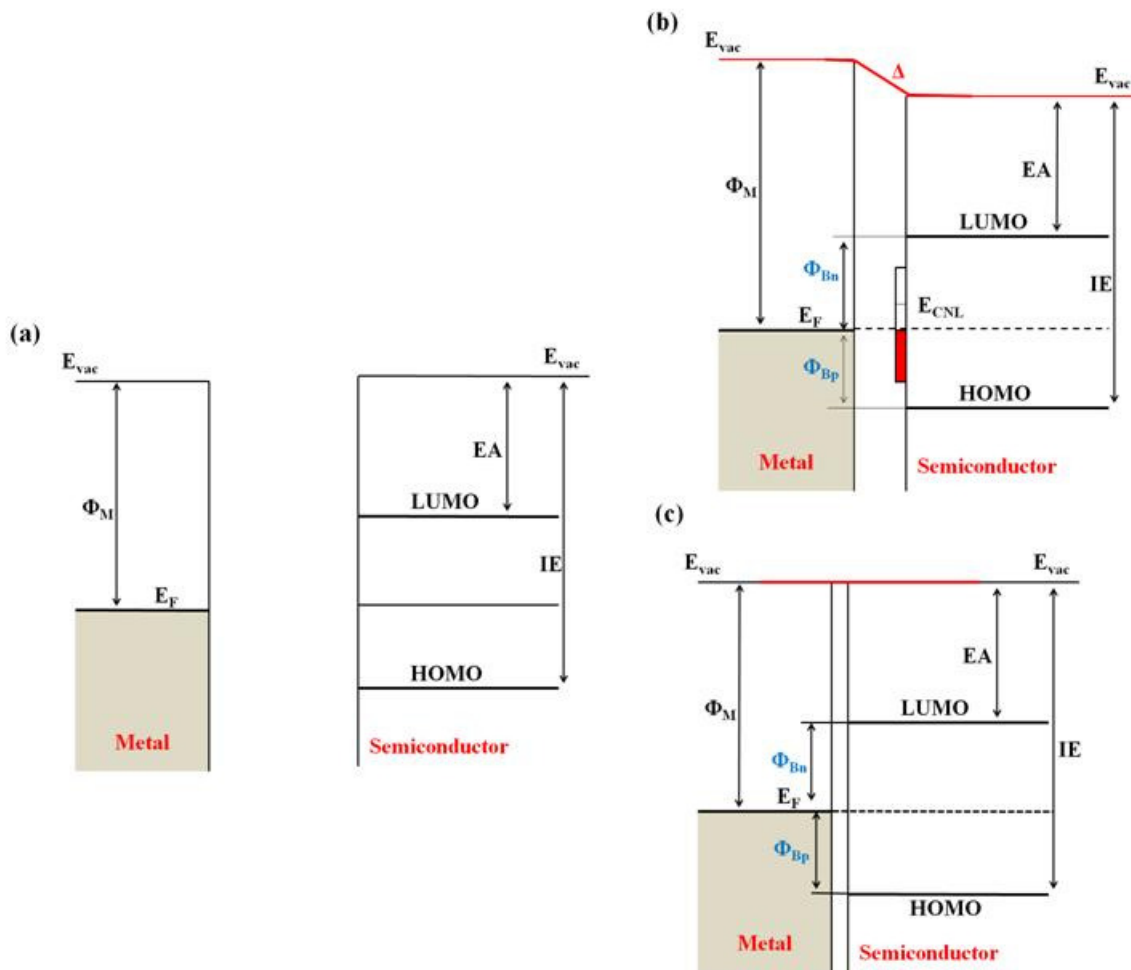


**Figure 1.7** (a) Electronic structure of a typical metal and organic semiconductor showing relevant energy levels when they are separated, (b) electronic structure of a metal organic semiconductor interface with interface dipole, (c) electronic structure of a metal organic semiconductor interface without interface dipole ( $\Delta = 0$ ) and therefore vacuum level aligns.

When a metal and a semiconductor (organic) are brought together to form an interface, as shown in Fig 1.7 (b), a dipole ( $\Delta$ ) is appeared due to interface gap states. These gap states have various origins. One is chemical i.e. the formation of chemical bonds or defects between the semiconductor and metal [36 - 38]. Second is induced density of interface states (IDIS) where the proximity of metal surface and the broadening of semiconductor states, due to overlap between continuum of metal surface and the semiconductor state, induces a density of states in the gap of semiconductor [39, 40]. In this scenario the injection barrier for electron and holes are  $\Phi_{Bn}$  and  $\Phi_{Bp}$ , respectively and the standard metal semiconductor interface treatment leads to the following equation for the electron injection barrier [41].

$$\Phi_{Bn} = S(\Phi_M - EA) + (1 - S)E_{CNL} \quad (1.1)$$

$$S = \frac{1}{1 + 4\pi e^2 D_{is} \delta} \quad (1.2)$$

Where  $\delta$  is the effective metal-semiconductor distance and  $E_{CNL}$  is the charge neutrality level of the interface and  $D_{is}$  is the density of interface gap states. In non-interactive metal-semiconductor interfaces the density of interface states are vanishingly small ( $\Delta = 0$ ) and thus the electron and hole barriers are given by  $\Phi_{Bn} = \Phi_M - EA$  and  $\Phi_{Bp} = IE - \Phi_M$ . These types of contacts are known as neutral contacts and schematic shown in Fig 1.7 (c). However, whether the charge conduction process is dominated by the electrode or bulk, depends on the value of  $\Phi_{Bn}$  ( $\Phi_{Bp}$ ) for electron (hole) injection and the relative Fermi level positions of metal and semiconductor. Generally a contact is considered to be Ohmic if the value of metal work function ( $\Phi_M$ ) is less than semiconductor work function ( $\Phi_S$ ) for n-type and vice versa for p-type semiconductor. On the other hand, a Schottky barrier appears when metal work function ( $\Phi_M$ ) is greater than semiconductor work function ( $\Phi_S$ ) for n-type

semiconductor. In this case the barrier height is given by the value of  $\Phi_{Bn}$  for electrons. Similar reasoning is also applicable for p-type semiconductors. However, an Ohmic contact between metal and semiconductor may be established if  $\Phi_{Bn}$  or  $\Phi_{Bp}$  is of the order of few  $kT$ .

In the case of Pc films the charge transport properties are widely studied using Au as electrodes. A typical Au/MPc interface is shown in Fig. 1.8, which indicates  $\Phi_{Bp}$  of 0.2 eV. This smaller  $\Phi_{Bp}$  value at room temperature results in an Ohmic contact at Au/MPc interface. In Pc films, traps (deep and shallow) are usually present, which depends on the nature of disorders and physisorbed or chemisorbed oxygen in the films. These traps strongly affect the charge transport of MPc films.

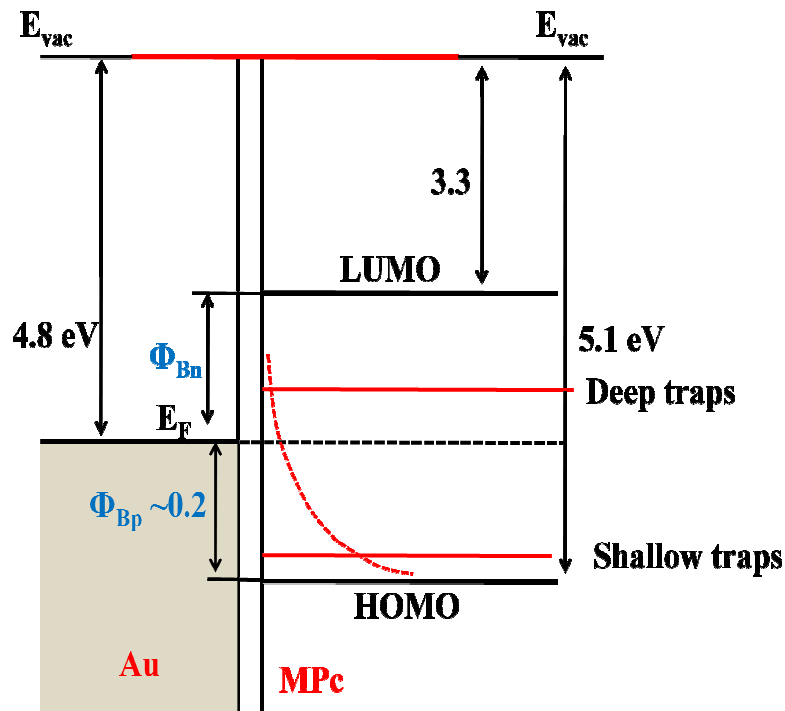


**Fig. 1.8** The electronic structure of the interface between MPc and Au electrode. The exponential distribution of traps is schematically shown in MPc films with shallow and deep states.

### 1.4.1 Charge injection mechanisms

If the contacts between metal electrodes and organic semiconductors are Schottky in nature, then the conduction is controlled by the electrode i.e. charge injection. Depending upon the applied electric bias, temperature and active layer thickness, different charge injection mechanism may occur at the metal/semiconductor interface. These mechanisms are discussed below.

#### 1.4.1.1 Tunneling mechanism

Tunneling is one of the major electrode limited processes where the charge carrier tunnel from one electrode to the other in spite of having lower energy than the finite potential barrier offered by the sandwich semiconductor having thickness less than 10 nm. The finite tunneling probability is due to the non-vanishing of metal electron wave function in the insulator despite the lack of allowed energy level there. The direct tunneling current density ( $J_{DT}$ ) as calculated by Simmons for trapezoidal barrier [shown in Fig. 1.9 (a)] is given by [42]

$$J_{DT} = \frac{\alpha}{d^2} e^{-Ad\sqrt{\phi}} - (\phi + eV)e^{-Ad\sqrt{\phi+eV}} \quad (1.3)$$

Where  $\alpha = e/4\pi\beta'\hbar$  and  $A = 2\beta'\sqrt{2m^*/\hbar}$  ( $e$  is the electron charge,  $m^*$  is the effective mass of electron in the insulator,  $\beta'$  is constant and has value  $\sim 1$ ,  $\hbar$  is the reduced Planck's constant),  $\phi$  is the average electron energy barrier height,  $d$  is the barrier width and  $V$  is applied voltage between the two electrodes.

It has been shown that at very small voltages i. e. for  $eV \ll \phi$  or in the vicinity of  $V \sim 0$ , the eq. 1.3 reduces to

$$J_{DT} = \frac{\gamma\sqrt{\phi}}{d} e^{-Ad\sqrt{\phi}} V \quad (1.4)$$

Where  $\gamma = \frac{e\sqrt{2m^*}}{4\beta\pi^2\hbar^2}$

Since  $eV \ll \phi$ , it can be considered that  $\phi$  does not depend on  $V$ . therefore, in this case  $J$  is proportional to  $V$ .

For intermediate voltage, i.e.  $eV < \phi/2$ , the eq. 1.3 is expressed as

$$J_{DT} = \frac{\gamma\sqrt{\phi}}{d} e^{-Ad\sqrt{\phi}} (V + \sigma V^3) \quad (1.5)$$

Where  $\sigma = \frac{(Ae)^2}{96\phi d^2} - \frac{Ae^2}{32d\phi^{3/2}}$

For high voltage range, i.e.  $eV > \phi/2$  the potential barrier takes a triangular shape, as shown in Fig.1.9 (b) and the eq. 1.3 reduces to the Fowler-Nordheim tunneling equation [43] i. e.

$$J_{FN} = BE^2 \exp\left(-\frac{C}{E}\right) \quad (1.6)$$

Where  $E=V/d$  is the field,  $B= e^3/16\pi^2\hbar m^* \phi$  and  $C = (4\sqrt{2m^*}/3e\hbar)\phi^{3/2}$ . If the current transport across a insulator layer is dominated by FN tunneling then a plot of  $\ln(J_{FN}/E^2)$  versus  $1/E$  –known as FN plot–should have a linear behavior.

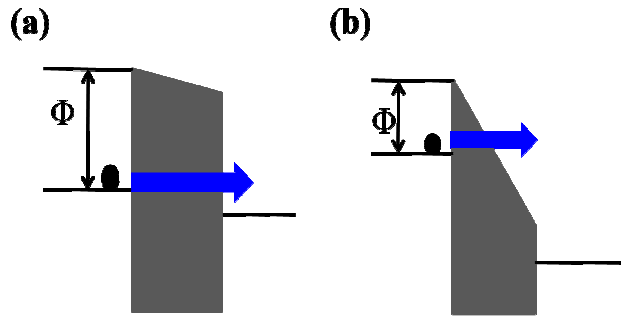


**Figure 1.9** (a) Schematic of carrier tunneling a trapezoidal potential barrier at lower voltage, (b) triangular shape of the potential barrier at higher voltage.

### 1.4.1.2 Multistep tunneling (MUST)

Apart from the direct tunneling which requires a higher voltage, there is a possibility of sequential tunneling of charge carrier from the metal electrode to the conduction or valence band of the semiconductor. The physical process is schematically shown in the Fig. 1.10. The interface between metal and semiconductor always contains some localized states, these localized states helps the charge carrier to tunnel sequentially from the electrode to bulk. In this model conductivity can be derived as [44]

$$\sigma = \sigma_0 \exp\left(-\sqrt{\frac{F_0}{F}}\right) \quad (1.7)$$

$$\text{With } F_0 = \frac{16\sqrt{2m}\alpha\Delta^{3/2}}{3e\hbar} \quad (1.8)$$

$F_0$  is related to the material through the potential barrier ( $\Delta$ ) and material parameter  $\alpha$  that depends weakly on the temperature. Here  $\alpha = \ln(p^{-1})$ , where  $p^N$  is the probability of forming a N-step tunneling path of the MUST. The important feature of the eq. 1.7 is its rather weak sensitivity to the concentration of the localized states in the gap, which is generally difficult to know.

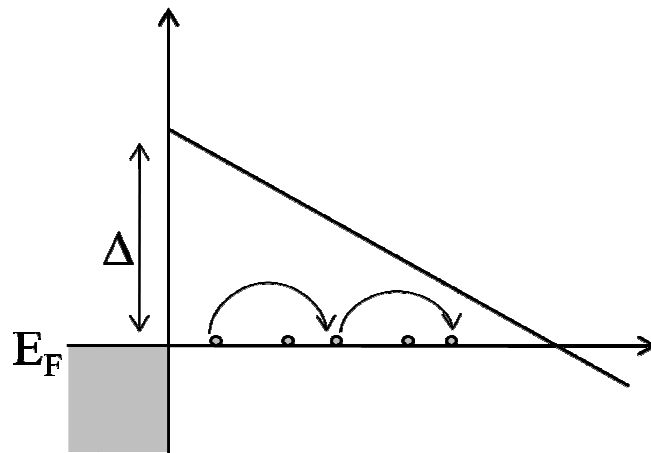


**Figure 1.10** Schematic of sequential tunneling of electron form metal electrode to the conduction band of insulator/semiconductor via localized states.

### 1.4.1.3 Schottky mechanism

When the barrier is too thick to tunnel from one electrode to other, the current flowing through the semiconductor is limited mainly by the rate at which electrons are thermally excited over the interfacial potential barrier into the semiconductor transport level. In this case current is given by the Richardson thermionic emission [45]:

$$J = \frac{4\pi m e k^2 T^2}{h^3} \exp\left(-\frac{\phi}{kT}\right) \equiv AT^2 \exp\left(-\frac{\phi}{kT}\right) \quad (1.9)$$

Where A ( $1.2 \times 10^6 \text{ Am}^{-2}\text{K}^{-2}$ ) is the Richardson constant and  $\phi$  is potential barrier independent of applied voltage. However, in practice  $\phi$  varies with applied field due to the image forces originates from the polarization of electrode surface by the ejected electrons. Thus current does not saturate, but rather is a function of applied field. The potential energy (shown in Fig. 1.11) of the electron due to the image force is given by

$$\phi_{im} = -\frac{e^2}{16\pi\epsilon_0 Kx} \quad (1.10)$$

So due to the presence of image potential and uniform electric field the shape of the original step potential barrier changes as shown in the Fig. 1.11. In view of modified potential the potential energy of an electron at a distance  $x$  from the interface is given by

$$\phi(x) = \phi_0 - \frac{e^2}{16\pi K\epsilon_0 x} - eFx \quad (1.11)$$

The potential has a maximum at  $x_m = (e/16\pi K\epsilon_0 F)^{1/2}$ . Therefore the attenuation  $\Delta\phi_S (= \phi_0 - \phi(x_m))$  of the barrier height due to the interaction of the applied field with the image potential is given by

$$\Delta\phi_S = \left(\frac{e^3}{4\pi K\epsilon_0}\right)^{1/2} F^{1/2} \equiv \beta_S F^{1/2} \quad (1.12)$$

In this modified barrier height the current density is given by Richardson-Schottky equation [46]

$$J = AT^2 \exp\left(-\frac{\phi_0}{kT}\right) \exp\left(\frac{\beta_S F^{1/2}}{kT}\right) \quad (1.13)$$

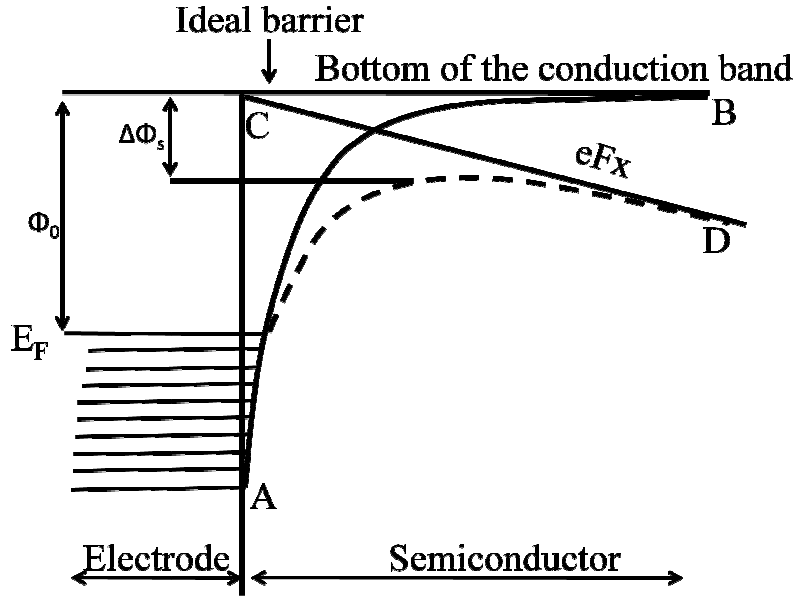


**Figure 1.11** Schematic of metal (electrode) organic (semiconductor) Schottky interface. In the figure ‘AB’, ‘CD’ represents potential variation due to image charge at electrode, and applied electric field, respectively. ‘AD’ represents the actual potential barrier at the interface.

## 1.4.2 Bulk limited charge transport

If the metal/organic interface is Ohmic type, then the charge transport is governed by the bulk of the semiconductor. Depending on the bias, temperature and nature of the traps present in the film, various charge transport mechanisms can operate in the films. These mechanisms are described in the following sections.

### 1.4.2.1 Ohmic conduction

At low bias, the injected charge carriers are negligible compared to the thermally generated carriers. Therefore charge carriers will drift from one electrode to another due to

the application of electric field. Under these conditions, the current density is linearly proportional to the applied bias, which is given by

$$J = n_0 e \mu V / L \quad (1.14)$$

Where  $n_0$  is the free carrier density and  $\mu$  is the charge carrier mobility.

#### ***1.4.2.2 Space charge limited conduction (SCLC)***

At higher bias, the carriers injected from the Ohmic contacts exceed that of the thermally generated carriers and these carriers start piling up in the vicinity of injecting electrode, which creates a space charge. These space charges control the conduction processes in the semiconductor. In space charge condition, the  $J$ - $V$  characteristics depend on the applied bias, temperature and the nature and density of traps in the semiconductor. Here we describe the details of space charge limited conduction (SCLC) in (i) trap free organic semiconductors and (ii) semiconductors with shallow/deep traps.

##### **(i) *Charge transport in trap-free organic semiconductor***

We first consider the perfect intrinsic semiconductor, free of traps and with small density of thermally generated free carrier ( $n_0$ ). The  $J$  can be written as

$$J = \rho v \quad (1.15)$$

Where  $\rho$  is the average charge density and  $v$  is the average drift velocity. The total charge,  $Q$  per unit area at a particular voltage  $V$ , an semiconductor can hold will depend on its capacitance ( $C = \epsilon/L$ ) and is given by

$$Q = \rho L = CV \approx \frac{\epsilon}{L} V \quad (1.16)$$

where  $L$  is the cathode-anode spacing. Assuming charges are injected from the Ohmic contacts i.e. current is not injection limited and combining eq. 1.15 and 1.16 we obtain

$$J \simeq \frac{\epsilon v V}{L^2} \quad (1.17)$$

At low field strength the average drift velocity is proportional to the average applied field ( $E$ ),  $v = \mu E \simeq \mu V/L$  where  $\mu$  is the free electron drift velocity. Substituting for  $v$  into eq. 1.17 gives

$$J \simeq \epsilon \mu \frac{V^2}{L^3} \quad (1.18)$$

The more exact result can be obtained by solving the current equation and Poisson equation and given by

$$J = \frac{9}{8} \epsilon \mu \frac{V^2}{L^3} \quad (1.19)$$

This is nothing but Mott- Gurney law describing current-voltage relation in a trap free insulator. It is evident from the eq. 1.19 that current density varies with square of voltage and by knowing the value of permittivity, mobility can be found out from the  $J$ - $V^2$  plot.

The situation will be different for a non-negligible density of thermal free carrier ( $n_0$ ) in the semiconductor. One expects Ohm's law to valid in low voltages. However with the increase of voltage the density of injected carrier ( $n_i$ ) increases and at a particular voltage they become comparable to each other. Thus the crossover from Ohm's law (eq. 1.14) to trap-free square law (eq. 1.19) is observed. The crossover voltage can be derived as  $V_X = \frac{9en_0L^2}{8\epsilon}$ . It can be shown that at this particular voltage the transit time of electron and dielectric relaxation time are equal and beyond this voltage transit time for electron is too short for their charge to be relaxed by the thermal carrier. Thus the injected electrons dominate the thermally generated electrons and SCLC condition arises.

(ii) **Trap mediated transport**

In the real samples, local states (traps) are always present, and therefore, reduce the current at lower injection level as they capture and immobilize most of the injected charge carrier. On the other hand, the trapped electrons do contribute to the  $Q=CV$  relation and the eq. 1.16 in this case becomes

$$Q = (\rho + \rho_t)L = CV \approx \frac{\epsilon}{L}V \quad (1.20)$$

where  $\rho_t$  is the average trapped charge density. It is possible to find the space charge limited  $J$ - $V$  relation using same argument as stated for trap free case provided the relationship between  $\rho$  and  $\rho_t$  is known. This relationship can be derived if the free and trapped carriers are in quasi-thermal equilibrium. These two parameters are connected via position of quasi-Fermi level ( $E_F$ ). The free ( $n$ ) and trapped ( $n_t$ ) carrier density is given by

$$n = N_C \exp\left(\frac{E_F}{kT}\right) \quad (1.21)$$

$$n_t(E) = h(E)f[E - E_F] \quad (1.22)$$

Where  $N_C$  is the density of extended states and  $f[E - E_F]$  is the Fermi-Dirac distribution function. So obviously, total trap density ( $N_t$ ) is given by:

$$N_t = \int_E n_t(E)dE \quad (1.23)$$

In general traps are distributed in energy space and the distribution function is  $h(E)$ . There are three types of distribution of traps are well known as given below

- A discrete local level at the energy  $E_t$

$$h(E) = N_t \delta(E - E_t) \quad (1.24)$$

- An exponential distribution

$$h(E) = \frac{N_t}{kT_c} \exp\left(-\frac{E}{kT_c}\right) \quad (1.25)$$

- A Gaussian distribution peaking at  $E_t$

$$h(E) = \frac{N_t}{\sigma\sqrt{2\pi}} \exp\left(-\frac{(E-E_t)^2}{2\sigma^2}\right) \quad (1.26)$$

Here,  $N_t$  is the total density of traps,  $T_c$  and  $\sigma$  are distribution parameters of local states for the exponential and Gaussian distribution of traps.

Let us now introduce the free to total carrier density ratio  $\Theta$  ( $\Theta \leq 1$ )

$$\Theta = \frac{n}{n+n_t} = \frac{\rho}{\rho+\rho_t} \quad (1.27)$$

Combining eq. 1.20 and 1.27 we get

$$Q = (\rho + \rho_t)L = \rho L/\Theta \simeq \varepsilon V/L \quad (1.28)$$

Substituting for  $\rho$  into eq. 1.15, we get

$$J \simeq \Theta \varepsilon \mu \frac{V^2}{L^3} \quad (1.29)$$

The correct analytically derived result has the numerical factor 9/8 in front of it, just as for the trap-free case. It is evident from the eq. 1.29 that SCL  $J$ - $V$  characteristics should not necessarily be proportional to the square of the voltage but it also depends on the voltage dependence of  $\Theta$ . In other word the shape of the SCL current-voltage characteristic depends on the position of the quasi-Fermi level (voltage dependent) with respect to energies of the distribution of traps.

Let us examine SCL current-voltage dependence controlled by a discrete level of traps, described by eq. 1.24. In this scenario  $\Theta$  can be expressed by

$$\frac{1}{\Theta} = 1 + \frac{n_t}{n} = 1 + \frac{N_t}{N_c \left[ \exp\left(-\frac{E_F}{kT}\right) + \exp\left(-\frac{E_t}{kT}\right) \right]} \quad (1.30)$$

An electron trap at  $E_t$  is said to be shallow if quasi Fermi level ( $E_F$ ) lies well below  $E_t$ :

$\frac{E_F}{kT} > \frac{E_t}{kT}$ . Thus  $E_{F0}$  must lie well below  $E_t$ , as for example with states at energy  $E_{t1}$  in Fig.

1.12 (a). Then the eq. 1.30 becomes  $\Theta = \frac{N_c}{N_t} \exp\left(-\frac{E_t}{kT}\right) < 1$ . It is evident that in this shallow trap situation  $\Theta$  is independent of voltage and the current is proportional to the square of applied voltage, it is, however smaller in magnitude than the trap free case (eq. 1.19). It should be noted that  $\Theta$ , although nearly independent of voltage range under consideration, does depend on the density of traps  $N_t$ . At higher injection level, where quasi-Fermi level crosses the trap level  $\Theta$  sharply increases to one and current merges to trap free current.

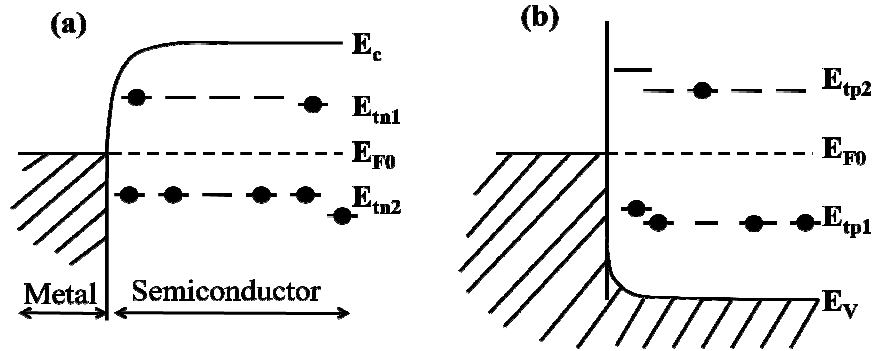


**Figure 1.12** (a) Schematic of shallow ( $E_{tn1}$ ) and deep ( $E_{tn2}$ ) traps for electrons. (Solid circle indicates traps occupied by an electron) (b) Schematic of shallow ( $E_{tp1}$ ) and deep ( $E_{tp2}$ ) traps for holes. (An electron-occupied trap is equivalent to a hole-unoccupied trap and conversely)

An electron trap at  $E_t$  is said to be deep if quasi-Fermi level ( $E_F$ ) lies above  $E_t$  :  $\frac{E_F}{kT} > \frac{E_t}{kT}$ . In this situation the single set of traps at  $E_t$  situated below  $E_{F0}$  as shown in Fig. 1.12 (a), where  $E_{tn2}$  is the deep trap level. It is evident from the eq. 1.30 that in presence of deep traps first term in the square bracket prevails and since  $E_F$  depends on the injection level (applied voltage)  $\Theta$  sharply increases to unity. Thus above some particular voltage called ‘trap-filled-limit voltage’ the sample behaves as trap free and current is given by eq. 1.19. The trap-filled-limit voltage ( $V_{TFL}$ ) is given by

$$V_{TFL} = \frac{ep_{t0}L^2}{2\varepsilon} \quad (1.31)$$

Where the  $p_{t0}$  is the density of traps not occupied by electrons, given by  $N_t \exp\left(\frac{E_{F0} - E_t}{kT}\right)$ .

Now we will discuss the complete  $J$ - $V$  characteristics for a single set of traps. A family of current-voltage characteristics is possible corresponding to a different energy location  $E_t$  of a single set of traps of density  $N_t$  with respect to a given position of the equilibrium Fermi level  $E_{F0}$ . This entire family is contained in a certain ‘triangle’ in the ( $\log J$ ,  $\log V$ ) plane, shown in Fig. 1.13. This triangle is bounded by Ohm’s law, the trap-free square law and a ‘vertical’ leg corresponding to the trap-filled-limit law. The family of ( $J$ ,  $V$ ) characteristic consists of two subfamily, one for which  $E_t$  lies below  $F_{F0}$  and other for which  $E_t$  lies above  $E_{F0}$ . The typical member of the former case shown in Fig. 1.13 labeled I. The vertical section occurs at the voltage  $V_{TFL,I}$ , given by eq. 1.31. The deeper is the trap level, i.e. the larger  $\left(\frac{E_{F0} - E_t}{kT}\right)$  the smaller is  $V_{TFL,I}$ . Finally, when the traps are so deep that the vertical portion disappears and the traps no longer affect the current flow. A typical example of latter case is shown in the Fig.1.13, labeled II. So long  $E_F$  lies below  $E_t$ , the traps are shallow and current follows the square law (eq. 1.29), with  $\Theta$  is given by  $\Theta = \frac{N_c}{N_t} \exp\left(-\frac{E_t}{kT}\right) < 1$ , after departing from Ohm’s law at crossover voltage  $V_X$ . In the neighborhood of  $V=V_{TFL}$ ,  $E_F$  crosses  $E_t$  and the ( $J$ ,  $V$ ) curve merges with the trap free case given by eq. 1.19. It should be noted that when  $E_t$  gets close enough to the conduction band so that  $\Theta \simeq 1$  the effect of the traps becomes negligible and only the trap-free square law is observed.

So far we have discussed about electron trap at a particular energy  $E_t$ . For single-crystal materials of high chemical and structural purity this is undoubtedly a good

approximation for the purpose of analyzing charge transport. On the other hand, especially for thin films there will be large number of traps originated from structural and chemical disorder at different energy. The net result will be a broad smearing out of trap level in energy. One simple possible representation of the many different sets of traps, all smeared out in energy, is the exponential distribution proposed by Rose and given by eq. 1.25. However, the dependence of SCL current on voltage depends on the energetic profile of the trap distribution. In particular, when the energetic distribution is exponential, the current-voltage characteristics can be written in the form [47]

$$J = \mu e^{1-l} N_c \left( \frac{\varepsilon_0 \varepsilon}{N_t} \right)^l \left( \frac{l}{l+1} \right)^l \left( \frac{2l+1}{l+1} \right)^{(l+1)} \frac{V^{(l+1)}}{L^{(2l+1)}} \quad (1.32)$$

Where  $e$  is the unit charge and  $l = T_c/T$ .

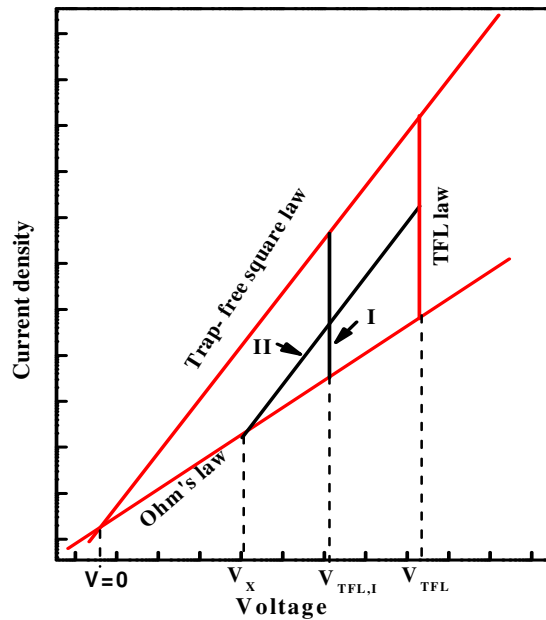


**Figure 1.13** Schematic current-voltage ( $J$ - $V$ ) characteristics for one-carrier space-charge-limited current controlled by a single set of traps in log-log plot. I corresponds to  $E_{F0}$  lying above trap level ( $E_t$ ) and II corresponds to  $E_{F0}$  lying below traps level ( $E_t$ ). All the  $J$ - $V$  characteristics will be contain inside the triangle (red color) depending on the relative position of Fermi level and trap level.

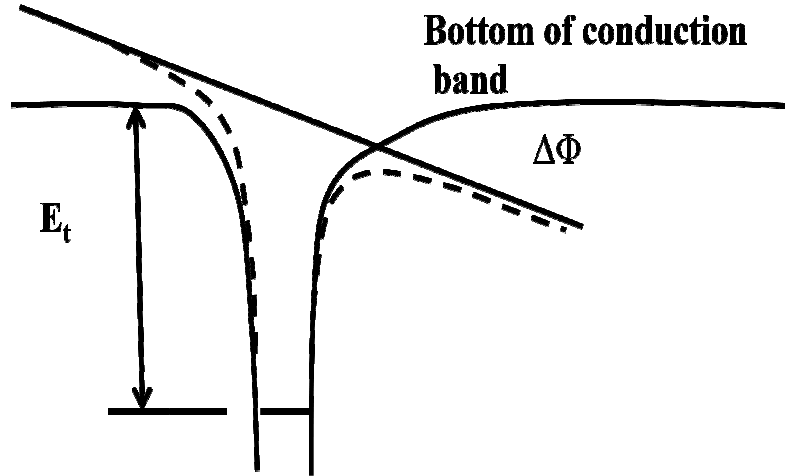


**Figure 1.14** Poole-Frankel effect at a trap in the bulk of the semiconductor.

### 1.4.2.3 Poole-Frankel effect

The Poole-Frankel effect is referred to as the bulk analogue of the Schottky effect, discussed above. When in the bulk a charge carrier is trapped in an impurity level it is unable to contribute to the conductivity until it overcomes the potential barrier and is promoted to the transport level. In the presence of high electric field the barrier is reduced by an amount  $eFx$  where  $e$  is the electronic charge,  $F$  is the applied electric field (see Fig. 1.14). In short the Poole-Frankel effect is the field-assisted lowering of the coulombic potential barrier ( $-e^2/4\pi\epsilon_0Kx$ ) between carriers at impurity levels and the edge of the conduction or valence bands and the amount of lowering of barrier  $\Delta\phi_{PF}$  is given by

$$\Delta\phi_{PF} = \beta_{PF}F^{1/2} \quad (1.33)$$

Where  $\beta_{PF} = \left(\frac{e^3}{\pi\epsilon_r\epsilon_0}\right)^{1/2}$  is the Poole-Frankel field lowering coefficient. The current density is given by [48]

$$J = J_0 \exp\left(\frac{\beta_{PF}F^{1/2}}{kT}\right) \quad (1.34)$$

Where  $J_0 = \sigma_0 F$  is the low field current density. Thus a linear plot of  $\log J$  against  $V^{1/2}$  should be obtained, from which a value of the field-lowering coefficient can be obtained and compared with the predicted theoretical value.

## 1.5 Models for temperature dependent resistivity

In semiconductor there will always be some localized energy states and in case of organic semiconductor also charge are intrinsically localized due to the weak wave function overlap between two adjacent molecules. Therefore upon application of electric field the charge carrier will hop from one localized state to another. At higher temperature where the charge carriers have sufficient energy the conductivity mechanism is mainly determined by hopping of carriers which are thermally activated into the band tail. The resistivity in this case can be described by the Arrhenius relation

$$\rho = \rho_0 \exp\left(\frac{\Delta E}{kT}\right) \quad (1.35)$$

Where  $\Delta E$  is the activation energy for the conduction. Essentially this process is a fixed range hopping process. At low temperature the hopping process may not be fixed range or nearest neighbor, rather it can be variable range as suggested by Mott. In this scenario the probability of hopping between two states of spatial separation  $R$  and energy separation  $W$  is given by

$$P(W, R) = \exp\left(-aR - \frac{W}{kT}\right) \quad (1.36)$$

With  $k$  Boltzmann's constant and ' $a$ ' is constant. The probability will be optimized with respect to  $R$  and  $W$ . Therefore carrier hopping may not be nearest neighbor but hopping distance will vary depending on the energy difference between the localized states. The variable range hopping model resistivity is expressed as [49]

$$\rho = \rho_0 \exp \left[ \left( \frac{T_0}{T} \right)^{1/4} \right] \quad (1.37)$$

Where  $T_0 = \frac{18\alpha^3}{kN(E_F)}$ ,  $N(E_F)$  be the density of localized states at the Fermi level and  $\alpha$  is the coefficient of exponential decay of the localized states wave function. The hopping parameters can also be determined from the following relations

$$R = \left[ \frac{9}{8\pi\alpha kTN(E_F)} \right]^{1/4} \quad \text{and} \quad W = \left[ \frac{3}{4\pi R^3 N(E_F)} \right] \quad (1.38)$$

The equation is valid for 3 D system. However, it can be generalized to  $d$  dimensional ( $d= 1, 2$  or  $3$ ) system, for which the variable range logarithmic resistivity is proportional to  $T^{\left(\frac{1}{d+1}\right)}$ .

## 1.6 Literature review on charge transport in phthalocyanine films

In literature, there is a significant amount of reports on the charge transport studies in Pc thin films. The Schottky effect in Al/CuPc/Ag structure was observed by Barkhalov and Vidadi [50] for the reverse bias. Similar effect have been studied by other groups in Al/M(Cu, Zn)Pc/Au structure [51, 52]. It was proposed that a layer of aluminium oxide grew at the interface of Pc and Al electrode, by the diffusion oxygen through the organic material. The barrier height was determined to be 1.27eV for ZnPc and Al electrode interface [52]. More recently Mahapatra et al reported that CuPc forms a Schottky barrier with Al and Cu whereas ITO and Au forms an Ohmic contact at room temperature [53]. Similarly Poole Frankel effect, which is bulk analogous of Schottky effect, was also reported for the Pc films. Poole-Frankel conductivity in a structure incorporating CuPc was first reported by Hassan and Gould [54]. Latter Poole-Frankel effect was also observed in several other structures, including Al/CuPc/Au [55], Au/PbPc/Al [56, 57]. In some cases field lowering co-efficient is

slightly higher than the theoretical value, which was attributed to the non-uniform internal electric field distribution.

SCLC mechanism is generally used to explain charge transport in OLEDs and OFETs where phthalocyanine films were used as active layer [58, 59]. SCLC conduction in Au/CuPc/Au structure is first extensively studied by Sussman and concluded that SCLC, dominated by exponential distribution of traps, was responsible for the conduction in temperature range 210-430K [60]. Space charge limited conduction, dominated by both discrete trap levels and exponential trap distributions has been identified in many Pc thin films [54, 55, 61 - 64]. From all these reports it is easily concluded that the total trap concentration for exponential distributions span a wide range from  $10^{20}$  to  $10^{26} \text{ m}^{-3}$ . However this variation is believed to be due to purity of material, preparation condition and oxygen contents. This window is comparably small ( $5 \times 10^{16}$  to  $5 \times 10^{19} \text{ m}^{-3}$ ) for single level of traps. The SCLC method, as described in the previous section, is most frequently used techniques to calculate mobility in these types of thin films. Although other methods, such as, time-of-flight [65], Seebeck measurements [66], FET measurements [67] were also used to determine the mobility. A literature survey on the mobility values determined using different techniques and the temperature ranges over the measurements were carried out is summarized in Table-1.2. The mobility for various Pc films is rather poor and varies in the range  $10^{-6}$ - $10^{-2} \text{ cm}^2 \text{ V}^{-1} \text{ s}^{-1}$  [60, 61, 68]. The low mobility values in Pc thin films mainly arises due to the weak van der Waals forces among molecules, leading to a poor overlap of the wave-function of  $\pi$ -electrons between adjacent molecules. This is further weakened due to presence of both energetic (diagonal and non-diagonal) and positional disorders. These disorders depend on the nature of molecular stacking (face-on or edge-on), adsorbed oxygen species and presence of

impurities [69]. Even in single crystals that are defect free, the  $\pi$ -electron wave-function overlapping of adjacent Pc molecules is not highest due to inherent edge-to-face on molecular packing, as shown in Fig. 1.5. A major consequence of the low mobility in Pc films is that their charge transport properties have been investigated only in the temperature range 473-175 K. The low temperature charge transport studies of Pc films below 175 K have never been investigated. The major reason for this is that due to poor mobility, the current at low temperatures goes below the measurable limits i.e. below pA. Thus in order to investigate the low temperature charge transport in Pc films, it essential that their mobility need to be improved.

**Table 1.2** Partial literature review of mobility values for phthalocyanine thin films.

| Device structure           | Mobility ( $\text{cm}^2\text{V}^{-1}\text{s}^{-1}$ )<br>(method of measurement) | Temperature range | Ref.    |
|----------------------------|---|-------------------|---------|
| Au/H <sub>2</sub> Pc/Au    | $1.63 \times 10^{-2}$ (SCLC)  | 290 - 473K        | [70]    |
| Au/NiPc/Al                 | $6.2 \times 10^{-2}$ (SCLC)   | 300 - 400K        | [71]    |
| Au/CuPc/Au                 | $5.1 \times 10^{-3}$ (Transient pulse)  | RT                | [72]    |
| ITO/CuPc/Al                | $1.4 \times 10^{-8}$ (SCLC)   | 200 - 320K        | [73]    |
| Al/ClAlPc/Al               | $10^{-4}$ (TOF)   | 213 - 333K        | [74]    |
| CuPc, single crys.         | 75 (hall mobility)  | Band transport    | [75]    |
| Cupc, single crys.         | 0.6 (FET)   | 175 - 400K        | [76]    |
| FePc, single crys.         | 0.3 (FET)   | -                 | [77]    |
| Au/NiPc/Au                 | $1 \times 10^{-3}$ (SCLC)   | 220 - 330K        | [78]    |
| Au/VoPc/Au                 | 1 (FET)   | -                 | [79]    |
| Au-Cr/TiOPc/Au             | $9 \times 10^{-6}$ (FET)  | 300 - 400K        | [80]    |
| Au/F <sub>16</sub> CuPc/Au | 0.11 (FET)  | -                 | [81,82] |
| Au/ZnPc/Au                 | 0.32 (FET)  | 300 - 200K        | [82,83] |
| Au/FePc/Au                 | $1 \times 10^{-6}$ (SCLC)   | 200 - 350K        | [84]    |

## 1.7 Scope of the thesis

As discussed in the previous section, the low temperature transport properties of Pc films, in particular below 150K, have never been investigated due to the poor mobility. The main motivation of present thesis is therefore to *grow high mobility metal phthalocyanine thin films and investigate their charge transport down to 25 K*. For this purpose, we have grown FePc and CoPc films using molecular beam epitaxy, which not only ensures clean growth environment but also allows precise control of various growth parameters, such as, substrate temperature, deposition rate, cleanliness of the substrates etc. The most innovative experiments carried out to control the orientation of molecules (edge-on or face-on) on substrates were to tailor the substrate surface. It has been shown that in the inert surface e.g. glass the molecules orient randomly. If the molecule substrate interaction is strong e.g. (0001) sapphire crystals, Pc molecules pack in the face-on configuration. However, if the substrate has controlled surface roughness e.g. natural twinned boundaries present in the (001) LaAlO<sub>3</sub> single crystals, then molecules pack in the edge-on stacking along the grain boundaries. The edge-on stacking of Pc molecules leads to a mobility of  $\sim 7 \text{ cm}^2\text{V}^{-1}\text{s}^{-1}$  at 300K. Motivated with this result, we have grown Pc films along a single grain boundary of 36.8° cut (001) SrTiO<sub>3</sub> bi-crystal substrates and these films exhibited a mobility of  $150 \text{ cm}^2\text{V}^{-1}\text{s}^{-1}$ , which is the highest reported value till date. These high mobility films were utilized for the investigation of the temperature dependent current-voltage characteristics in the temperature range of 300-25K, and we have obtained several new results. In addition, the suitability of these films has been extensively investigated for the gas sensing application. This thesis comprises of the description of the experimental methods on the growth and characterization of FePc and CoPc films, results on temperature dependent  $J$ - $V$  as well as

resistivity and their analyses and gas sensing applications of the grown films. The thesis encompasses following chapters.

Chapter 2 describes the experimental procedure of thin films growth of FePc and CoPc by MBE. The detail of MBE and other characterization techniques, such as SEM, AFM, XPS, FTIR, UV-Visible spectroscopy etc, used to characterize the films are presented. In addition, the detail of charge transport and gas sensing measurement configuration and setup are discussed in this chapter.

Chapter 3 deals with the optimization of the growth parameters for FePc and CoPc thin films by MBE technique. It has been shown that on the glass substrate the FePc /CoPc yields amorphous films when deposited at room temperature. The films grown at elevated temperature yields polycrystalline with edge-on stacking of molecule. On the other hand, at low thickness (<25 nm) CoPc stack in the face-on configurations on (0001) sapphires substrates, which however at higher thickness changed to edge-on stacking and leading to a polycrystalline nature. It has been demonstrated that an ordered films of CoPc grows along the twin boundary of LaAlO<sub>3</sub>, as the molecules stack in the edge-on configuration along the twin boundary. A very high level of edge-on stacking of CoPc molecules has been obtained using 36.8° bicrystal boundary of SrTiO<sub>3</sub> as a template.

Chapter 4 deals with the description of the results on the charge transport studies carried on amorphous and polycrystalline CoPc and FePc films grown on glass and sapphire substrates. It has been shown that the charge transport in amorphous and polycrystalline films grown on glass substrates are dominated by the deep-trap controlled space charge limited conduction (SCLC) in the temperature range of 300 – 220K. At low temperature range transport is govern by Poole Frankel mechanisms. Due to low mobility ( $0.2 \text{ cm}^2\text{V}^{-1}\text{s}^{-1}$ ), it is

difficult to measure the transport properties below 150 K. On the other hand, the mobility ( $0.98 \text{ cm}^2\text{V}^{-1}\text{s}^{-1}$ ) of polycrystalline films grown on sapphire are comparatively high, and thus, charge transport could be measured down to 75K. The charge transport in this case and is controlled by the shallow trap limited SCLC. This difference between the two types of polycrystalline films i.e. on glass and sapphire is attributed to the difference in their morphology.

Chapter 5 describes the results of charge transport measurement on highly ordered CoPc films. It has been demonstrated that very high mobility of  $7 \text{ cm}^2\text{V}^{-1}\text{s}^{-1}$  and  $150 \text{ cm}^2\text{V}^{-1}\text{s}^{-1}$  can be achieved when measured on CoPc films deposited along the twin boundary of  $\text{LaAlO}_3$  and  $36.8^\circ$  cut bicrystal boundary of  $\text{SrTiO}_3$ , respectively. It is further shown that at higher temperature charge transport mechanism is dominated by bulk limited processes whereas at low temperature transport mechanism is governed by electrode limited process in CoPc films deposited along the twin boundary of  $\text{LaAlO}_3$ . Based on the charge transport mechanism we have proposed a new temperature-bias phase diagram for describing charge transport mechanism in ordered CoPc films on twined  $\text{LaAlO}_3$  substrates. The charge transport studies carried on CoPc films deposited along the  $36.8^\circ$  cut bicrystal boundary of  $\text{SrTiO}_3$  indicates that the conductivity of these films are in critical region of the metal-insulator transition.

Chapter 6 deals with the gas sensing of CoPc thin films deposited on various substrates. It has been demonstrated that 20 nm CoPc films grown on sapphire substrates are the appropriate films for  $\text{Cl}_2$  gas sensing. The lowest  $\text{Cl}_2$  sensing limit of these sensors was found to be 5 ppb gas. The sensors exhibited a linear variation in sensitivity in the range 5 -

2000 ppb. The sensors were also very stable and reproducible. The sensing mechanism and the Cl<sub>2</sub> adsorption kinetics has been described.

The summary of the present thesis work and the directions for the future research associated with this thesis are presented in Chapter 7.

---

# **Experimental techniques**

---

## 2.1 Introduction

## 2.2 Phthalocyanine thin films deposition by MBE

### *2.2.1 Configuration details of RIBER-32 EVA MBE system*

### *2.2.2 Experimental procedure for phthalocyanine film deposition*

#### *2.2.2.1 Substrates and their preparation*

#### *2.2.2.2 Deposition protocol*

## 2.3 Characterization techniques

### *2.3.1 X-ray diffraction*

#### *2.3.1.1 Powder X-ray diffraction*

#### *2.3.1.2 Grazing angle X-ray diffraction*

#### *2.3.1.3 X-ray rocking measurement*

### *2.3.2 X-ray reflectivity measurement*

### *2.3.3 Atomic force microscopy*

### *2.3.4 Scanning electron microscopy*

### *2.3.5 X-ray photo-electron spectroscopy*

### *2.3.6 Fourier transform spectroscopy*

### *2.3.7 UV-Visible spectroscopy*

## 2.4 Charge transport measurement

### *2.4.1 Electrode deposition*

### *2.4.2 Low temperature charge transport*

### *2.4.3 Transient voltage pulse method for mobility measurement*

## 2.5 Gas sensing setup

## 2.1 Introduction

This chapter deals with the description of the process and equipment utilized for the growth of FePc and CoPc films as well as the technique used for their structural and morphological characterization. In addition, we present the details of charge transport and gas sensing measurement setups.

## 2.2 Phthalocyanine thin films deposition by MBE

Conceptually organic molecular beam epitaxy is technologically an improved version of the conventional thermal evaporation technique. The MBE technique is unique for its following characteristics: (i) The beam nature of the mass flow from source to substrate; (ii) Precise control over growth parameters; and (iii) In-situ growth characterization of the films. The details of these features are described below.

The molecules evaporated from a source in a vacuum chamber assume the features of a beam when the mean free path ( $\lambda$ ) of the molecules is much larger than the source-to-substrate distance. The occurrence of beam nature, therefore, depends on  $\lambda$  of evaporating molecules and concentration of residual gas molecules in the evaporation chamber. Both these conditions are associated with vacuum conditions of the growth chamber. The  $\lambda$  is related with pressure (p) as [85]

$$\lambda = 3.11 \times 10^{-24} \frac{T}{pd^2} \quad (2.1)$$

where  $d$  is the diameter of the molecules. The growth chamber is maintained at better than  $10^{-8}$  torr vacuum level during growth and at this pressure mean free path ( $\lambda$ ) for the phthalocyanine molecule is  $4 \times 10^4$  m as calculated using eq. 2.1. The value of  $\lambda$  is clearly greater than the typical source to substrate distance (40 cm) and thus ensuring the beam

nature of the molecule. Apart from the pressure during growth the residual gas pressure is also pumped down to better than  $10^{-9}$  torr which ensure the low concentration of residual gas molecules which affect the beam nature of the molecule. This low residual gas pressure also confirms that no monolayer of residual gas formed during deposition even when the film is deposited at very slow growth rate.

The molecular beams are generated under UHV conditions from sources of effusion cells [85]. The beam flux and hence, the deposition rate, is monitored by a gauge located near to the substrate. The beam flux can be controlled, with a stability of better than 1%, by controlling the temperature of the cell. The precise control over the molecular beams enables to keep the growth rate of the film as low as 1 monolayer per second and thus confirming excellent uniformity in film thickness as well as in composition on a large area substrate and high reproducibility of film preparation. The MBE also equipped with some characterizations tool such as RHEED, XPS, UPS etc which enable us to study the online and offline growth of the films.

The requirements of control, reproducible, defect free growth of phtalocyanine films on different substrate drive us to choose the MBE as film deposition technique. Prior to the discussion of deposition protocol the configuration details of MBE system used is presented.

### **2.2.1 Configuration details of RIBER-32 EVA MBE system**

The photograph of the MBE system (RIBER EVA 32 E) used for thin film deposition in the present study is shown in Fig. 2.1. It consists of three chambers namely, Introduction Chamber, Analysis Chamber and Growth Chamber. All of them are UHV chambers and are made of stainless steel. All seals are made of OFHC copper gaskets. This construction allows

high temperature baking ( $\sim 200^{\circ}\text{C}$ ) of the entire system to reduce out gassing from the walls. Analysis and Growth chambers are situated in a line, whereas, the Introduction Chamber is situated at  $37^{\circ}$  off the line joining Analysis and Growth Chambers. Introduction chamber is connected with Analysis chamber and similarly Analysis chamber with Growth chamber are connected through gate valves. There are two magnetically coupled sample transfer mechanisms. One is used to transfer the sample from Introduction to Analysis Chamber and the second is used to transfer sample from Analysis to Growth Chamber. Therefore, substrate cleaning and characterization, film deposition and characterization are performed in-situ under UHV conditions. The details of the three chambers are presented below.

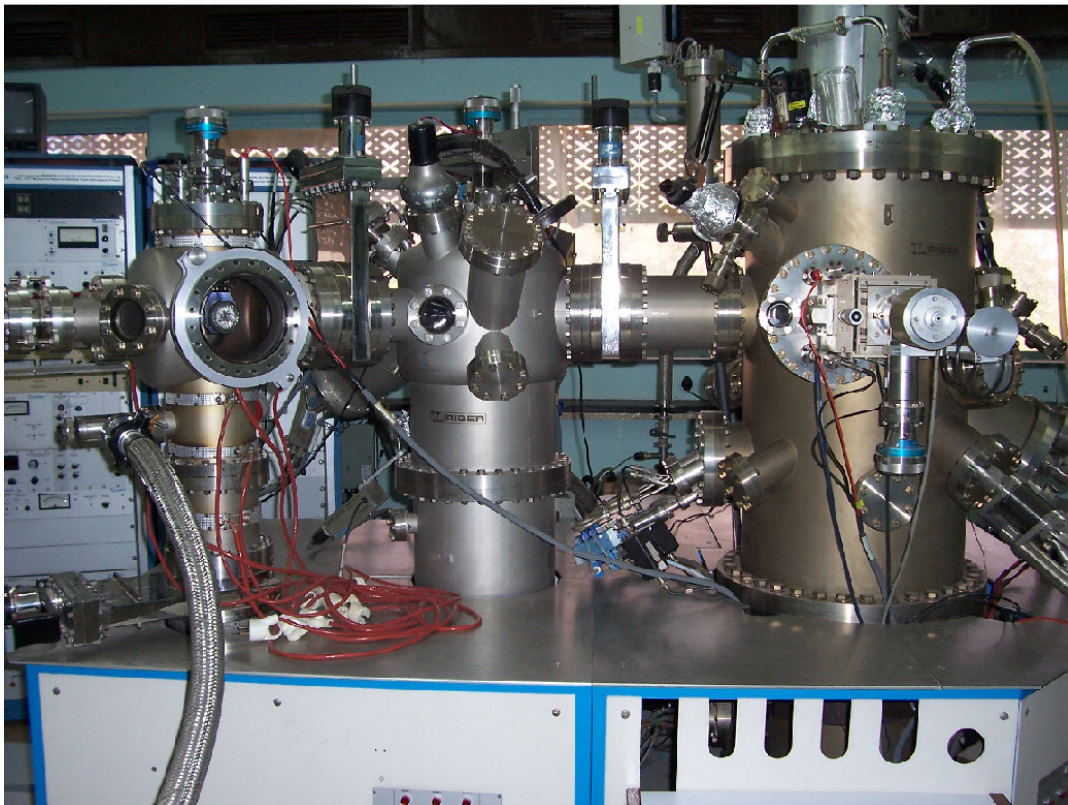


**Figure 2.1** A photograph of MBE deposition system (RIBER EVA 32 E) used for the deposition of MPC films.

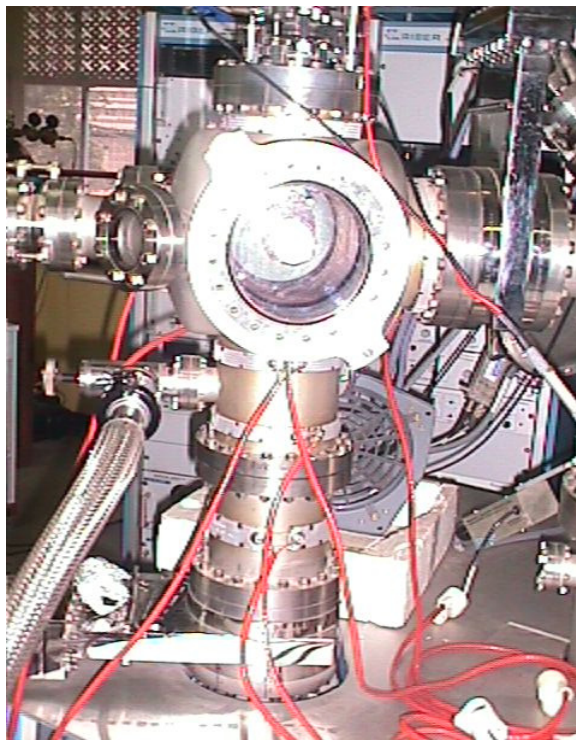


**Figure 2.2** A close-up photograph of the Introduction Chamber.

**(i) *Introduction chamber***

In this chamber, shown in Fig. 2.2, the substrates are loaded through the front opening flange. The substrates are fixed on a heater assembly using silver paste, and the substrates can be cleaned by degassing the substrate up to a temperature of 800°C. After loading the sample it is rapidly pumped down from atmospheric pressure to  $\sim 10^{-9}$  Torr with sorption and ion pumps. The heater assembly having the substrate is transferred to the Analysis and/or Growth Chambers using the transfer rods.

**(ii) *Analysis chamber***

This chamber (Fig. 2.3), serves the following two purposes

- (i) Cleaning of the substrates by ion etching.

- (ii) Surface characterization of substrates and grown films using X-ray photoelectron spectroscopy.

This chamber is equipped with a substrate heater which can be heated upto 800°C. In order to determine the level of cleanliness of the substrate and, chemical state and composition of the substrate and grown films the chamber is equipped with X-ray photoelectron spectroscopy (XPS) techniques. The details of XPS system are described in a later section.

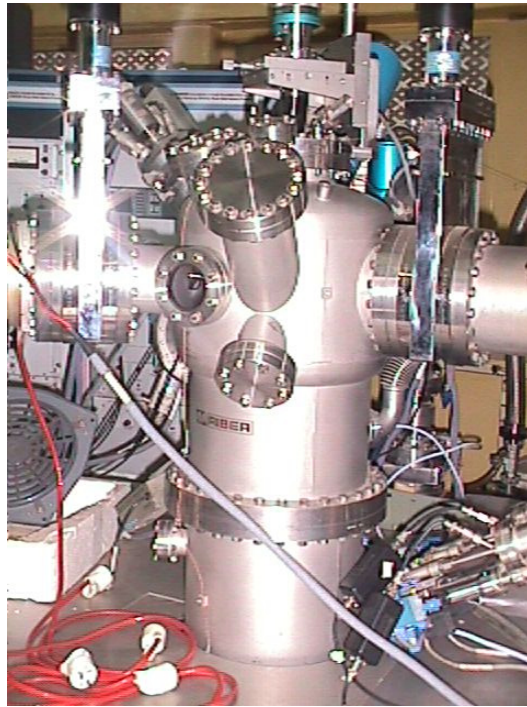


**Figure 2.3** A close-up photograph of the Analysis Chamber.

**(iii) *Growth chamber***

The growth chamber is the most important part of the MBE system. In this chamber all the controlling elements, such as, beam sources with their individual shutters, a main

shutter, and manipulator with substrate heater and rotation, pressure control system etc. are located. The side view of the growth chamber is shown in Fig. 2.4. The details of the different parts of the chamber are as follows.

***Pumping system:***

The Growth chamber can be evacuated to better than  $10^{-9}$  torr by using a combination of turbomolecular pump and ion pump with a fully cryoshrouded titanium sublimation pump. A helium closed-loop cryopump is also mounted for supplementary pumping.

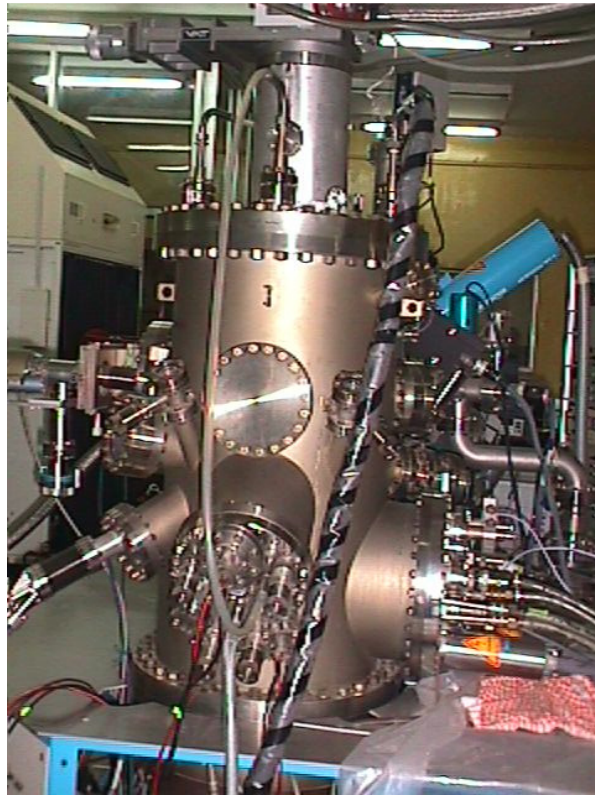


**Figure 2.4** A close up photograph of the Growth chamber.

***Effusion cells:***

Effusion cells are the key components of an MBE system, because they must provide excellent flux stability and uniformity, and material purity [85]. The chamber contains three

effusion cells. In the present study, we have used two effusion cells loaded with CoPc (99.99% ) and FePc (99.99%), respectively. Each effusion cell includes an oven (filament + thermocouple) and fully degassed thick PBN crucible, surrounded by adequate tantalum shielding for use in proximity of a cryoshroud. PBN crucibles are designed to provide a very stable flux during charge depletion. The heating filament is made of high purity tantalum foil. The contact thermocouple is located at the bottom of the crucible. Electrical insulators are made of PBN. The cell can be operated upto the 1400°C, and its temperature can be controlled with an accuracy of 1°C. The source mounting flange houses power and thermocouple feedthroughs. Power supply and temperature control are implemented by the use of microprocessor-based controllers.

***Manipulator:***

The manipulator consists of a gauge head and a substrate heater which can be heated upto 800°C. The manipulator allows the azimuthal rotation of the substrate during growth. The substrates are positioned to maximize growth uniformity for a substrate of size 1 × 1 inch.

***Deposition rate monitors:***

Quartz crystals monitor are mounted near the substrate to monitor the deposition rate. Alternatively deposition rate are also monitor by the flux gauge.

***View ports:***

View ports are provided for observation substrate transfers and manipulator position. This also allows us to view the inside chamber.

## 2.2.2 Experimental procedure for phthalocyanine film deposition

In this section experimental procedure for phthalocyanine film deposition are discussed which includes substrate preparation and actual deposition protocol.

### 2.2.2.1 Substrates and their preparation

In this research work we have used different substrates i.e. glass, (0001) sapphire, twined (001)  $\text{LaAlO}_3$  and  $36.8^\circ$  cut (001)  $\text{SrTiO}_3$  bi-crystal for the deposition of FePc and CoPc thin films. Before discussing the substrate preparation we present the structure of each substrate.

#### (i) *Glass*

The commercially available glass substrates were used to deposit Pc thin films. Glass substrates are amorphous in nature. The glass substrates are interesting because of their chemical inertness (i.e. Pc molecules do not chemically react with glass). The natural surface roughness of these substrates are quite high (15 nm), as discussed in Chapter-3.

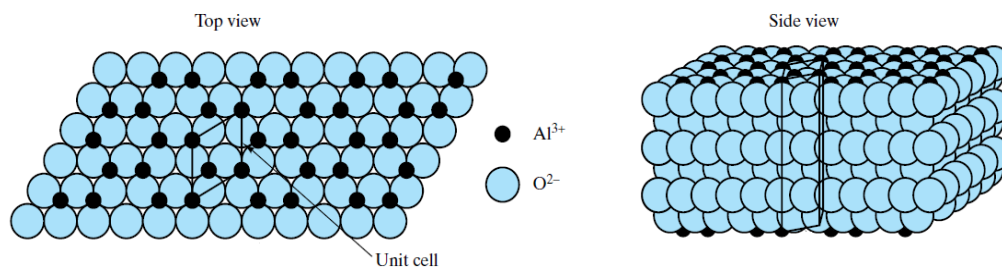


**Figure 2.5** The unit cell structure of sapphire showing top (Left) and side (Right) views.

#### (ii) *Sapphire*

The structure of the sapphire ( $\text{Al}_2\text{O}_3$ ) consists of a hexagonal close packed layer sequence of oxygen, with aluminium occupying two-thirds of the octahedral holes. The

oxygen stacking sequence runs along the  $c$  axis, and a unit cell consists of six oxygen layers, giving six formula units per unit cell. A typical top and side view of unit cell is shown in Fig. 2.5. The unit cell parameters are  $a = 4.757 \text{ \AA}$ ,  $b = 4.757 \text{ \AA}$ ,  $c = 12.9877 \text{ \AA}$  and  $\alpha = 90^\circ$ ,  $\beta = 90^\circ$ ,  $\gamma = 120^\circ$  [86]. The normal termination for the clean (0001)  $\alpha\text{-Al}_2\text{O}_3$  is one Al ion per three O ions with Al terminal ion slightly above the plane of closely packed oxygen [87]. The Al terminated surface or some time hydroxylated Al terminated surface become very reactive to the phthalocyanine molecules [88].

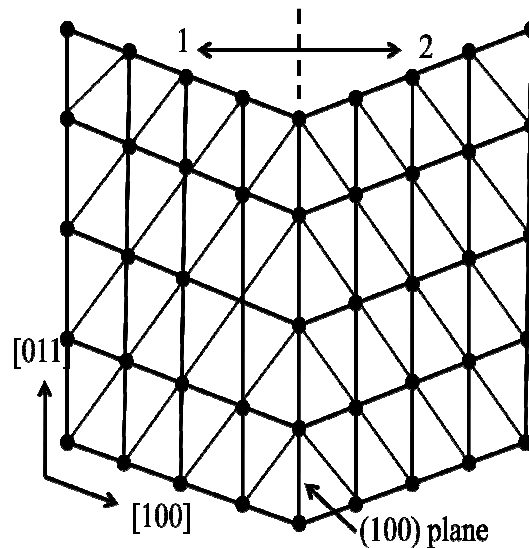


**Figure 2.6** Schematic diagram of  $\text{LaAlO}_3$  (100) twin.

**(iii) Twined (001)  $\text{LaAlO}_3$**

The high temperature phase of  $\text{LaAlO}_3$  is cubic whereas the room temperature structure is rhombohedral. The lattice parameters of rhombohedral  $\text{LaAlO}_3$  at room temperature are  $a = 5.357 \text{ \AA}$ ,  $\alpha = 60^\circ 6'$ , which corresponds to  $a = 3.79 \text{ \AA}$ ,  $\alpha = 90^\circ 5'$  based on a pseudo-cubic cell [89]. Since  $\alpha$  is larger than  $90^\circ$ ,  $\text{LaAlO}_3$  is associated with a spontaneous

strain along the cubic  $\langle 111 \rangle$  directions during the cubic to rhombohedral transition. To compensate this spontaneous strain the twinning arises. In general any structural transition associated with loss of symmetry element will result twins [90]. The lost symmetry elements of  $\text{LaAlO}_3$  are cubic (100) and (110) mirror planes, thus, (100) and (110) twins are present in rhombohedral  $\text{LaAlO}_3$ . The schematic of LAO (100) twins are shown in Fig. 2.6.

(iv) *Bi-crystal (001)  $\text{SrTiO}_3$*

The  $\text{SrTiO}_3$  has cubic structure, as shown in Fig. 2.7 (a) with lattice parameter  $a = 3.9 \text{ \AA}$  at room temperature. It goes through a structural phase transition from cubic to tetragonal at  $105^\circ\text{C}$  [91]. In our present study we have used symmetric  $36.8^\circ$  [100] tilt  $\text{SrTiO}_3$  bicrystal substrates with the two halves of each crystal i. e. A and B as shown in Fig. 2.7 (b) sharing a common (001) surface. These bi-crystals are known to have (130) interface and have zigzag bicrystal boundary along [100] and [010] axes of  $\text{SrTiO}_3$  with facets on both A and B sides of the boundary, which form almost periodic triangularly shaped grooves having a depth of 2–4 nm (schematically shown in Fig.2.7 (b)) [92, 93].

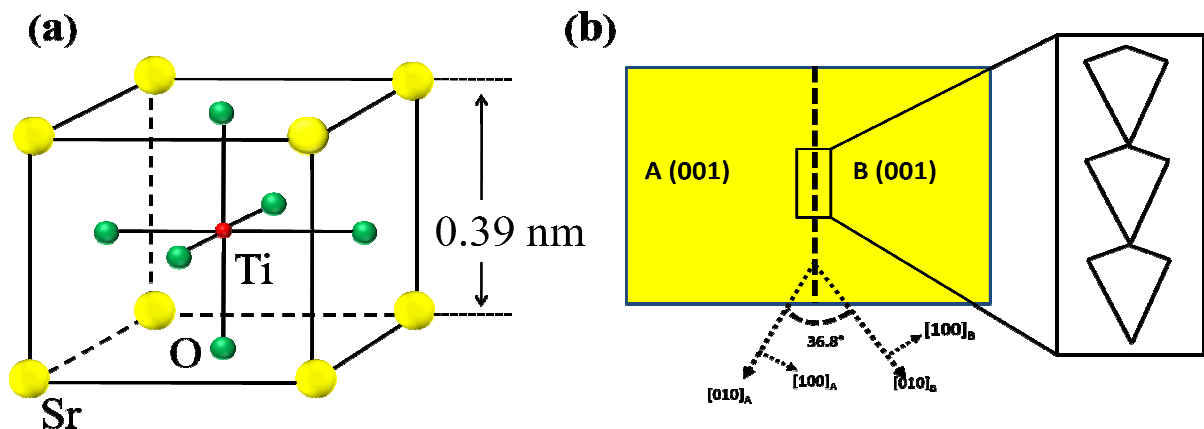


**Figure 2.7** (a)  $\text{SrTiO}_3$  unit cell at room temperature which shows a cubic structure. (b) Schematic of  $36.8^\circ$  cut (001)  $\text{SrTiO}_3$  bicrystal. Expanded view shows the schematic of the interface structure.

The cleanliness of the substrates is of crucial importance for the subsequent growth of the films. Thus substrate preparation is very important step before growth studies. Prior to the introduction in the in the MBE chamber the substrates are thoroughly cleaned in different organic solvents. In the first step the substrates were ultrasonicated in trichloroethylene bath for 10 minutes to remove oil, grease etc. Thereafter the substrates were sonicated in acetone and methanol separately to remove polar and non-polar organic, inorganic impurities and dust particles. To remove the solvent, the substrates were dried under the jet flow of dry high purity Ar gas. Finally films are loaded in the introduction chamber of MBE system.

#### ***2.2.2.2 Deposition protocol***

For the deposition of Pc films on different substrates the protocol shown in the Fig. 2.8 is followed. In the first step the pre-cleaned substrate were loaded in the introduction chamber of and the chamber is pumped down to  $10^{-7}$  torr and the sample is transfer to analysis chamber. In the substrate were heated to  $500^{\circ}\text{C}$  to remove the residual solvent particle and other impurities. The XPS studies were carried out on substrate surface to check for the trace of residual impurities. If the substrates are found to be perfect, they were transfer to the growth chamber for deposition where source materials were preloaded. Prior to the deposition the source materials were degassed at  $200^{\circ}\text{C}$  for 2 to 3 times for the removal of volatile impurities. During deposition the pressure of the growth chamber was maintained better than  $10^{-9}$  torr. The films were deposited at various substrate temperatures ( $25^{\circ}\text{C}$  to  $250^{\circ}\text{C}$ ) and the substrate heater can be controlled within  $\pm 1^{\circ}\text{C}$  accuracy of temperature. The deposition rate of the film is monitored by the flux gauge and the deposition rate was varied between 0.02 and 0.5 nm/s by controlling the effusion cell temperature. In order to achieve

excellent uniformity in composition and thickness, the source-to-substrate distance was kept comparatively large (40 cm) and the substrates were rotated during the deposition. After the deposition, the films were transferred to the analysis chamber again and films were characterized by XPS. Finally the films were taken out through the introduction chamber for further ex-situ characterization and charge transport measurements.

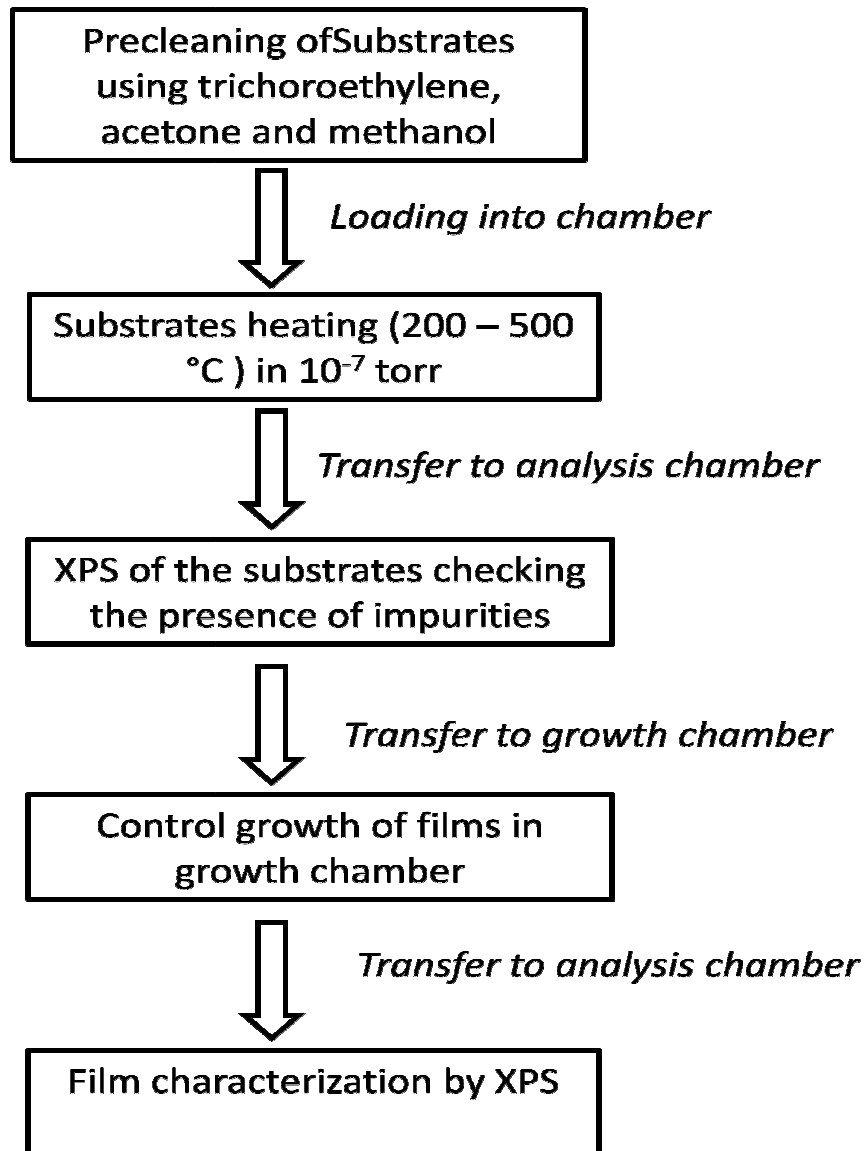


**Figure 2.8** Protocol for the phthalocyanine film deposition.

## 2.3 Characterization techniques

### 2.3.1 X-ray diffraction

For the determination of the structure and morphology of the deposited films, X-ray diffraction in different configurations are carried out. These are discussed as follows.

#### 2.3.1.1 Powder X-ray diffraction

We have used powder X-ray diffractometer (Seifert XRD 3003TT) in  $\theta$ - $2\theta$  scan mode to characterize the orientation and structure of the grown Pc thin films. Fig. 2.9 shows the schematic diagram of the diffractometer, which consists of an X-ray source, and a goniometer for mounting sample and X-ray detector. The X-ray source used was Cu  $K_{\alpha}$  having wavelength of  $1.54056\text{\AA}$ , which has been selected using a Graphite monochromator. For mounting thin films, a specially designed Perspex holder (having a groove of dimension  $10\text{ mm}\times 10\text{ mm}\times 1\text{ mm}$ ) was employed. The films were mounted on this groove using red wax in such a way that X-rays fall on the film plane. Since the wavelength ( $\lambda$ ) of X-rays coincides with the atomic spacing ( $d$ ) in the solids, it diffracts in those orientations of  $2\theta$ , where the Bragg condition of diffraction [94, 95] i.e.  $2d \sin\theta = n\lambda$  ( $\theta$  being the angle which incident beam makes with the plane of sample) is satisfied. While recording the diffraction pattern with detector, the sample is synchronously rotated along with the detector, such that the incident X-ray incident beam makes an angle  $\theta$  with the plane of sample whereas detector is at angle  $2\theta$  with respect to incident beam. This is commonly known as  $\theta$ - $2\theta$  scan of X-ray diffraction. The recorded diffraction pattern is compared with standard pattern to get information about the phase of the samples. The lattice parameters are obtained by fitting the recorded diffraction peaks using least-square fitting software.

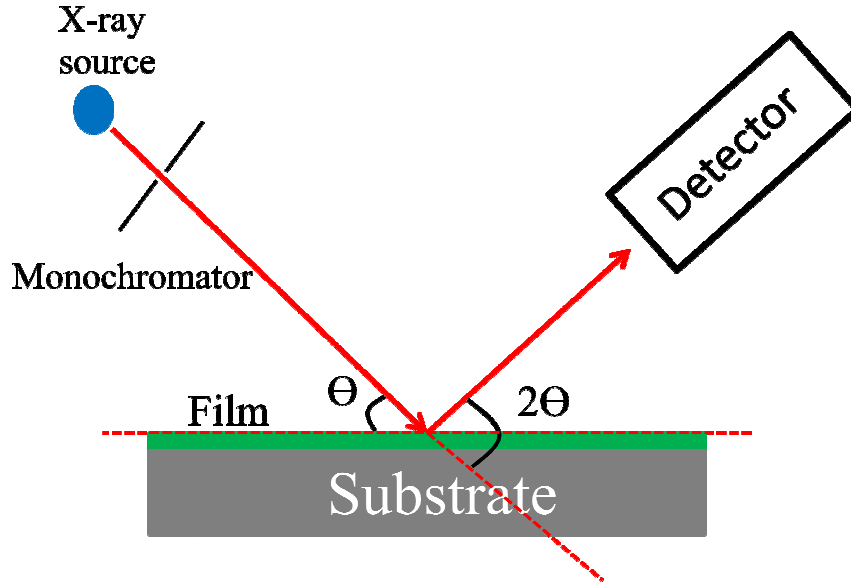


**Figure 2.9** Schematic diagram of powder X-Ray diffractometer.

### 2.3.1.2 Grazing angle X-ray diffraction

In powder or normal geometry the peak corresponding to the substrates are also present. Therefore the structures of the very thin films (typically less than 20 nm) were investigated by Grazing angle X-ray diffractometer. The schematic of this diffraction configuration is shown in the Fig. 2.10. In this configuration, incident X-ray is fixed at a very small angle (e.g. 0.1°) with the sample surface and detector does 2θ scan. The sampling depth (D) is related with angle of incidence (φ) by the formula,

$$D(\varphi) = \frac{\lambda}{4\pi q} \quad (2.2)$$

where  $\lambda$  is the x-ray wave length (1.541Å), and

$$q = \left[ \sqrt{(\varphi^2 - \varphi_c^2) + 4(\delta_i)^2} + \varphi_c^2 - \varphi^2 \right]^{\frac{1}{2}} (\sqrt{2})^{-1} \quad (2.3)$$

$\delta_i = \lambda \left( \frac{\mu}{4\pi} \right)$ ,  $\varphi_c$  is the critical angle of incidence and  $\mu$  is the linear absorption coefficient

[96]. In the present studies, we have employed  $\varphi = 0.1^\circ$ , which leads to a sampling depth of ~

10 nm; and thus this technique becomes ideal for analyzing the structure of very thin films without having interference from the substrates.

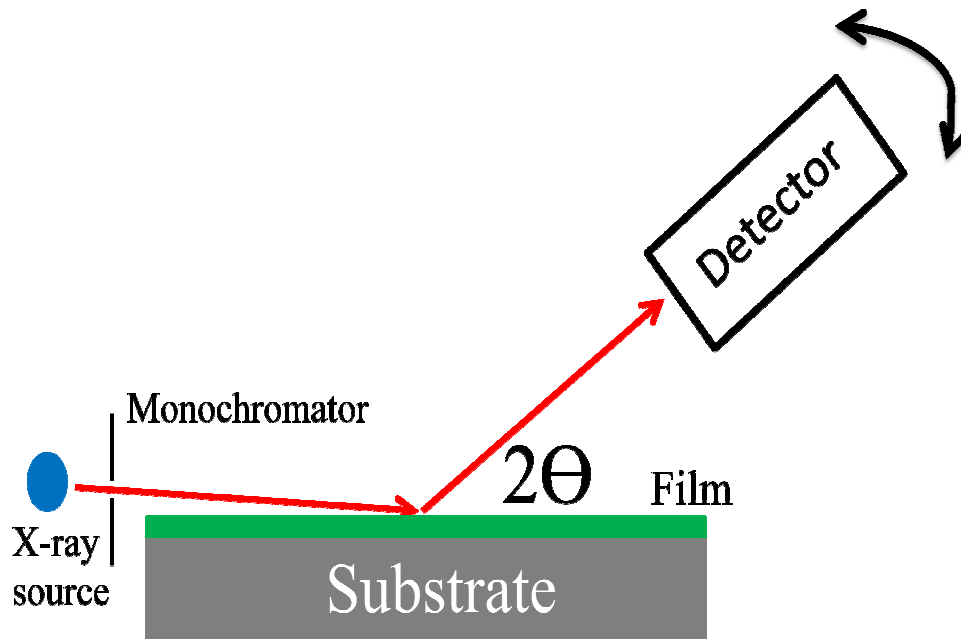


**Figure 2.10** The schematic of the grazing angle X-ray diffraction.

### ***2.3.1.3 X-ray rocking measurement***

In this mode of diffraction, schematically shown in the Fig. 2.11, the detector is fixed at  $2\theta$  position i.e. at some Bragg peak and the sample is scanned around  $\omega$ . The mosaic defect of the sample in vertical direction will cause the width of the peak broaden and the width is inversely proportional to the defect density. Thus from the rocking pattern quality of the sample is determined [97, 98].

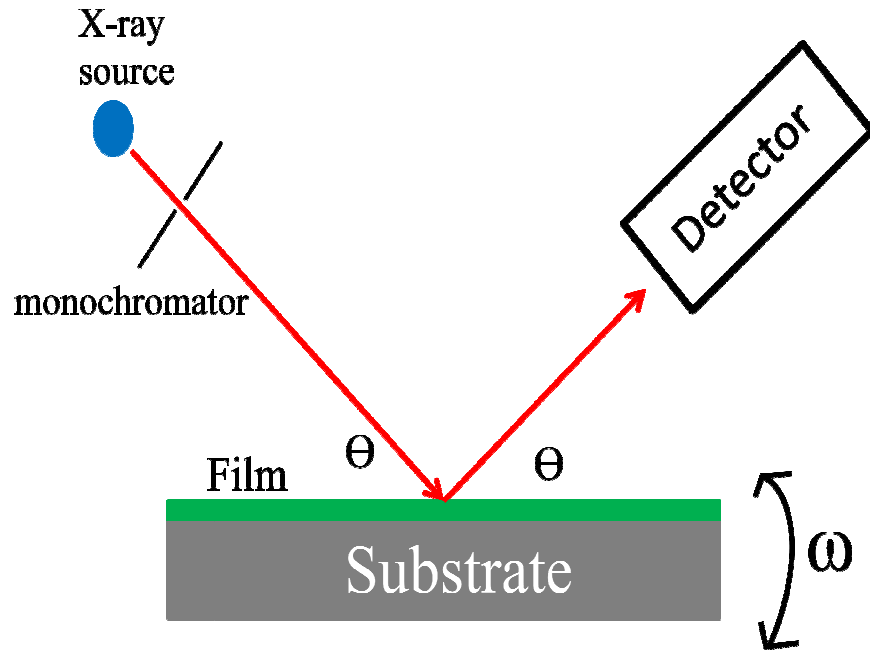


**Figure 2.11** Schematic of X-ray rocking measurements.

### 2.3.2 X-ray reflectivity measurement

When X-ray beam falls on a surface it under goes total external reflection below certain critical angle ( $\theta_c$ ). Above the  $\theta_c$ , the X-ray starts penetrating inside the layer and the reflectivity of the sample falls off with a slope depending on the incidence angle and the roughness of the interface. The oscillation on the reflectivity spectrum above  $\theta_c$  (generally known as the Kiessig oscillations) is due to the finite thickness of the layer. In general, the thickness of the film can be obtained from the frequency of oscillation, while the slope of the curve gives the roughness of the interface [99]. Grazing incidence X-ray reflectivity (GIXRR) for Pc thin films was carried out using  $\text{CuK}_\alpha$  radiation ( $1.54 \text{ \AA}$ ) on a computer-controlled reflectometer (Kristalloflex 710 D X-ray generator (SIMENS) and D5000

diffractometer) and the obtain reflectivity data fitted theoretically to extract thickness and interface roughness.

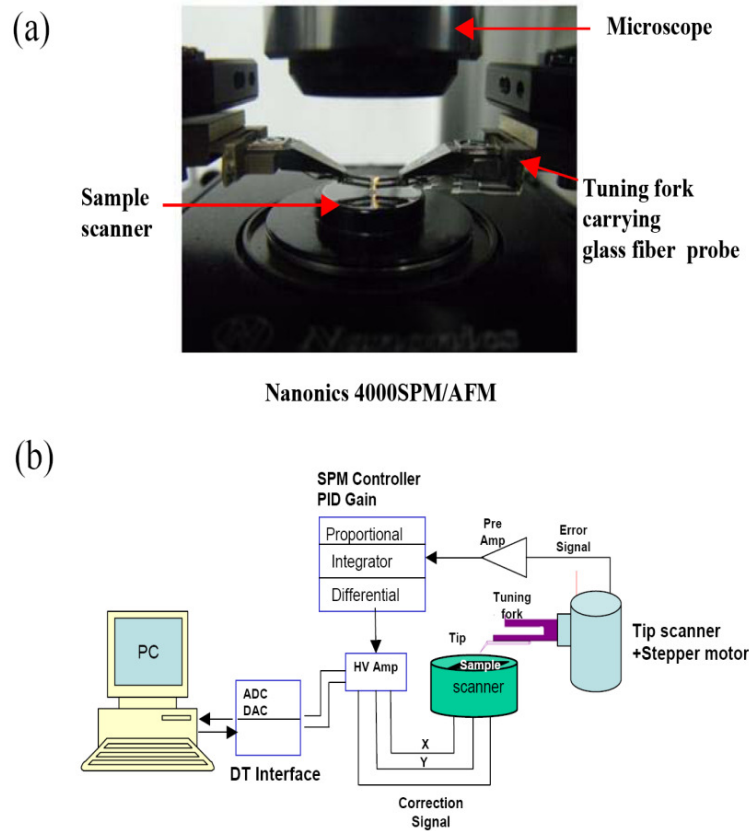


**Figure 2.12** (a) a real snap of AFM tip and sample stage. (b) Block diagram of AFM.

### 2.3.3 Atomic force microscopy

The atomic force microscope used in the present studies was Nanonics 4000SPM/AFM system, as shown in Fig. 2.12. In this case, the probe is made of the glass fiber tip (diameter 10nm) which is attached to tuning fork with piezocrystal [100]. The images are recorded in the tapping mode by oscillating the tip at resonance frequency (20-50 kHz depending on the tips). The probe was scanned in phase mode. During scan, phase

changes due to tip surface interaction. The difference in signal called an error signal; this signal is sent to proportional, integrator and differentiator (PID) controller. PID sends the feedback via high voltage piezo driver to make constant phase by moving piezodriver in z direction at that x, y point. This way an image is generated. A schematic diagram of signal processing is shown in the Fig. 2.12 (b). The image so generated was processed (like smoothing, flattening etc) by NWS software [101]. This software was also used to study surface roughness by extracting line profile from the image.

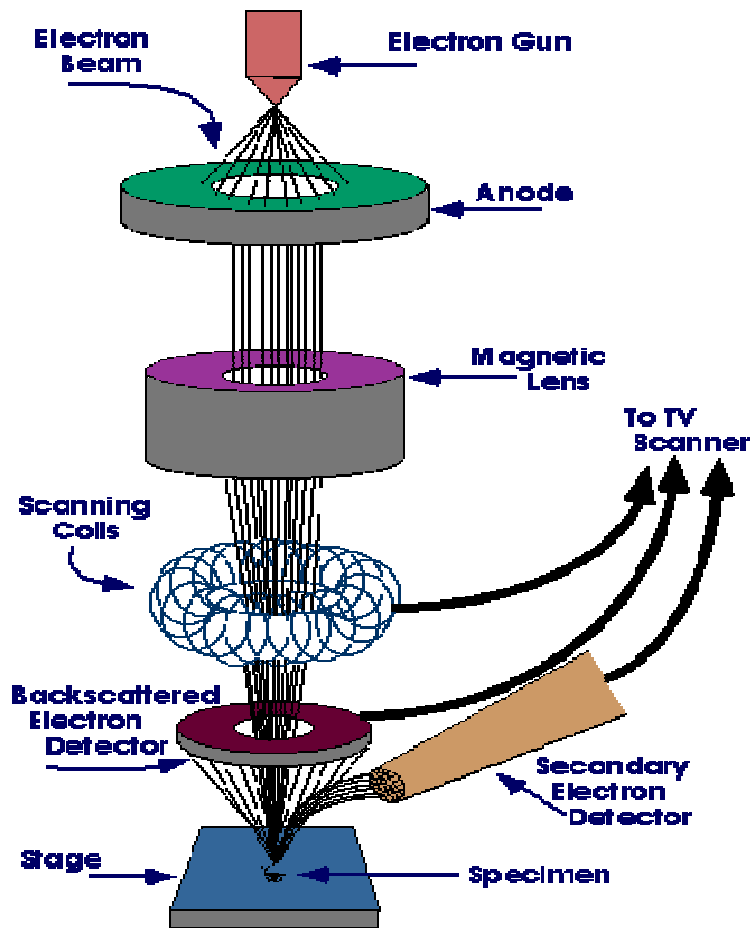


**Figure 2.13** Block diagram of a typical SEM setup.

### **2.3.4 Scanning electron microscopy**

We have used scanning electron microscope (TESCAN VEGA) to investigate the surface morphology of the films. The scanning electron microscope (SEM) provides information relating to topographical features, morphology and phase distribution [102, 103]. The block diagram of typical SEM set up is shown in Fig. 2.13. The working principle of SEM is briefly described below. The SEM is the focused probe of electrons accelerated to a moderately high energy and positioned on to the sample by electro-magnetic fields. These beam electrons interact with atoms of the specimen by inelastic (energy is transferred to the sample leads to secondary electrons emission) and elastic (energy is not transferred to the sample leads to back scattered electrons emission) collisions.

The most widely utilized signal, produced by the inelastic interaction of the primary electron beam with the sample, is the secondary electron signal. Secondary electrons are characterized from other electrons by having energy of less than 50 eV. The secondary electron is emitted from an outer shell of the specimen atom upon impact of the incident beam. It is the most useful signal for examining surface structure and gives the best resolution image of 10 nm or better. Since the secondary electron intensity is a function of the surface orientation with respect to the beam and the secondary electron detector and thus, produces an image of the specimen morphology. The secondary electron intensity is also influenced by the chemical bonding, charging effects and back scattered electron intensity, since the back scattered electron generated secondary electrons are significant part of the secondary electric signal.

The detector is Everhart-Thornley detector composed of a scintillator, collector, light pipe, and photo multiplier tube. First electrons striking the positively biased scintillator and

converted to a burst of photons, that travel through the light pipe to a photomultiplier tube which converts the photons of light into a voltage. The strength of this voltage depends on the number of secondary electrons that are striking the detector. Thus the secondary electrons produced from a small area of the specimen give rise to a voltage signal of a particular strength. The voltage is led out of the microscope column to an electric console, where it is processed and amplified to generate a point of brightness on the cathode ray tube screen. Contrast in the SEM image is the difference in intensity, or brightness of the pixels that make up the image. The difference in intensity represents difference in signal from corresponding picture elements on the sample.

The back scattered electron signal can also be used to show surface topography and is often used to show atomic number contrast, in which areas of higher average atomic number produce more back scattered electrons, and thus appear brighter than lower atomic number regions. The contrast in this image is not due to color differences but is produced by different intensities of electrons back scattering from the layers with different average atomic number.

### **2.3.5 X-ray photoelectron spectroscopy**

XPS uses a soft X-ray source ( $\text{Al-k}_\alpha$  and  $\text{Mg-k}_\alpha$ ) to ionize electrons (by knocking out the core-level electron) from the surface of a solid sample (top few atomic layers). The binding energies of these electrons are measured, which are characteristics of the elements and associated with chemical bonds (chemical state). The advantages of XPS technique are (i) quantitative analysis of elements and chemical states of all elements except hydrogen and helium, (ii) typical element detection limits are 0.1 atomic percentage from the top few nm, and (iii) samples can be conductors, semiconductors or insulators [104-106].

As mentioned earlier, the XPS system is mounted in the analysis chamber of the MBE system, and thus the in-situ (i.e. without breaking vacuum) and ex-situ (i.e. exposing to ambient) study of the deposited films were carried out. The XPS system (RIBER system model: FCX 700) consists of Al-K $\alpha$ (1486.6eV) and Mg-K $\alpha$  (1253.6eV) X-ray sources and MAC-2 electron analyzer. The binding energy scale was calibrated to Au-4f $_{7/2}$  line of 83.95eV. For charge referencing adventitious C-1s peak set at 285eV was used. Each data set was first corrected for the non-linear emission background. The data was then fitted with Gaussian function to find the peak positions.

### **2.3.6 Fourier transform infrared spectroscopy**

The frequencies and intensities of the vibrational modes observed in FTIR provide detailed information about the nature of the bonding in the molecule [107]. FTIR spectra were recorded using Bruker system (vertex 80V). The necessary condition for the infrared absorbance is the presence of permanent dipole moment or change in dipole moment of the chemical bond (between two atoms) when it interacts with IR. The absorption of IR leads to change in vibration level. So IR absorption helps to identify the characteristic vibrational frequencies of organic functional group. Most of the organic molecules have vibrational frequencies in the mid infrared range of 4000 to 400 cm $^{-1}$ . FTIR works on the principle of interferometer that gives an interferogram, a plot of light intensity versus optical path difference. The ray diagram of formation of interferogram is shown in the Fig. 2.14. This interferogram is finally Fourier transformed to give a spectrum of infrared radiation intensity versus wave number.

For our experimental purpose, FTIR spectra were recorded in two different spectroscopy modes: attenuated total reflection (ATR) and diffuse reflectance mode. In the ATR mode, an infrared beam is directed onto an optically dense crystal with a high refractive index at a certain angle. This internal reflectance creates an evanescent wave (see Fig. 2.15) that extends beyond the surface of the crystal into the sample held in contact with the crystal. This evanescent wave protrudes only a few microns ( $0.5 - 5 \mu\text{m}$ ) beyond the crystal surface and into the sample. Consequently, there must be good contact between the sample and the crystal surface. In regions of the infrared spectrum where the sample absorbs energy, the evanescent wave will be attenuated or altered. The attenuated energy from each evanescent wave is passed back to the IR beam, which then exits the opposite end of the crystal and is passed to the detector in the IR spectrometer. The system then generates an infrared spectrum. This mode is very good technique to measure FTIR spectra of the film.

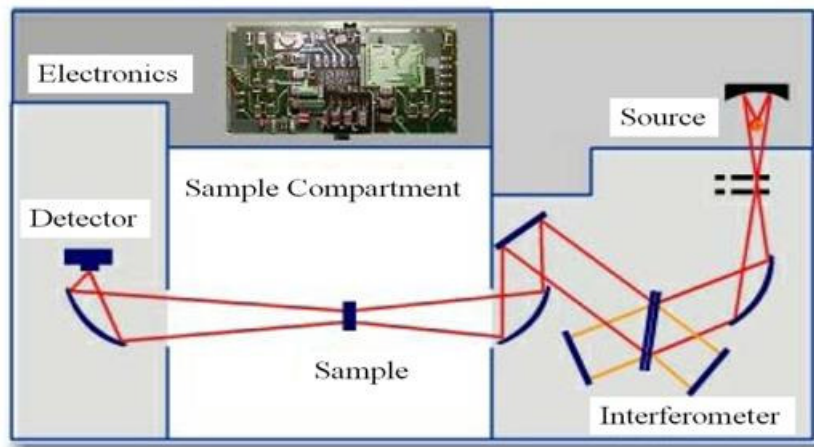


**Figure 2.14** Ray diagram of recording FTIR spectra along with electronic circuit of system vertex 80 V.

In diffuse reflectance (DR) mode, after the IR beam enters the sample, it can either be reflected off the surface of a particle or be transmitted through a particle. The IR energy reflecting off the surface is typically lost. The IR beam that passes through a particle can either reflect off the next particle or be transmitted through the next particle. This transmission-reflectance event can occur many times in the sample, which increases the path length. Finally, a spherical mirror that is focused onto the detector collects such scattered IR energy. The detected IR light is partially absorbed by particles of the sample, bringing the sample information.

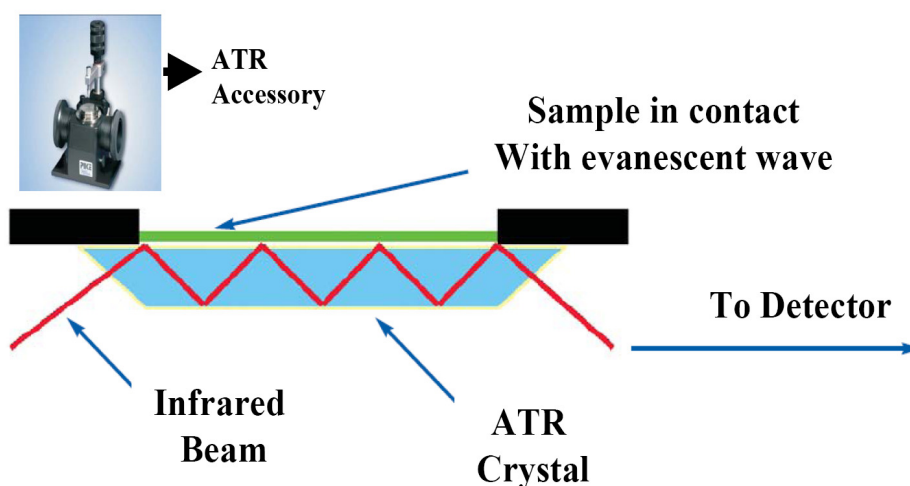


**Figure 2.15** The ray diagram of recording FTIR spectra in ATR mode. The accessory used for ATR spectra is also shown in the inset of the diagram.

### 2.3.7 UV- visible spectroscopy

UV- visible spectroscopy is generally used to study the electronic transition in molecule. The absorption of ultraviolet or visible radiation generally results from excitation of bonding electrons ( $\pi$ ,  $\sigma$  or even non bonding electrons); as a consequence, the wavelength

of absorption peaks can be correlated with the type of bonds in the spices [108]. The absorption may sometime occur due to the  $d$  and  $f$  electron and also due to charge transfer electrons. So this absorption study is very important tool to indentify the molecule or functional group in the molecule. For our experiment we have use JASCO B430 spectrometer. The schematic of the double beam single monochromator spectrometer is shown in Fig 2.16. In this spectrometer the intensity ( $I$ ) of the beam passing through the sample is compared with a reference beam ( $I_0$ ) and in output we get absorbance ( $A = \log_{10}I/I_0$ ) vs wavelength.

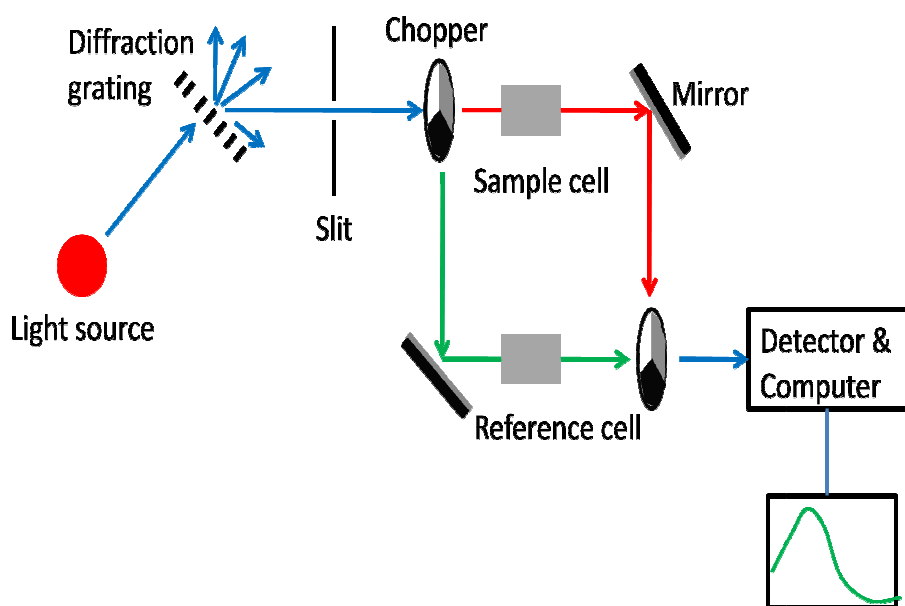


**Figure 2.16** Block diagram of a typical double beam single monochromator UV-spectrometer.

## 2.4 Charge transport measurement

The experimental procedure for electrode deposition and the charge transport measurements are discussed in this section.

### 2.4.1 Electrode deposition by thermal evaporator

To measure charge conduction and gas sensing properties, gold electrodes were deposited using a thermal evaporation system, as schematically shown in Fig. 2.17. Gold pads (size: 2 mm  $\times$  3 mm) were deposited through a metal mask with different electrode spacing (7-20  $\mu$ m). The films are loaded in vacuum chamber which is connected to a TMP based vacuum pumping system. To deposit gold electrodes, 99.99% pure gold wire is loaded on a tungsten filament, which was resistively heated by external power supply. To prevent diffusion of gold atoms into the Pc films, electrodes are deposited with very slow rate (0.5  $\text{\AA}/\text{s}$ ). The deposition rate and thickness of the deposited electrodes is monitored through a quartz crystal monitor.

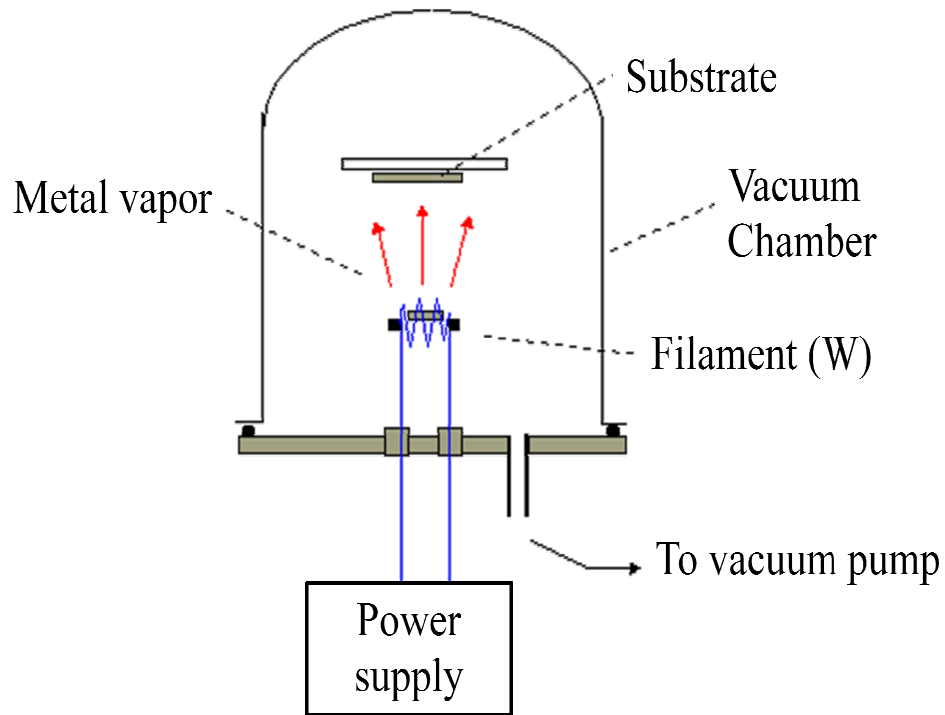


**Figure 2.17** Schematic of the thermal evaporation system used for the gold electrode deposition.

## 2.4.2 Low temperature charge transport

The charge transport measurements were carried out using in planar geometry. The in-plane geometry, as shown in Fig. 2.18, has following distinct advantages over the out-of-plane geometry in which films is sandwiched between two electrodes.

- (i) In the out-of-plane geometry, metal atoms from the electrode can get incorporated in the films, which can act as charge trapping centers, and hence, can give rise to hysteresis in  $J - V$  characteristics [109]. This makes it difficult to isolate the intrinsic hysteretic effect. This problem will not arise in the in-plane geometry, as the electrodes are far apart ( $12 \mu\text{m}$ ).
- (ii) Large electrode spacing also indicates that the contribution of contact resistance is very small compared to the film resistance.

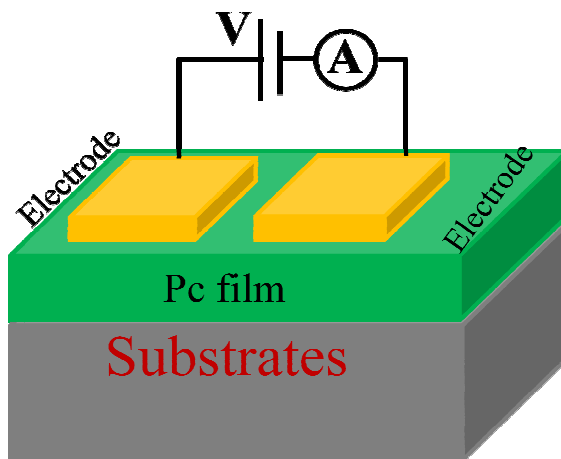


**Figure 2.18** A schematic of in plane charge transport measurement geometry.

Therefore in our studies we measured  $J - V$  characteristics using two-probe in-plane geometry. To measure  $J - V$  characteristics a silver wire is attached to the previously deposited

electrode by conducting silver paint. Keithley 6487 picoammeter/voltage source and computer based data acquisition system were used to record the  $J$ - $V$  characteristics. All measurements were carried out in dark to avoid the problem of photoconductivity. In order to rule out the effect of film inhomogeneities,  $J$ - $V$  characteristics were measured on at least three pairs of electrodes deposited on a film at different positions. For measuring the temperature dependence of the resistivity and temperature dependent  $J$ - $V$  characteristics, the samples were mounted in a closed cycle cryostat. The cryostat (CCR APD Cryogenics make) consists of a compressor, which compresses the Helium gas and expands it in the vicinity of the sample chamber. Because of Joule Thomson expansion of Helium gas, its temperature falls and it cools the region surrounding it. Platinum resistance sensors (Pt-100) are used to monitor the temperature. Lakeshore temperature controller (Lakeshore 330 auto tuning temperature controller) controls temperature of the sample chamber. A small manganin heater was used to heat the sample for measurements of transport properties at different temperatures.

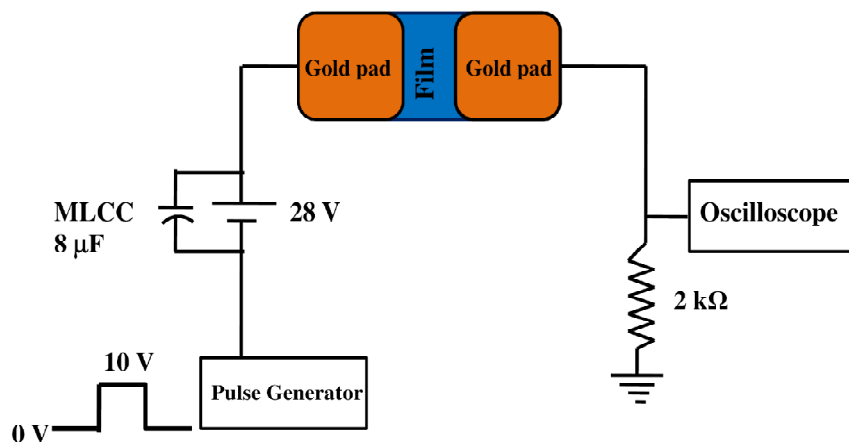


**Figure 2.19** Schematic of mobility measurement set up using transient voltage pulse method.

### 2.4.3 Transient voltage pulse method for mobility measurement

The mobility measurements were carried out using transient voltage pulse (TVP) method. In the TVP method, the mobility is defined as

$$\mu = 0.786d^2/V\tau_0 \quad (2.4)$$

where  $d$  is the channel length and  $\tau_0$  is the transit time of the fastest carrier introduced by the transient pulse [110]. Square voltage pulse (with pulse rise time of 50 ns and pulse width 100  $\mu$ s) from HAMEG function generator (15 MHz Arbitrary Function Generator HM8131-2) was used to cycle the two terminal devices. The input and output signals were measured using an oscilloscope (Tektronics model no. TDS224, 100 MHz bandwidth). To avoid the device capacitance problem sample was biased with an external DC voltage source at 28 V and output signal is measured across a 2k $\Omega$  load resistance connected in series with the sample. The schematic of the mobility measurement set up shown in Fig. 2. 19.

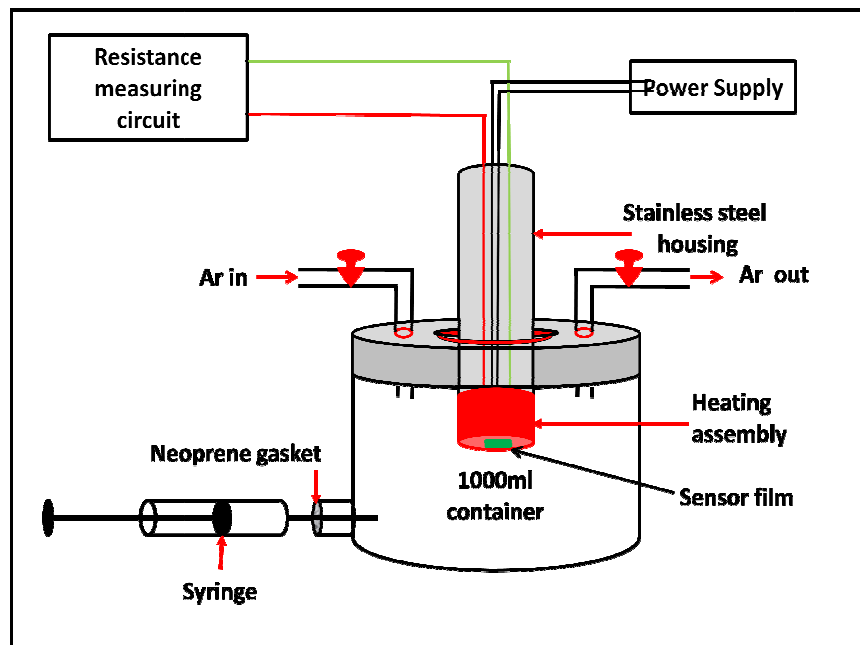


Figure 2.20 Schematic of gas sensing measurement setup.

## **2.5 Gas sensing setup**

The gas sensitivity of the films was measured using a home-made gas sensitivity measurement setup, as shown in Fig 2.20. The sensor films are mounted on a heater surface. The temperature of the heater was controlled by an external power supply and temperature controller. The sensor assembly was mounted in a leak tight 1000 ml stainless steel container, and the known amount of gas (to be sensed) was injected into the chamber using a micro-syringe. To measure the response of the sensor films for a particular gas, current at a particular bias as a function of time was measured by Keithley make 6487 picoammeter/voltage source and computer based data acquisition system. For the recovery of the sensor, the chamber was exposed to the ambient atmosphere.

---

# **Growth of amorphous, poly-crystalline and highly ordered phthalocyanine films**

---

## 3.1 Introduction

## 3.2 Growth of phthalocyanine films on glass

### *3.2.1 Structure & morphology as a function of growth parameter*

#### *3.2.1.1 Effect of growth temperature*

#### *3.2.1.2 Effect of film thickness*

#### *3.2.1.3 Effect of deposition rate*

#### *3.2.1.4 Optical absorption study*

### *3.2.2 Understanding of the morphology evolution*

#### *3.2.2.1 Growth mechanism of nano-web and nano-brush*

#### *3.2.2.2 Growth mechanism of granular and densely packed morphology*

## 3.3 Growth of phthalocyanine films on (0001) sapphire

## 3.4 Growth of phthalocyanine films on twined (001) $\text{LaAlO}_3$

## 3.5 Growth of phthalocyanine films on $36.8^\circ$ cut bicrystal (001) $\text{SrTiO}_3$

## 3.6 Conclusions

### 3.1 Introduction

In this chapter, we present deposition of FePc and CoPc films on different substrates using molecular beam epitaxy and investigate the growth mechanism(s). While thin film growth mechanisms of metal and inorganic-semiconductors are well established, there is hardly any understanding on the growth mechanisms of organic films. The metal and inorganic-semiconductors films grow on different substrates by three well known growth modes, as schematically shown in Fig. 3.1, which depend on the relative surface energy of the film with respect to the substrate [i.e.  $(\gamma_s - \gamma_f)/\gamma_f$ , where  $\gamma_s$  and  $\gamma_f$  are, respectively, free surface energy per unit area of the substrate and the film] and the lattice mismatch [i.e.  $(a_s - a_f)/a_f$ , where  $a_s$  and  $a_f$  are, respectively, lattice parameter of the substrate and the film]. Three growth modes are as follows.

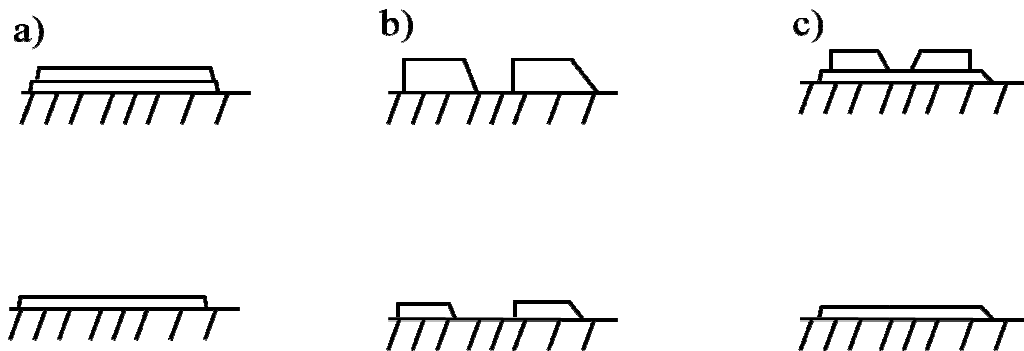


**Figure 3.1** Schematic of three different growth modes of inorganic thin films on inorganic substrate, namely Frank-van der Merwe mode (a), Volmer–Weber mode (b), Stranski– Krastanov mode (c).

- (i) *Frank-van der Merwe mode*: In this mode layer-by-layer growth occurs if  $\gamma_s > \gamma_f$  and the lattice mismatch is zero, as shown in Fig. 3.1 (a).

- (ii) *Volmer–Weber mode*: In this mode the film grows in the form of islands to minimize the overall surface energy if  $\gamma_s < \gamma_f$ , as shown in Fig. 3.1 (b).
- (iii) *Stranski– Krastanov mode*: In this mode islands are formed after some layer growth due to large lattice mismatch although  $\gamma_s > \gamma_f$ , as shown in Fig. 3.1 (c).

The growth mechanisms of organic films, on the other hand, are more complex. Though, in principle, above growth modes may be applicable to organic thin films but other issues, specific to the organic molecules, can lead to very different growth behaviors. Some of the critical issues involved in the organic film growth are as follows [111].

- (i) *Extended nature of organic molecule*: The organic molecules exist in different dimensionality i.e. 1D, 2D, 3D and long chains as shown in Fig. 1.1. The extended nature of organic molecules contributes to additional internal degrees of freedom i. e. orientational and vibrational degrees of freedom. The orientational degrees of freedom may facilitate adsorption of molecules on the surface of the substrate either ‘lying-down’ or ‘standing-up’ configurations, which can result in an altogether different growth mechanism. The vibrational degrees of freedom can influence the interaction of molecule with the surface as well as their diffusion at surface.
- (ii) *Large lattice mismatch*: The typical unit cell dimensions of organic crystal are much larger than that of the inorganic substrate leading to a high mismatch of lattice parameter of the film and substrate, therefore impeding epitaxial growth.
- (iii) *Molecule-molecule and molecule-substrate interaction*: The molecule-molecule interaction is weak van-der-Waals interactions; whereas depending upon the nature of the substrate molecule-substrate interaction is electrostatic, covalent or

Van-der-Waals. Therefore, a balance between molecule-molecule and molecule-substrate interactions decides the overall growth mode. If the molecule-substrate interaction is dominant over molecule-molecule interaction the ‘face-on’ growth of molecule on the substrate is preferred. Otherwise molecule will grow in ‘edge-on’ configuration.

Apart from these above factors the low symmetry of organic crystal and existence of polymorphism also affect the growth mechanism of organic thin films. Thus the growth behavior of organic films on inorganic substrate is very complex process. The above mention factors influencing the growth of organic films can be modified by controlling various growth parameters, such as substrates, deposition temperature, growth rate etc.

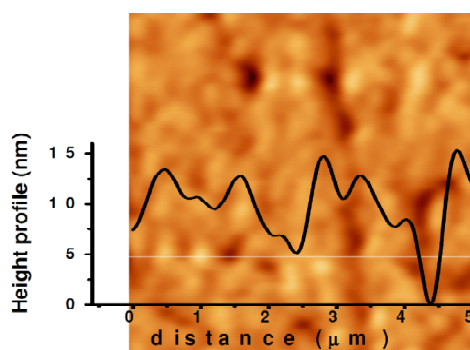


**Figure 3.2** AFM image of the glass substrate.

### **3.2 Growth of phthalocyanine films on glass**

The glass substrates are widely used to deposit organic films. Glass substrates are amorphous in nature and are chemically non-interactive to MPC molecule. Thus there is minimum substrate-molecule interaction between phthalocyanine and glass substrate. However, the growth morphology of phthalocyanine films is affected by the mosaic disorder and the roughness of the glass substrates. The roughness of the glass substrate, used in this

this work, is found to be 15 nm as calculated from the height profile of the AFM image (shown in Fig. 3.2.)

### 3.2.1 Structure & morphology as a function of growth parameter

We have grown both FePc and CoPc films using MBE under different growth conditions. Results show that both yield nearly similar morphologies if grown under identical conditions. This is expected as they have nearly similar molecular structures. In this section, we discuss the effect of various growth parameters, such as growth temperature, film thickness, and deposition rate, on the structure and morphology of FePc films.

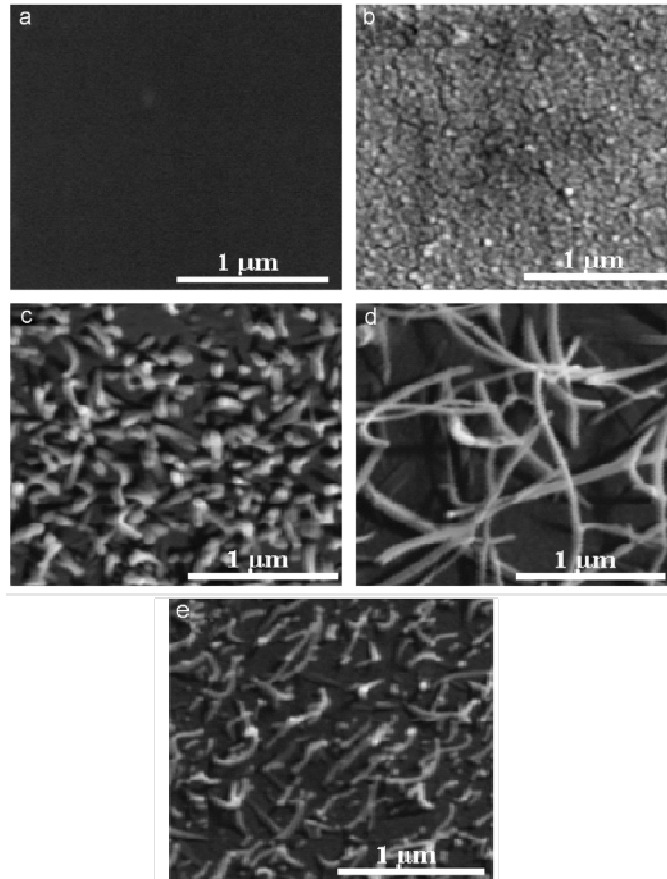


**Figure 3.3** SEM photographs of FePc thin films (nominal thickness 60 nm, deposition rate 0.07 nm/s) grown on glass substrate at (a) 25°C, (b) 50°C, (c) 100°C, (d) 200°C, (e) 300°C.

### 3.2.1.1 Effect of growth temperature

In order to investigate the effect of growth temperature on the morphology of films, other growth parameters are kept constant: growth rate = 0.07 nm/s, nominal thickness = 60 nm. Under these conditions the films have been prepared with different substrate temperature (25 to 300 °C) and the SEM images depicting the evolution of film morphology are shown in Fig. 3.3. At 25°C, no features are seen, indicating amorphous character of the film. At a substrate temperature of 50°C, the film morphology consists of densely packed grains of an average size of ~70 nm. At 100°C, the FePc grains are seen to get elongated in the plane of the substrate. At 200°C, long FePc nanowires (~100 nm diameter and upto 2 μm length), lying horizontally in the plane of the substrate are seen to grow, forming a nanoweb like structure. However, further increasing substrate temperature to 300°C, the length of nanowires decreases drastically to <500 nm. There are two possible reasons for this effect: (i) increased desorption of molecules and (ii) the transformation from  $\alpha$ - to  $\beta$ -FePc phase at elevated temperatures. These two factors are discussed below.

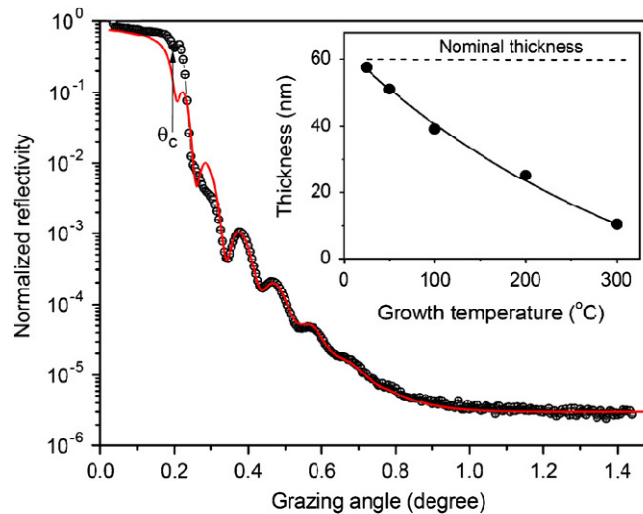


**Figure 3.4** GIXRR spectrum (open circles) for a FePc film grown at 25°C with best-fit theoretical curve (full curve). Inset shows variation of actual thickness as a function of growth temperature.

**(i) Desorption of molecules**

The increase of desorption of molecule at higher temperature actually governs the morphology as well as the actual thickness of the films. At substrate higher temperature the actual thickness of the films decreases due to the decrease of sticking coefficient. To investigate the decrease of sticking coefficient/ desorption of molecule at higher temperature the actual thickness of the films (grown at different temperature varied between 25 to 300°C), having a nominal thickness of 60 nm (measured from the flux measurement), were determined from grazing incidence X-ray reflectivity (GIXRR) measurement. A typical GIXRR plot for FePc film grown at 25°C is shown in Fig. 3.4. It is seen that the reflectivity of the sample is found to decrease rapidly above the critical angle ( $\theta_c$ ). Below the  $\theta_c$ , the X-ray reflectivity should ideally be 100% due to the total external reflection. However, at this extremely narrow grazing angle of incidence, the footprint of the beam becomes very large and infinitely long sample is required to cover the whole beam. Due to the practical limitation in the size of the samples the experimental reflectivity curve does not come out to be 100%. Above the  $\theta_c$ , the X-ray starts penetrating inside the layer and the reflectivity of the sample falls off with a slope affected by the roughness of the interface. The oscillation on the reflectivity spectrum above  $\theta_c$  (generally known as the Kiessig oscillations) is due to the finite thickness of the layer. In general, the thickness of the film can be obtained from the frequency of oscillation, while the slope of the curve gives the roughness of the interface. However, in the present case, we have determined the film thickness by fitting the experimental spectrum using a theoretical formalism of x-ray reflectivity [112], which takes interface roughness into account. A best-fit theoretical simulation of the data obtained by fitting three adjustable parameters namely, density ( $1.6 \text{ g/cm}^3$ ), film thicknesses (58.6 nm),

and interface roughness (15 nm) is shown in Fig. 3.4. The actual thickness of the FePc films, determined from GIXRR analyses, grown at different substrate temperatures is plotted in the inset of the Fig.3.4. The thickness of the film deposited at 25°C is 58.6 nm, which is close to the nominal thickness. This indicates that at 25°C the sticking coefficient of FePc molecules on glass substrate is close to unity. However, with increasing substrate temperature, the film thickness reduces sharply and, this result is not surprising as at higher temperature the probability of desorption of molecules from the surface of the substrate increases.

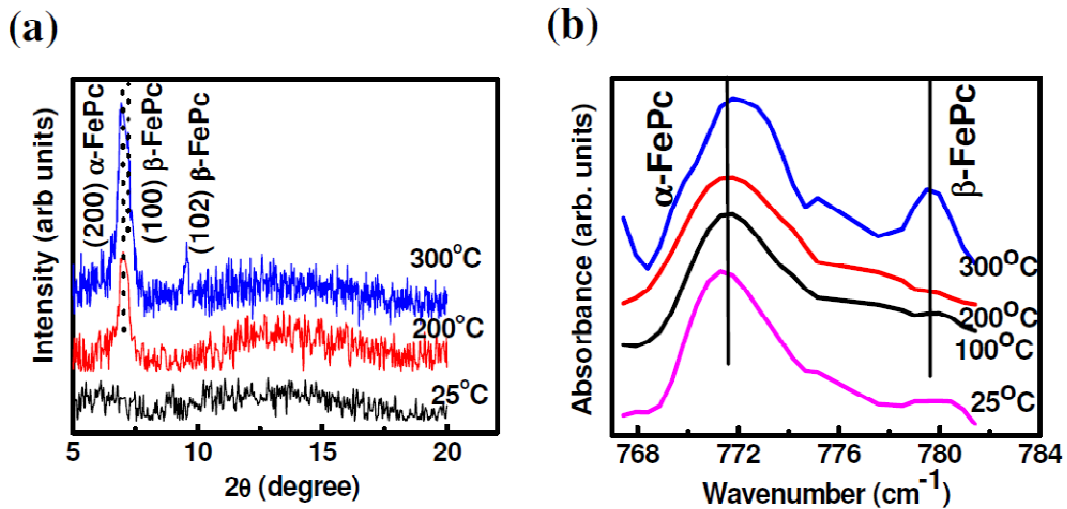


**Figure 3.5** (a) GIXRD patterns and (b) FTIR spectra recorded for 60nm (nominal thickness) FePc films deposited at different substrate temperatures.

### (ii) $\alpha$ to $\beta$ phase transition

In order to investigate the molecular stacking, crystallinity and phase formation, we have recorded GIXRD and FTIR spectra for the films deposited at different temperature, and the results are presented in Fig. 3.5. As shown in Fig.3.5 (a), the film deposited at 25°C is amorphous in character, supporting the inference drawn from the SEM images. For films grown upto at a temperature of 200°C, presence of a single peak appears at  $2\theta = 6.96^\circ$ , which corresponds to the (200) peak of the  $\alpha$ -FePc phase. Presence of only (200) peak in the entire

spectrum indicates that  $a$ -axis is preferentially orientated normal to the substrate plane, indicating the edge-on stacking of the FePc molecules. The value of  $a$ -lattice parameter computed from the XRD data is 2.54 nm, which is in agreement with the reported values [113]. However, for films grown at 300°C, two additional peaks at  $2\theta = 7.01$  and  $9.6$  have been observed in the GIXRD spectrum, which have been attributed to the (100) and (102) peaks of the  $\beta$ -FePc phase [114, 115]. Thus, at growth temperatures  $\geq 300^\circ\text{C}$ , the preferentially oriented  $\alpha$  FePc transforms into polycrystalline  $\beta$ -FePc phase. A further confirmation to the GIXRD results has been obtained from the FTIR data, as shown in Fig. 3.5 (b). It is known that the characteristics peak of  $\nu(\text{C-N})$  stretching vibration for  $\alpha$  and  $\beta$ -phase occur at around 773 and 780  $\text{cm}^{-1}$ , respectively [116, 117]. It is evident from Fig.3.5(b) that upto a growth temperature of 200°C, the films consists of pure  $\alpha$ -FePc phase. However, at growth temperature 300°C, appearance of an additional peak at 780  $\text{cm}^{-1}$  indicates that a partial transformation from  $\alpha$ - to  $\beta$ -phase takes place. From these studies, it is evident that the nanoweb structure of pure  $\alpha$ - FePc is formed for a film of nominal thickness of 60 nm deposited at 200°C.

### ***3.2.1.2 Effect of film thickness***

In order to gain insight into the evolution of nanoweb structures, as observed in Fig. 3.3 (d), the effect of film thickness is investigated. For this purpose films of thickness varying between 30 and 500 nm were deposited at 200°C using a fixed deposition rate of 0.07 nm/s. Typical SEM images of these films are shown in Fig. 3.6. For a nominal thickness of 30 nm, isolated nanowires, an average diameter of 70 nm, with an aspect ratio (length/diameter) of  $\sim 4$ , are found to grow. As the film thickness increases to 50 nm,

nanowires grow both in diameter as well as length, forming a nanoweb structure. The aspect ratio in this case dramatically increases to  $\sim 20$ . Further increasing nominal thickness to 100 nm, nanowires not only grow in diameter and length but also grow vertically from the surface of nanowires. The vertical growth of nanowires becomes more apparent for a thickness of 200 nm. This indicates the preferential molecular stacking becomes random as the thickness increases, and evidence for this comes for a film of 500 nm thick, which is polycrystalline in nature and was confirmed by GIXRD data. Thus, 50-60 nm is the optimum nominal thickness for growing nanoweb structure on the glass substrates.

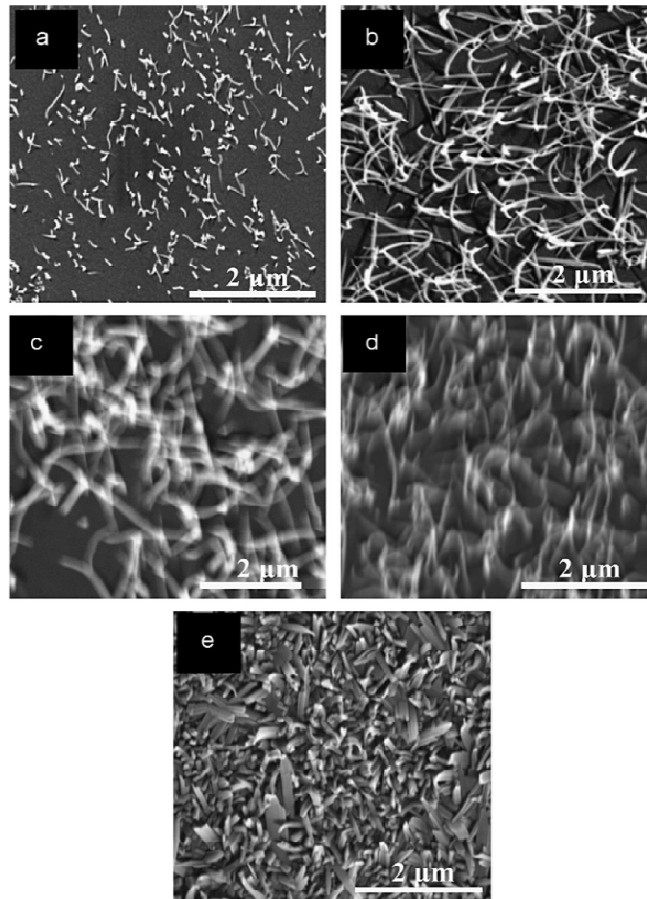


**Figure 3.6** SEM photographs of FePc thin films, grown at a substrate temperature of 200°C using a deposition rate of 0.07 nm/s having different nominal thickness (a) 30 nm, (b) 50 nm, (c) 100 nm, (d) 200 nm and (e) 500 nm.

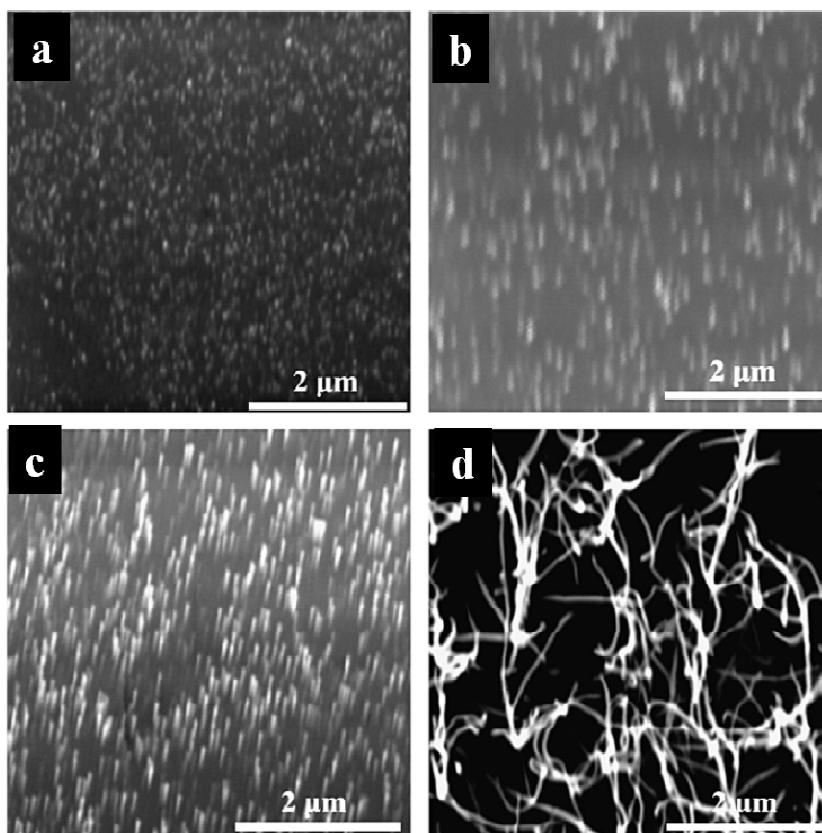


**Figure 3.7** SEM photographs of 60 nm FePc thin films grown at the rate of 0.02 nm/s at different substrate temperatures (a) 50°C, (b) 100°C, (c) 200°C and (d) 300°C.

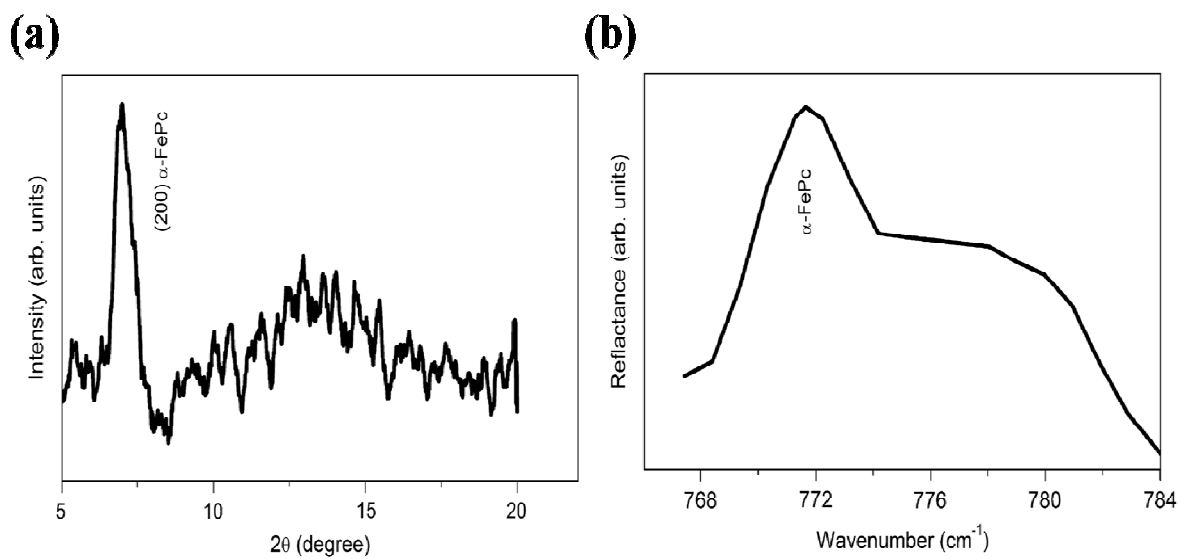


**Figure 3.8** GIXRD pattern (a) and FTIR spectrum recorded for FePc nanobrush sample.

### 3.2.1.3 Effect of deposition rate

The effect of deposition rate on the film growth has also been investigated. For this purpose following two experiments were carried out.

- (i) Keeping 60 nm as a nominal thickness of the films, morphology was investigated at a deposition rate of 0.02 nm/s, while the deposition temperature was varied from 50°C to 300 °C. The morphology evolution with temperature is shown in Fig. 3.7. It can be seen that the morphology of the films is radically different that that obtained at a deposition rate of 0.07nm/s (Fig. 3.3). At low substrate temperature (e.g. 50°C), FePc nucleates in the needle tip like structures pointing out perpendicular to the substrate plane. As the substrate temperature is increased to 100°C, the vertical growth of the needle-like tips is apparent. At 200°C, these needles further grow to form well defined vertical nanorods and this morphology resembles to that of nanobrush. Surprisingly, the GIXRD and FTIR data recorded (see Fig. 3.8) for the nanobrush sample indicate that the vertical nanorods also have  $\alpha$ -FePc phase with  $a$ -axis oriented perpendicular to the substrate plane. However, as the growth temperature is further increased to 300°C, growth of nanobrush is not observed, instead nanoweb structure is seen to grow, which consists of mixed  $\alpha$ -and  $\beta$ -FePc phases.
- (ii) Keeping nominal thickness 100 nm and growth temperature 200 °C the films are deposited with various deposition rate and the evolution of morphology is shown in Fig. 3.9. The granular morphology is observed at low deposition rate (0.02 nm/s), unlike nano-brush morphology at low thickness (see Fig. 3.7(c)). As deposition rate increases the morphology changes from granular to nano-web and

finally at 0.5 nm/s deposition rate a densely packed polycrystalline film is observed.

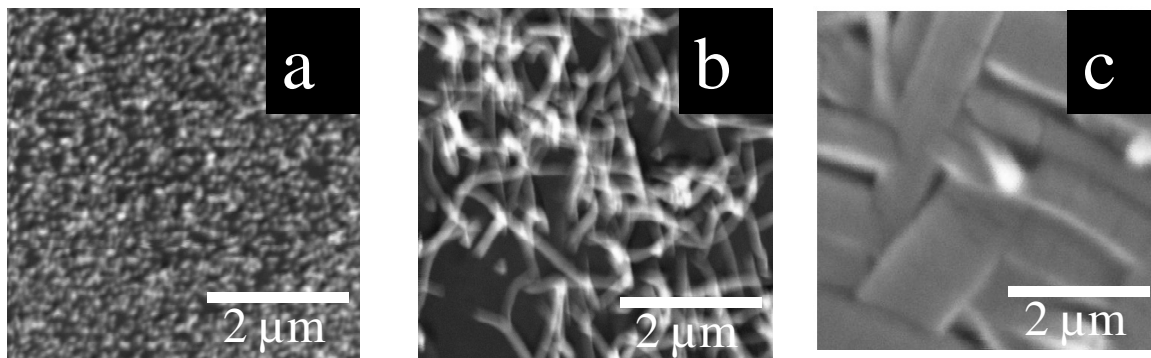


**Figure 3.9** SEM photographs of 100 nm FePc thin films grown at substrate temperatures 200°C with different deposition rate (a) 0.02 nm/s, (b) 0.07 nm/s, (c) 0.5 nm/s.

#### **3.2.1.4 Optical absorption study**

The most surprising result of the above studies is that despite radically different morphologies of nanoweb and nanobrush, the  $a$ -axis in both the cases is perpendicular to the plane of the substrate. Different morphology could mean different types of molecular packing, and therefore one could expect possibly different energy band gaps. To investigate this, we have recorded the electronic absorption spectra for amorphous, nanoweb, nanobrush and, amorphous samples and the obtained results are presented in Fig. 3.10. It is known that the UV-Vis spectrum of MPc originates from the molecular orbitals within the aromatic  $18\pi$  electron systems and from overlapping orbitals on the central atom. [118] In the near UV-region, the B-band or Sorret band representing the  $\pi\text{-}\pi^*$  transition, appears with a peak position in the range between 330-345 nm, depending upon the molecular stacking. However, in our case, this peak occurs at 333 nm irrespective of the morphology of the film. The absorption band in the visible region, usually referred to as the Q band, originates from

the singlet  $\pi$ - $\pi^*$  transition in the porphyrin ring (intramolecular excitation), and has a doublet due to the Davydov splitting.[119] The extent of Davydov splitting is related to the differences in relative orientation of molecules, which are close enough to give electronic transitions, namely, interactions between transition dipole moments from adjacent molecule. From Fig. 3.10, it is evident that the peak positions of Q band (633 nm and 711 nm) as well as the Davydov splitting (1733  $\text{cm}^{-1}$ ) are independent of the film morphology. Further, the direct energy gap ( $E$ ) in the B-band was calculated by fitting the data of Fig. 8 using the expression  $\alpha = \alpha_0(h\nu - E)^{1/2}$  where  $\alpha$  is the absorption coefficient, constant, and  $h\nu$  is the photon energy [120]. For all the three samples the value of energy gap was found to be  $1.8 \pm 0.1$  eV. Thus, the energy gap is also independent of the morphology, indicating almost similar molecular packing for both nanoweb and nanobrush. From Fig. 3.10, it is also evident that the intensity of the higher-energy peak (633 nm) is larger than that of the lower-energy peak (711 nm), which is a characteristic feature of the  $\alpha$ -MPc phase. This further supports our GIXRD and FTIR data, discussed earlier. Interestingly for all the three samples, we have also observed a peak at 566 nm, which is known to arise due to the charge-transfer (CT) excitations, that is, intermolecular electronic excitations [121]. MPc's being planar molecules, get stacked along the  $b$ -axis, resulting in the formation of a linear face-to-face array of molecules and, therefore CT excitations are often mixed with intramolecular excitations (Q-band). Presence of CT band, even in the amorphous FePc sample (as evidenced by SEM and GIXRD data), indicates that the stacking of FePc molecules, despite being short range, is good enough to give CT excitation.

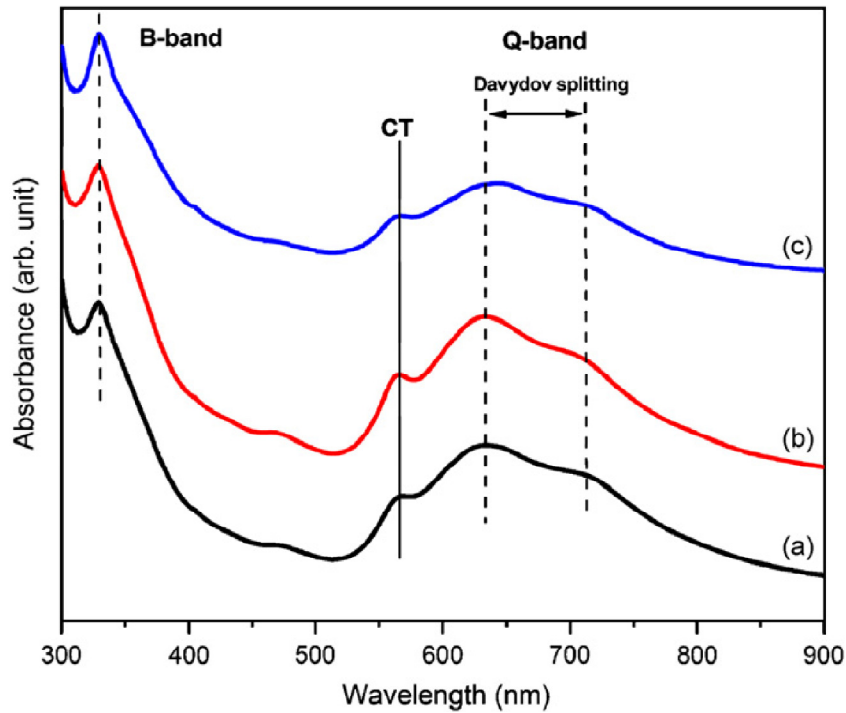


**Figure 3.10** Optical absorption spectra recorded for (a) amorphous (b) nanoweb and (c) nanobrush  $\alpha$ -phase FePc films.

### 3.2.2 Understanding of the morphology evolution

The main features of the studies described in the preceding section are:

- (i) At low thickness (<60 nm), by changing deposition rate from 0.02 nm/s to 0.07 nm/s and at a fixed growth temperature = 200°C the morphology changes from nano-web (Fig. 3.3 (d)) to nano-brush (Fig. 3.7 (c)).
- (ii) At high thickness (> 100 nm), by changing deposition rate from 0.02 to 0.5 nm/s and at a constant growth temperature of 200°C, the morphology changes from granular to densely packed polycrystalline structure, Fig 3.9.

In the following section we discuss the growth mechanisms in both the cases based on the results of GIXRD and optical absorption study.

### 3.2.2.1 Growth mechanism of nano-web and nano-brush

We have proposed a growth model that explains the evolution of the two different nanostructures, that is, nanoweb and nanobrush morphologies of FePc films, which are found to grow at same growth temperature (200°C) and nominal thickness (60nm) but using different deposition rates 0.07 and 0.02nm/s, respectively. Due to the moderate substrate temperature (200°C), the growth proceeds in two steps, as schematically shown in Fig. 3.11.

In the first step, the landing of FePc molecules on the substrate surface is followed by their random 2-D movement and accidental impacts with each other, which leads to the formation of seeding nanoscopic islands or nuclei. Since molecule-molecule interaction in the present case is stronger than molecule-substrate interaction, the nuclei grow in the ‘standing-up’ configuration. This implies that the molecules in the nuclei are stacked along *b*-axis that lies parallel to the substrate surface. The fact that GIXRD show only presence of (200) peak, indicating that *a*-axis of the nuclei is normal to the substrate plane and therefore confirms the edge-on interaction of molecules with substrate. This type of oriented nuclei formation when the interfacial forces are of van der Waals-type only is known as van der Waals epitaxy (vdWE) [122, 123]. In fact, the vdWE concept was first introduced by Koma for heteroepitaxial growth of NbSe<sub>2</sub> films on a non-interacting 2H-MoS<sub>2</sub> substrate. A unique aspect of van der Waals epitaxy is that the films are not subject to coherency strain, and are therefore grow in an elastically relaxed state, even for the first submonolayer of growth.

In the second step, as shown in Fig. 3.11, the growth of nuclei takes place, which strongly depends on the deposition rate. It may be noted that deposition rates of 0.02 and 0.07 nm/s were achieved by heating the effusion cell to 350°C and 450°C, respectively. Therefore, when the deposition rate is high (0.07 nm/s), molecules arrive at the substrate

surface with a relatively high kinetic energy, allowing them to make a faster diffusion across the surface of the substrate and this facilitates the face-on interaction. Therefore, nuclei grow predominantly along  $b$ -axis, leading to the formation of nanowire like structure at low coverage. At high coverage, these nanowires grow further and merge together to form nanoweb structure. On the other hand, at low deposition rate (i.e. 0.02 nm/s), due to lower kinetic energy, molecules preferentially attach to the existing nuclei in the edge-on configuration, leading to a growth along  $a$ -axis. Therefore, vdWE along  $a$ -axis results in the growth of nanorods, and hence, to a nanobrush morphology. The proposed mechanism explains the GIXRD data that both nanoweb and nanobrush have same crystallographic orientation (i.e.  $a$ -axis perpendicular to the substrate plane).

### ***3.2.2.2 Growth mechanism of granular and densely packed morphology***

As discussed above, for low thickness (60 nm) and low deposition rate (0.02 nm/s) FePc stack along  $a$  axis to form nano-brush. Under identical conditions, if the thickness is increased to 100 nm, a granular morphology is obtained (see Fig. 3.9). This can be explained due to an increase in diameter of the nano-brush, as the nominal thickness films is increased. The increased diameter of the nano-brush results in the granular morphology. However at higher thickness (100 nm) and higher deposition rate (0.07 nm/s), since the molecules are deposited at higher effusion cell temperature, therefore the molecules will have higher kinetic energy. Due to the higher kinetic energy the molecules stack in the face-on configuration and grow along  $b$  axis, forming nano-web structure. At still higher deposition rate (0.5 nm/s), the molecules have sufficient kinetic energy to diffuse at the substrate surface that leads to the

merger of nano-webs. This process eventually leads to the formation of a densely packed polycrystalline structure.

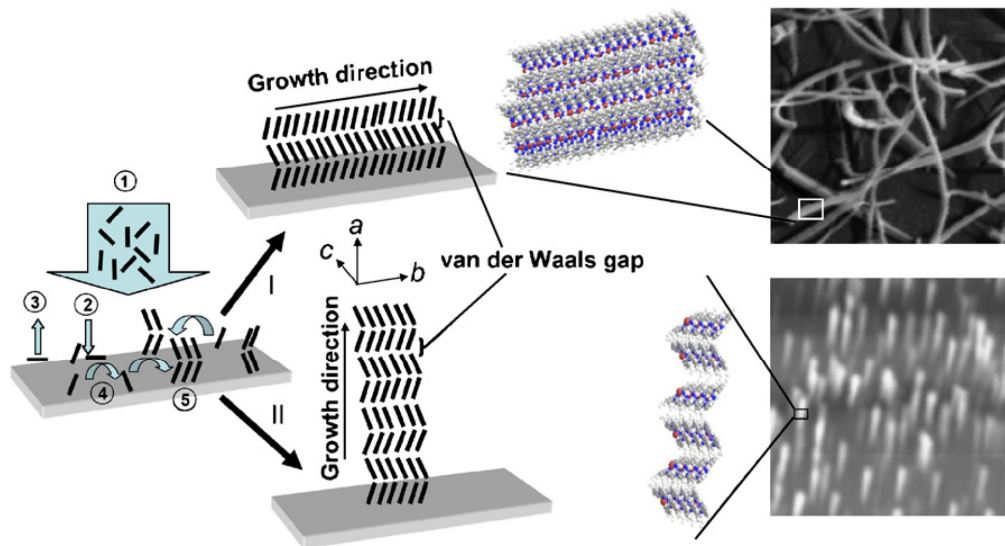


**Figure 3.11** Schematic representation depicting the growth mechanism of FePc nanoweb and nanobrush. Left: The molecular beam: (1) consisting of planar molecules impinges the substrate; molecules may undergo various processes at the surface of the substrate, such as, adsorption in ‘lying-down’ or ‘standing-up’ configurations (2), desorption (3), diffusion (4), and formation of nucleus (5). The growth of nucleus may proceed in two different ways depending upon the deposition rate: (I) at a deposition rate of 0.07nm/s, the growth direction is along b-axis, which is due to face-on (p-stacking) of the molecules, leading to the formation of nanowires lying in the plane of the substrates, (II) at a deposition rate of 0.02nm/s, the growth direction is along a-axis due to the vdW epitaxy, resulting in the formation of the nanorod aligned vertical to the substrate plane. Right: 3-D schematic representation of growth processes I and II, eventually leading to the formation of nanoweb and nanobrush morphology as shown in SEM images.

### 3.3 Growth of phthalocyanine films on (0001) sapphire

In this section we discuss the growth of CoPc films on (0001) sapphire substrate. The AFM image shown of the (0001) sapphire substrate is shown in Fig. 3.12 that has a roughness of < 0.25 nm. The CoPc films are grown at an optimum deposition temperature of

200°C and growth rate of 0.5 nm /s with two different thicknesses of 20 and 100 nm and results are discussed below.

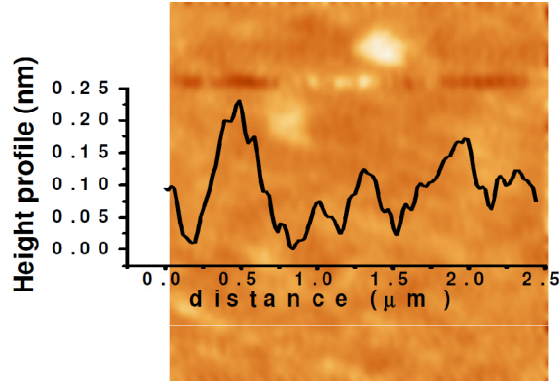


**Figure 3.12** AFM image of (0001) sapphire substrate.

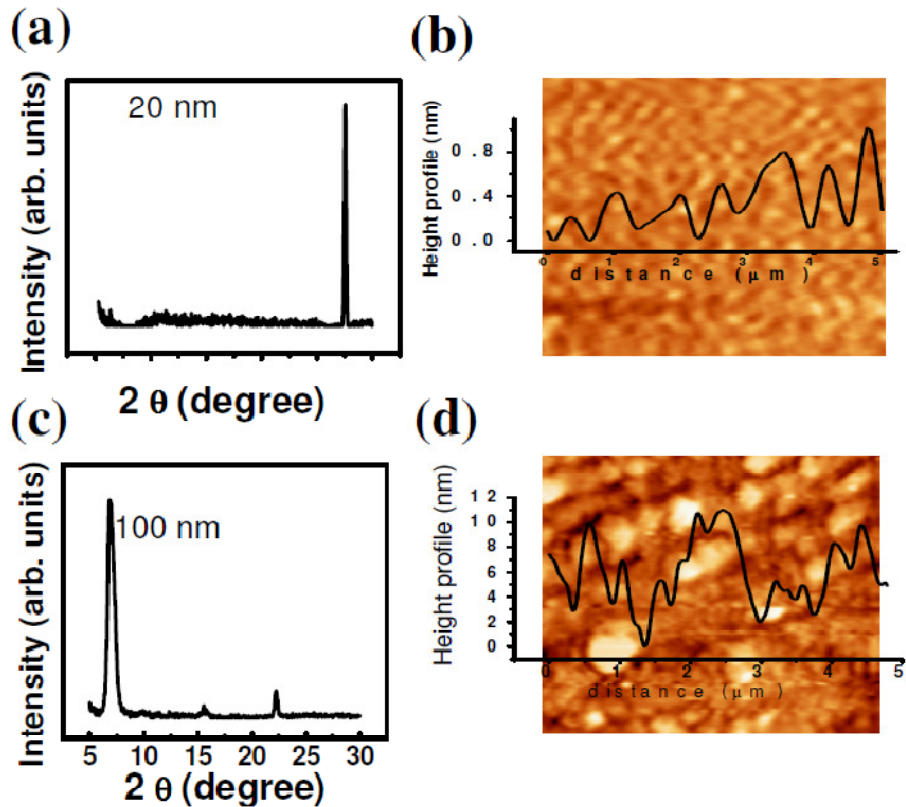


**Figure 3.13** (a,b) GIXRD pattern and 5μm × 5μm AFM image for 20 nm CoPc films on sapphire substrate. (c, d) GIXRD pattern and 5μm × 5μm AFM image for 100 nm CoPc films on sapphire substrate.

As shown in Fig. 3. 13 (a), the GIXRD for the 20 nm CoPc films exhibit a single peak at  $2\theta = 27.3^\circ$ , which corresponds to a spacing of 0.32 nm, indicating that the CoPc molecules are lying flat on the substrate and are stacked face-to-face with b-axis parallel to the surface normal [124]. The full-width at half-maximum (FWHM) of this Bragg peak is  $0.16^\circ$ , indicating high crystallinity of the films. This is further confirmed by AFM image, as shown Fig. 3.13 (b), which reveals growth of a very smooth film with an average surface roughness of  $< 1$  nm). On the other hand, GIXRD pattern (shown in Fig 3. 13 (c)) of 100 nm films revealed presence of major peaks at  $2\theta = 6.96^\circ$ ,  $15.62^\circ$  and  $22.20^\circ$ . The highest intensity peak appears at  $2\theta = 6.96^\circ$  corresponds to the (200) peak of the CoPc, indicating preferred edge-on stacking of molecules with a-axis parallel to the surface normal [113]. The FWHM of (200) peak was found to be fairly large i.e.  $0.59^\circ$ . In addition, growth of other planes corresponding to Bragg peaks at  $15.62^\circ$  and  $22.20^\circ$  is also observed. The AFM image of 100 nm films indicates a granular morphology with an average roughness of 10 nm, see Fig. 3.13 (d). Thus with increasing thickness, the orientation of the CoPc films changes from ‘face on’ to ‘edge on’. This orientation change can be explained on the basis of previously discussed ‘molecule-molecule’ and ‘molecule-substrate’ interactions. As the sapphire surface is Al terminated, the strong interaction between the Al and the  $\pi$ -electrons of the molecules guide molecules to stack in the face-on configuration. Therefore, at lower thickness films grow with b-axis parallel to the surface normal. However, as film thickness increases, the influence of molecule-substrate interaction becomes weaker and molecule-molecule interaction dominates, which allows edge-on stacking of molecules. As a result, the film grows in the polycrystalline form at higher film thickness. It may be added here that the these polycrystalline films are likely to be better in terms of the molecular packing as compared to

the polycrystalline films grown on the glass substrate in which molecules randomly stack in the edge-on configuration.

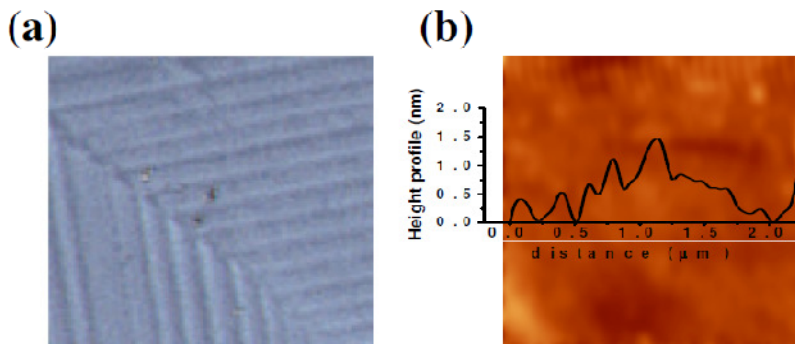


**Figure 3.14** Polarized light microscopy image (a) and AFM image (b) of twined (001)  $\text{LaAlO}_3$ .

### 3.4 Growth of phthalocyanine films on twined (001) $\text{LaAlO}_3$

Our earlier studies show that MPC molecules yield polycrystalline films with edge-on stacking on glass substrates. But due to highly disorder nature of these films it may not results a high mobility films. On the other hand the MPC grow on sapphire substrate with ‘face-on’ stacking to form very good crystalline films. But these films are not suitable for charge transport measurement in planar configuration as the molecular wave functions of adjacent molecule are not overlapping face to face. Although at higher thickness MPC molecule stack face to face along charge transport direction but at this thickness the quality of films become poor. Thus we need to deposit MPC molecule on such a substrate so that it can induce ordering in some direction as well as molecule stack face to face along charge transport direction. For this purpose we choose twined (001)  $\text{LaAlO}_3$  which has very low roughness of less 1 nm (AFM image shown in Fig 3. 14 (b)) and natural twin boundaries (polarized light microscopy image shown in Fig. 3.14(a)). These natural twin boundaries can act as template for the molecule to order along the twin boundary with edge-on

configuration. The films are deposited on twined (001)  $\text{LaAlO}_3$  at deposition temperature of  $200^\circ\text{C}$  with two different thicknesses of 20 and 100 nm and results are as follows.

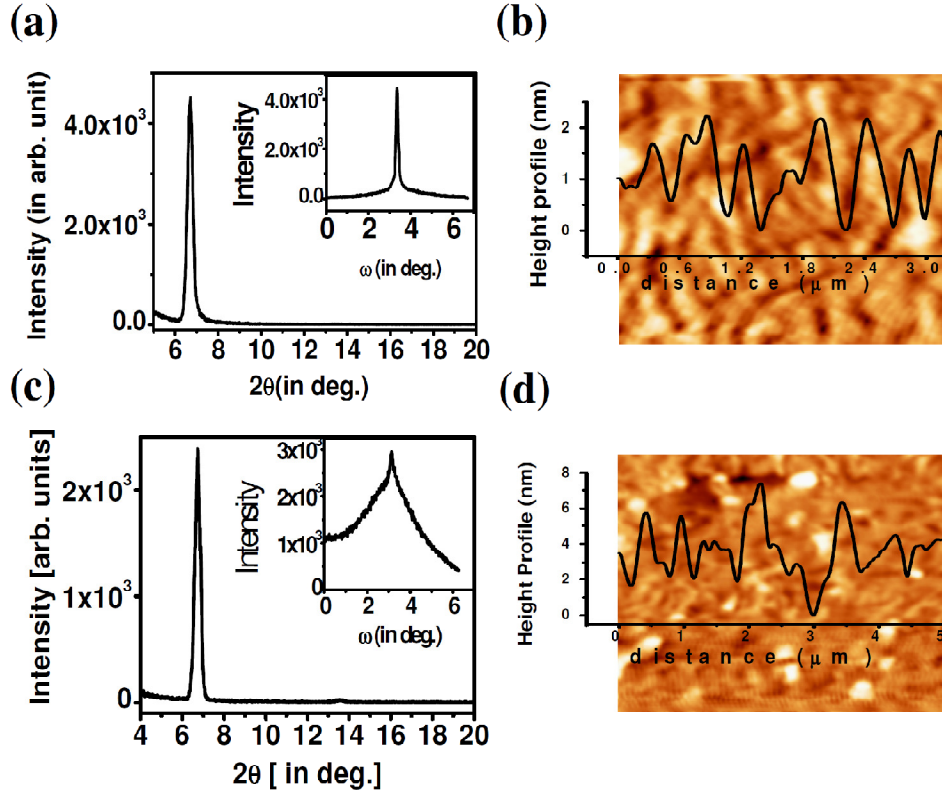


**Figure 3.15** X-ray diffraction pattern reordered for (a) 20nm and (c) 100 nm thick CoPc film. The upper inset shows the rocking curve of (200) Bragg peak with a peak position at  $3.35^\circ$ . AFM image of 20nm (c) and 100 nm (d) thick CoPc film on twined (001)  $\text{LaAlO}_3$ .

Fig. 3.15 (a and c) shows a typical XRD spectrum recorded for the 20 nm and 100 nm CoPc films grown on (001)  $\text{LaAlO}_3$  substrate. Presence of a highly intense Bragg peak for both the films at  $6.7^\circ$ , corresponding to the (200) peak of the  $\alpha$ -CoPc phase, indicates that the film is highly crystalline with  $a$ -axis normal to the substrate. It should be noted that the intensity of 20 nm film is double compared to 100 nm films which indicates that better ordering in 20 nm films. This may be due to the weakening of molecule substrate interaction

at higher thickness. The degree of ordering is further confirmed by recording the rocking curve of (200) Bragg peak, as shown in the inset of Fig.3.15 (a, c), for both the films. It is seen from the figure that an intense rocking peak at  $3.35^\circ$  (exactly at half of the value of Bragg peak position) with a full-width-half-maximum (FWHM) value of only  $0.11^\circ$ , is present for 20 nm films whereas for 100 nm films the FWHM increase to  $2.1^\circ$ . This study further indicates that the 20 nm films have better ordering than the 100 nm films. It should be noted that presence of natural twins in  $\text{LaAlO}_3$  substrate act as a template for the growth of ordered CoPc films. AFM image (see Fig. 3.15 (b) and (d)) of 20 nm films also shows a low roughness of less than 2 nm whereas 100 nm films are having average roughness of 6 nm which further indicates that at higher thickness films get disorder due to weakening of substrate interactions. To further prove this we have recorded the rocking pattern of 100 nm CoPc films grown on glass substrates. It is clear from the Fig. 3.16 that although the films are polycrystalline (a Bragg peak at  $6.7^\circ$ ) but the very broad hump in rocking pattern indicates the absence of ordering of CoPc molecule in glass substrate.

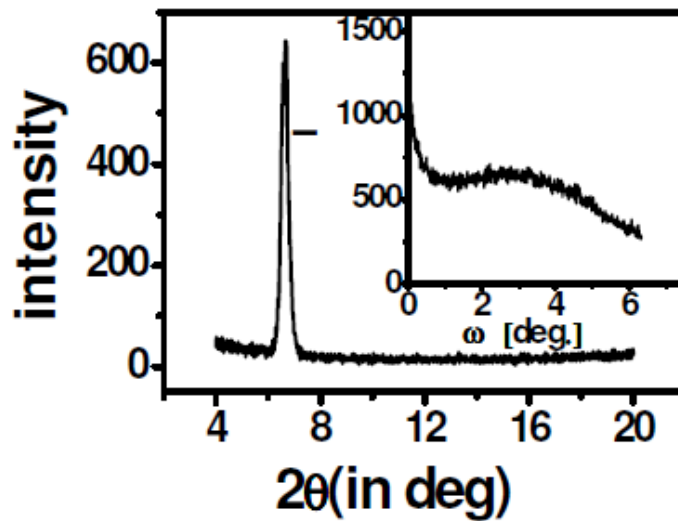


**Figure 3.16** X-ray diffraction pattern reordered for 100 nm CoPc film grown on glass substrate. The upper inset shows the rocking curve of (200) Bragg peak indicating absence of ordering.

### 3.5 Growth of phthalocyanine films on 36.8° cut bicrystal SrTiO<sub>3</sub>

It has been seen from the previous section that for low film thickness, the CoPc molecules stack along the twin boundary of (001) LaAlO<sub>3</sub> in the edge-on configuration. Unfortunately in (001) LaAlO<sub>3</sub> the twin boundaries run in the perpendicular directions, which hampers the quality of the films. Taking a clue from these studies, we have selected a bi-crystal (001) SrTiO<sub>3</sub> substrate for the deposition of CoPc films. As already discussed in Chapter-2, the bicrystal has a single grain boundary, which consists of periodic triangularly shaped grooves (depth of 2–4 nm). 20 nm thick CoPc films were deposited on the bi-crystal under the optimum deposition temperature of 200°C. Since the bicrystal boundary has a very small width of 2-3 nm, therefore, it is expected that CoPc films grown with edge-on stacking will only be in this narrow zone (as schematically depicted in Fig. 3.17). At rest of the place the molecules will stack randomly similar to the glass substrate. Precisely due to this reason, XRD pattern did not reveal the strong (200) reflection. Also, it was very difficult to capture the AFM image of the films grown along the bicrystal boundary. Nevertheless, as will be discussed in Chapter-5, the transport studies do confirm that CoPc molecules stack in the edge-on configuration along the grain boundary.

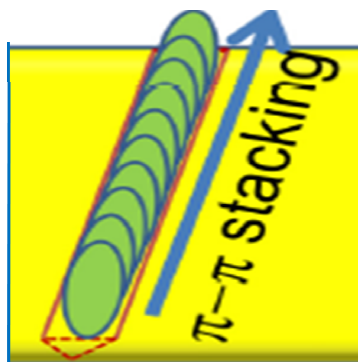


**Figure 3.17** Schematic depiction of CoPc molecules stacking along the bi-crystal boundary of SrTiO<sub>3</sub> in edge-on configuration.

### 3.6 Conclusions

We have deposited FePc and CoPc films on various substrates under different growth parameters. The results show that various FePc and CoPc films with controlled morphology can be reproducibly deposited. A summary of obtained results is given below.

- (i) Amorphous films of FePc or CoPc on glass or sapphire when deposited at room temperature using a very low growth rate (0.07 nm/s).
- (ii) Nano-web or nano-brush morphology on glass substrates when deposited at 200 °C using growth rate of 0.07 nm/s and 0.02 nm/s, respectively.
- (iii) Densely packed polycrystalline FePc or CoPc films on glass and sapphire when deposited at 200 °C using a growth rate of 0.5 nm/s.
- (iv) Polycrystalline films with ‘face-on’ stacking of CoPc molecules are obtained on sapphire at low thickness (< 20 nm) and deposition temperature of 200 °C.
- (v) Highly ordered films with edge-on stacking of CoPc molecule are grown along twin boundary of twined (001) LaAlO<sub>3</sub> at a deposition temperature of 200 °C and at low thickness (< 20 nm).
- (vi) Highly ordered films with edge-on stacking of CoPc molecule are grown when deposited along the boundary of a bicrystal (001) SrTiO<sub>3</sub>.

In the remaining chapters of this thesis, we will describe the charge transport study of the grown FePc or CoPc films. Since the charge transport studies require a good grain to grain connectivity across the two metallic electrodes, therefore we have not selected nanoweb and nanobrush films. In chapter 4, we describe the charge transport study of amorphous and polycrystalline films grown on glass and sapphire substrates. In Chapter 5, we will discuss

the charge transport studies of highly ordered films grown on twined (001)  $\text{LaAlO}_3$  and  $36.8^\circ$  cut bicrystal (001)  $\text{SrTiO}_3$  substrates.

---

# **Charge transport in amorphous and polycrystalline films**

---

4.1 Introduction

4.2 Interaction of oxygen with MPc films

*4.2.1 XPS measurements*

*4.2.2 Conductivity measurements*

4.3 Charge transport in amorphous and polycrystalline FePc films deposited on glass

*4.3.1 Charge transport at 300K*

*4.3.2 Temperature dependent conductivity*

4.4 Charge transport in polycrystalline CoPc films on glass

4.5 Charge transport in polycrystalline CoPc films on sapphire

*4.5.1 Temperature dependent J-V characteristics*

*4.5.2 Electric field & carrier distribution*

*4.5.3 Mobility measurement by transient voltage pulse method*

4.6 Trap distribution in polycrystalline CoPc films grown on glass and sapphire

4.7 Conclusions

## 4.1 Introduction

In this chapter, we describe the charge transport properties of the following amorphous and polycrystalline Pc films:

- (i) Amorphous FePc films on glass
- (ii) Polycrystalline FePc films on glass
- (iii) Polycrystalline CoPc films on glass
- (iv) Polycrystalline CoPc films on sapphire

Before we describe the charge transport properties of the Pc films, it is important to investigate how the adsorbed oxygen from the ambient interacts with Pc films. This information is very essential; as we will demonstrate later that adsorbed oxygen – depending upon the crystallinity of the films – can act as shallow and/or deep traps, and hence, govern the charge transport properties.

## 4.2 Interaction of oxygen with MPc films

In order to investigate the interaction between the ambient oxygen and Pc films, following two sets of experiments were carried out.

- (i) In-situ XPS studies (i.e. without exposing to ambient) on FePc or CoPc films as well as after exposing them to ambient atmosphere for prolonged period (e.g. 12 hrs.).
- (ii) Repeatedly measuring the conductivity of the Pc films by alternatively switching them to vacuum ( $\sim 10^{-2}$  torr) and ambient conditions.

#### 4.2.1 XPS measurements

The interaction between FePc/CoPc films and ambient oxygen were investigated for CoPc and FePc films (thickness 100 nm), deposited at 200°C on glass and sapphire substrates.

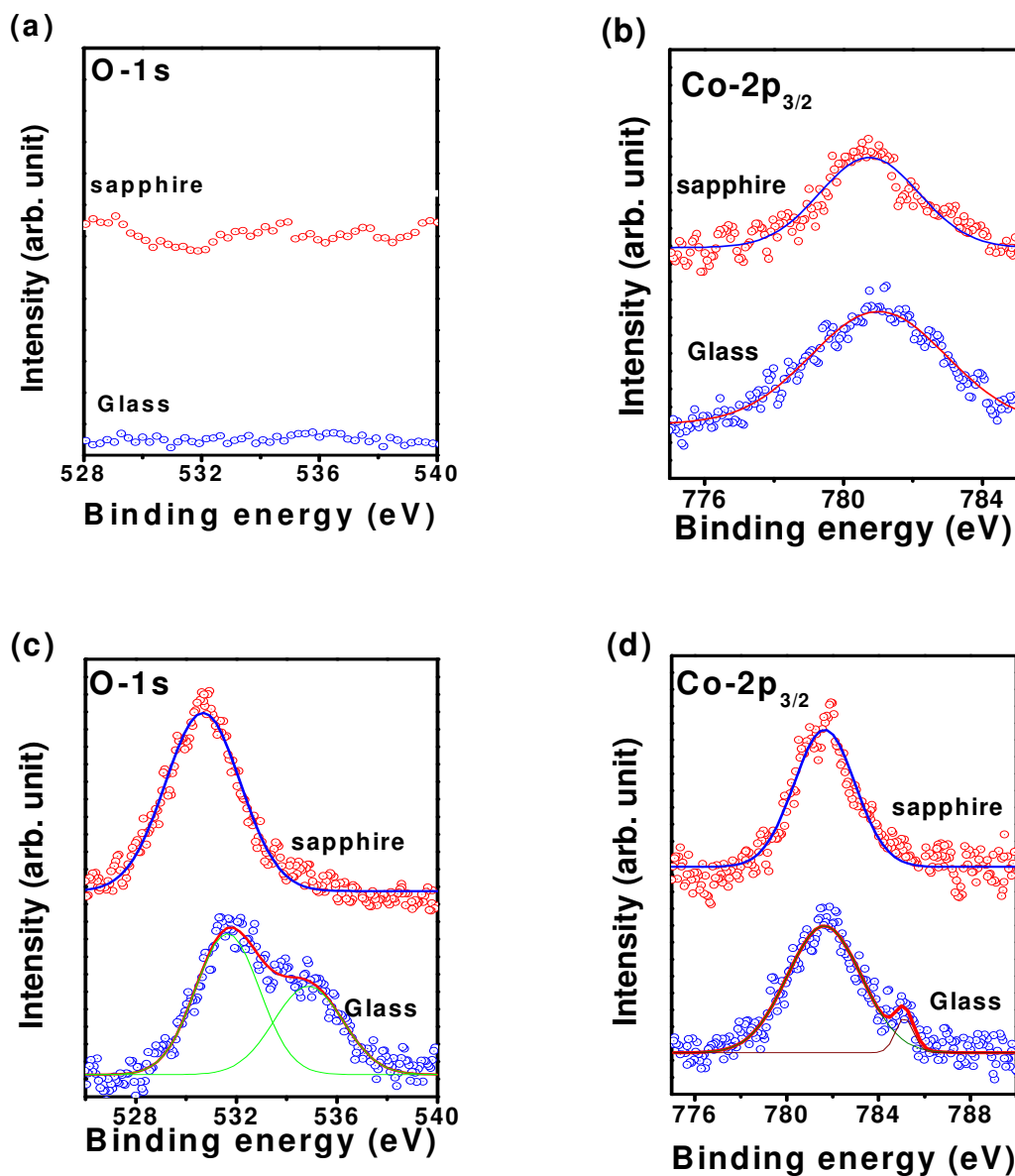


**Figure 4.1** (a), (b) Core level O-1s and Co-2p<sub>3/2</sub> XPS spectra of fresh CoPc films on glass (blue data points) and sapphire (red data points) substrate. (c), (d) Core level O-1s and Co-2p<sub>3/2</sub> XPS spectra of air exposed CoPc films on glass (blue data points) and sapphire (red data points) substrate.

Typical XPS spectra recorded for in-situ grown CoPc films on glass and sapphire and the films exposed to ambient for 12 hrs are shown in Fig. 4.1. It is seen that for both the as-deposited films (grown on glass and sapphire), see Fig. 4.1 (a) and (b), oxygen is completely absent and the cobalt is present in  $\text{Co}^{2+}$  state, which is a signature of CoPc. However, a marked difference in the XPS spectra of films grown on glass and sapphire, as shown in Fig. 4.1 (c) and (d), is observed when they were exposed to atmosphere. For CoPc films deposited on sapphire, O-1s spectrum exhibited a single peak at  $\sim 531\text{eV}$ , corresponding to physisorbed oxygen [106]. On the other hand, the O-1s spectrum for the CoPc films on glass substrates has two distinct components at binding energies of 531 and 535 eV, corresponding to physisorbed and chemisorbed oxygen, respectively [63, 106, 125]. Chemisorptions of oxygen by the CoPc films on glass is further confirmed from the core level XPS spectra of Co-2p<sub>3/2</sub> which has two peaks at 782 and 785 eV corresponding to  $\text{Co}^{2+}$  and  $\text{Co}^{3+}$  state whereas for the films grown on sapphire, only one peak at 782 eV, corresponding to  $\text{Co}^{2+}$ .

The amount of oxygen adsorption by MPc films depends on the structure and morphology (amorphous and poly-crystalline) of the films even grown on same substrate. Typical XPS measurements results recorded for amorphous and poly-crystalline FePc films deposited on glass substrates are shown in Fig. 4.2. For both the films on ambient exposure, the Fe 2p<sub>3/2</sub> peak could be deconvoluted into two peaks with binding energies of 708 and 711 eV, corresponding to  $\text{Fe}^{2+}$  and  $\text{Fe}^{3+}$  states, respectively [106]. The  $\text{Fe}^{2+}$  state is the original state present in the FePc molecule, whereas the presence of  $\text{Fe}^{3+}$  states at the surface is attributed to the formation of charge transfer complex between Fe and chemisorbed oxygen. The formation of Fe-O charge transfer complex was further confirmed by the analysis of the O-1s spectra. For both the air exposed films, O-1s spectrum showed two components at

binding energies of 531 and 533 eV attributed to physisorbed and chemisorbed oxygen respectively [63, 106, 125]. The area under  $\text{Fe}^{2+}$  and  $\text{Fe}^{3+}$  peak is directly proportional to the amount FePc molecule which have not reacted and reacted with oxygen. Thus the ratio of the area under these two peaks gives the relative amount of chemisorbed oxygen. For air exposed samples, the  $\text{Fe}^{3+}/\text{Fe}^{2+}$  ratio was found to be 0.94 and 0.78 for amorphous and polycrystalline samples respectively, indicating stronger interaction of oxygen with amorphous films.

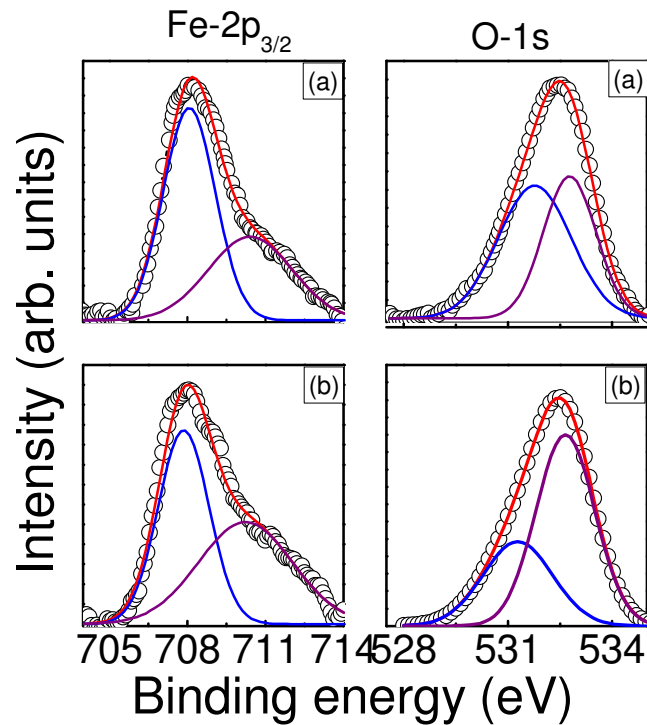


**Figure 4.2** Core level  $\text{Fe-2p}_{3/2}$  and  $\text{O-1s}$  XPS spectra of (a) air exposed FePc films in polycrystalline form. (b) Air exposed FePc amorphous films.

#### 4.2.2 Conductivity measurements

In order to investigate the effect of physisorbed/chemisorbed oxygen on the conductivity of the CoPc films grown on glass and sapphire substrates, we have repeatedly

measured the conductance by exposing them to air from a base vacuum of ( $10^{-2}$  torr) and vice versa. The typical obtained results are shown in Fig. 4.3. The conductance, measured under vacuum, for films deposited on glass and sapphire substrates are  $5 \times 10^{-8}$  and  $1 \times 10^{-7} \Omega^{-1}$ , respectively. A low conductance of CoPc films is attributed to their intrinsically insulating nature with a gap between HOMO and LUMO, which is of the order of 2 eV [126].

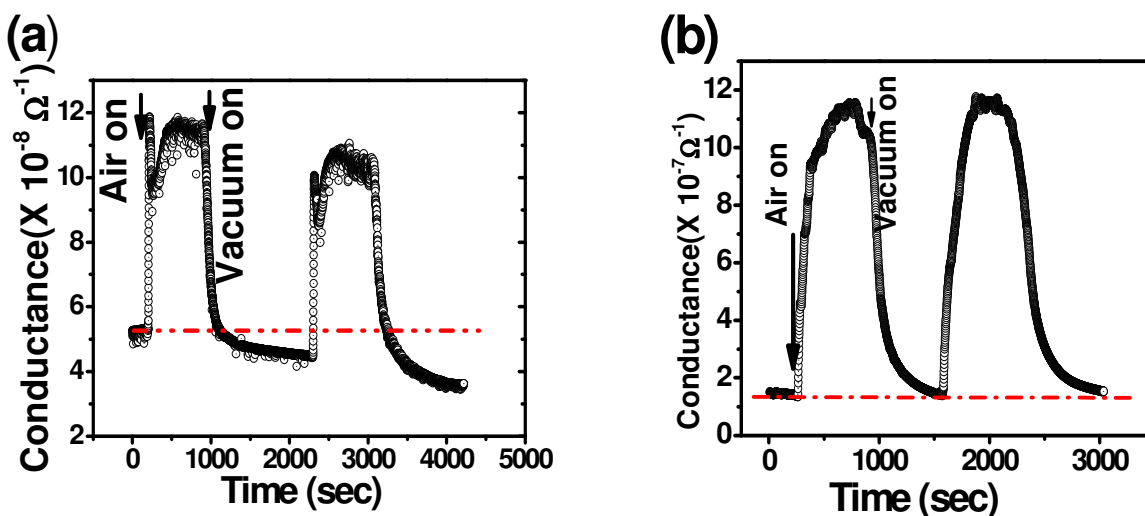


**Figure 4.3** (a) Conductance change of the CoPc films on glass upon exposure of air. b) Conductance change of the CoPc films on sapphire upon exposure of air.

For CoPc films on glass, as shown in Fig. 4.3 (a), the conductance increases by three fold on exposing to the air, which is attributed to the hole doping by the chemisorbed oxygen. However, on restoring the vacuum, conductance falls down much lower than the original value, and this phenomenon continues with each vacuum/air exposure cycle. This result implies that some of the chemisorbed oxygen acts as deep traps. These deep traps lower down the charge mobility, and hence, reduce the conductance. On the other hand, for CoPc

films on sapphire, the conductance, as shown in Fig.4.3 (b), follows a reversible cycle on repeated exposures to vacuum and air, indicating only physisorption of oxygen and this is in agreement with XPS results. The traps created in the films may be shallow or deep depending on where the localized energy state is created. The shallow and deep traps have two distinct affect on the  $I-V$  characteristics. In air we see a pronounce hysteresis, in the  $I-V$  characteristics of the films grown on glass, where as negligible hysteresis in vacuum, as shown in Fig 4.4 (a). This confirms the deep traps, created by chemisorb  $O_2$  in the film grown on glass, induces the hysteresis in the  $I-V$  characteristics. On the other hand no hysteresis, in the  $I-V$  characteristics (shown in Fig. 4.4 (b)), is observed in the films grown on sapphire that is indicative of only shallow traps may be present in the film. A detailed discussion on the influence of physisorption/chemisorption of oxygen on the charge transport properties of MPC films is presented in the following sections.

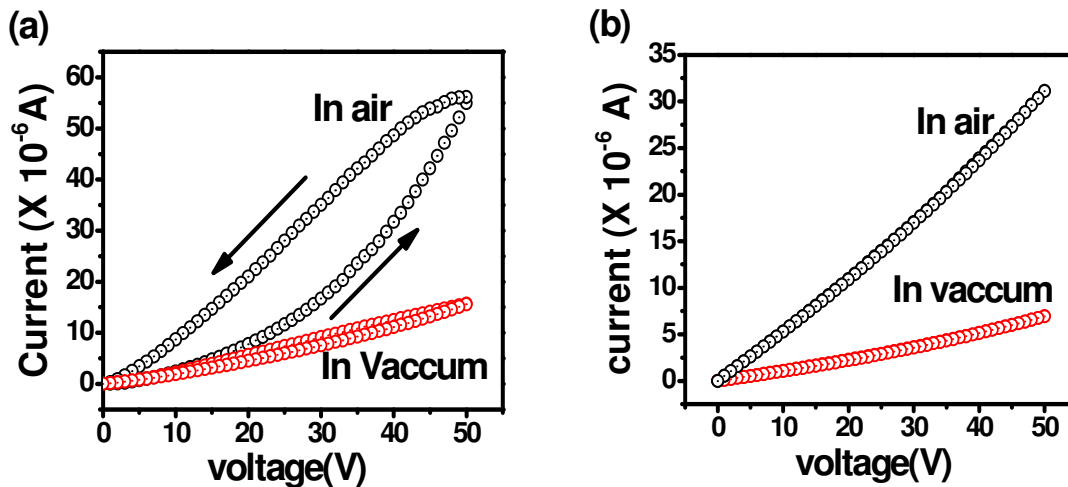


**Figure 4.4** (a)  $I-V$  characteristics in ambient and in vacuum of CoPc films grown on glass. (b)  $I-V$  characteristics in ambient and in vacuum of CoPc films grown on sapphire.

### 4.3 Charge transport in amorphous and polycrystalline FePc films deposited on glass

It has been shown in the previous section that different amount of oxygen is absorbed by the amorphous and polycrystalline FePc films grown on glass. Thus charge transport in these films will be different. In this section we present a comparative study of charge transport measured at room temperature as well as low temperatures for amorphous and polycrystalline FePc films grown on glass substrate.

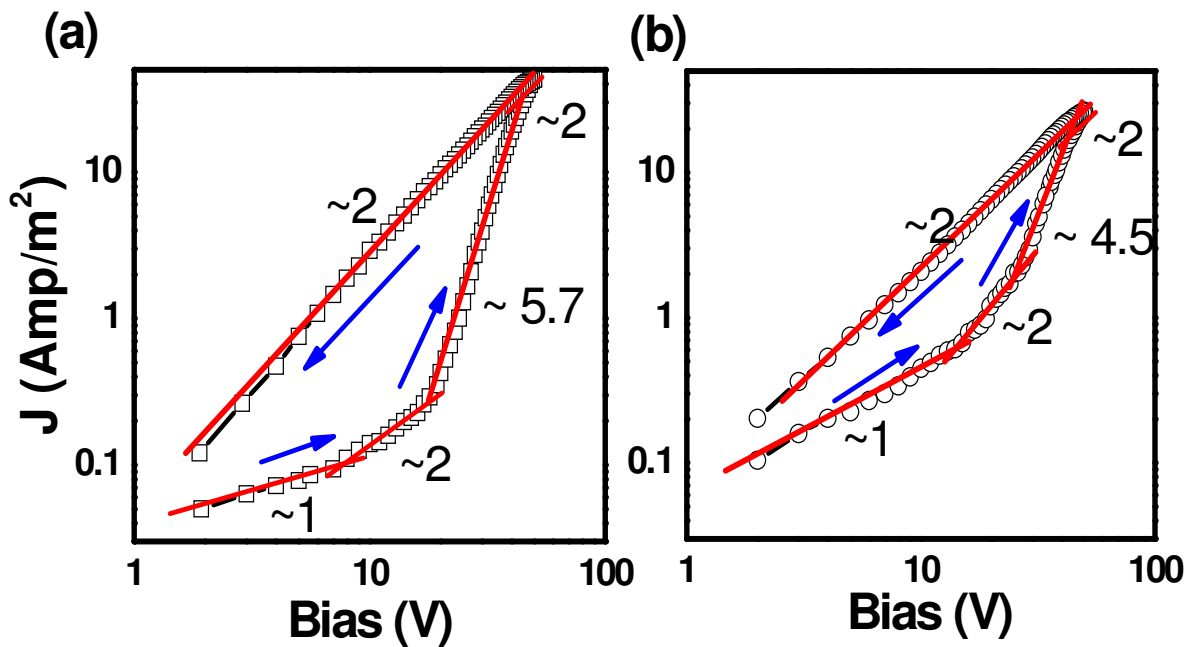


**Figure 4.5**  $J$ - $V$  characteristics for (a) amorphous and (b) polycrystalline films recorded at 300 K in log-log scale.

#### 4.3.1 Charge transport at 300K

To compare the charge transport mechanism between polycrystalline and amorphous films, we have measured room temperature  $J$ - $V$  characteristics for both the films and shown in Fig 4.5. A power law behavior of  $J$ - $V$  characteristics ( $J \sim V^\alpha$ ) is observed in different

regions with exponent ( $\alpha$ ) increasing (for increasing voltage scan) from  $\sim 1$  at low voltages to a value of  $\sim 5$  at voltage of about 25 V and finally to 2 at higher voltages. For reducing voltage scan the exponent has constant value of 2 at all voltages. Value of exponent is an indication of conduction mechanism and its variations indicate crossover in conduction mechanisms as a function of voltage. For voltages  $< 10$  V,  $\alpha \sim 1$  and linear  $J$ - $V$  may be described by Ohmic conduction. In the Ohmic regime, the density of injected charge carriers is much less than the thermally generated carrier density leading to linear behavior and the variation of current density with voltage is given by eq. 1.14. The room temperature values of free carriers ( $n_0$ ) were determined by from Ohmic regime and are given in Table – 4.1 for both the films [28, 127]. For voltage range of 10 - 20 volts, characteristics ( $\alpha \sim 2$ ) indicate space charge limited conduction (SCLC) with shallow traps. SCLC occurs if the injection electrode forms an ohmic contact with the organic film and at a voltage where the injected carrier concentration exceeds that of thermally generated carriers. Due to presence of very small energy barrier of 0.2 eV at Au/FePc interface an ohmic contact is expected [128]. Therefore, the observed slope of 2 in the bias range 10-20 volts is attributed to SCLC with the shallow traps and the current density is given by eq. 1.29.

For voltage range of 20-40 volts, the current rises rapidly with power exponent  $\alpha \sim 5.7$  for amorphous films and  $\sim 4.5$  for polycrystalline films. The higher value of exponent ( $> 2$ ) suggests SCLC mechanism in the presence of deep traps, which are distributed exponentially in energy above the valence band edge. In this regime the  $J$ - $V$  characteristics may be described by eq. 1.32. Using reported values of  $N$  ( $10^{27} \text{ m}^{-3}$ ) and  $\epsilon$  ( $2.43 \times 10^{-5} \text{ F/m}$ ) for MPc, values of characteristic temperature of trap distribution ( $T_t$ ), trap density per unit

energy range at valence band edge ( $P_0$ ), total trap density ( $N_t$ ) were determined from this region and are tabulated in Table - 4.1.

For voltages  $> 40$  volts, current rises slowly and exponent again reduces to  $\sim 2$ . It is attributed to filling of all traps so that the sample behaves like trap free sample [28, 127]. In this regime, the  $J$ - $V$  characteristic follows the Child's law and given by eq. 1.19 [129].

Summing up, as the voltage is scanned from 0 to 50 V, the carrier transport mechanism changes from Ohmic to SCLC controlled by shallow traps to SCLC controlled by traps exponentially distributed in energy and finally to SCLC controlled by Child's law. On the reverse scan, the films show high conductance with  $\alpha \sim 2$ , indicating that trapped carriers are not released. Thus the film behaves like trap free sample and the  $J$ - $V$  characteristic follows the Child's law. The data shows that hysteresis arises from trapping of carriers on application of voltage (leading to high conductivity state) and their release on reduction of voltage (yielding lower conductivity state).

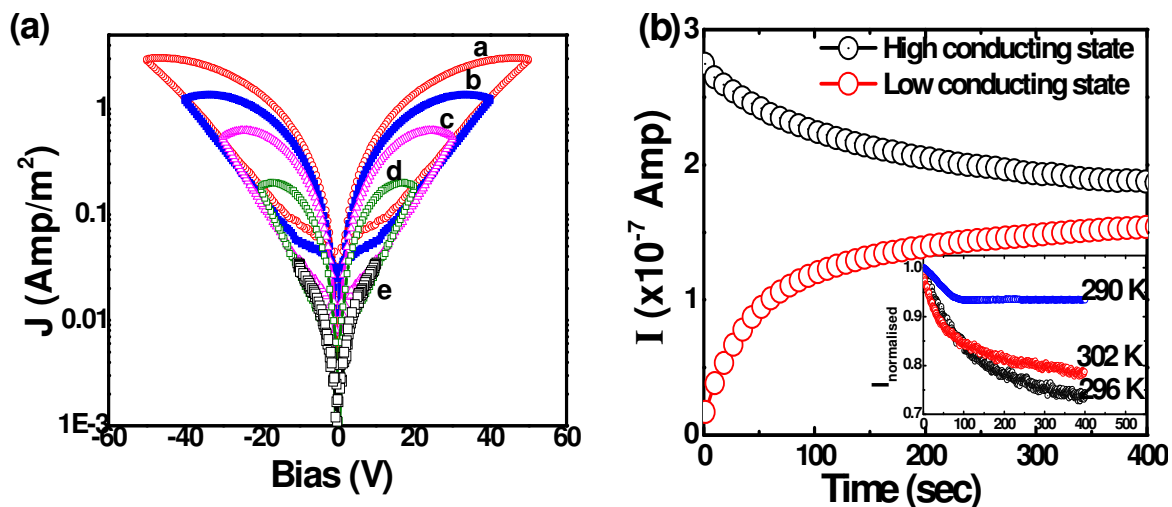
**Table-4.1** Parameters of FePc films determined from  $J$ - $V$  characteristics.

| Sample          | Hole concentration ( $n_0$ ) | Trap characteristics temperature ( $T_t$ ) | Total trap density ( $N_t, m^{-3}$ ) | trap concentration at valence band edge ( $P_0 eV^{-1} m^{-3}$ ) | $\mu$ ( $cm^2 V^{-1} s^{-1}$ ) |
|-----------------|------------------------------|--|--------------------------------------|--|--------------------------------|
| Amorphous       | $6.4 \times 10^{17} m^{-3}$  | 1410 K                                     | $1.03 \times 10^{23}$                | $3.3 \times 10^{24}$   | 0.2                            |
| polycrystalline | $2 \times 10^{18} m^{-3}$    | 1050 K                                     | $3.9 \times 10^{21}$                 | $1.6 \times 10^{42}$   | 0.35                           |

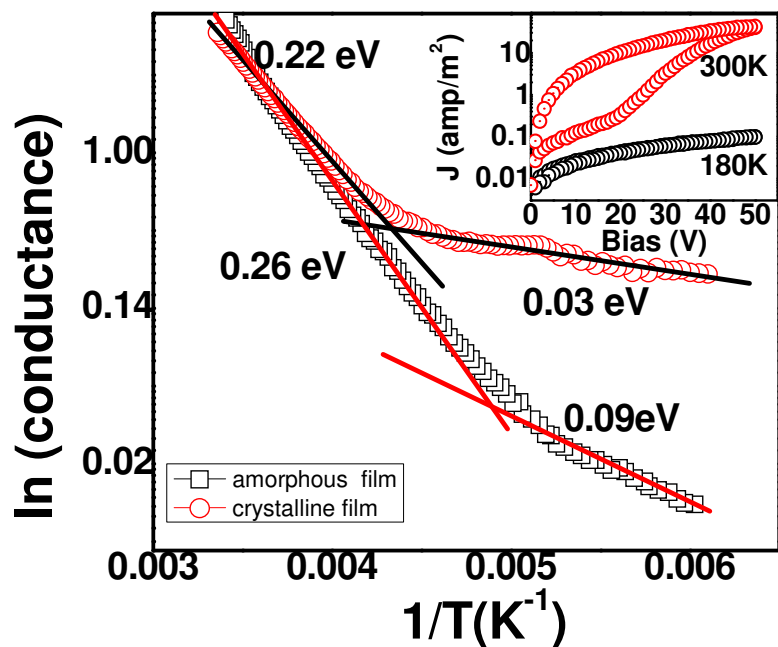
It is clear from the previous study that the hysteresis in FePc films grown on glass substrates are due the deep traps created by the chemisorptions of oxygen. As seen from the

Table-4.1 that the value of total traps density for amorphous films is two orders higher than that of the crystalline films and thus higher hysteresis in amorphous films. The obvious reason is that the amorphous films have higher defect density and so higher number of active sites available for the oxygen. This result is also in confirmation with the results of XPS measurements, describe in Section- 4.2.1.

In order to investigate the pronounce hysteresis effect in amorphous FePc films, we have recorded  $J$ - $V$  characteristics as a function of maximum applied bias and results are shown in Fig. 4.6 (a). Clearly, the hysteresis is absent for applied voltages  $< 10$  volts because until this voltage injected carriers are not sufficient to start filling up the traps. The amount of hysteresis increases with the increase of voltage as more and more traps are filled by the injected carriers. Clearly hysteresis in  $J$ - $V$  characteristics yields two conductivity states at a particular voltage. One is low conductivity state arises due to filling of charge carriers when voltage increases and other is high conductivity state which is achieved during voltage decreasing scan. In order to investigate the time dependence of these two states we have measured the time dependence of current at 30 volts during voltage increasing and decreasing cycle. The results are shown in Fig. 4.6 (b). Ratio of currents in these two states reduces from initial value of  $\sim 19$  to 1.4 after 400 seconds. The decrease in current ratio is attributed to relaxation of trapped charge carriers. To investigate the relaxation mechanism, we studied time dependence of current (at applied voltage of 30 V) starting from high conductivity state at different temperatures and the results are shown in the inset of Fig. 4. 6 (b). It is observed that the relaxation rate increases with temperature indicating that the relaxation process is predominantly thermally activated.



**Figure 4.6** (a)  $J$ - $V$  characteristics recorded at 300 K with different values of maximum voltage bias. (b) Time dependence of the current recorded for high and low conducting states measured at a voltage of 30 V. Inset shows the time dependence of current starting from high conducting state at different temperature.



**Figure 4.7** Temperature dependence of the conductance recorded for amorphous (black data points) and crystalline (red data points) FePc films. Inset shows  $J$ - $V$  characteristics of amorphous films at 300K and 180K.

### 4.3.2 Temperature dependent conductivity

To further gain insight into the conduction mechanism, the conductivity of both amorphous and polycrystalline films were measured as a function of temperature. The obtained results are shown in the form of Arrhenius plot in Fig. 4.7. The data could be fitted using two distinct straight lines, indicating a change in conduction mechanism at a temperature of  $\sim 200$  K. Fitting of the temperature dependence of conductance to thermally activated model:  $\sigma = \sigma_0 \exp(-\Delta E/kT)$ , reveals two activation energies,  $\Delta E_1 = 0.22$  eV ( $T > 220$  K) and  $\Delta E_2 = 0.03$  eV ( $T < 220$  K) for polycrystalline films and  $\Delta E_1 = 0.26$  eV ( $T > 200$  K) and  $\Delta E_2 = 0.09$  eV ( $T < 200$  K) for amorphous films. Presence of two different activation energies indicates the possibility of two different types of charge trap states in the films: (i) surface traps arising due to chemisorbed oxygen and (ii) bulk traps due to impurity/structural defects. The first activation energy ( $\Delta E_1$ ) is very close to the value of 0.26 eV reported for metal phthalocyanine – oxygen interaction [130]. It should be noted that the higher activation energy for both the films are almost same as it is due to the deep traps created by chemisorbed oxygen. At higher temperature these deep traps are responsible for hysteretic current voltage characteristics. On the other hand lower activation energy effective at temperatures  $< 200$  K is attributed to shallow traps. The lower activation energies for the two films are different as it arises due to the structural defects. The amorphous films are having more structural defects and thus they have higher activation energy compared to the polycrystalline films. The low temperature transport is governed by these shallow traps and thus no hysteresis is observed (shown in the inset Fig. 4.7).

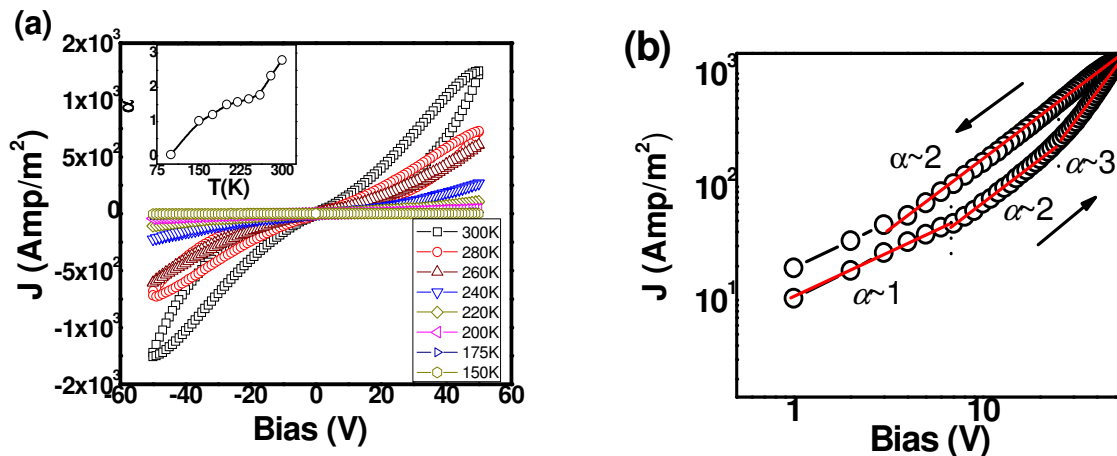


**Figure 4.8** (a) Temperature dependence of  $J$ - $V$  characteristics for the films grown on glass substrate. Inset shows the temperature dependence of voltage exponent  $\alpha$ . (b) Room temperature  $J$ - $V$  characteristics of polycrystalline CoPc films grown on glass.

#### 4.4 Charge transport in polycrystalline CoPc films on glass

In order to investigate the charge transport in polycrystalline CoPc films on glass substrate, we have measured temperature dependent  $J$ - $V$  characteristics and are shown in the Fig. 4.8 (a). It is seen that  $J$ - $V$  characteristics are hysteric in nature upto 220K as seen in case of FePc films on glass substrate also. This is expected as both FePc and CoPc films grown on glass are having chemisorbed oxygen. The chemisorbed oxygen is responsible for creating deep traps in the MPC films grown on glass. As the amount of chemisorbed oxygen are different in both the films thus different amount of hysteresis. To further understand the hysteretic current voltage characteristics we have re-plotted the room temperature  $J$ - $V$  characteristics in  $\log$ - $\log$  plot in Fig. 4.8 (b). In this case also current density follow power law behavior with different exponent at different applied bias. It is clear from the exponent shown in the Fig. 4.8 (b) that at low voltage charge is transported by Ohmic process whereas

at high voltage ( $> 25$  V) charge transport is controlled by SCLC with deep traps. The calculated value of mobility ( $\mu$ ), total trap density ( $N_t$ ) and the characteristic temperature ( $T_f$ ) of trap distribution are tabulated in Table-4.2.

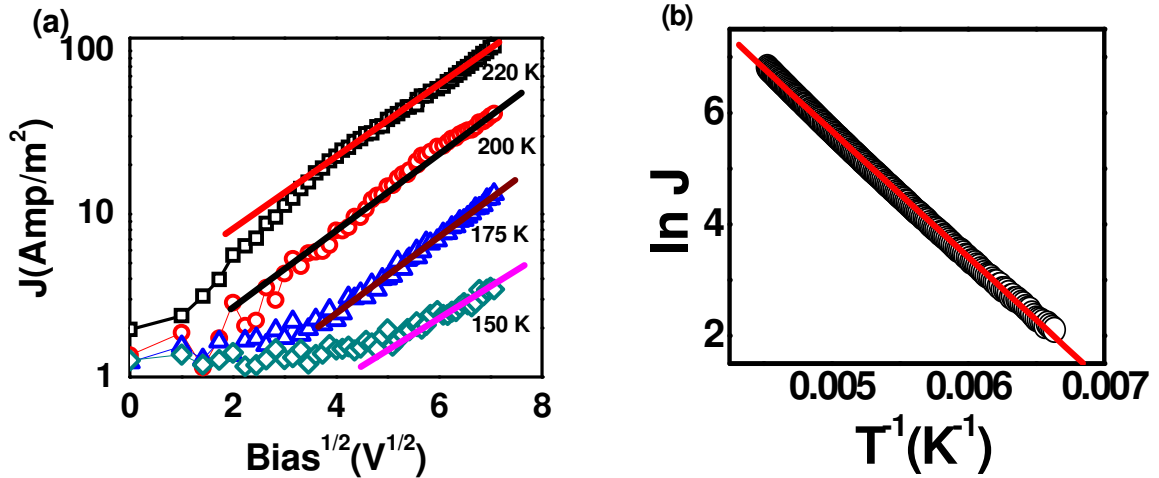


**Figure 4.9** (a)  $\ln J$  vs  $V^{1/2}$  plots at different temperatures showing Poole Frankel behavior. (b)  $\ln J$  versus  $1/T$  plot obtained at bias of 50 V.

It is evident from the Fig. 4.8 (a) that the hysteresis decreases systematically with lowering temperature, and eventually vanishes at 220 K. Moreover, below 150 K, films do not transport any current. As shown in the inset of Fig. 8(a), the value of  $\alpha$  decreases with lowering temperature and becomes  $<2$  for temperatures below 230 K. This implies in the temperature range 230–150 K, the SCLC transport mechanism is not valid. This is because due to disorder present in the films, at low temperatures there is strong charge localization, density of free carriers is very small and conduction occurs by hopping of trapped charges. At this low temperature the localized charge carriers can be promoted to the transport level by the application of field which is nothing but Poole-Frankel effect. The charge transport mechanisms in temperature range 230–150 K were analyzed using Poole-Frankel (PF)

models where the current density is given by eq. 1.34. The Linear dependence of  $\ln J$  on  $V^{1/2}$  for  $T < 220$  K, as shown in Fig. 4.9(a), indicates agreement with PF behavior. Average value of  $\beta$  determined from slopes of characteristics at different temperatures was found to be  $\sim 3.5 \times 10^{-5} \text{ eVm}^{1/2}\text{V}^{-1/2}$  [28]. Value of  $\beta$  was also calculated from the slope of  $\ln J$  versus  $1/T$  (measured at 50 V) characteristics shown in inset of Fig. 4.9 (b) to be  $4.7 \times 10^{-5} \text{ eVm}^{1/2}\text{V}^{-1/2}$ . These values of  $\beta$  indicate PF mechanism of charge transport.

## 4.5 Charge transport in polycrystalline CoPc films on sapphire

### 4.5.1 Temperature dependent $J$ - $V$ characteristics

In this section we present the results of charge transport measurements on CoPc films grown on sapphire substrate. A typical  $J$ - $V$  characteristic at room temperature is shown in Fig. 4.10 (a). No hysteresis is observed in the  $J$ - $V$  characteristic indicates the absence of deep traps. The absence of chemisorbed oxygen, which causes deep traps, are previously confirmed by the XPS results, discussed in Section 4.2.1. A log-log plot of room temperature  $J$ - $V$  data, as shown in inset of Fig. 4.10(a), indicates a power law behavior of  $J$ - $V$  characteristics i.e.  $J \sim V^\alpha$ , with a crossover in exponent ( $\alpha$ ) from 1 to 2 at a bias of  $\sim 20$  V. This indicates that charge transport is ohmic in the bias range 0-20 V, and at higher bias the transport mechanism changes to shallow trap mediated SCLC as described by eq. 1.29. In case of SCLC mechanism with shallow traps, linear dependence of  $J$  on  $d^3$  has been predicted. Therefore, we had made measurements on a single film with different spacing between electrodes ( $d = 12, 15$  and  $20 \mu\text{m}$ ) and the results shown in of Fig. 4. 10(b) confirms the validity of SCLC mechanism. Using slope of  $J$ - $V^2$  plots and assuming literature value of  $\epsilon_0\epsilon_r$  ( $2.43 \times 10^{-11} \text{ F/m}$ ), value of mobility ( $\mu$ ) was determined to be  $0.98 \text{ cm}^2\text{V}^{-1}\text{s}^{-1}$ . Using this

value of  $\mu$ , we find the thermally generated hole concentration ( $n_0$ ) of  $9.6 \times 10^{18} \text{ m}^{-3}$  (at 300 K) from the Ohmic region. Here, we have assumed  $\theta = 1$  (as justified later). Values of different parameters calculated above are given in Table-4.2.

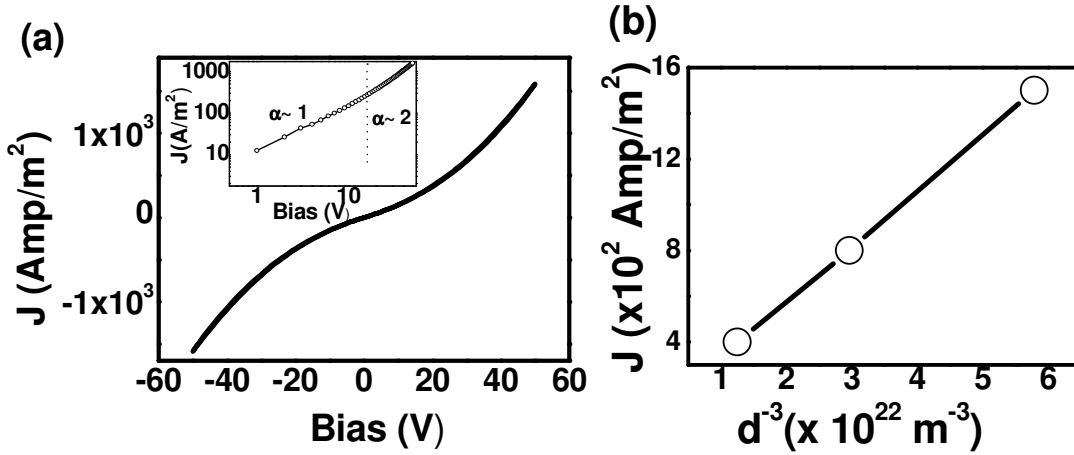


**Figure 4.10** (a) Room temperature  $J$ - $V$  characteristics recorded on CoPc films grown on sapphire substrate. The inset shows same data in log-log scale. (b) Linear variation of current density with  $d^{-3}$  confirming the SCLC.

In order to estimate the concentration of shallow traps, we have measured  $J$ - $V$  characteristics for CoPc films on sapphire substrates at lower temperatures and results for temperatures in 300-75 K range are shown in Fig. 4.11(a). It is seen that the  $J$ - $V$  characteristics are non-hysteretic even at low temperatures though the value of  $J$  decreases significantly. In Fig. 4.11(b), we plot the data's of Fig. 5.11(a) in log-log scale. It is seen that  $J$ - $V$  characteristics at different temperatures converge to  $V_c = 460$  V, indicating that the current is temperature independent (for  $V = V_c$ ) and the activation energy is zero. The voltage  $V_c$  is related to trap density  $N_t$  by equation:  $V_c = qN_t d^2 / 2\epsilon_0 \epsilon_r$  [131]. Using this equation, we obtain  $N_t = 9.8 \times 10^{20} / \text{m}^3$ . The trap characteristic temperature  $T_t$  can be determined using exponent of  $J$ - $V$  characteristics ( $\alpha = l+1$ ) determined at different temperatures from data of

Fig. 4.11(b). A plot of  $\alpha$  versus  $1/T$  is shown in the inset of Fig. 4.11(a). Using  $\alpha = l + 1 = T/T_i + 1$ , the slope of the curve gives the value of  $T_i$  ( $\sim 236$  K). A transition from trap free SCLC regime at room temperature to exponentially distributed trap controlled SCLC at low temperature can occur due to free carrier density at room temperature being higher than the trapped carrier density. However, as the temperature is reduced the free carrier density is reduced and the trapped carrier density increases, resulting in exponentially distributed trap controlled SCLC characteristics.

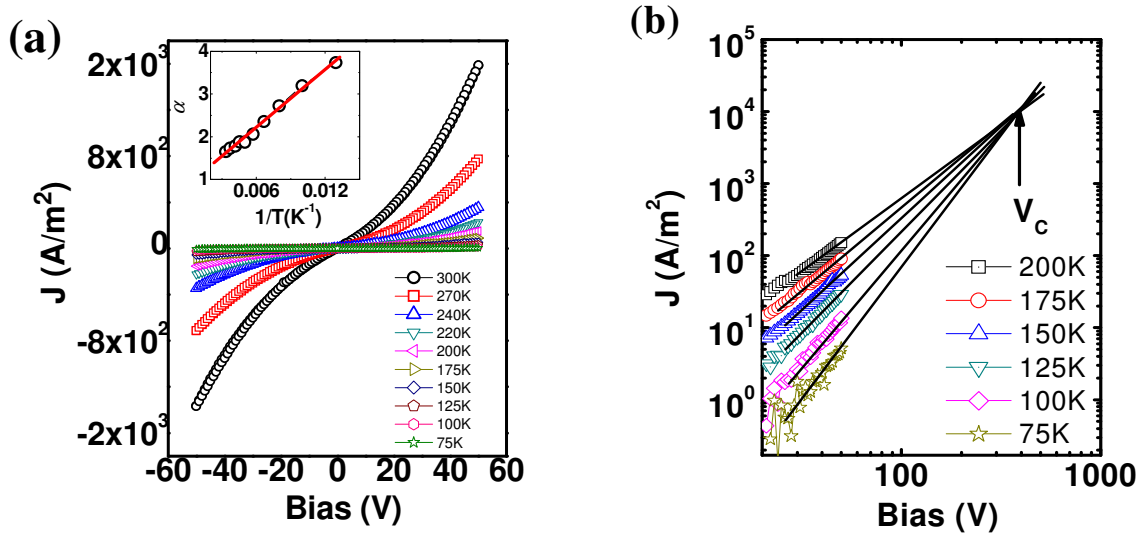


**Figure 4.11** (a) Temperature dependence of  $J$ - $V$  characteristics for films on sapphire substrate. Inset shows the temperature dependence of exponent ( $\alpha$ ,  $J \sim V^\alpha$ ) (b) Power law fit of data of Fig. 4.11 (a). The fits meet at cross over voltage  $V_c = 460$  V.

#### 4.5.2 Electric field & carrier distribution

We can estimate the injected carrier concentration  $n_{inj}$  as well as show field independent mobility (assumed in above analysis on sapphire substrate) using the approach of Wu et. al. [132]. Under SCLC conditions, the  $J$ - $V$  characteristics can be described by two following equation:

$$J = n_{inj}(x)e\mu[E(x)]E(x) \quad 4.1$$

$$\frac{\varepsilon}{e} \frac{dE(x)}{dx} = n_{inj}(x) \quad 4.2$$

Where  $n_{inj}$  is the space charge density at position  $x$  which are injected from the electrode.  $\mu[E(x)]$  is carrier mobility and implicit function of  $x$  through electric field  $E(x)$ . We define a function  $g = g(E)$  satisfying  $\mu(E)E = dg(E)/dE$  with  $g(0) = 0$ . For an ohmic contact at  $x = 0$  and  $E=0$  (at  $x = 0$ ) we obtain:

$$\frac{J}{\varepsilon}x = g(E) \text{ or } E = g^{-1}\left(\frac{J}{\varepsilon}x\right) \quad 4.3$$

Where  $g^{-1}$  is the inverse function of  $g$ . We define another function  $F = F(y)$  such that  $dF/dy = g^{-1}(y)$  and integration of Eq. 4.3 with respect to  $x$  from  $x = 0$  (injecting electrode) to  $x = d$  (collecting electrode) gives:

$$\frac{VJ}{\varepsilon} = \left[ F\left(\frac{dJ}{\varepsilon}\right) - F(0) \right] \quad 4.4$$

Taking derivative of Eq. (8) with respect to  $J$ , we get:

$$g\left(\frac{V}{d} + \frac{J}{d} \frac{dV}{dJ}\right) = \frac{dJ}{\varepsilon} \quad 4.5$$

Using Eq. 4.5 and experimental  $J$ - $V$  characteristics, one can calculate the  $g$  as a function of  $E$ . For a fixed value of  $J$ , we can also find (from Eq. 4.3) the  $g(E)$  for different  $x$ . By comparing these two data set for  $g(E)$ , we can find out  $E$  as a function of  $x$ . The  $n_{inj}(x)$  can be calculated using Eq. 4.2. Mobility ( $\mu$ ) as function of  $E$  can be determined using:

$$\mu = \frac{1}{E} \frac{dg(E)}{dE} \quad 4.6$$

The room temperature  $J$ - $V$  characteristic, shown in Fig. 4.10 (a), was used to calculate the  $g(E)$  function using to eq. 4.5. From the calculated  $g(E)$  function the we have determined

mobility for the CoPc films at room temperature using eq. 4.6 and shown in Fig. 4.12 (b). It can be seen from the Fig. 4.12 (b), the mobility is field independent and very closely matches with earlier derived SCLC mobility assuming  $\theta$  as 1. The field independent mobility confirms application of SCLC model to data on sapphire. Further, the electric field distribution is calculated at  $1.5 \times 10^3$  Amp/m<sup>2</sup> current density and shown in the Fig. 4.12 (a). It is seen from the figure that the electric field follow a power law,  $E \propto x^\alpha$  with  $\alpha = 0.5$ . The distribution of carrier density is also calculated from the electric field distribution using eq. 4.2 and shown in the inset of Fig. 4.12 (a). It is evident from the figure that a space charge is formed in the vicinity of the injecting electrode and the injected carrier density is significantly larger than thermally generated carrier density (Table-4.2).

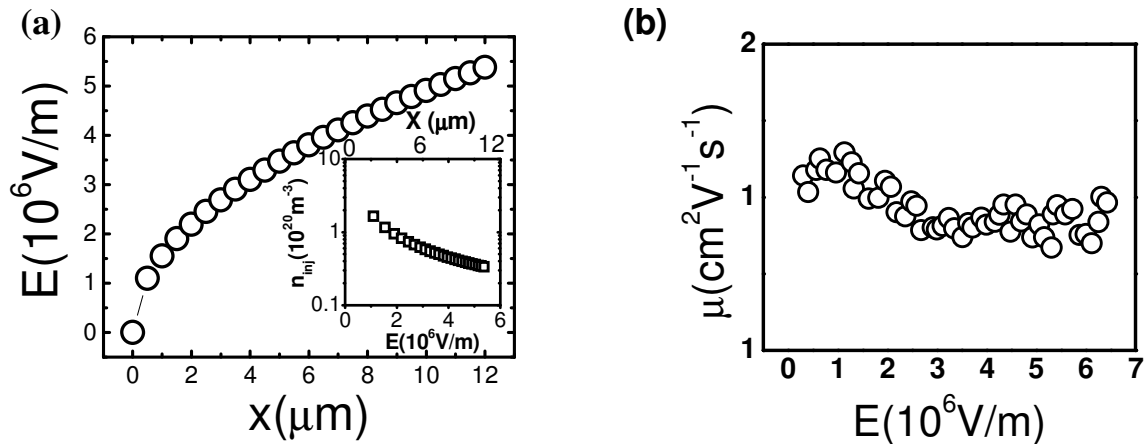


**Figure 4.12** (a) Spatial distribution of the electric field  $E$  at bias voltage of 50 V, inset shows the injected hole concentration  $n_{inj}$  (at bias of 50 V) as a function of field and distance. (b) Field dependence of mobility for the CoPc films on (0001) sapphire substrates.

#### 4.5.3 Mobility measurement by transient voltage pulse method

The mobility of the polycrystalline CoPc films on sapphire were further measured by transient voltage pulse method as described in Chapter 2. For this purpose a square voltage

pulse, with pulse rise time of 50 ns and pulse width 100  $\mu\text{s}$ , were used to cycle the two terminal devices prepared on sapphire substrate. A typical input and output signal are shown in Fig. 4.13. The transit time of fastest charge carrier was found to be 12 ns for a channel width of 12  $\mu\text{m}$  device. The calculated mobility for this device, using eq. 2.4, is  $1.2 \text{ cm}^2\text{V}^{-1}\text{s}^{-1}$ . This value is in agreement with the value calculated from SCLC.

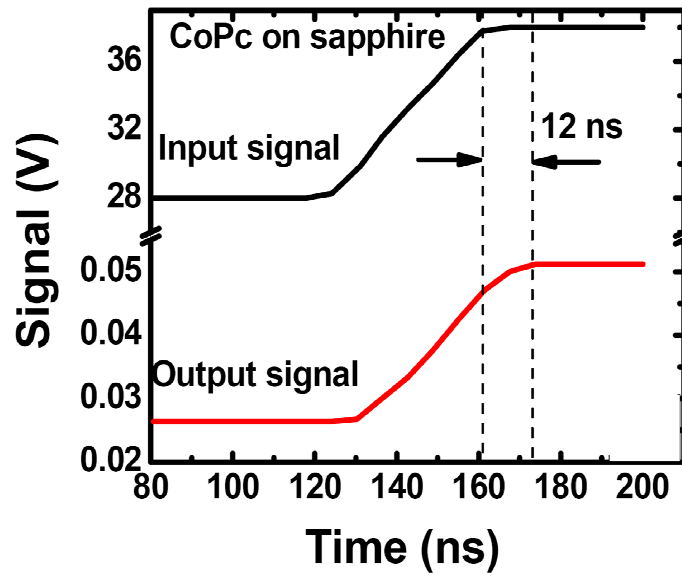


**Figure 4.13** The input and output signal transient voltage pulse data recorded for CoPc film on sapphire.

**Table 4.2** Different parameters calculated from temperature dependent  $J$ - $V$  characteristics of CoPc films grown on glass and (0001) sapphire substrate.

| Films          | $n_0$ ( $\text{m}^{-3}$ ) | $T_i$ (K) | $N_t$ ( $\text{m}^{-3}$ ) | $P_0$ ( $\text{eV}^{-1}\text{m}^{-3}$ ) | $\mu$ ( $\text{cm}^2\text{V}^{-1}\text{s}^{-1}$ ) |
|----------------|---------------------------|-----------|---------------------------|---|---|
| Glass          | $2.5 \times 10^{18}$      | 600       | $4.5 \times 10^{21}$      | $8.7 \times 10^{24}$                    | 0.45  |
| (0001)Sapphire | $9.6 \times 10^{18}$      | 236       | $9.8 \times 10^{20}$      | $1.9 \times 10^{22}$                    | 0.98  |

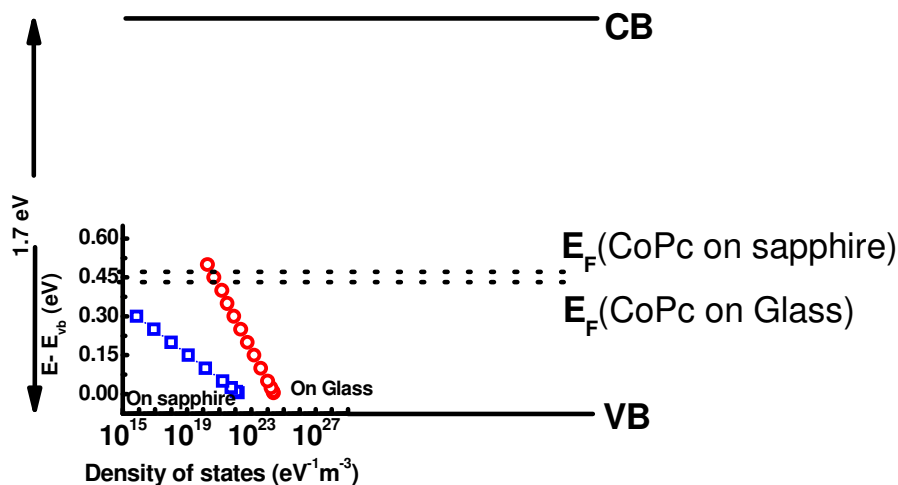


**Figure 4.14** Fermi level positions with respect to the valence band and trap distributions are shown for the CoPc films grown in glass and sapphire.

#### 4.6 Trap distribution in polycrystalline CoPc films grown on glass and sapphire

In this section we describe the trap distribution poly polycrystalline CoPc films grown on sapphire and glass. The value of Fermi energy  $E_F$  (at room temperature) for both the films are determined [using eq. 1.21] from free carrier density ( $n_0$ ), as seen in Table-4.2 and literature value of effective density of states in valence band  $N_c = 10^{27} \text{ m}^{-3}$ . The relative positions of Fermi energy at room temperature are shown the Fig. 4.14 considering valence band as zero. We have also calculated the distribution of traps for both the films assuming an exponential distribution according to eq. 1.25. The trap distributions are also shown in the Fig. 4.14. It is seen that the trap distribution in the films grown on sapphire is sharper than the trap distribution in films grown on glass. This means the higher no of deep traps in the films grown on glass. It is seen that at the energy 0.15 eV the trap density of the films grown on sapphire is  $1 \times 10^{19} \text{ eV}^{-1} \text{ m}^{-3}$  and at this energy the probability of occupancy by hole is

calculated (using Fermi-Dirac distribution) to be  $10^{-3}$ . Thus total trapped carrier density is of the order of  $10^{16} \text{ m}^{-3}$  which very less compared to the free carrier density ( $9.6 \times 10^{19} \text{ m}^{-3}$ ). This justifies the assumption of  $\theta = 1$  at room temperature. On the other hand, it is seen from the Fig. 4.14 that the trapped carrier density is very high ( $\sim 10^{20} \text{ m}^{-3}$ ) in CoPc films grown on glass as compared to the free carrier density ( $2.5 \times 10^{18} \text{ m}^{-3}$ ).

## 4.7 Conclusions

We studied the temperature dependent  $J$ - $V$  characteristics and conductivity of amorphous and polycrystalline FePc/CoPc films grown on glass and sapphire substrates. The main conclusions drawn are as follows:

- (i) XPS and conductivity measurements show that ambient oxygen is gets chemisorbed and physisorbed at MPc films, which create deep or shallow traps.
- (ii) The hysteresis in the  $J$ - $V$  characteristics of amorphous FePc films grown on glass substrate is induced by the deep traps created by the chemisorptions of oxygen. Due to the high value of trap density ( $1.03 \times 10^{23} \text{ m}^{-3}$ ) and low mobility ( $0.2 \text{ cm}^2 \text{ V}^{-1} \text{ s}^{-1}$ ) it is difficult to measure the transport properties below 200K.
- (iii) In the polycrystalline FePc/CoPc films grown on glass, the density of deep traps ( $\sim 4 \times 10^{21} \text{ m}^{-3}$ ) is less compared to the amorphous films. The charge transport is governed by SCLC with exponential distribution of deep traps in the temperature range 300 to 220K. Due to lesser trap density the charge transport measurement down to 150K is possible. In the low temperature the transport is govern by Poole Frankel mechanism.

- (iv) Due to the absence of deep traps and relatively high mobility ( $0.98 \text{ cm}^2\text{V}^{-1}\text{s}^{-1}$ ) the charge transport in Polycrystalline CoPc films grown on sapphire substrate can be measured down to 75 K. The charge transport can be describe in whole temperature range by shallow trap limited SCLC.

---

# Charge transport in highly ordered films

---

5.1 Introduction

5.2 Charge transport in CoPc films grown on twined (001) LaAlO<sub>3</sub>

*5.2.1 Charge transport in CoPc films grown along twin boundaries of (001)*

*LaAlO<sub>3</sub>*

*5.2.1.1 Charge transport in the high temperature range, 300 -100K  
(Regions I & II)*

*5.2.1.2 Charge transport below 100K (Regions III & IV)*

*5.2.2 Charge transport in CoPc films grown across twin boundaries of (001)*

*LaAlO<sub>3</sub>*

5.3 Charge transport in CoPc films grown on bi-crystal (001) SrTiO<sub>3</sub>

*5.3.1 Charge transport in CoPc films grown along the bi-crystal boundary*

*5.3.2 Charge transport in CoPc films grown on single crystalline region*

5.4 Conclusions

## 5.1 Introduction

In this chapter we discuss charge transport properties of ordered CoPc films deposited on twined (001) LaAlO<sub>3</sub> substrate as well as those grown along the 36.8° bi-crystal boundary (001) SrTiO<sub>3</sub> substrates. We have analyzed the bias dependent  $J$ - $V$  characteristics of these films in the temperature range 300-25 K. The obtained results are discussed in the following sections.

## 5.2 Charge transport in CoPc films grown on twined (001) LaAlO<sub>3</sub>

It has been shown in the Chapter 3 that highly ordered films of CoPc are grown on twined (001) LaAlO<sub>3</sub> when film thickness is around 20 nm, whereas at higher thickness (e. g. 100 nm) due to weakening of substrate-molecule interaction the ordering of molecules decreases. These twin boundaries act as a template for the edge-on stacking of the molecules. This conjecture, however, could not be verified by XRD or AFM. In order to examine this, we have deposited pairs of Au electrodes (separated by 7  $\mu$ m) onto CoPc films, as schematically shown in Fig. 5.1(a), in such a way that the  $J$ - $V$  characteristics are measured for:

- (i) CoPc films along the twin boundaries, and
- (ii) CoPc films across the twin boundary.

Typical room temperature  $J$ - $V$  characteristics measured in these two configurations are shown in the Fig. 5.1 (b). It is seen that current density for CoPc films along the twined boundaries is higher by four orders of magnitude higher as compared to that measured across the twin boundaries. This clearly indicates that the CoPc molecules are better ordered along the twin boundary of LaAlO<sub>3</sub>. To gain further insight of charge transport mechanisms

we have measured temperature dependent  $J$ - $V$  characteristics in both the configurations. The results are discussed in the following sections.

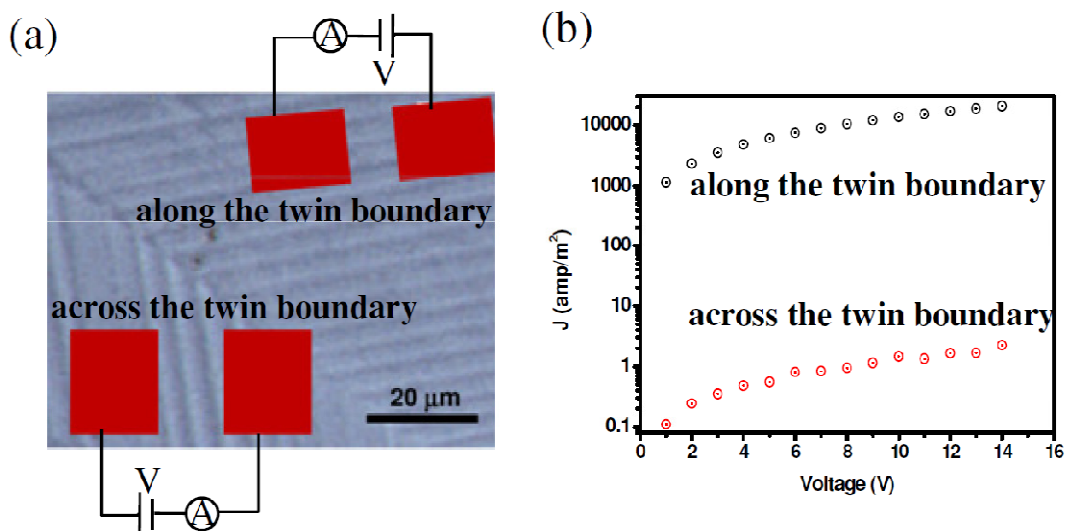


**Figure 5.1** (a) Schematic of two charge transport measurement geometries (i.e. along and across the twin boundaries) on 20 nm CoPc thin film grown on twined (001) LaAlO<sub>3</sub>. (b) Room temperature  $J$ - $V$  characteristics measured for CoPc film along (black data) and across (red data) the twin boundaries.

### 5.2.1 Charge transport in CoPc films grown along twin boundaries of (001) LaAlO<sub>3</sub>

Typical  $J$ - $V$  characteristics recorded for 20 nm CoPc films grown along the twin boundaries on LaAlO<sub>3</sub> are shown in Fig. 5.2. The results indicate that variation of current density depends on both applied bias as well as the temperature. Unlike disordered films, as discussed in Chapter- 4, no hysteresis is observed in the present case. Based on the nature of current dependence on bias and temperature, four distinct regions (marked as I to IV) have been identified. Broadly, regions I and II belong to the temperature region of 300-100 K, whereas regions III and IV lie in the temperature zone below 100 K. The analyses of these regions are described below.

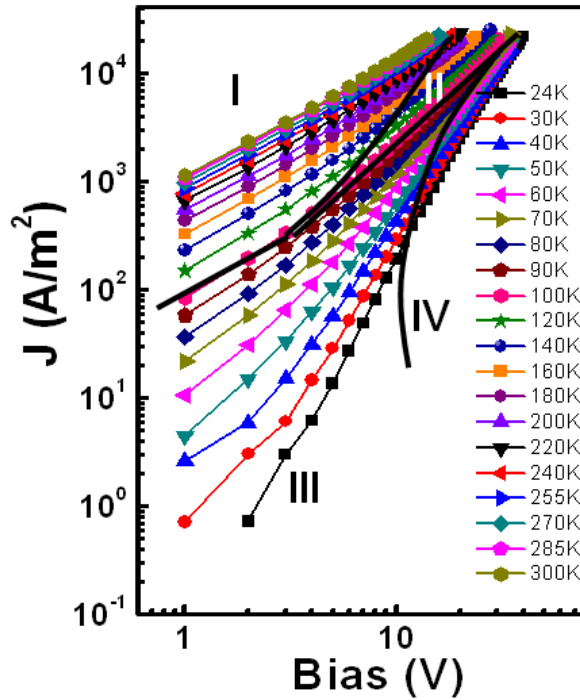


**Figure 5.2** Log-log plots showing current-voltage characteristics of 20 nm CoPc films at different temperatures. Due to different dependence of the current on applied bias or temperature, four regions (I, II, III, IV) have been identified.

### 5.2.1.1 Charge transport in the high temperature range, 300 -100K (Regions I & II)

As seen from Fig. 5.2, for temperature range 300-180 K, the current density varies linearly in the whole measured bias range, indicating Ohmic conduction. For temperature range 180-100 K, as shown in Fig. 5.3, a transition from region I to region II takes place as a function of applied bias. In the region I, the slope of the linear fit to the data is one, indicating an Ohmic conduction. In molecular semiconductors, an ohmic conduction normally occurs if the thermally generated carriers exceed that of injected carriers through the electrode, and the  $J$  in this case is given by eq. 1.14. However, the value of  $J$ - $V$  slope in region II is  $\sim 2$ , indicating that the charge transport is via trap-free space-charge limited characteristics (SCLC). As discussed in Chapter -1 the SCLC occurs if the injected carrier density is higher

than the thermally generated carrier density and current density is given by eq. 1.19. The values of density of free carrier ( $n_0$ ) is determined from the crossover voltage ( $V_X$ ), as shown in Fig. 5.3 , using the relationship:  $V_X = 8n_0eL^2/9\epsilon$ . The estimated value of  $n_0$  is  $1 \times 10^{20} \text{ m}^{-3}$ , which is in accordance with reported literature [28].

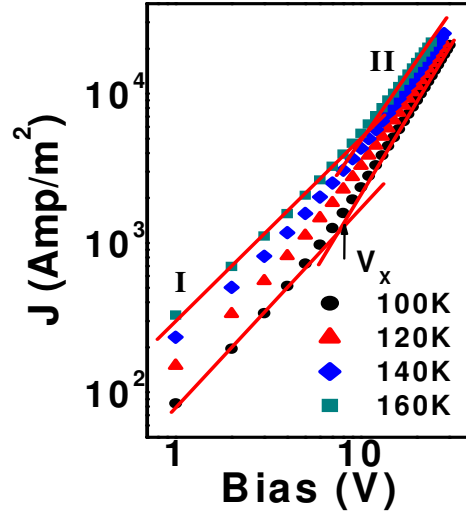


**Figure 5.3** Log-log plots of current-voltage characteristics in the temperature range 160-100K. A transition of slopes of the linear fit to data from 1 to 2 is clearly observed.  $V_X$  is the crossover bias.

The  $\mu$  values at different temperatures were calculated by least square fitting of  $J$ - $V$  data in region two II with eq. 1.19. Here we have used the permittivity for our film as  $2.75 \times 10^{-11} \text{ F/m}$ . The permittivity of our films is experimentally determined by measuring capacitance of the films. The temperature dependence of  $\mu$  is plotted in Fig. 5.4 (a), which is found to obey the Arrhenius behavior ( $\ln \mu \sim 1/T$ ). Since in the temperature range 300-220 K, we have only Ohmic region in the entire bias, the value of  $\mu$  at 300K was obtained by extrapolation, and is found to be  $\sim 7 \text{ cm}^2\text{V}^{-1}\text{s}^{-1}$ , which is nearly two orders higher in magnitude as compared to that reported for disordered films [133, 134]. Here it is worth commenting on the observed Arrhenius behavior of  $\mu$ . It may be noted that for molecular

single crystals,  $\mu$  decreases with increasing temperature ( $\mu \sim 1/T^n$ , with  $n = 1.5-2.7$ ), which is typical of band transport and originates from enhanced scattering process by lattice phonons [69]. Clearly, our highly crystalline films do not exhibit this behavior. On the other hand, theoretical charge transport models developed for disordered organic semiconductors predict non-Arrhenius temperature dependence for the mobility i.e.  $\mu(T) = \mu_0 \exp\{-(2\sigma/3kT)^2\}$ , where  $\sigma$  is standard deviation of the disorder distribution [135]. It is clear from the Fig. 5.4 (b) that our films also do not fall under the category of the highly disordered molecular semiconductor. In fact, for molecular semiconductor Arrhenius-like dependence of mobility has been predicted using polaron effective mass approach, which considers intermediate electron-phonon interactions [69]. The temperature dependence of mobility in this is given by:

$$\mu(T) = \mu_0 \exp(-E_{pol}/2kT) \quad (5.1)$$

where  $E_{pol}$  is the polaron binding energy [69]. By least square fitting of temperature dependent mobility data, shown in Fig. 5.4 (a), with eq. 5.1 we have estimated the value of  $E_{pol}$  equal to 30 meV, which is in agreement with reported literature [136]. Further, a recent analyses show that non-Arrhenius dependence ( $\ln \mu \sim 1/T^2$ ) provides a more consisting description of charge transport if the electrode/film contact is blocking in nature [137]. However, if the contact is Ohmic in nature, then in order to align the Fermi level charge carriers diffuse from Ohmic contact to the film and it was demonstrated that presence of extrinsic charge carriers in the film modifies the transport to Arrhenius-like ( $\ln \mu \sim 1/T$ ) [137]. Due to ohmic character of Au/CoPc interface in the temperature range 300-100 K, the Arrhenius-like behavior is consistence with this model.

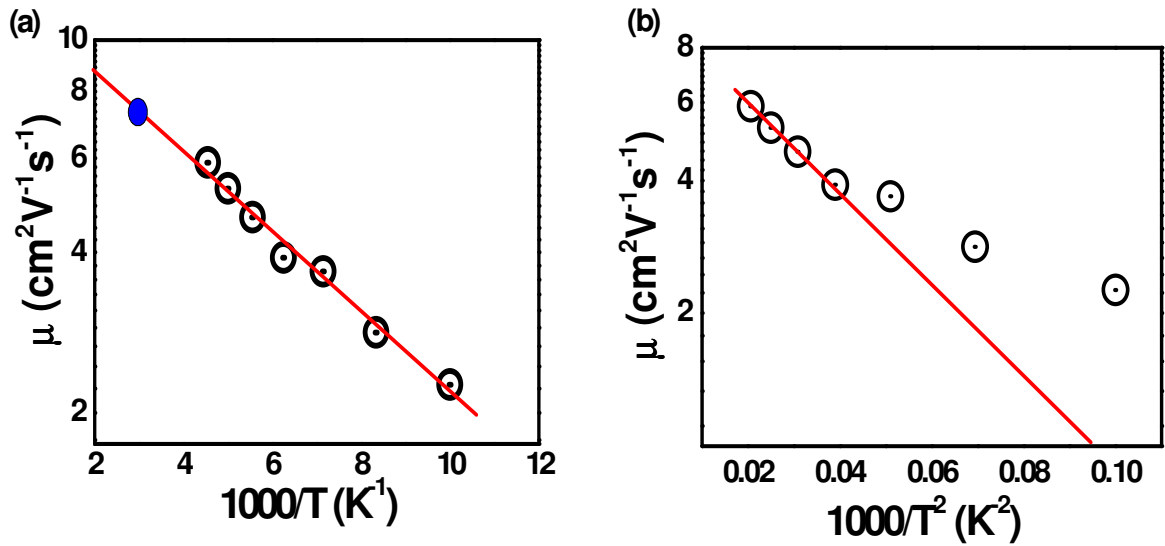


**Figure 5.4** (a) Arrhenius plot of mobility determined from the SCLC data in region II. (b) Mobility ( $\mu$ ) vs  $1/T^2$  plot showing inapplicability of disorder model.

### 5.2.1.2 Charge transport below 100K (Regions III & IV)

As shown in Fig. 5.2, for temperatures  $<100\text{K}$ , the  $J$ - $V$  characteristics show very different behaviors in the regions III and IV. In region III i.e. at low bias, the current drops sharply with lowering temperature, whereas in region IV i.e. at very high bias, the current show a very weak dependence on temperature. These data, as we analyze below, indicate that the electrode-limited processes govern the charge transport at low temperatures. In region III, the linear fit of data plotted as  $J$  vs  $V^{1/2}$  in the semi-log scale, see Fig. 5.5 (a), indicates that the charge transport is governed by Schottky model [28]: where current is given by eq. 1.13. For Au/CoPc interface, the obtained values of  $\beta_S$  and  $\phi$  are respectively,  $1.8 \times 10^{-5} \text{ eVm}^{1/2}\text{V}^{-1/2}$  and  $\sim 0.2 \text{ eV}$ . The experimentally determined value of  $\beta_S$  is close to its theoretical value ( $2 \times 10^{-5} \text{ eVm}^{1/2}\text{V}^{-1/2}$ ), which supports Schottky barrier limited conduction mechanism in region III [28]. A smaller value of  $\phi$  (0.2 eV) as compared to 0.8 eV measured

experimentally using UPS [138, 139], supports earlier results of inverse photoemission spectroscopy that Au Fermi level pins at the energy gap of Pc's [140].

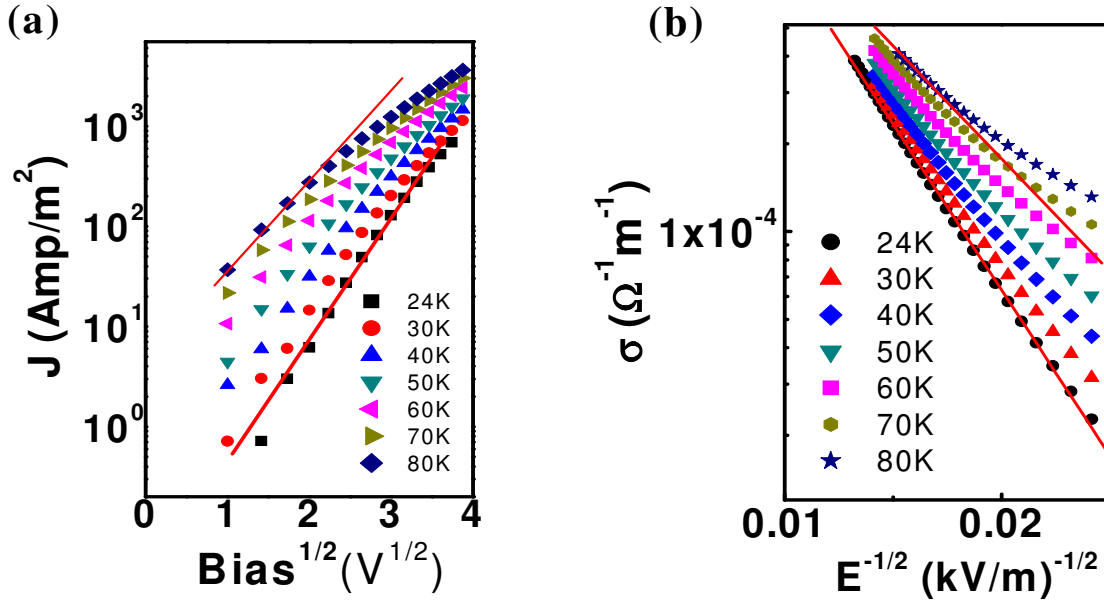


**Figure 5.5** (a) For temperature in the 80-24 K range and at low bias,  $\ln J$  varies as  $V^{1/2}$ , indicating a Schottky barrier limited conduction. (b) For temperature in the 80-24 K range and at higher bias, conductivity varying exponentially on the inverse of the square-root of electric field, indicating the transport is governed by multistep tunneling.

A weak temperature dependence of current in the region IV indicates possibility of tunneling mechanism [141]. It has already been discussed in Chapter -1 that if localized states are present in the gap then these states assist sequential tunneling of the charge carries from the Fermi level of the electrode to the conduction level of film and, this process is known as multi-step tunneling (MUST) [44, 142]. It has been shown that MUST is observed only in high  $\mu$  devices and this mechanism leads to an inverse square-root field dependence

of conductivity [142, 143] i.e.  $\sigma \propto \exp\left(-\sqrt{\frac{E_0}{E}}\right)$ , where  $E_0 = \frac{16\sqrt{2m\alpha\phi}^{3/2}}{3e\hbar}$ .  $E_0$  is related to

the material through the potential barrier ( $\phi$ ) and a parameter  $\alpha$  given by  $\alpha = \ln(p^{-1})$ , where  $p^N$  is the probability of forming a N-step tunneling path. As shown in Fig. 5.5 (b), in region IV the conductivity varies as the inverse square-root of the field, confirming the MUST mechanism. We have obtained the value of  $E_0$  as 800 kV/cm by least square fitting of data at 24 K. Using  $\phi = 0.2$  eV and  $p = 0.95$ , the theoretically calculated value of  $E_0$  is 780 kV/cm, which is consistent with experimentally observed value. MUST mechanism has experimentally been reported in organic field effect transistors and organic light emitting diodes [44, 142, 143]. The experimentally observed  $E_0$  value in these cases was  $\sim 6400$  kV/cm. A higher  $E_0$  value in these cases is due to higher value of interface barrier ( $\phi = 0.5$  eV).

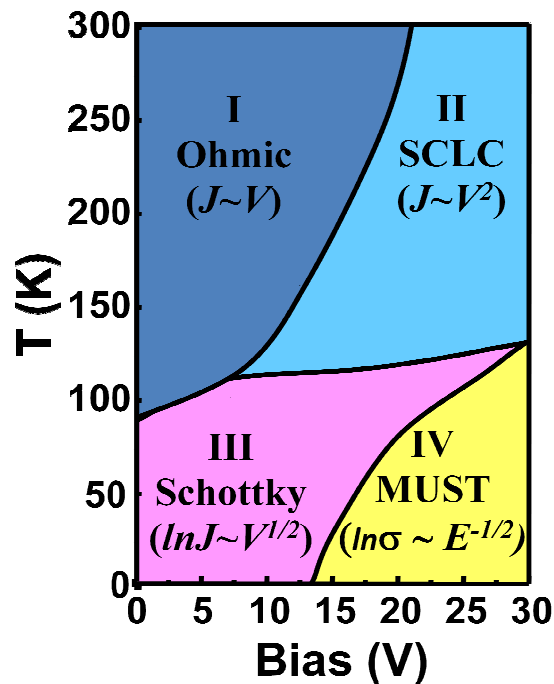


**Figure 5.6** A temperature-bias plane summarizing the various conduction mechanisms in high mobility CoPc films.

Based on the above discussed charge transport mechanism we have proposed a new temperature bias phase diagram, which is schematically depicted in Fig. 5.6. This phase diagram describes the charge transport mechanisms in CoPc films on LaAlO<sub>3</sub> at the different temperature and bias range. It is clear from the Fig. 5.6 that at higher temperature (>100K) the charge conduction is mainly dominated by the bulk. In the bulk limited process we see a transition from Ohmic to SCLC depending on the applied bias. In other word, Ohmic to SCLC occurs when injected carrier suppress the thermally generated carrier. On the other hand at low temperature (< 100K) the transport is controlled by the electrode. At low temperature and low bias the charge transport is dominated by Schottky mechanism whereas at high bias we see a sequential tunneling of charge carrier from electrode to transport level of CoPc via some localized states.

### **5.2.2 Charge transport in CoPc films grown across twin boundaries of (001) LaAlO<sub>3</sub>**

In the previous section we have studied charge transport of high mobility CoPc films along the twin boundaries of (001) LaAlO<sub>3</sub>. It has been shown that the high mobility is due to the ordering of CoPc molecule along the twin boundaries. To further prove this conjecture we have measured the charge transport of CoPc films grown across the twin boundaries, as shown schematically in Fig. 5.1(a). Typical temperature dependent *J-V* characteristics measured across the ordered direction are shown in Fig. 5.7. In this configuration also low bias charge transport can be described by Ohmic mechanism as confirmed from the linear variation of current density with voltage. At higher voltages current density follow power law and the power varies inversely proportional to temperature as shown in the inset of Fig. 5.7. This behavior is in accordance with the description of space charge limited conduction with

exponentially distributed traps and current density is given by eq. 1.32. In this model current density ( $J$ ) follow power law with exponent  $\alpha (= l+1)$  where  $l$  is the ratio of  $T_t/T$ , where  $T$  is the absolute temperature and  $T_t$  is the temperature characterizing the trap distribution. This process is thermally activated process and hence all the  $J$ - $V$  characteristics will merge at a common voltage where the current will be temperature independent and the voltage ( $V_c$ ) is given by  $V_c = N_t e d^2 / 2\epsilon$  [131], where  $N_t$  is the total trap density,  $e$  is electronic charge and  $\epsilon$  is the permittivity. The calculated trap density is  $2 \times 10^{21} \text{ m}^{-3}$  using  $V_c = 480 \text{ V}$  (calculated from Fig. 5.7). So we propose that between two ordered regions there are structurally disordered region which act as charge traps, and hence, limits the current. Due to the disorders and traps it is difficult to get any measurable current below the temperature 240K, and this situation is analogous to the amorphous films grown on the glass substrates.

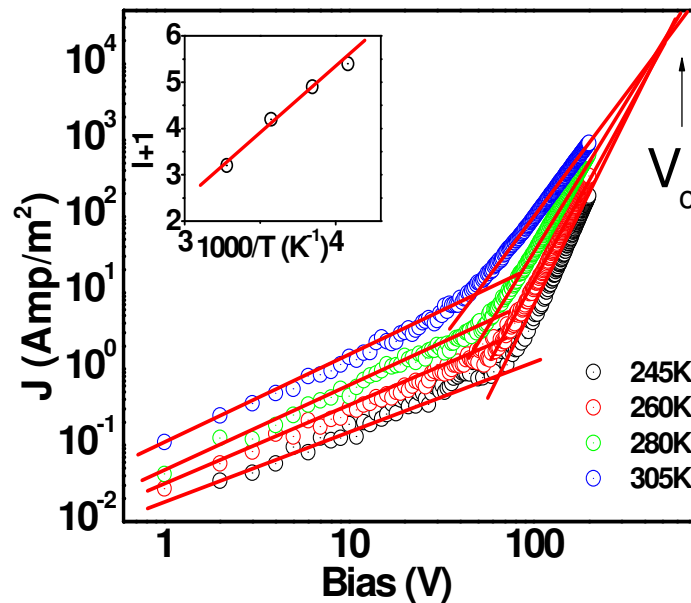


**Figure 5.7** A typical temperature dependent current density Vs bias of 20 nm CoPc films measured across the ordered direction. Inset shows inverse proportionality of slope of  $J$ - $V$  characteristics with temperature.

### 5.3 Charge transport in CoPc films grown on bi-crystal (001) SrTiO<sub>3</sub>

In the previous section we have demonstrated that the high mobility in CoPc films grown along the natural twin boundary of (001) LaAlO<sub>3</sub> is due to the ordering of CoPc molecule along the twin boundaries. Here we present results on the charge transport measurements carried out on the CoPc films grown along a single grain boundary, which is the 36.8° boundary of the (001) SrTiO<sub>3</sub> bicrystal substrate, as schematically shown in Fig. 5.8. In order to investigate the role of bicrystal boundary, charge transport properties of the CoPc films grown ‘along the boundary’ (ATB) and as well as that grown in ‘single crystalline region’ (SCR) on (001) SrTiO<sub>3</sub>, as shown in Fig. 5.8, were measured.

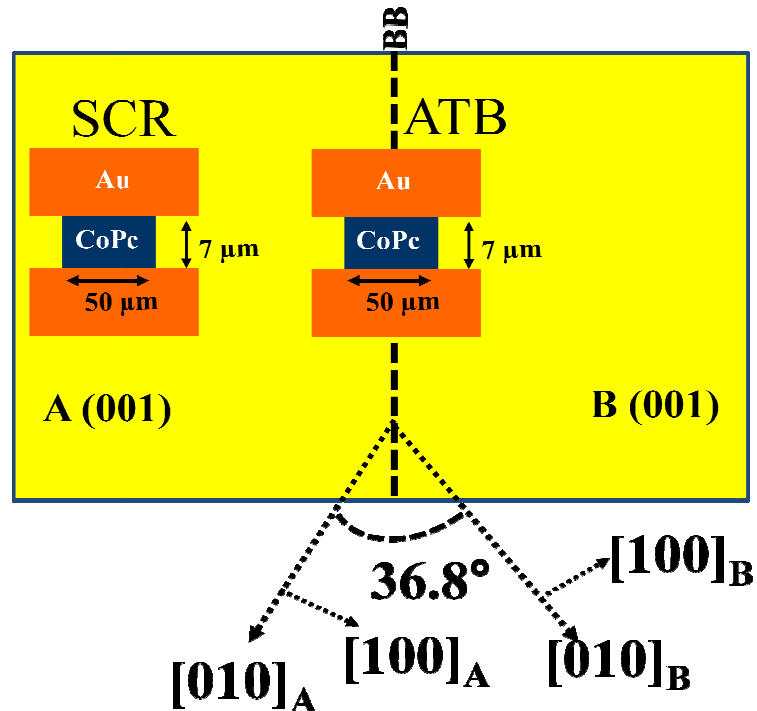


**Figure 5.8** A schematic of two charge transport measurement configuration. (i) Along the boundary (ATB) of the bi-crystal SrTiO<sub>3</sub>, (ii) Single crystalline region (SCR) of SrTiO<sub>3</sub>.

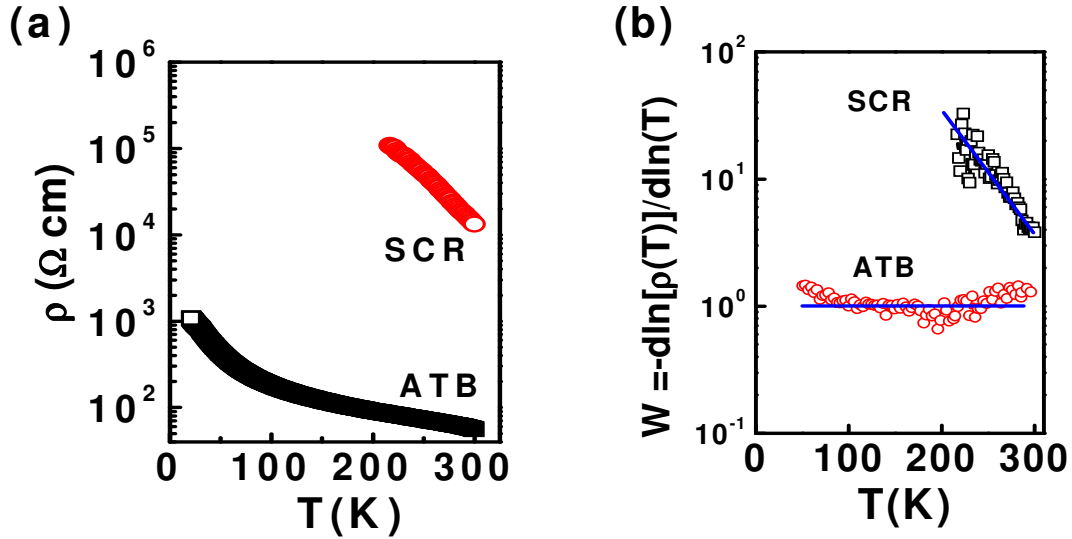


**Figure 5.9** (a) Temperature dependence of resistivity (plotted in log-log scale) of film deposited at bicrystal boundary (ATB) and single crystalline regions (SCR) (b) Plots of reduced activation energy  $W (= -d \ln[\rho(T)]/d \ln T)$  for ATB and SCR films.

We have measured the variation of resistivity ( $\rho$ ) as a function of temperature ( $T$ ) for ATB and SCR CoPc films and the results are shown in Fig.5.9 (a). It is seen that the value of  $\rho$  (300 K) for ATB film ( $50 \Omega \text{ cm}$ ) is lower by three orders in magnitude as compared to SCR films ( $1.08 \times 10^4 \Omega \text{ cm}$ ). In general, the  $\rho$  (at room temperature) increases as the disorder in the film increases. It has been well established that the disorder in the system creates charge localization, leading to a critical or insulating behavior. In fact an increase in  $\rho$  with decreasing temperature for both the films suggests their critical or insulating behavior, which in fact can be identified through Zhabrodkii plots i.e. temperature dependence of the reduced activation energy, described by [144]

$$W = -d \ln[\rho(T)]/d \ln T \quad (5.2)$$

Positive, zero and negative slopes of  $W$  versus  $T$  corresponds to the metallic, critical and insulating regimes, respectively [144]. Using temperature dependent resistivity data shown in

Fig. 5.9(a) the reduced activation energy ( $W$ ) is calculated using eq. 5.2 and the variation of  $W$  with  $T$  for both ATB and SCR films is plotted in Fig. 5.9(b). It is seen that for ATB film the value of  $W$  is  $\sim 1$  and is nearly independent of the temperature i.e. slope is zero, which indicates that they are in the critical regime. On the other hand, a negative slope of  $W$  versus  $T$  data for SCR films indicates the insulating regime (discussed in detail in the next section). In the following section we will present the results of charge transport measurement.

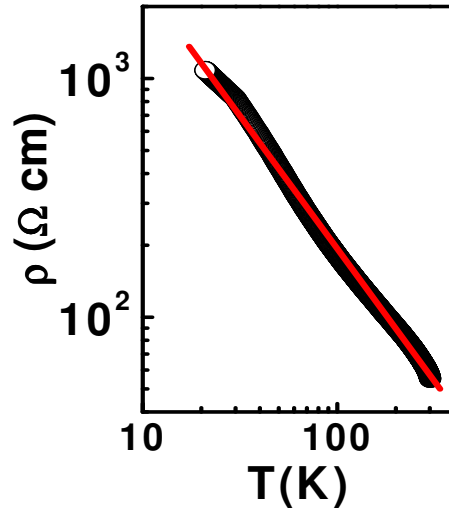


**Figure 5.10** Power law behavior of resistivity of the films deposited along bi-crystal boundary (ATB) indicating critical behavior.

### 5.3.1 Charge transport in CoPc films grown along the bi-crystal boundary

In the critical regime, the theory predicts that the resistivity should follow a power law i.e.

$$\rho(T) \propto T^{-\beta} \quad (5.3)$$

with  $\beta = W$ . Here  $\beta$  is a constant and the power law dependence is valid for  $0.3 < \beta < 1$  [144].

As shown in Fig.5.10, the log-log plot of  $\rho$  versus  $T$  shows a linear fit of the data for the ATB

films, indicating a power law behavior. The slope of the linear fit gives value of  $\beta$  equals to  $\sim 1$ , which is same as that of W. Thus the ATB films are in the critical regime. In ATB films the bicrystal boundary acts as a template and aligns the molecules in a preferred orientation. As a result, the disorder in the ATB films is decreased and exhibit critical behavior.

To further gain insight of the charge transport we have studied the temperature dependent  $J$ - $V$  characteristics for ATB films and are shown in Fig.5.11(a). In the temperature region of 300-170 K,  $J$ - $V$  characteristics are linear in the entire bias range, which are attributed to the ohmic conduction. For temperatures  $<170$  K, at low bias the conduction is ohmic, while for high bias the slope of  $J$ - $V$  characteristics changes to  $\sim 2$ , indicating that the charge transport is via trap-free SCLC and the current density is given by eq. 1.19. The  $\mu$  values at different temperatures were calculated from the slopes of  $J$ - $V^2$  plots and plotted in Fig. 5.11(b). A straight line fit of  $\ln \mu$  versus  $1/T$  data indicates that the temperature dependence of  $\mu$  obeys Arrhenius behavior and the temperature variation of mobility is given by eq. 5.1 [69]. From the slope of  $\ln \mu$  versus  $1/T$ , we estimated value of  $E_{pol}$  comes out to be 14 meV. It may be noted that the value of  $E_{pol}$  increases with amount of disorder in the film. For example, in polyparaphenylenevinylene derivatives with very low mobilities ( $<10^{-6} \text{ cm}^2 \text{ V}^{-1} \text{ s}^{-1}$ ),  $E_{pol}$  is estimated to be 0.3-0.5 eV [145]. A very low value of  $E_{pol}$  in the case of ATB film shows that these films are highly ordered. Since in the temperature range 300-170 K, we have only ohmic region in the entire bias range, the value of  $\mu$  at 300K was obtained by the extrapolation of data, which is found to be  $\sim 148 \text{ cm}^2 \text{ V}^{-1} \text{ s}^{-1}$ . This is the highest mobility reported for phthalocyanine thin films. The extreme high mobility also proves the ordering of CoPc molecule along the bi-crystal boundary.

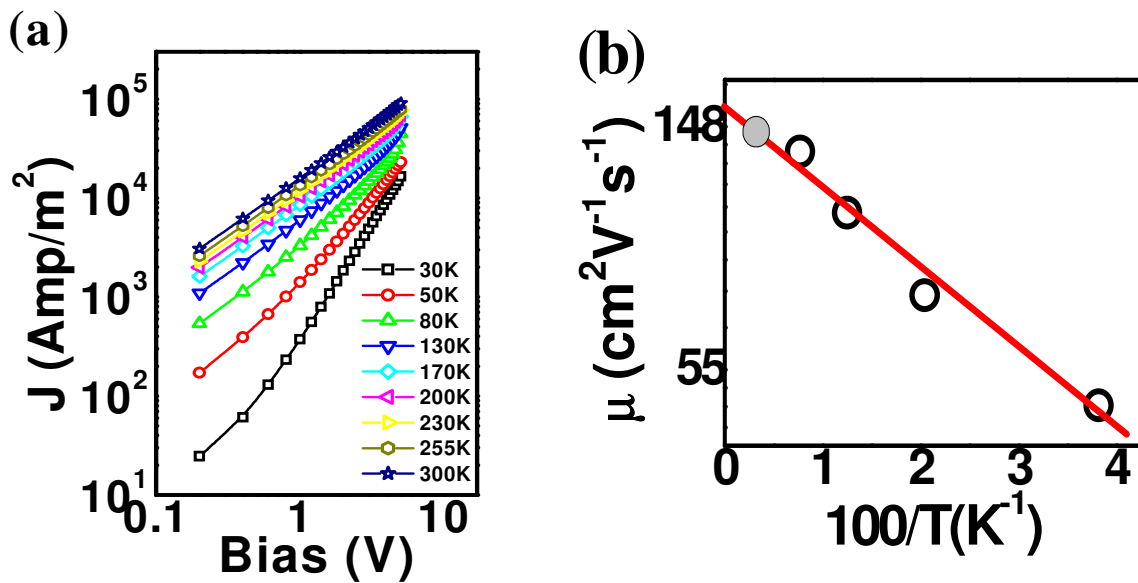


**Figure 5.11** (a) Log-log plots of  $J$ - $V$  characteristics in the temperature range 300-30K for ATB films. (b) Arrhenius plot of mobility determined from the slope of  $J$ - $V^2$  data in the temperature range of 170 K- 30K. Grey color filled circle shows the room temperature mobility value.

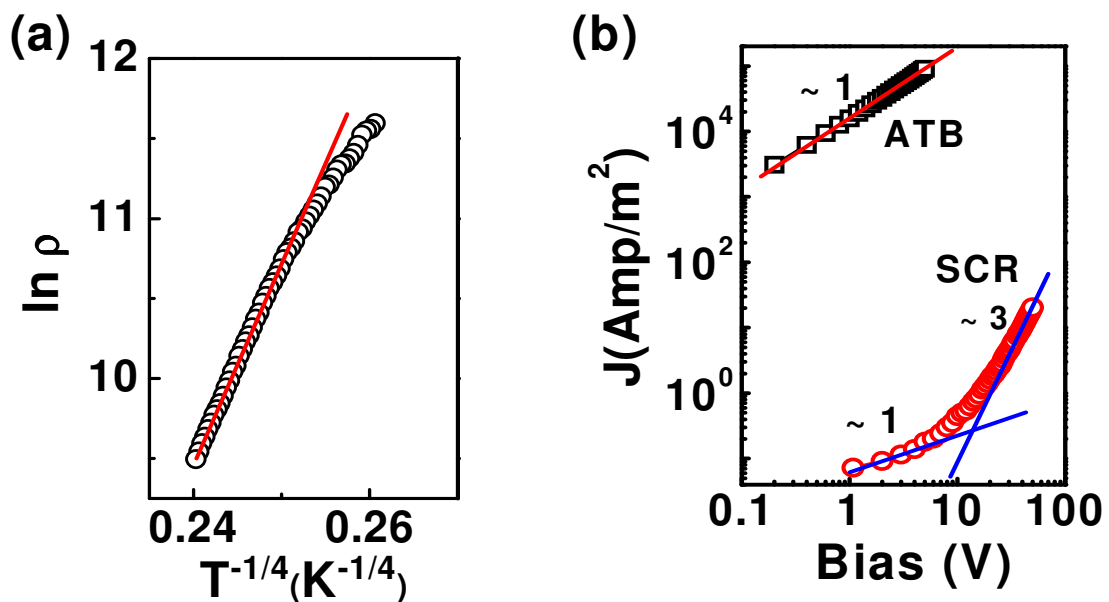


**Figure 5.12** (a) A linear fit of  $\ln \rho$  vs  $T^{-1/4}$  for SCR films indicating Mott 3D-VRH. (b) Log-log plots showing room temperature current-voltage ( $J$ - $V$ ) characteristics of ATB and SCR films.

### 5.3.2 Charge transport in CoPc films grown on single crystalline region

It has been shown in the previous section that the CoPc films, deposited on the single crystalline region (SCR), are in insulating regime. As discussed in Chapter-1 that in insulator, transport occurs through variable range hopping (VRH) among localized states and for Mott 3D-VRH conduction (non-interacting carriers), resistivity ( $\rho$ ) is given by eq. 1.37. For SCR films, a linear fit of  $\ln \rho$  vs  $T^{-1/4}$ , as shown in Fig. 5.12 (a), indicates charge transport is governed by 3-D VRH mechanism. These studies clearly demonstrate that the SCR films are highly disordered, and therefore, exhibit insulating behavior.

Further the role of disorder is clear from the  $J$ - $V$  (shown in Fig.5.12 (b)) measured at room temperature on SCR films. For the comparison we have plotted the  $J$ - $V$  characteristics of ATB film also. It is seen from the Fig. 5.12 (b) that the current density is four order less in SCR films as compared to the CoPc films along the boundary. The lower current is attributed to the traps present in the disorder CoPc films grown on single crystalline region. It is seen from the Fig. 5.12 (b) that the slope of  $J$ - $V$  characteristic of SCR films is  $\sim 1$  at voltage below 15V. This indicates that at low voltage transport is govern by ohmic process as expected. At further higher voltage ( $>15V$ ) the slope become 3, suggests the SCLC mechanism in the presence of traps, which are distributed exponentially in energy above the valence band edge and the current voltage can be described by eq. 1.32. To calculate the trap density, the temperature dependent  $J$ - $V$  characteristics were measured in the temperature range 300 – 200K and results are shown in Fig. 5.13. It is seen that  $J$ - $V$  characteristics at different temperatures converge to  $V_c = 205$  V, indicating that the current is temperature independent (for  $V = V_c$ ) and the activation energy is zero [131]. Using value of  $V_c$ , the trap density  $N_t$  is

found to be  $7.6 \times 10^{20} \text{ m}^{-3}$  using equation:  $V_c = qN_t d^2 / 2\epsilon$ . In the view of above discussion it further proves that the SCR films have poor structural order than the ATB films.

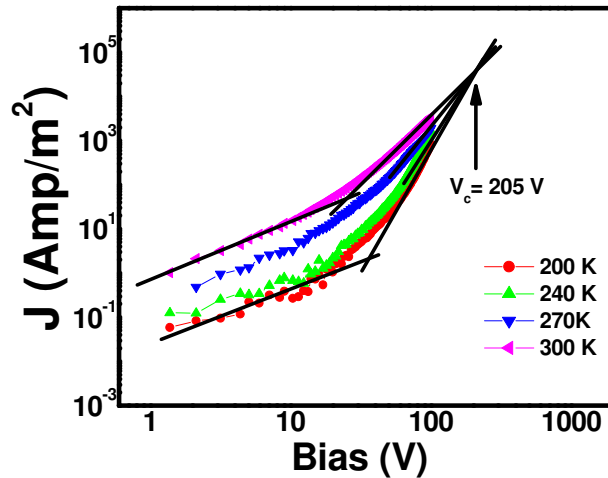


**Figure 5.13** Log-log plots showing current-voltage ( $J$ - $V$ ) characteristics of 20 nm CoPc films grown on single crystalline region in the temperature range 300 K - 200 K.

## 5.4 Conclusions

In this chapter we have studied charge transport properties of highly ordered CoPc films grown on twined (001)  $\text{LaAlO}_3$  and bicrystal (001)  $\text{SrTiO}_3$ . The main conclusions drawn from the studies are as follows.

- (i) The ordering of CoPc molecules along the twin boundaries of (001)  $\text{LaAlO}_3$  yields high charge carrier mobility of  $\sim 7 \text{ cm}^2 \text{ V}^{-1} \text{ s}^{-1}$ . Due to the high mobility it was possible to measure charge transport down to 25K.
- (ii) The analyses of temperature dependent  $J$ - $V$  characteristics of CoPc measured along the twin boundaries of (001)  $\text{LaAlO}_3$  indicate that in the temperature range (300- 100K) the charge transport is dominated by bulk, whereas in the temperature range (100-25K) transport is govern by the electrode limited

processes. These results yielded in a new temperature-bias phase diagram for high mobility films.

- (iii) A critical behavior is observed in the CoPc films deposited along bicrystal boundary of (001) SrTiO<sub>3</sub>, whereas insulating behavior is observed in the CoPc films deposited in the single crystalline region.
- (iv) A very high mobility value ( $\sim 150 \text{ cm}^2\text{V}^{-1}\text{s}^{-1}$ ) is obtained in CoPc films grown along the bicrystal boundary of (001) SrTiO<sub>3</sub> and the charge conduction down to 30K can be described by Ohmic conduction followed by trap free SCLC at higher voltage.

---

## **CoPc films as ppb level Cl<sub>2</sub> sensor**

---

6.1 Introduction

6.2 Configuration of chemiresistive sensors using MPc films

6.3 Gas sensing characteristics of CoPc films grown on different substrates

6.4 Optimization of gas sensing parameters of CoPc films on sapphire

*6.4.1 Operating temperature*

*6.4.2 Film thickness*

6.5 Gas sensing characteristics of 20 nm CoPc films deposited on sapphire

*6.5.1 Linearity*

*6.5.2 Selectivity*

*6.5.3 Stability & Repeatability*

6.6 Degradation of the sensor films

6.7 Mechanism of gas sensing by CoPc films

6.8 Impedance spectroscopy study

6.9 Kinetics of CoPc sensor

6.10 Elovich isotherm

6.11 Conclusions

## 6.1 Introduction

Clean environment requires the vital gases of the atmosphere like  $O_2$ , humidity etc should be kept at an adequate level and also emission of hazardous gas should be controlled below toxic limit. An efficient gas sensor is essential to control the emission of hazardous gases. The inorganic semiconductors are successfully used as chemiresistive gas sensor especially different metal oxide semiconductor, such as,  $SnO_2$ ,  $ZnO$ ,  $WO_3$ ,  $In_2O_3$ ,  $V_2O_5$ ,  $MoO_3$ ,  $CuO$ ,  $NiO$  [146 - 149]. Although there is good number of papers which deals with understanding of gas sensing mechanism still the process is mostly empirical. Organic semiconductors offer unique characteristics such as tunability of electronic properties via chemical synthesis, compatibility with mechanically flexible substrates, low-cost manufacturing, and facile integration with chemical functionalities. Due these advantages organic semiconductors (both small molecule and polymers) have widely been explored for chemiresistive sensors for the last two decades [150-152]. Among all the small molecule based chemiresistive gas sensors phthalocyanine has its own advantages (as discussed in Chapter - 1) and due to which different groups have investigated its gas sensing properties. The sensing of different gases like  $NO_2$ ,  $NO$ ,  $NH_3$  etc, by various MPC's (e. g.  $PbPc$ ,  $CuPc$ ,  $NiPc$  etc) has been studied. A brief review of gas sensing by phthalocyanine are given in Table-1. As seen from the Table-1 that all these sensors sense upto some ppm level of toxic gas at an elevated temperature. We have reported sub ppm (upto 5 ppb) level chlorine gas (toxic limit: 8 hrs. time weighted average 0.5 ppm) by  $CoPc$  films. In this chapter we have discussed the optimization of the sensor parameters, sensor characteristics and the mechanism of sensing of the sensors based on 20 nm  $CoPc$  films.

**Table 6.1** A partial review of gas sensing characteristics of various MPc films.

| Films  | Test gas          | Reported con. Range (ppm)       | Operating temperature (°C) | Ref.  |
|--|-------------------|---------------------------------|----------------------------|-------|
| FePc & CuPc  | NO <sub>2</sub>   | 0.8 to 12.5                     | 190                        | [153] |
| CuPc   | Cl <sub>2</sub>   | 0.1 to 35                       | 170                        | [154] |
| NiPc & CuPc  | NH <sub>3</sub>   | 300 to 800                      | 350                        | [155] |
| PbPc   | NO <sub>2</sub>   | 1 to 100                        | 250                        | [156] |
| CuPc   | NO <sub>2</sub>   | 10 to 100                       | 225                        | [157] |
| NiPc   | NO                | 5 to 500                        | 160                        | [158] |
| PbPc   | NO                | 20 to 100                       | 180                        | [159] |
| Copper tetra 4- (2, 4 ditert<br>amylphenoxy) phthalocyanine                | NH <sub>3</sub>   | 2 to 10                         | RT                         | [160] |
| CoPc & CuPc  | humidity          | 15 to 50 % relative<br>humidity | 50                         | [161] |
| TiOPc  | NO <sub>2</sub>   | 10 to 100                       | 180                        | [162] |
| CuPc   | ethanol           | 3200 to 6400                    | RT                         | [163] |
| tetra-<br>(tert-butyl) phthalocyanine<br>copper (CuPc(t-Bu) <sub>4</sub> ) | NH <sub>3</sub> & | 0.1 to 100 &                    | RT                         | [164] |
|  | NO <sub>2</sub>   | 30 to 80                        |                            |       |
| CuPc   | NO <sub>2</sub>   | 0.5 to 5                        | 170                        | [165] |
| VOPC   | NO <sub>2</sub>   | 10 to 25                        | RT                         | [166] |
| ZnPc, CuPc, CoPc, NiPc   | Toluene           | -                               | RT                         | [167] |

## 6.2 Configuration of chemiresistive sensors using MPc films

A chemiresistive sensor essentially is a “resistor” whose electric resistance is very sensitive to the chemical environment. In the simplest form, chemiresistive sensor consists of a film of semiconductor and two electrical contacts are made on it for resistance measurements, as shown in Fig. 6.1(a). In our case, CoPc films are deposited by MBE on different substrates and electrical contacts are made by thermally evaporating Au on MPc films. A change in electrical resistance of the device is measured as a function of time for known amount of exposed gas. An equivalent circuit diagram of the sensor device is presented in Fig. 6.1(b), which consists of the contact resistances ( $R_c$ ), bulk resistance of MPc film ( $R_f$ ), resistance of the interface layers at substrate-film ( $R_{s-f}$ ) and film-air ( $R_{f-a}$ ). A change in any of these resistances will cause a consequential change of overall resistance of the sensor. Due to the interaction of electrophilic gas molecule and MPc molecule on the surface, charge carrier are induced and consequently electrical resistance of the film-air interface changes. The diffusion of gas molecules in the bulk and subsequent interaction with MPc molecules also results a change in the bulk resistance as well as film and substrate interface resistance.

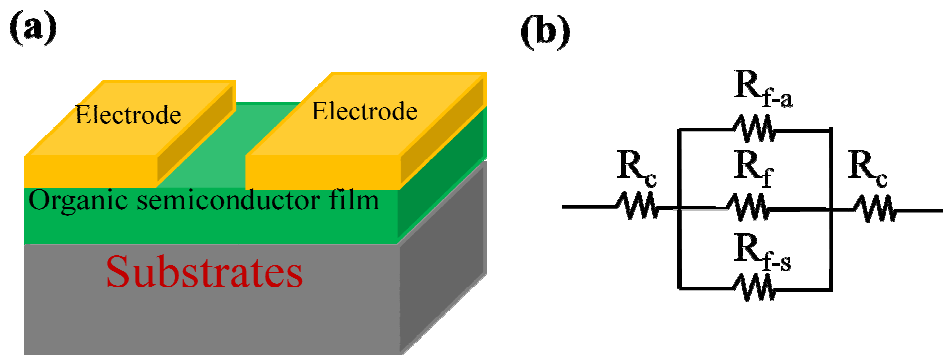


**Figure 6.1** (a) Schematic showing the configuration of a chemiresistive sensor and (b) its equivalent circuit.

A chemiresistive sensor is characterized by following five parameters: (i) sensitivity, (ii) response time, (iii) recovery time, (iv) selectivity and (v) long term stability. The sensitivity ( $S$ ) of a sensor can be defined by many ways, including (a) A ratio of resistance in air to that in gas i.e.  $S = R_{\text{air}}/R_{\text{gas}}$ , (b)  $S (\%) = 100 \times (R_{\text{air}} - R_{\text{gas}})/R_{\text{air}}$ . A positive value of  $S$  implies film resistance decreases on gas exposure and vice versa or (c)  $S = \{(C_g - C_a)/C_a\} \times 100$ , where  $C_g$  and  $C_a$  are the conductance in gas and air respectively [168]. In this thesis we have adopted the third definition throughout. The response time ( $T_{\text{res}}$ ) is the time interval over which conductance attains a fixed percentage (usually 90%) of final value when the sensor is exposed to full-scale concentration of the gas. Recovery time ( $T_{\text{rec}}$ ) is the time interval over which sensor conductance reduces to 10% of the saturation value when the sensor is exposed to full-scale concentration of the gas and then placed in the clean air. A good sensor should have a small response and recovery times so that sensor can be used over and over again. Moreover, the sensor should be selective to a particular gas only and sensor should not degrade on continuous operations for long durations.

### **6.3 Gas sensing characteristics of CoPc films grown on different substrates**

The efficient gas sensing of any MPc films depends on two processes, (i) adsorption of gas molecule on MPc films and consequently charge carrier generation and (ii) efficient transport of generated charge carrier to the respected electrodes. The first process requires active sites in the films for the interaction of gas molecules and MPc films. The second process requires high mobility of the films. These two parameters will depend on the morphology of the films and ordering of CoPc molecules. In previous chapters we have seen that CoPc films have different morphology and ordering on different substrates. Thus these

films have different sensitivity for chlorine gas. To investigate the effect of substrate on the sensitivity of CoPc films, we have measured the response of 20 nm CoPc films grown on different substrates, such as glass, sapphire, twined (001) LaAlO<sub>3</sub> and 36.8° cut bicrystal (001) SrTiO<sub>3</sub>, for 2 ppm Cl<sub>2</sub> gas. The typical response curves for these films are shown in Fig. 6.2. The sensor parameters calculated from the Fig. 6.2 are tabulated in the Table – 6.1.

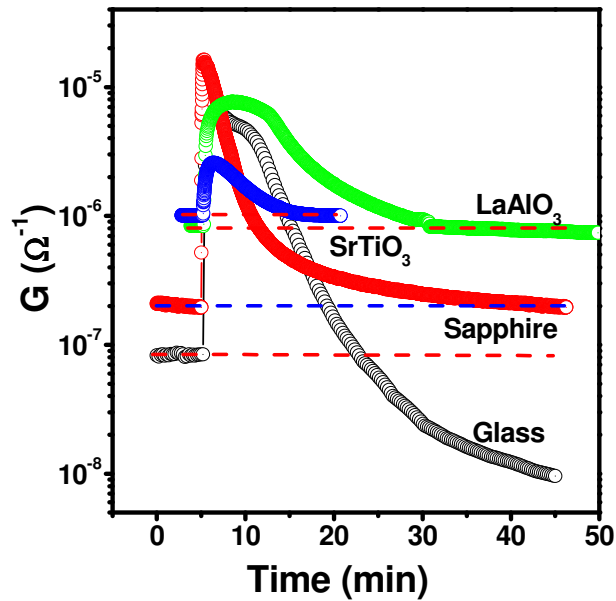


**Figure 6.2** Typical response of 20 nm CoPc films grown on glass, sapphire, twined (001) LaAlO<sub>3</sub> and 36.8° cut bicrystal (001) SrTiO<sub>3</sub> for 2 ppm Cl<sub>2</sub> gas.

It is seen from the Fig. 6.2 that the conductivity of the films deposited on glass drifts below initial base conductivity after exposure of Cl<sub>2</sub> gas. This drift can be explained by the deep traps created by chemisorption of oxygen by CoPc molecules. In the Chapter – 4, we have seen that ambient oxygen gets physisorbed as well as chemisorbed onto CoPc films, deposited on glass due to their disordered morphology. The chemisorption of oxygen results deep traps in these disordered CoPc films, which leads to (i) the drift of room temperature

conductivity with time, see Fig. 4.3 (a) and (ii) reduction in charge mobility. Although the CoPc films have enough sites to interact with Cl<sub>2</sub> molecule but due to low mobility and drift in the conductivity these films are not suitable for gas sensing application. On the other hand the films deposited on the sapphire do not have these problems, and therefore, they show a reversible response with very high sensitivity and fast response and recovery, which is very essential for the sensor application. It is seen from the Table 6. 2 that the highly ordered CoPc films, grown along twin boundary of twined (001) LaAlO<sub>3</sub> and along bicrystal boundary of (001) SrTiO<sub>3</sub> have lower sensitivity for Cl<sub>2</sub> gas as compared to that grown on sapphire. As discussed in Chapter-5 that these films are having very high mobility due to the ordering of molecules along twin boundary (in case of LaAlO<sub>3</sub>) or along the bi-crystal boundary (in case of bi-crystalline SrTiO<sub>3</sub>). Due to the ordering of CoPc molecules, the available interaction sites reduces and thereby less sensitive to Cl<sub>2</sub> gas. As the CoPc films grown on sapphire substrate have highest sensitivity with very fast response and recovery, we will discuss Cl<sub>2</sub> gas sensing of these films in detail.

**Table 6.2** Comparison of sensitivity of CoPc films (20 nm) grown on different substrate for 2 ppm Cl<sub>2</sub> gas.

| Sensors  | Sensitivity (S in %) | Response time (s) | Recovery time (s) |
|--|----------------------|-------------------|-------------------|
| Polycrystalline CoPc films on Glass            | $7.2 \times 10^3$    | 35                | 510               |
| Polycrystalline CoPc films on Sapphire         | $9.2 \times 10^3$    | 15                | 230               |
| Ordered CoPc films on (001) LaAlO <sub>3</sub> | $7.8 \times 10^2$    | 90                | 1440              |
| Ordered CoPc films on (001) SrTiO <sub>3</sub> | $1.57 \times 10^2$   | 55                | 480               |

## 6.4 Optimization of gas sensing parameters of CoPc films on sapphire

The gas sensing characteristics of CoPc films depends on the various parameters such as (i) operating temperature, (ii) thickness of the sensor films. In this section we discuss about the optimization of these parameters.

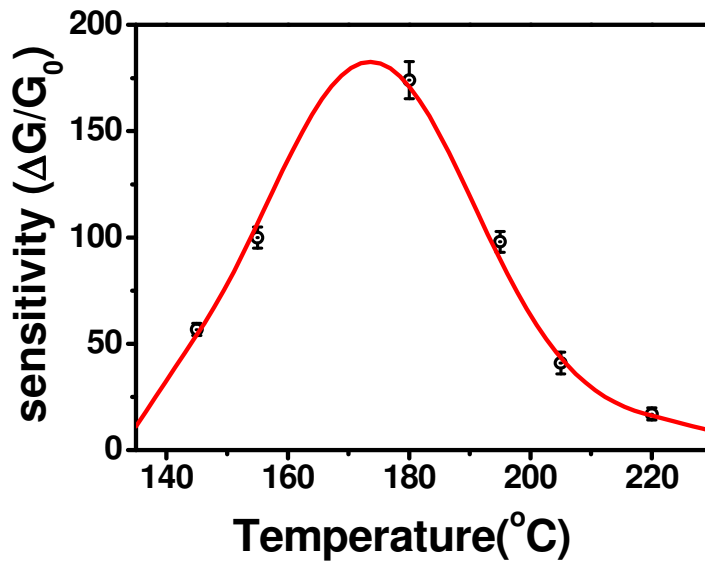


**Figure 6.3** A typical temperature variation sensitivity of 20 nm CoPc films deposited on sapphire substrate for 2 ppm  $\text{Cl}_2$  gas in the temperature range of 145°C to 220°C.

### 6.4.1 Operating temperature

To optimize the operating temperature of the sensor films we have measured the sensitivity of the films with different operating temperature (145°C to 220°C) for 2 ppm  $\text{Cl}_2$  gas. The obtained results are shown the Fig. 6.3. The temperature variation of sensitivity shows a peak at around 180°C. Thus maximum sensitivity is obtained at an operating temperature of 180°C and below and above this temperature the sensitivity decreases subsequently. Hence we have carried out the gas sensing study on CoPc films deposited on

sapphire at an optimum operating temperature of 180°C. The variation of the sensitivity with temperature can be explained by following described model.

When a gas is injected into the test chamber the gas molecule adsorb on the film surface as well as diffuse inside the bulk, which causes an increase in the film conductivity. At the same time desorption of gas molecules also take place. All these three process are rate process having different rate constant. The concentration of the gas molecule  $[C(x,t)]$  at any time at any place inside the film can be found out by solving diffusion equation (eq. 6.1) with proper boundary condition [169].

$$\frac{\partial C}{\partial t} = D \frac{\partial^2 C}{\partial x^2} \quad (6.1)$$

Where D is the diffusion constant. In real system we do not measure the concentration of reacted gas molecule instead we measure the conductivity change of the film due the adsorption of gas molecule within the film. Therefore we assume that the conductance change in the film is given by the following equation:

$$G - G_0 = \Delta G = \int_0^l \beta C(x, t) dx \quad (6.2)$$

Where  $\beta$  is the scaling constant,  $G_0$  is the initial conductivity of the film and  $l$  is the thickness of the film. Now the conductance change can be calculated by knowing the concentration profile of gas  $[C(x, t)]$  inside the films as

$$\Delta G = \Delta G_{max} - \sum_{n=1}^{\infty} B_n \exp\left(-\frac{t}{\tau_n}\right) \quad (6.3)$$

Where,

$B_n = \frac{4a\beta \sin^2 \lambda_n l}{2\lambda_n l + \sin(2\lambda_n l)} \frac{1}{\lambda_n}$  and  $\tau_n$  is characteristic time of diffusion and depend inversely on

the diffusion constant (D). The eq. 6.3 describes the response with time of the sensor for a certain amount of test gas. The first term in this equation corresponds to the maximum change of conductance and the first term corresponds to the transient change in the conductance. It is evident from the eq. 6.3 that after certain time depending on the diffusion constant a steady state will arrive and second term will die out. Therefore in steady state conductance change will be given by the first term i. e.  $\Delta G_{max}$  and given by

$$\Delta G = \Delta G_{max} = \left[ \frac{k_a}{k_a + k_d} \right] \beta C_0 l \quad (6.4)$$

Here  $k_a$  and  $k_d$  are the rate constant of adsorption and desorption respectively and  $C_0$  is the initial gas concentration.

The maximum conductance change is related to the operating temperature for a particular amount of injected gas as given by eq. 6.4. Here  $\beta$  is related to the extrinsic conductance of the film with temperature. During the interaction of acceptor gas with MPc films free holes are created in the film and it also forms an acceptor level in the MPc energy gap. At low temperature created holes freeze at shallow acceptor level. With increase of temperature, more and more holes are ionized and enter the valence band as free holes and thus conductivity increases. At very high temperature all those shallow acceptor levels are ionized and all the holes created by the interaction of gas are free at valence band. Thus extrinsic conductivity saturates. Therefore it is expected that  $\beta$  will increase first with temperature and then saturate at a constant  $\beta_{max}$  with temperature. It can be seen from the eq. 6.4 that when  $k_a \gg k_d$  the maximum conductance change ( $\Delta G_{max}$ ) increase with temperature due to the increase of extrinsic conductivity ( $\beta$ ) upto a particular temperature where  $\beta$  attains

its maximum value  $\beta_{max}$ . At still higher temperature, the desorption rate increase and become higher than adsorption rate ( $k_d > k_a$ ), and thus maximum conductance change will decrease.

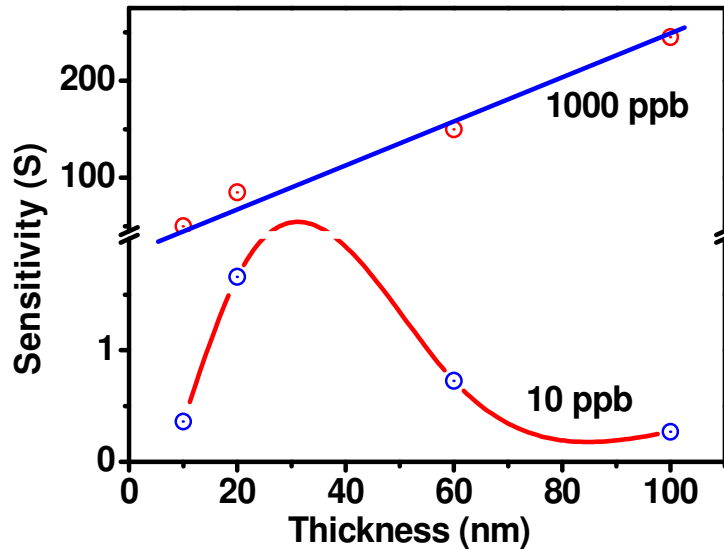


**Figure 6.4** Variation of sensitivity of CoPc sensor for 10 ppb (blue data) and 1000 ppb (red data)  $\text{Cl}_2$  gas. The solid lines are for eye guidance.

#### 6.4.2 Film thickness

To optimize the film thickness we have prepared different thickness CoPc films on sapphire and study their gas sensing properties. A typical result is shown in the Fig. 6.4. It is evident from the figure that sensitivity increases monotonically with film thickness for higher concentration of  $\text{Cl}_2$  gas (1 ppm). On the other hand for lower concentration of  $\text{Cl}_2$  gas the sensitivity shows a maximum at around film thickness 20 nm. As previously discussed in Chapter-2 that at lower thickness the ‘face-on’ growth of CoPc leads to smooth films. At higher thickness due to change in the growth configuration the films become more disorder and polycrystalline. This phenomenon results a higher mobility in lower thickness films. At

lower concentration fewer numbers of free holes are created and in low thickness films these free holes are efficiently transported due to the higher mobility and thus sensitivity is high in low thickness films compared to thicker films. But for higher concentration of test gas, the number of free carrier, generated by the interaction of CoPc and Cl<sub>2</sub> molecules, are very high and thus the reduction of mobility at high thickness is not prominent. It is always desirable that any toxic gas is detected at its lower concentration. Therefore 20 nm thickness is the optimum thickness for the sensor application.

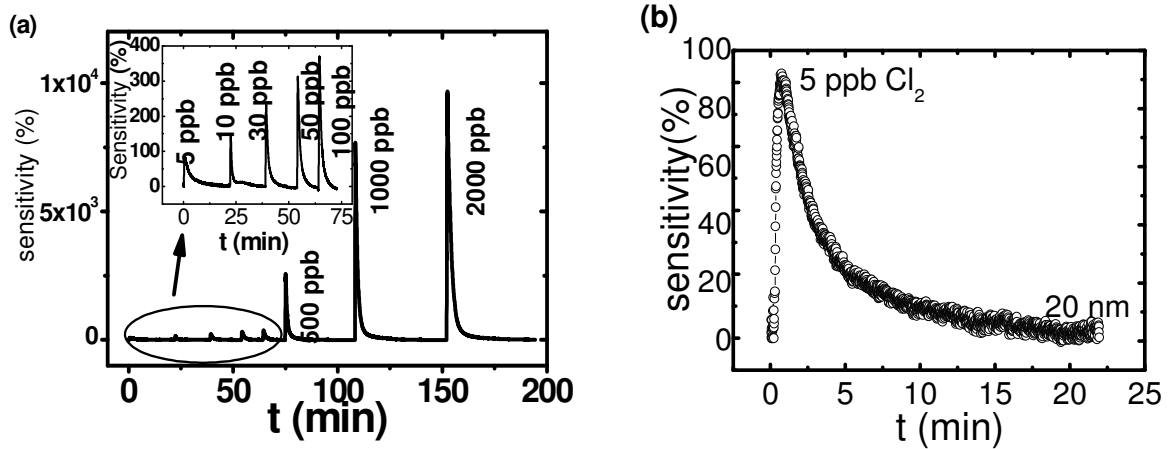


**Figure 6.5** (a) Response curve of 20 nm CoPc films for different Cl<sub>2</sub> dose (5–2000 ppb). Inset shows magnified response curve in 5–100 ppb range. (b) Response curves of 20 nm CoPc films for 5 ppb Cl<sub>2</sub>.

### 6.5 Gas sensing characteristics of 20 nm CoPc films deposited on sapphire

It is clear from the previous section that 20 nm CoPc films on sapphire substrate at an operating temperature of 180°C is the best for lower concentration Cl<sub>2</sub> sensing application. A typical response of the sensor towards different concentration of Cl<sub>2</sub> gas in the range 5 to 2000 ppb is shown in Fig. 6.5 (a). We are the first to demonstrate the detection of as low as 5

ppb  $\text{Cl}_2$  gas by ultra thin CoPc sensor. The Fig 6.5 (b) shows the sensitivity of the sensor is almost 80 % with very fast response (18 s) and recovery (900 s) time. In the following section we will describe the different sensor parameters.

### 6.5.1 Linearity

For a practical sensor the sensitivity should vary linearly with gas concentration. Theory also predicts, as evident from eq. 6.4, the linearity of sensitivity with concentration of injected gas in a certain range of gas concentration. In case of our CoPc sensor the sensitivity varies linearly with  $\text{Cl}_2$  concentration in the range 5 to 2000 ppb (see Fig. 6.6). Therefore it can be used for  $\text{Cl}_2$  sensing in that range. The sensitivity deviates from its linear behavior beyond 2000 ppb due to permanent reaction of  $\text{Cl}_2$  with CoPc molecule.

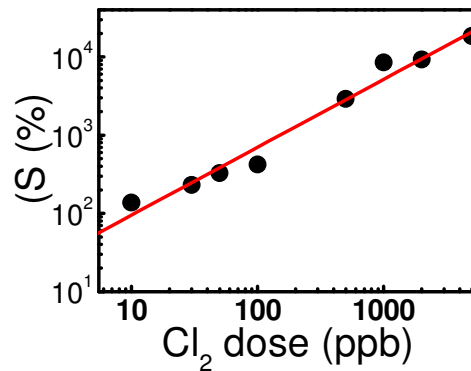


**Figure 6.6** Sensitivity of 20 nm CoPc films as a function of  $\text{Cl}_2$  dose.

### 6.5.2 Selectivity

In the real application sensor has to sense a particular gas from a mixture various gases. Therefore the selectivity of a sensor is a very important parameter. In order to

investigate the selectivity of CoPc films we have measured the response of the CoPc films for 2 ppm of different gas, such as Cl<sub>2</sub>, NO<sub>2</sub>, NO and NH<sub>3</sub> and the sensitivity of various gases are shown in Fig. 6.7. It is evident from the figure that the sensor is very much sensitive to the Cl<sub>2</sub> gas as compared to the other gases. The higher sensitivity towards Cl<sub>2</sub> may be due to the higher electro-negativity of Cl<sub>2</sub> molecule.

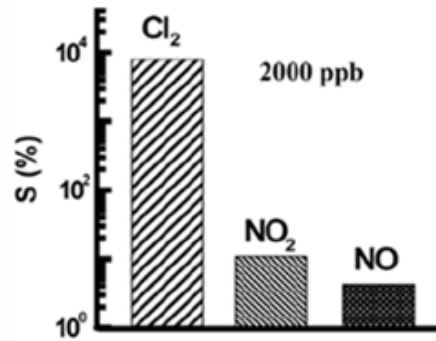


**Figure 6.7** Bar chart showing sensitivity for different gases, which reveals high selectivity for Cl<sub>2</sub>.

### 6.5.3 Stability & Repeatability

Life of the sensing element of a sensor is an important issue from economical point of view. Ideally sensing element should not change its characteristics under repeated gas exposure, but in practice its sensitivity degrades over the time under repeated exposure or due to higher exposure limit. In order to investigate the stability and repeatability of the CoPc sensors we performed cyclic measurements by giving repeated exposure of 500 ppb Cl<sub>2</sub> gas for more than few hundred times. The typical results for five exposures are shown in Fig. 6.8. It was found that sensitivity does not decrease for repeated exposure of 500 ppb Cl<sub>2</sub> gas. The base line resistance drift over a period of one month was found to be very small (< 5%).

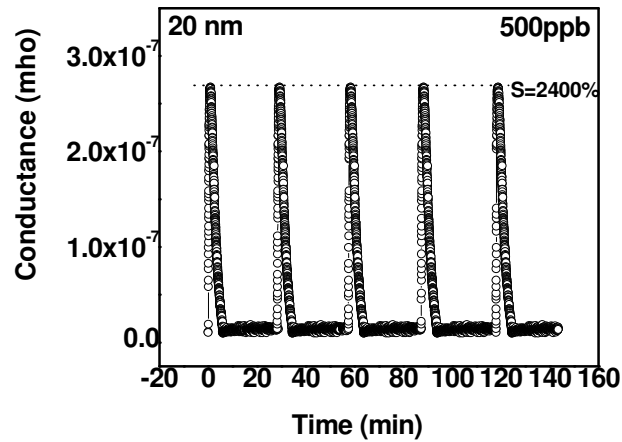


**Figure 6.8** Response of 20 nm CoPc films on repetitive exposure of 500 ppb Cl<sub>2</sub> gas.

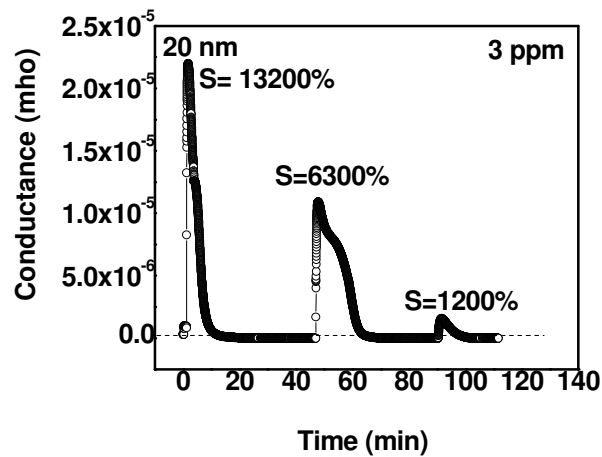


**Figure 6.9** The response of CoPc films showing a degradation of its performance due to application of higher dose of 3 ppm Cl<sub>2</sub> gas.

## 6.6 Degradation of the sensor films

As seen in the previous sections that the sensor is linear, stable and repeatable for the 5 to 2000 ppb Cl<sub>2</sub> gas exposure. However a very high concentration of gas exposure causes degradation in the sensor characteristics. To study the degradation of the sensor we recorded the response of the CoPc films for repetitive exposure of 3 ppm Cl<sub>2</sub> gas. Typical results are

shown in Fig. 6.9. It can be easily seen that when films were repetitively exposed to 3 ppm Cl<sub>2</sub> the sensitivity ( $s = 13200\%$ ) sharply decreased subsequently by a factor of 2 ( $s = 6300\%$ ) and 11 ( $s = 1200\%$ ) in 2<sup>nd</sup> and 3<sup>rd</sup> exposure. So 3 ppm is the higher exposure limit for 20 nm film and it can't be used for further higher dose. It seems that there might be some permanent reaction / damage in the film and as a result interaction sites becomes less when higher dose is applied. In order to investigate further we performed XPS studies on the repeated gas exposed films and the results are shown in Fig. 6.10. The permanent binding of Cl<sub>2</sub> molecule with Co atom of CoPc molecule is confirmed by the 2 eV shift in the Co-2p peak. It is further confirmed by the 2.1 eV shift in Cl-2p peak at 200.6 eV which indicates the formation of hydrocarbon-Chloride (C<sub>6</sub>H<sub>5</sub>Cl). The increase in the full width half maxima (FWHM) of C-1s (from 2.5 eV to 4.1 eV) and N-1s (from 2.8 eV to 4.6 eV) peaks also strongly supports permanent interaction of Cl<sub>2</sub> with CoPc.

## 6.7 Mechanism of gas sensing by CoPc films

In this section we describe the mechanism of gas sensing. It is well known that MPc's show a high sensitivity to electrophilic gases such as NO<sub>2</sub>, Cl<sub>2</sub>, Br<sub>2</sub> etc. When adsorbed on MPc surface, an electrophilic gas withdraws electrons from MPcs and holes are created and delocalise on phthalocyanine (Pc) ring. The gas-sensing process can be classified into three steps (i) the adsorption of gas on solid surface; (ii) the charge transfer between the adsorbed gas and the surface, (iii) the charge delocalisation [170].



The first process i.e. adsorption of gas molecules on solid surface mainly depend on the film morphology. Depending on the morphologies of the film surface it will present a range of different absorption sites corresponding to different crystal faces and structural defect site such as grain surface and grain boundaries etc. The adsorption of the gas molecule on grain surface and grain boundary can be investigated by carrying out impedance measurement and in the next section we will concentrate on that.

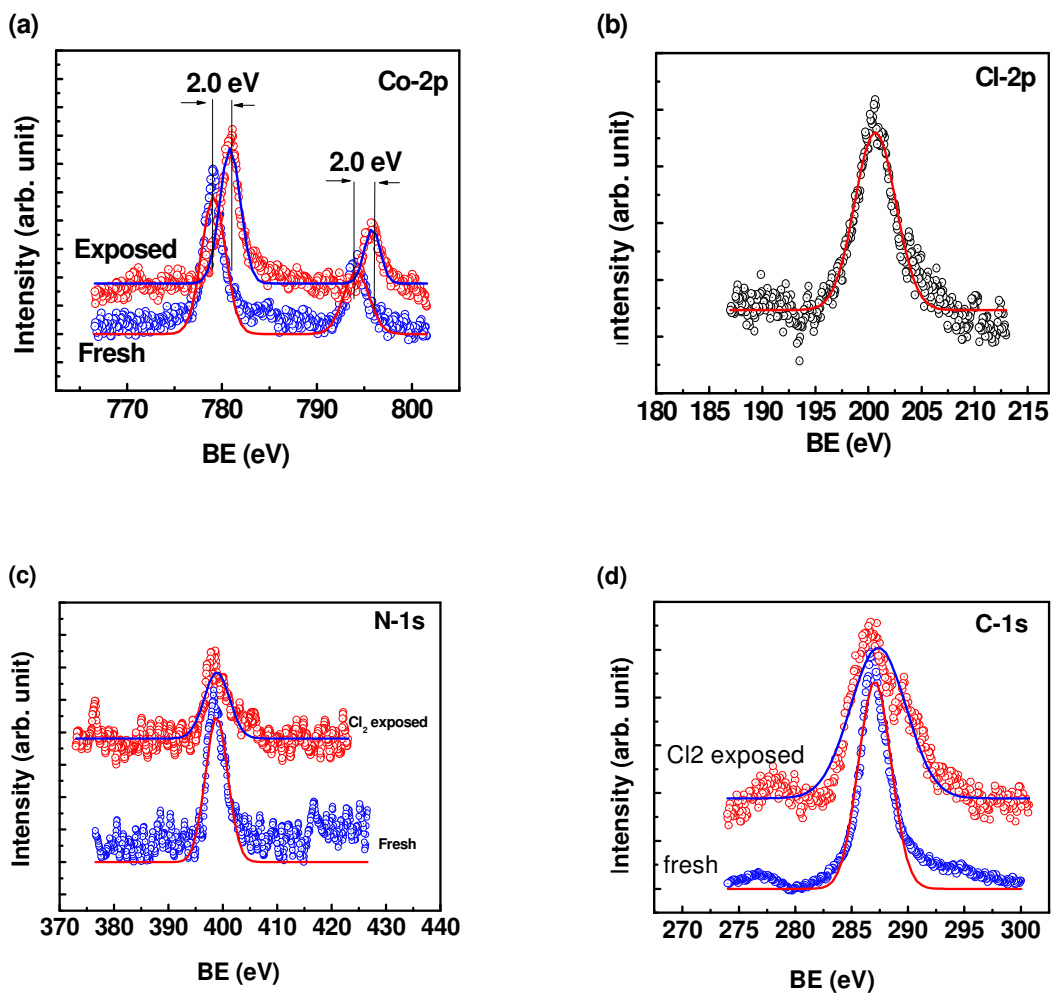


**Figure 6.10** XPS spectra of fresh (blue) and a high dose  $\text{Cl}_2$  exposed (red) CoPc films. (a), (b), (c), (d) corresponds to Co-2p, Cl-2p, N-1s, C-1s peaks respectively.

The second process is very important for the gas sensing of CoPc films. In this process charge is transferred between adsorbed gas molecule and MPc molecule. In this step ambient oxygen has a great role to play. It is well known that the formation of charge transfer complexes by coordination of  $O_2$  to MPc metal center at air / phthalocyanine interface leads to formation of  $MPc^+$  and  $O_2^-$  species and injection of hole carriers into the bulk solid. As a surface dopant  $O_2$  occupies only a fraction of binding sites [171] on the film therefore interaction with gas molecules in air could result in two different mechanisms, gas molecule could bind either to open surface metal coordination site or compete with  $O_2$  for the occupied metal surface sites [172, 173]. The kinetics of the first process is faster than the second. The schematic of this model is shown in Fig. 6.11.

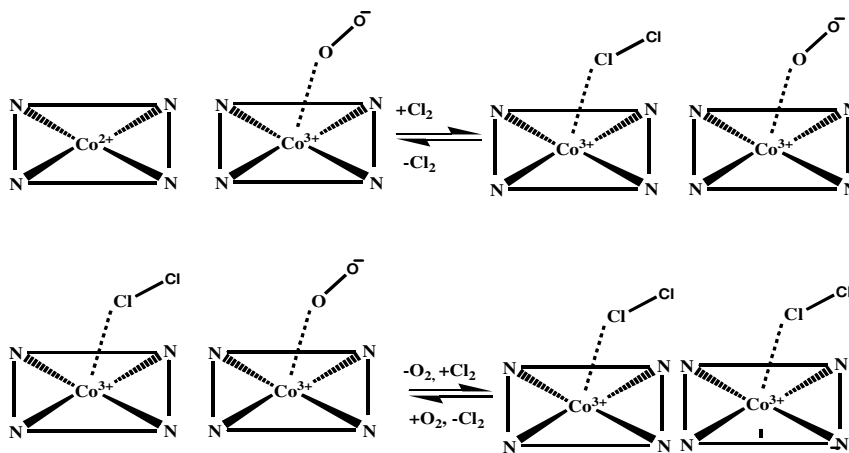


**Figure 6.11** Model of chemisorptions of  $Cl_2$  on to MPc surface. It may bind at free metal sites or replace oxygen to bind at metal sites.

Although there is another possibility of weak binding of gas molecule to  $\pi$  electron of the Pc. This binding may be governed by the weak hydrophobic or partial charge transfer interaction. The chemical binding of  $Cl_2$  molecule with the Co atom is also supported by

theoretical work where it has been shown that oxidizing gases strongly chemisorbs to the central metal atom of MPCs and physisorbs to all non metal sites [174].

To prove the above conjecture we have measured the CoPc sensor response to a dose of 50 ppb  $\text{Cl}_2$  gas at temperature  $180^\circ\text{C}$  and shown in Fig. 6.12. The figure shows that there are two type of kinetics in the response and recovery of the sensor. The initial fast response (a) corresponds to maximum current change followed by a slower response (b). Similarly faster recovery (c) (corresponding to the faster response) followed by a slower recovery (d). In this model faster response corresponds to binding of  $\text{Cl}_2$  at the oxygen free sites and slower response corresponds to displacement oxygen from central metal atom. Similarly for the recovery. However some people have suggested faster and slower response corresponds to displacement of oxygen from weak and strongly bound site [158].

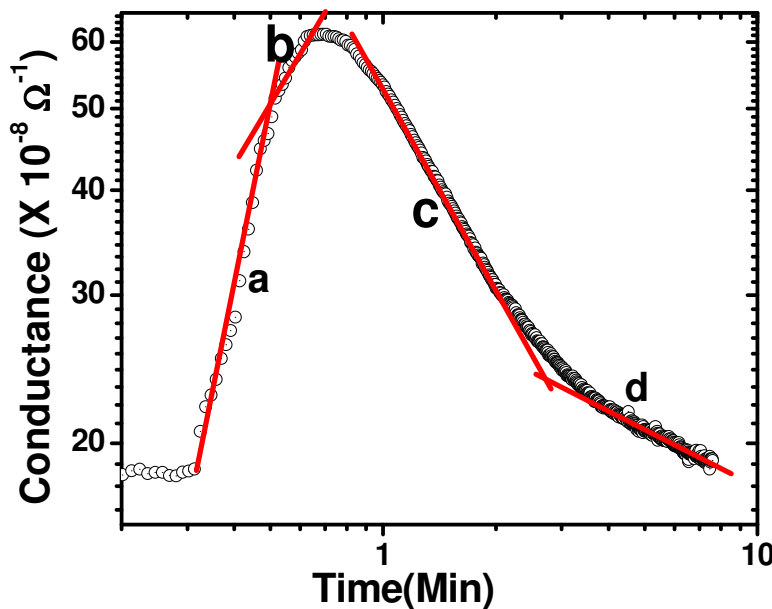


**Figure 6.12** A typical response curve of CoPc sensor showing faster (a,c) and slower (b, d) response and recovery due to two different processes of chemisorptions of  $\text{Cl}_2$  on to the CoPc surface.

The last step is the charge delocalization process where the created hole delocalized on the entire molecule. This process is a low activation energy process and quite faster compared to the previous two processes.

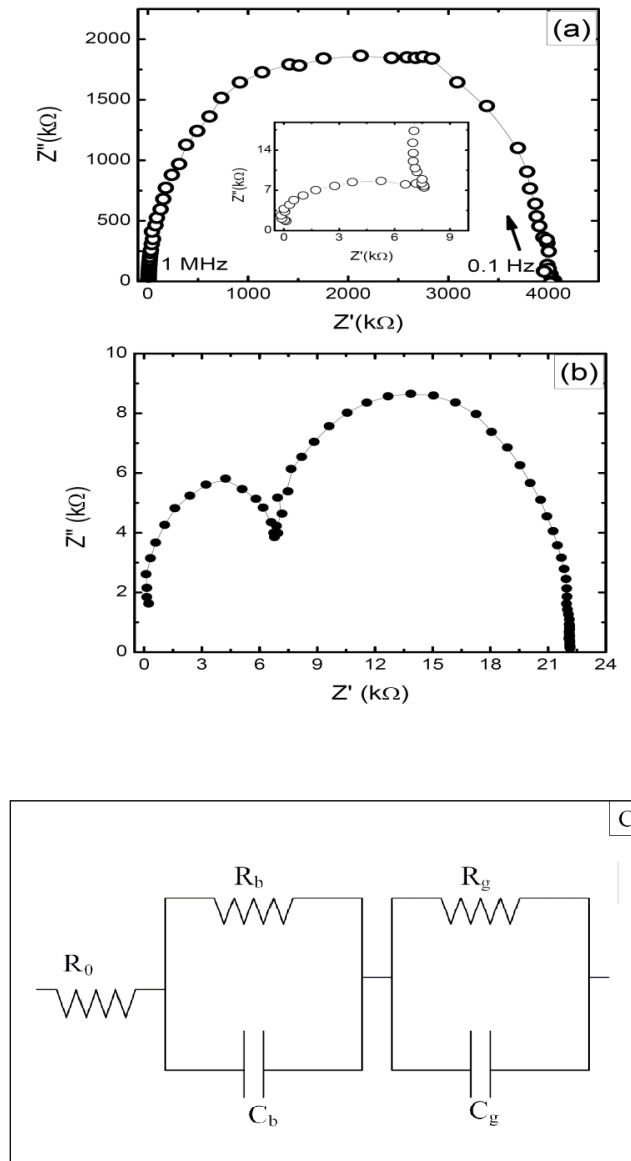


**Figure 6.13** Impedance spectra of CoPc film in cole-cole plot (a) fresh film, inset shows the expanded view of high frequency region (b) after 2 ppm Cl<sub>2</sub> gas exposure (c) the equivalent circuit model used to analyses the data.

## 6.8 Impedance spectroscopy study

In the previous section we have discussed about the adsorption of  $\text{Cl}_2$  molecule on to the CoPc molecule. But in the films there will be adsorption sites at grains and as well as at grain boundaries. To distinguish between these two adsorption sites we have studied Impedance spectroscopy. Impedance spectroscopy is a technique in which a variable frequency AC signals is used to simultaneously measure the frequency dependent resistance and capacitance. It helps to delineate the different contributions to electrical conduction arising from bulk, grain boundaries and electrode sample interface [175]. We performed the impedance measurement (in the frequency range 0.1Hz to 1MHz) on CoPc film before and after exposure to 2 ppm of  $\text{Cl}_2$  gas. The results are shown in Fig. 6.13 in the form of cole - cole plot. In this measurement frequency increases from right to left, from 0.1 Hz to 1 MHz. For a circuit with an ideal resistor and capacitor in parallel, one perfect semicircle should be observed in the complex plane ( $Z''$  vs  $Z'$ ). As shown in Fig 6.13 (a) and (b), two semicircles are observed, the low frequency semicircle is attributed to the grain boundaries because of longer charge relaxation times. The high frequency semicircle is attributed to the bulk because bulk is more ordered than the grain boundaries therefore have faster charge relaxation [176]. In view of this impedance spectrum was analyzed using equivalent circuit shown in Fig 6.13 (c).  $R_0$  is the dc resistance, which is independent of frequency and is attributed to the bulk and surface contributions to the total resistance.  $R_b$  and  $C_b$  are the resistance and capacitance of intra-grain (bulk) regions, while the  $R_g$  and  $C_g$  are the resistance and capacitance of grain boundaries. Values of these parameters are found by fitting the curve in Fig 6.13. (a) and (b) and shown in Table – 6.3.

**Table 6.3** Resistance and capacitance value obtain from the fitting of Figure 6.13 for exposed and unexposed CoPc films to 2 ppm chlorine gas.

|           | $R_0(\Omega)$ | $R_b(\text{k}\Omega)$ | $C_b(\text{nF})$ | $R_g(\text{k}\Omega)$ | $C_g(\text{nF})$ |
|-----------|---------------|-----------------------|------------------|-----------------------|------------------|
| Unexposed | 40            | 7.0                   | 0.039            | 4004                  | 0.07             |
| Exposed   | 75            | 6.6                   | 0.097            | 14.6                  | 0.63             |

It is seen from Table- 6.2 that on exposure to  $\text{Cl}_2$  the grain boundaries resistance ( $R_g$ ) decreases by 270 times, while the intra-grain resistance ( $R_b$ ) almost remains the same. It indicates that exposed area at grain boundaries mainly contributes to the gas sensitivity. In such a tight crystal structure of grains the maximum possibility of interaction of gas molecules with the central cobalt metal atoms occurs only at the grain boundaries.

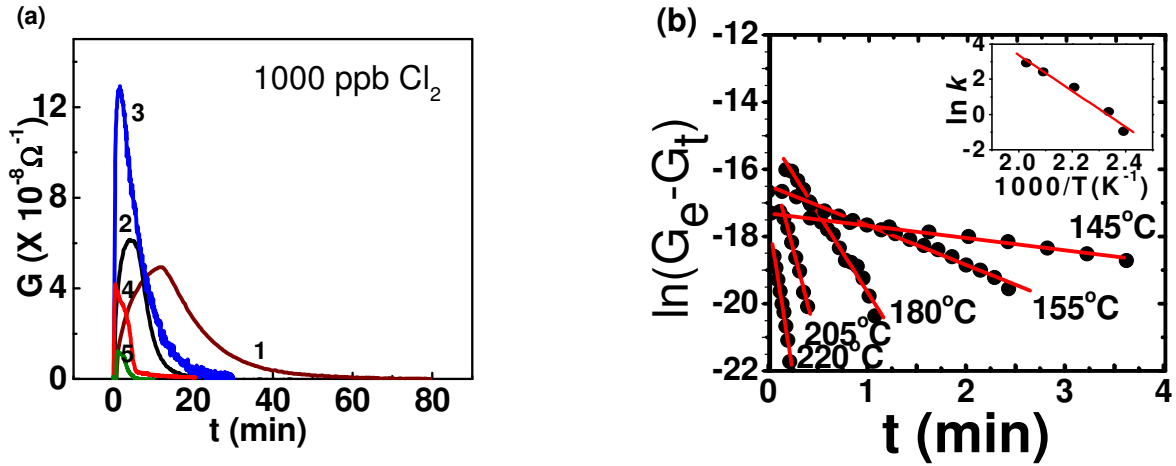


**Figure 6.14** (a) Variation in conductance with time on 1000 ppb  $\text{Cl}_2$  exposures at temperatures 145°C (1), 155°C (2), 180°C (3), 205°C (4), 220°C (5). (b) Plots of  $\ln(G_e - G_t)$  vs  $t$  at different temperature. The slopes of linear fits correspond to  $k$  values. Inset shows Arrhenius plot of  $k$ .

## 6.9 Kinetics of CoPc sensor

In this section we discuss the kinetics of the CoPc sensor. Before discussing kinetics of CoPc sensor we consider a general reaction and discuss kinetic theory. For a general

reaction,  $A \rightarrow$  products, the reactant reacts to give the products. The reaction rate,  $v$ , is given by [177]

$$v = -\frac{d[A]}{dt} = k[A]^n \quad (6.5)$$

Where  $[A]$  is the concentration of reactant A,  $t$  is time,  $k$  is rate constant and  $n$  is the order of reaction. The rate equation for the first order reaction is given by

$$v = -\frac{d[A]}{dt} = k[A] \quad (6.6)$$

By integration the above equation become

$$\ln[A_t] = \ln[A_0] - kt \quad (6.7)$$

Where  $A_0$  is the initial concentration of the reactant. In case of that the output signal (such as the electrical conductance) of the product (which increases with time) is measured and the system can give the signal even when no product is obtained. In this situation  $A_0$  is proportional to  $(G_e - G_o)$ , where  $G_e$  and  $G_o$  are the output signal at the end and the beginning of the reaction and  $A_t$  will proportional to  $(G_e - G_t)$ , where  $G_t$  is the output signal at any time  $t$ . So for the first order reaction integrated rate equation in terms of output signal (electrical conductance) become

$$\ln(G_e - G_t) = \ln(G_e - G_o) - kt \quad (6.8)$$

It is evident from the above equation that for first order reaction the plot of  $\ln(G_e - G_t)$  vs time ( $t$ ) will be linear and the slope of the line will be decided by the rate constant of the reaction. It is well known that the rate constant of any reaction will depend on two factors: (i) the frequency of collision of reactant molecules and (ii) the value of the activation energy

( $E_a$ ) of the reaction. The rate constant and the activation energy are related by the famous Arrhenius equation,

$$k = P \exp(-E_a/RT) \quad (6.9)$$

Where  $P$  is a constant known as frequency factor,  $R$  is the gas constant ( $8.315 \text{ J mol}^{-1} \text{ K}^{-1}$ ) and  $T$  is the absolute temperature. The activation energy can be obtained from the slope of the linear plot of  $\ln k$  vs  $1/T$ .

After discussing the order and rate of any general chemical reaction we have applied this approach to our sensor films. In order to investigate the kinetics of the reaction of  $\text{Cl}_2$  molecule 20 nm CoPc films, conductance as function of time was measured for 1000 ppb  $\text{Cl}_2$  exposure at different operating temperature ( $145^\circ\text{C} - 220^\circ\text{C}$ ), as shown in Fig 6.14(a). In this figure the increase in the conductivity is due to the reaction of  $\text{Cl}_2$  with CoPc molecule. We have re-plotted this transient region as  $\ln (G_e - G_t)$  vs  $t$  (time) at different temperature and shown in Fig 6.14(b), where  $G_e$  and  $G_t$  defined earlier in this section. The linear behavior of  $\ln (G_e - G_t)$  with time at fixed temperature, as evident from the Fig. 6.14(b), confirms the first order reaction kinetics. The rate constant of the reaction at different temperature is extracted from the slope of the linear fit and presented in Arrhenius plot, as shown in the inset of Fig 6.14(b). The activation energy, as extracted from the Arrhenius plot, is  $84.8 \text{ kJ mol}^{-1}$ , which confirms chemisorption of  $\text{Cl}_2$  on CoPc film surface [178].

## 6.10 Elovich isotherm

In reactions involving chemical adsorption of gases on a solid surface without desorption of the products, the adsorption rate decreases with time due to an increase in

surface coverage [179, 180]. One of the most useful models for describing such activated chemical adsorption is the Elovich equation, which is given by

$$\frac{d\theta}{dt} = a \exp(-b\theta) \quad (6.10)$$

where  $\theta$  is the amount of gas adsorbed at time  $t$  and  $a$ ,  $b$  are constants [180]. The Elovich isotherm describes adsorption phenomena occurring on surfaces, which are energetically heterogenous or on surfaces where the adsorption process induces an energetic heterogeneity [179, 181]. The CoPc films contain many adsorption sites, i.e., Co-sites,  $O_2^-$ , hydrocarbon ring and surface defects, which may differ in adsorption energy. Also,  $Cl_2$  adsorption leads to a charge-transfer between CoPc film and  $Cl_2$ . However, this process is limited by a ‘potential barrier’ formed from the dipole layer created by the redistribution of charge between the  $Cl_2$  molecule and the CoPc film. The increase of this potential barrier with successive adsorption events provides an adsorption induced surface heterogeneity. The adsorbate–adsorbate interactions are known to make the heat of adsorption and desorption dependent on the coverage [181]. This makes adsorption rate to decrease exponentially with time due to an increase in surface coverage. In the Elovich equation, constant  $a$  is regarded as the initial adsorption rate because  $d\theta/dt$  approaches  $a$  when  $\theta$  approaches zero and it depends on the activation energy [181]. Constant  $b$  is related to a measure of the extent to which the surface has been screened by ‘potential barrier’ for successive adsorption. Assuming the change of conductance ( $\Delta G$ ) is proportional to the adsorbed  $Cl_2$  molecule ( $\theta$ ) the eq. 6.10 in integrated form can be written as:

$$\Delta G = \frac{1}{b'} \ln(a'b') + \frac{1}{b'} \ln [t + (1/a'b')] \quad (6.11)$$

Where  $a'$  and  $b'$  are different constants. It is evident from the eq. 6.11 that if the reaction obeys Elovich equation then  $\Delta G$  should follow linear variation with  $\ln(t)$  after certain time (this is due to the factor  $\ln(1/a'b')$ ). In our present case  $\Delta G$  vs.  $\ln(t)$ , which is derived from the Fig. 6.5 (a), is shown in Fig. 6.15 (a) and shows a linear behavior after certain time ( $\ln(t) > 1.5$ ), indicating that the reaction obeys Elovich equation. From the slopes, the values of  $b'$  are calculated at different  $\text{Cl}_2$  concentration  $[\text{Cl}_2]$ . As shown in Fig 6.15 (b), the plot of  $\ln(b')$  vs  $\ln[\text{Cl}_2]$  is linear, which provides an alternative way of estimating  $\text{Cl}_2$  concentration apart from the sensitivity plot.

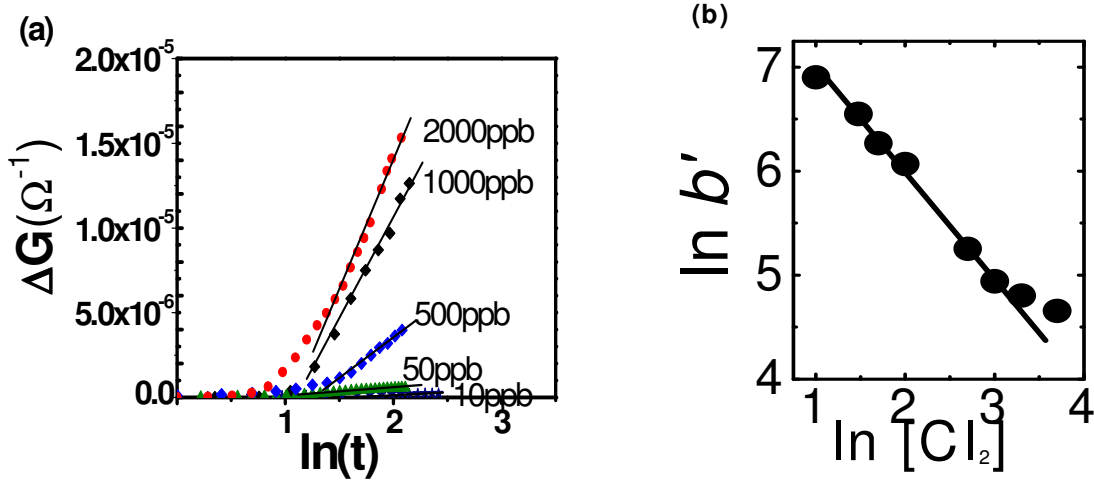


**Figure 6.15** (a) Change in conductance ( $\Delta G$ ) as a function of  $\ln(t)$  for different dose of  $\text{Cl}_2$ , which is derived from Fig. 6.5 (a). Straight-line fit of data is in accordance with Elovich equation and the slope of linear fits yields parameter  $b'$ . (b) A linear correlation between  $\ln b'$  and  $\ln [\text{Cl}_2]$ .

## 6.11 Conclusions

In this chapter we have studied  $\text{Cl}_2$  gas sensing properties of CoPc films deposited on various substrates. The main conclusions drawn are as follows:

- (i) The 20 nm CoPc films deposited on sapphire substrates shows very high sensitivity ( $9.2 \times 10^3$  %) with very fast response (15 s) and recovery (230 s) for 2 ppm of Cl<sub>2</sub> gas as compared to the CoPc films deposited on glass, twined (001) LaAlO<sub>3</sub> and 36.8° cut bicrystal (001) SrTiO<sub>3</sub>.
- (ii) We have demonstrated 5 ppb Cl<sub>2</sub> gas sensing with very high sensitivity (80 %) and fast response (18 s) and recovery (80 s) at an operating temperature of 180°C.
- (iii) The sensors are linear, repeatable, stable, and selective for Cl<sub>2</sub> gas in the concentration range 5 to 2000 ppb.
- (iv) The reaction between Cl<sub>2</sub> and CoPc molecule is first order and the adsorption process obey Elovich equation which provides an alternative way of estimating Cl<sub>2</sub> concentration.

---

## **Summary and conclusions**

---

This thesis was aimed at growing high mobility phthalocyanine films using MBE. MBE technique was chosen to grow FePc and CoPc films for maintaining the pure environment, a perfect control over growth parameters (deposition rate, film thickness, substrate temperature etc) and in-situ characterization of films by x-ray photoelectron spectroscopy. The grown films were ex-situ characterized by several techniques, such as, XRD, XRR, SEM, AFM, etc. The charge transport studies of the grown films were investigated as a function of applied bias in the temperature range 300-25 K. In addition, the suitability of the grown films was examined for their possible application as chemiresistive gas sensors. The major conclusions are already presented at the end of each chapter. Here we make a summary of the main results obtained during the thesis work.

We have demonstrated that amorphous, polycrystalline and crystalline (with face-on as well as edge-on stacking) thin films of FePc/CoPc can be reproducibly grown by optimization of growth parameters as well as employing the appropriate substrate. The amorphous and polycrystalline films can be grown on glass substrate by varying the deposition temperature. It has been shown that ultrathin films (20 nm) grow in face-on stacking configuration on sapphire substrates due to strong molecule-substrate interactions. The crystalline films with edge-on stacking configurations were obtained by employing the grain boundaries of the substrate as template e.g. natural twin boundaries of LaAlO<sub>3</sub>, and singly grain-boundary of SrTiO<sub>3</sub> bicrystal.

The FePc/CoPc films were found to be highly susceptible to the ambient atmosphere, as the oxygen was found to physisorb and/or chemisorb on the film surface. The XPS, conductivity and mobility measurements suggest that the physisorption and chemisorption of oxygen strongly depend on the crystalline nature of the films, which is schematically

presented in the Fig. 7.1. In the case of random stacking (i.e. amorphous or polycrystalline films), the metal atom of the Pc ring can lead to the chemisorptions of the ambient oxygen, while the  $\pi$ -electron cloud of the Pc ring interact with oxygen through van der Waals interactions (i.e. physisorption). In case of highly ordered films (face-on or edge-on stacking), since only  $\pi$ -electron cloud is exposed to ambient therefore oxygen is mostly in the form of physisorbed. Face-on or edge-on stacking also leads to direction of the  $\pi$ -electron overlapping respectively perpendicular and parallel to the substrate plane, and are therefore, are the preferable direction of easy charge transport. It has been also demonstrated that chemisorbed oxygen leads to the formation of the deep traps in the film.

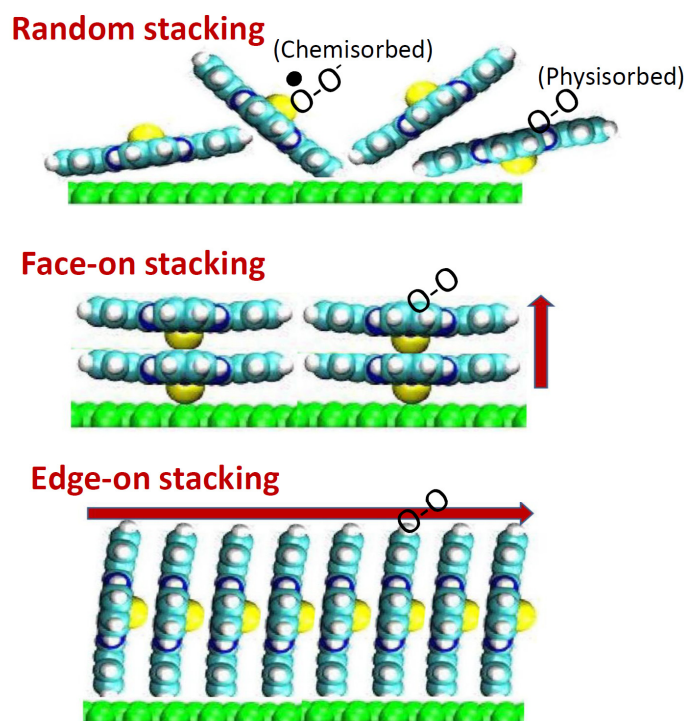


**Figure 7.1** Schematic depicting the physisorption and chemisorption of ambient oxygen on FePc/CoPc films with different types of molecular stacking. The arrows show the direction of  $\pi$ -electron overlapping, and hence preferable direction of easy charge transport.

In the case of amorphous films, the presence of disorders and chemisorbed oxygen (i.e. deep-traps), the charge carrier mobility was very low  $< 0.2 \text{ cm}^2\text{V}^{-1}\text{s}^{-1}$ . The presence of deep-traps resulted in the hysteretic  $J$ - $V$  characteristics, which in the temperature range 300 – 220K could be described by deep-trap limited SCLC. In the temperature range 200 – 150K, the transport properties in these films were found to be governed by the Poole Frankel mechanism. However, at temperature  $<150 \text{ K}$ , due to poor mobility the current values were below the measurable limits of a picometer, and hence, the charge transport could not be investigated.

For polycrystalline films, the charge mobility was found to be  $0.98 \text{ cm}^2\text{V}^{-1}\text{s}^{-1}$ , which was independently confirmed by the transient voltage pulse method. In these films no deep traps were found, and therefore,  $J$ - $V$  characteristics were non-hysteretic and could be well described by trap-free SCLC in the entire investigated temperature range (300-75 K).

Highly order CoPc films have been grown on twin-boundaries of  $\text{LaAlO}_3$  single crystal. The mobility measured along the twin boundaries was found to be very high ( $\sim 7 \text{ cm}^2\text{V}^{-1}\text{s}^{-1}$ ) as compared to that measured across the twin boundaries. Due to high mobility along the grain boundaries, the  $J$ - $V$  characteristics could be measured, for the first time, down to 24 K. These measurements allowed us to generate a new bias-temperature phase diagram. According to this phase diagram, in the temperature range 300- 100K, the conduction mechanism changes from Ohmic to trap-free SCLC with applied bias. However, at temperatures  $<100 \text{ K}$ , the electrode limited processes dominate. It has been shown that the conduction mechanism changes from Schottky to multi-step tunneling with applied bias.

In the case of highly ordered CoPc films grown along the  $36.8^\circ$  grain boundary of  $\text{SrTiO}_3$  bicrystal, the measured mobility was  $150 \text{ cm}^2\text{V}^{-1}\text{s}^{-1}$ , which the highest reported value

till date. This value is even higher than that of PC single crystals ( $75 \text{ cm}^2\text{V}^{-1}\text{s}^{-1}$ ) [75]. The mobility of single crystal is limited due to the edge-to-face on packing of molecules. In the temperature range 300-160 K, the  $J$ - $V$  were found to be linear; whereas in the temperature range 160-30 K, the  $J$ - $V$  exhibited a bias dependent Ohmic to trap free SCLC mechanism.

Finally, we have demonstrated the applicability of ordered CoPc films for the ppb level  $\text{Cl}_2$  sensing. The CoPc chemiresistive sensor, exhibit faster response times (18 s), higher base-line stabilities (<5% drift) and enhanced sensitivity (80%) for 5 ppb  $\text{Cl}_2$ . It has been further shown that  $\text{Cl}_2$  chemisorption obeys Elovich equation that permits quantitative determination of  $\text{Cl}_2$  concentration from response rate of sensor.

### **Future scope of the work**

The research work of present thesis opens up various new areas of research. Some of these are:

- (i) Use of high mobility films for the fabrication of field effect transistors. In particular, the top gate geometry can be explored.
- (ii) Investigation of magnetic properties in the ordered CoPc or FePc films. Due to improved ordering one expects a magnetic correlation among Co or Fe sites.
- (iii) The binuclear (Co-Fe)Pc films can also be grown by MBE. The binuclear molecules have two Pc rings: one contains Fe while other contains Co. Such binuclear films have improved conjugation due to their large size, and therefore, are expected to have better mobilities.

- (iv) We have investigated CoPc and FePc films, and both of them have hole as charge carrier. One can also grow Pc having electrons as charge carrier (e.g. F<sub>16</sub>CuPc) by MBE, and investigate the charge transport.
- (v) Bilayer heterostructures consisting of electron and hole Pc layers can be grown to investigate the interfacial properties.

## BIBLIOGRAPHY

- [1] D. K. Aswal, S. Lenfant, D. Guerin, J.V. Yakhmi, D. Vuillaume, *Anal. Chim. Acta.* **568** 84 (2006).
- [2] C. Joachim, J.K. Gimzewski, A. Aviram, *Nature* **408** 541 (2000).
- [3] D.J. Wold, C.D. Frisbie, *J. Am. Chem. Soc.* **122** 2970 (2000).
- [4] S.P. Koiry, P. Jha, D.K. Aswal, S.K. Nayak, C. Majumdar, S. Chattopadhyay, S.K. Gupta, J.V. Yakhmi, *Chem. Phys.Lett.* **485** 137 (2010).
- [5] S.P. Koiry, D.K. Aswal, A.K. Chauhan, V. Saxena, S.K. Nayak, S.K. Gupta, J.V. Yakhmi, *Chem. Phys.Lett.* **453** 68 (2008).
- [6] G. Cuniberti, G. Fagas, K. Richter, *Introducing Molecular Electronics*, Springer, Berlin, (2005).
- [7] C. D. Dimitrakopoulos, P. R. L. Malenfant, *Adv. Mater.* **14** 99 (2002).
- [8] W. D. Howard, O. F. Prache, *IBM J. Res & Dev.* **45** 115 (2001).
- [9] D. K. Aswal, J.V. Yakhmi, *Molecular and Organic Electronics Devices*, Nova Science Publishers, Inc, New York (2010).
- [10] J. M. Shaw, P. F. Seidler, *Org. Electron.* **45** 1 (2001).
- [11] D. Wohrle, D. Meissner, *Adv. Mater.* **3** 129 (1991).
- [12] H. Y. Choi, S. H. Kim, J. Jang, *Adv. Mater.* **16** 732 (2004).
- [13] T. Tsutsui, K. Fujita, *Adv. Mater.* **14** 949 (2002).
- [14] D. Wohrle, D. Meissner *Adv. Mater.* **3** 129 (1991).
- [15] A. Salomon, D. Cahen, S.M. Lindsay, J. Tomfohr, V.B. Engelkes, C.D. Frisbie, *Adv. Mater.* **15** 1881 (2003).
- [16] A. Braun, J. Tcherniac, *Ber. Deutsch. Chem. Ges.* **40** 2709 (1907).

- [17] R.P. Linstead, A. R. Lowe, *J. Chem. Soc.* 1022 (1934).
- [18] Y. Iyechika, K. Yakushi, I. Ikemoto, H. Kuroda, *Acta. Cryst. B* **38** 766 (1982).
- [19] D. Eley, *Nature* **162** 819 (1948).
- [20] D. Gu, Q. Chen, X. Tang, F. Gan, S. Shen, K. Liu and H. Xu, *Optics Communication* **121** 125 (1995).
- [21] C.C. Leznoff and A.B. P. Lever. *Phthalocyanines: properties and Application*. VCH Publishers Inc, New York, (1989).
- [22] Meng sheng Liao, Steve Scheiner, *J. Chem Phys.* **114** 9780 (2001).
- [23] Z. Bao, A. J. Lovinger, J. Brown, *J. Am. Chem. Soc.* **120** 207 (1998).
- [24] J. A. Rogers, Z. Bao, A. Dodabalapur, A. Makhija, *IEEE Electron. Dev. Lett.* **21** 100 (2000).
- [25] Y. Y. Lin, A. Dodabalapur, R. Sarpeshkar, Z. Bao, W. Li, K. Balwin, V. R. Raju, H. E. Katz, *Appl. Phys. Lett.* **74** 2714 (1999).
- [26] B. Crone, A. Dodabalapur, Y. Y. Lin, R. W. Filas, Z. Bao, A. Laduca, R. Sarpeshkar, H. E. Katz, W. Li, *Nature* **403** 521 (2000).
- [27] J.A. Rogers, Z. Bao, K. Baldwin, A. Dodabalapur, B. Crone, V. R. Raju, V. Kuck, H. Katz, K. Amundson, J. Ewing, P. Drzaic. *Proc. Natl. Acad. Sci.* **98** 4835 (2000).
- [28] R. D. Gould, *Coord. Chem. Rev.* **156** 237 (1996).
- [29] S. M. Bayliss, S. Heutz, G. Rumbles and T. S. Jones. *Phys. Chem. Chem. Phys.* **1** 3673 (1999).
- [30] J. M. Robertson, *J. Chem. Soc.* 615 (1935).
- [31] C. J. Brown, *J. Chem. Soc.* 2488 (1968).
- [32] Josep Oriol Osso Torne, PhD thesis.

- [33] M. Ashida, N. Uyeda and E. Suito, *J. Cryst. Growth*, **8** 45 (1971).
- [34] J. F. Kirner, W. Dow, W. R. Scheidt, *Inorg. Chem.* **19** 1685 (1976).
- [35] G.A. Williams, B. N. Figgis, R. Mason, S.A. Mason, P. F. Fielding, *J. Chem. Soc. Dalton Trans.* 1688 (1980).
- [36] W.E. Spicer, I. Lindau, P.E. Gregory, C.M. Garner, P. Pianetta, P.W. Chye, *J. Vac. Sci. Technol.* **13** 780 (1976).
- [37] W.E. Spicer, P.W. Chye, P.R. Skeath, C.Y. Su, I. Lindau, *J. Vac. Sci. Technol.* **16** 1422 (1979).
- [38] W.E. Spicer, Z. Liliental-Weber, E. Weber, N. Newman, T. Kendelewicz, R. Cao, C. McCants, P. Mahowald, K. Miyano, I. Lindau, *J. Vac. Sci. Technol. B* **6** 1245 (1988).
- [39] H. Vazquez, R. Oszwaldowski, P. Pou, J. Ortega, R. Perez, F. Flores, A. Kahn, *Euro Phys. Lett.* **65** 802 (2004).
- [40] H. Vazquez, F. Flores, R. Oszwaldowski, J. Ortega, R. Perez, A. Kahn, *Appl. Surf. Sci.* **234** 107 (2004).
- [41] S.M. Sze, *Physics of Semiconductor Devices*, 2nd ed., Wiley, New York, (1981).
- [42] J.G. Simmons, *J. Appl. Phys.* **34** 2581 (1963).
- [43] R.H. Fowler, L. Nordheim, *Proceedings of the Royal Society of London* **119** 173 (1928).
- [44] M. Raikh, X. Wei, *Mol. Cryst. Liq. Cryst.* **256** 563 (1994).
- [45] C. R. Crowell, *Solid state Electronics* **8** 395 (1965).
- [46] J.G. Simmons, *Phys. Rev.* **166** 3 (1968).
- [47] M. A. Lampert, *Rep. Prog. Phys.* **27** 329 (1964).

- [48] J. G. Simmons, *J. Phys. D: Appl. Phys.* **4** 613 (1971).
- [49] N. F. Mott *Phil. Mag.* **19** 835 (1969).
- [50] B. Sh. Barkhalov, Yu. A. Vidadi, *Thin solid Films*, **40** L5 (1977).
- [51] C. Hamann, C. Tantzsch, *Thin Solid Films*, **36** 81 (1976).
- [52] F.R. Fan, L. R. Faulkner, *J. Chem. Phys.* **69** 3334 (1978).
- [53] A. K. Mahapatra et al, *Appl. Phys. Lett.* **80** 4840 (2002).
- [54] A. K. Hasan, R. D. Gould, *J. Phys D* **22** 1162 (1989).
- [55] A. K. Hassan, R. D. Gould, *Int. J. Electron* **69** 11 (1990).
- [56] T. S. Shafai, R. D. Gould, *Int. J. Electron* **73** 307 (1992).
- [57] T. S. Shafai, R. D. Gould, *Int. J. Electron* **73** 1043 (1992).
- [58] T. Matsushima, H. Sasabe, C. Adachi, *Appl. Phys. Lett.* **88** 033508 (2006).
- [59] K. Xiao, Y. Liu, G. Yu, D. Zhu, *Appl. Phys. A* **77** 367 (2003).
- [60] A. Sussman, *J. Appl. Phys.* **38** 2738 (1967).
- [61] C. Hamann. *Phys. Status Solidi.* **26** 311 (1968).
- [62] R. D. Gould. *J. Phys. D.* **9** 1785 (1986).
- [63] A. K. Hassan, R. D. Gould, *J. Phys. Condens Matter.* **1** 6679 (1989).
- [64] R. D. Gould, R. I. R. Blyth. *Phys. Status. Solidi A* **120** K57 (1990).
- [65] W. Mycielski, B. Ziokowska, A. Lipinski, *Thin Solid Films* **91** 335 (1982).
- [66] W. Mycielski, M. Zabkowski-Waclawek, *Thin Solid Films.* **146** 1 (1987).
- [67] Z. Bao, A. J. Lovinger, A. Dodabalapur. *Appl. Phys. Lett.* **69**, 3066 (1996).
- [68] G. M. Delaete, J. P. Fillard, F. J. Marco, *Solid State Commun.*, **2** 373 (1964).
- [69] Veaceslav Coropceanu, J. Cornil, D. A. de Silva Filho, Y. Olivier, R. Silbey, J. L. Bredus, *Chem. Rev.* **107** 926 (2007).

- [70] M. M. El-Nahass, A. M. Farid, A. A. Attia, H. A. M. Ali, *Appl. Surf. Sci.* **252** 7553 (2006).
- [71] A. S. Riad, *Physica B*, **270** 148 (1999).
- [72] W. Mycielski, B. Ziolkowska, A. Lipinski, *Thin Solid Films* **91** 335 (1982).
- [73] Ruchi Agrawal, Pramod Kumar, Subhasis Ghosh, Ajit Kumar Mahapatro, *Appl. Phys. Lett.* **93**, 073311 (2008).
- [74] A. Ioannidis, J. P. Dodelet, *J. Phys. Chem. B* **101** 891 (1997).
- [75] George H. Heilmeyer, Sol. E. Harrison, *Phys. Rev.* **232** 5 (1963).
- [76] Koichi Yamada, J. Takeya, K. Shigeto, K. Tsukagoshi, Y. Aoyagi, Y. Iwasa, *Appl. Phys. Lett.* **88**, 122110 (2006).
- [77] R. W. I. de Boer, A. F. Stassen, M. F. Craciun, C. L. Mulder, A. Molinari, S. Rogge, A. F. Morpurgo, *Appl. Phys. Lett.* **86** 262109 (2005).
- [78] R. D. Gould, M. S. Rahman, *J. Phys. D: Appl. Phys.* **14** 79 (1981).
- [79] Haibo Wang, De Song, Junliang Yang, Bo Yu, Yanhou Geng, and Donghang Yan, *Appl. Phys. Lett.* **90** 253510 (2007).
- [80] Hirokazu Tada, Hiroshi Touda, Masaki Takada, Kazumi Matsushige, *Appl. Phys. Lett.* **76** 873 (2000).
- [81] Z. Bao, A. J. Lovinger, J. J. Brown. *J. Am. Chem. Soc.* **120** 207 (1998).
- [82] H. Wang, F. Zhu, J. Yang, Y. Geng, D. Yan. *Adv. Mater.* **19**, 2168 (2007).
- [83] Z. Bao, A. J. Lovinger, A. Dodabalapur. *Adv. Mater.* **9**, 42 (1997).
- [84] H. S. Soliman, M. M. El-Nahass, A. M. Farid et al *Eur. Phys. J. Ap.* **21** 187 (2003).
- [85] Krishna Seshan, *Handbook of Thin Film Deposition Techniques* William Andrew Inc., (2002).

- [86] A. Kirfel, K. Eichhorn, *Acta Crystallogr. A* **46** 271 (1990).
- [87] J. Ahn, J. W. Rabalais, *Surf. Sci.* **388** 121 (1997).
- [88] Peter J. Eng et al, *Science* **288** 1029 (2000).
- [89] S. Geller, V.B. Bala, *Acta Crystallogr.* **9** 1019 (1956).
- [90] G. W. Berkestresser, A. J. Valentino, C. d. brindle, *J. crystal growth* **109** 467 (1991).
- [91] Lixin Cao, E. Sozontov, J. Zegenhager, *Phys. Stat. sol. (a)* **181** 387 (2000).
- [92] Q.D. Jiang, Z.J. Huang, A. Brazdeikis, M. Dezaneti, C.L. Chen, P. Jin, C.W. Chu, J. Zegenhagen, *Mater. Sci. Eng. B* **56** 100 (1998).
- [93] Q. D. Jiang, X. Q. Pan, J. Zegenhagen, *Phys. Rev. B* **56** 6947 (1997).
- [94] *The Crystalline State*, W. L. Bragg, Vol. 1, A General Survey, London: George Bell, (1993).
- [95] B. D. Cullity, *Elements of X-ray Diffraction*, second edition, Addison-Wesley, (1978).
- [96] M.F. Toney, T.C. Haung, S. Brennan, Zophia Rek, *J. Mater. Res.* **3** 351 (1988).
- [97] Liqiang Li, Qingxin Tang, Hongxiang Li, Wenping Hu *J. Phys. Chem. B*, **112** 10405 (2008).
- [98] E. Barrena, J.O. Osso, F. Schreiber, M. Garriga and M.I. Alonso, H. Dosch, *J. Mater. Res.* **19** 7 (2004).
- [99] V. Holy, *Phys. Rev. B.* **47** 15896 (1993).
- [100] Instruction Manual, Multiview 4000SPM/AFM, Nanonics Imaging Pvt. Ltd, Israel.
- [101] I. Horcas, R. Fernández, J. M. Gómez-Rodríguez, J. Colchero, J. Gómez-Herrero, A. M. Baro, *Rev. Sci. Instrum.* **78** 013705 (2007).

- [102] Ian M. Watt, *The Principles and practice of electron microscopy*, Cambridge University Press, (1985).
- [103] P. J. Goodhew, F. J. Humphreys, *Electron Microscopy and Analysis*, second edition, Taylor and Francis (1988).
- [104] D. Briggs, M.P. Seah, *Practical Surface Analysis by Auger and X-ray Photoelectron Spectroscopy*, Wiley, (1983).
- [105] John F. Watts, John Wolstenholme, *An Introduction to Surface Analysis by XPS and AES*, John Wiley and Sons, (2003).
- [106] J. F. Moulder, W.F. Stickle, P.E. Sobol, K. D. Bomben, *Handbook of X-ray Photoelectron Spectroscopy*, Physical electronics, USA, (1995).
- [107] W. Kemp, *Organic Spectroscopy*, ELBS-McMillan, London, (1979).
- [108] Skoog, Holler, Nieman, *Principles of instrumental analysis*, 5<sup>th</sup> ed, Brooks Cole, (1998).
- [109] D. Tondelier, K. Lmimouni, D. Vuillaume, *Appl. Phys. Lett.* **85** 5763 (2004).
- [110] S. Tiwari, N. C. Greenham, *Opt. Quan. Electron.* **4** 69 (2009).
- [111] F. Schreiber, *Phys. stat. sol. (a)* **201** 1037 (2004).
- [112] D. Bhattacharyya, D. Joseph, A.K. Poswal, *Nucl. Instrum. Methods Phys. Res. B* **248** 264 (2006).
- [113] C.W. Miller, A. Sharoni, G. Liu, C.N. Colesniue, B. Fruhberber, I.K. Schuller, *Phys. Rev. B* **72** 104113 (2005).
- [114] T. Nonaka, Y. Nakagawa, Y. Mori, M. Hirai, T. Matsunobe, M. Nakamura, T. Takahagi, A. Ishitani, H. Lin, K. Koumoto, *Thin Solid films* **256** 262 (1995).
- [115] R. Seoudi, G.S. El-Bahy, Z.A.El. Sayed, *J. Mol. Struct.* **753** 119 (2005).

- [116] M.J. Cook, N.B. McKeown, J.M. Simmons, A.J. Thomson, M.F. Daniel, K.J. Harrison, R.M. Richardson, S.J. Roser, *J. Mater. Chem.* **1** 121 (1991).
- [117] J. Mack, M.J. Stillman, *Inorg. Chem.* **40** 812 (2001).
- [118] T.N. Misra, *Rev. Pure Appl. Chem.* **15** 39 (1965).
- [119] J.T. Pankove, *Optical Processes in Semiconductors*, Prentice-Hall Inc., Englewood Cliffs, New Jersey, USA, (1970).
- [120] H. Yoshida, Y. Tokura, T. Koda, *Chem. Phys.* **109** 375 (1986).
- [121] Y. Tokura, T. Koda, Y. Nechika, H. Kurda, *Chem. Phys. Lett.* **102** 174 (1983).
- [122] A. Koma, K. Sunouchi, T. Miyajima, *Microelectron. Eng.* **2** 129 (1984).
- [123] A. Koma, *J. Cryst. Growth* **236** 201 (1999).
- [124] S.D. Wang, X. Dong, C.S. Lee, S.T. Lee, *J. Phys. Chem. B* **108** 1529 (2004).
- [125] T. Kawabe, K. Tabata, E. Suzuki, Y. Yamaguchi, Y. Nagasawa, *J. Phys. Chem. B* **105** (2001) 4239.
- [126] Haan de, A., Debliquy, M., & Decroly, A. *Sensor and Actuators B*, **57** 69 (1999).
- [127] . T. D. Anthopoulos and T. S. Shafai, *J. Vac. Sci. Technol. A* **20**, 295 (2002).
- [128] A. K. Mahapatro and S. Ghosh, *J. Appl. Phys.* **101**, 034318 (2007).
- [129] D. S. Shang, L. D. Chen, Q. Wang, W. Q. Zhang, Z. H. Wu, and X. M. Li, *Appl. Phys. Lett.* **89** 172102 (2006).
- [130] I. Zhivkov, E. Spassova, D. Dimov, and G. Danev, *Vacuum* **76**, 237 (2004).
- [131] M.A. Rafiq, Y. Tsuchiya, H. Mizuta, S. Oda, S. Uno, Z.A. Durrani, W.I. Mine, *Appl. Phys. Lett.* **87** 182101 (2005).
- [132] Y.Z. Wu, C.R. Chang, D.J. Zhang, *Appl. Phys. Lett.* **95** 033508 (2009).
- [133] C. D. Dimitrakopoulos, D. J. Masearo, *IBM J. Res. Develop.* **45** 11 (2001).

- [134] Z. Wei, W. Xu, W. Hu, D. Zhu, *Langmuir* **25**, 3349 (2009).
- [135] H. Bässler, *Phys. Status Solidi B* **175** 15 (1993).
- [136] L. Wang, D. Fine, D. Basu, A. Dodabalpur, *J. Appl. Phys.* **101** 054515 (2007).
- [137] N. I. Craciun, J. Wildeman, P. W. M. Blom, *Phys. Rev. Lett.* **100** 056601 (2008).
- [138] L. Lozzi, S. Santucci, S. L. Rosa, *J. Vac. Sci. Technol. A* **22** 1477 (2004).
- [139] F. Petraki, V. Papaefthimiou, S. Kennou, *J. Phys.: Conf. Ser.* **10** 135 (2005).
- [140] N. J. Watkins, L. Yan, Y. Gao, C. W. Tang, *Proc. SPIE* **4800** 248 (2003).
- [141] D. K. Aswal, S. Lenfant, D. Guerin, J. V. Yakhmi, and D. Vuillaume, *Small* **1** 725 (2005).
- [142] J. H. Wei, Y. L. Gao, and X. R. Wang, *Appl. Phys. Lett.* **94** 073301 (2009).
- [143] A. S. Dhoot, G. M. Wang, D. Moses, and A. J. Heeger, *Phys. Rev. Lett.* **96** 246403 (2006).
- [144] T. A. Skotheim, R. L. Elsenbaumer, J. R. Reynolds, *Handbook of Conducting Polymers*, 2<sup>nd</sup> ed. Marcel Dekker Inc. Newyork (1998).
- [145] P. W. M. Blom, M. J. M. de Jong, M. G. van Munster, *Phys. Rev. B* **55** R656 (1997).
- [146] J. L. Solis, S. Saukko, L.B. Kish, C.G. Granqvist, V. Lantto, *Sens. Actuat. B* **77** 316 (2001).
- [147] Korotcenkov G., *Sens. Actuat. B* **107** 209 (2005).
- [148] J. Liu, X. Wang, Q. Peng, T. Li, *Sens. Actuat. B* **115** 481 (2006).
- [149] Hotovy I., V. Rehacek, P. Siciliano, S. Capone, L. Spiess, *Thin Solid Films* **418** 9 (2002).
- [150] Bai H., G. Shi, *Sensors* **7** 267 (2007).
- [151] Potje K. Kamloth, *Chem. Rev.* **108** 367 (2008).

- [152] Hatchett D. W., M.Josowicz, *Chem. Rev.* **108** 746 (2008).
- [153] Q. Zhou, R.D. Gould, *Thin Solid Films* **317** 436 (1998).
- [154] Toshihiro Miyata, Seiji Kawaguchi, Makoto Ishii, Tadastugu Minami, *Thin Solid Films* **425** 255 (2003).
- [155] Collins R.A., K.A. Mohammed, *J. Phys. D: Appl. Phys.* **21** 154 (1988).
- [156] C. J. Liu, J. C. Hsieh, and Y. H. Ju. *J. Vac. Sci. Technol. A* **14** 3 (1996).
- [157] Yuh-Lang Lee, Chuan-Yi Hsiao, Chien-Hsiang Chang, Yu-Min Yang, *Sens. Actuat. B* **94** 169 (2003).
- [158] Kuo Chuan Ho, Yi- Ham Tsou, *Sens. Actuat. B* **77** 253 (2001).
- [159] Kuo-Chuan Ho, Chun-Ming Chena, Jung-Yu Liao, *Sens. Actuat. B* **108** 418 (2005).
- [160] D. P. Jiang, A. D. Lu, Y. J. Li, X. M. Pang, Y. L. Hua, *Thin solid films* **199** 173 (1991).
- [161] A. Belghachi, R. A. Collins, *J. Phys. D: Appl. Phys.* **21** 1647 (1988).
- [162] C.J. Liu, C.H. Peng, Y.H. Ju, J.C. Hsieh, *Sens. Actuat. B* **52** 264 (1998).
- [163] Xian Li, Ya-Dong Jiang, Guang-Zhong Xie, Xiao-Song Du, Hui-Ling Tai, Jian-Fei Yan, Song-Qi Fu, *IEEE explorer* 978-1-4244-8026-5.
- [164] Bin Wang, Xia Zuo, Yiqun Wu, Zhimim Chen, Chunying He, Wubiao Duan, *Sens. Actuat. B* **152** 191 (2011).
- [165] M.I. Newton, T.K.H. Starke, M.R. Willis, G. McHale, *Sens. Actuat. B* **67** 307 (2000).
- [166] Xiujin Wang, Shiliang Ji, Haibo Wang, Donghang Yana, *Sens. Actuat. B* **160** 115 (2011).
- [167] M. Bora, D. Schut, M. A. Baldo, *Anal. Chem.* **79** 3298 (2007).

- [168] D.K. Aswal and S.K. Gupta, *Science and Technology of Chemiresistor Gas Sensors*, Nova Science Publisher, New York, (2007).
- [169] Hong-Ying Wang, Jerome B. Lando, *Langmuir* **10** 790 (1994).
- [170] M. Passard, C. Maleysson, A. Pauly, S. Dogo, J.P. Germain, J.P. Blanc, *Sens. Actuat. B.* **489** 18 (1994).
- [171] Kerp, H. R., Westerdui, K. T., van Veen, A. T., van Faassen, E. E. *J.Mater. Res.* **16** 503 (2001).
- [172] Bohrer, F. I., Sharoni, A., Colesniuc, C., Park, J., Schuller, I. K., Kummel, A. C., Trogler, W. C. *J. Am. Chem. Soc.* **129** 5640 (2007).
- [173] Park, J., Yang, R. D., Colesniuc, C., Sharoni, A., Jin, S., Schuller, I. K., Trogler, W. C., Kummel, A. C. *Appl. Phys. Lett.* **92** 193311 (2008).
- [174] N. L. Tran, A. C. Kummel, *J. Chem. Phys.* **127** 214701 (2007).
- [175] J. R. Macdonald, *Impedance Spectroscopy*, Wiley, New York (1987).
- [176] K. A. Miler, R. D. Yang, M. J. Hale, J. Park, B. Fruhberger, C. N. Colesniuc, I. K. Schuller, A. C. Kummel, W. C. Trogler, *J. Phys. Chem. B* **110** 361 (2006).
- [177] K. J. Laidler, *Chemical kinetics*, 3<sup>rd</sup> ed. Pearson education, (1987).
- [178] E.S. Kolesar, T.M. Wiseman, *Anal. Chem.* **61** 2355 (1989).
- [179] E.F. Vansant, P. Van Der Voort, K.C. Vrancken, *Characterization and Chemical Modification of the Silica Surface*, Elsevier, The Netherlands, p. 341 (1995).
- [180] R. Tongpool, S. Yoriya, *Thin Solid Films* **477** 148 (2005).
- [181] Richard I. Masel, *Principles of Adsorption and Reaction on Solid Surfaces*, Wiley-Interscience, New York, p. 519 (1996).